

Bangor University

DOCTOR OF PHILOSOPHY

Effect of Chemically Modified Transport Layers on Photovoltaic Behavior of P3HT:IC70BA-Based Organic Solar Cell

Almutairi, Fahad Naif A

Award date:
2021

Awarding institution:
Bangor University

[Link to publication](#)

General rights

Copyright and moral rights for the publications made accessible in the public portal are retained by the authors and/or other copyright owners and it is a condition of accessing publications that users recognise and abide by the legal requirements associated with these rights.

- Users may download and print one copy of any publication from the public portal for the purpose of private study or research.
- You may not further distribute the material or use it for any profit-making activity or commercial gain
- You may freely distribute the URL identifying the publication in the public portal ?

Take down policy

If you believe that this document breaches copyright please contact us providing details, and we will remove access to the work immediately and investigate your claim.



PRIFYSGOL
BANGOR
UNIVERSITY

Effect of Chemically Modified Transport Layers on Photovoltaic Behavior of P3HT:IC₇₀BA-Based Organic Solar Cell

By

Fahad Naif A Almutairi

A thesis submitted in partial fulfilment for

the degree of Doctor of Philosophy in the

College of Environmental Science and Engineering

School of Computer Science and Electronic Engineering

in collaboration with Biocomposites Centre at Bangor University

February 2021

Declaration and Consent

Details of the Work

I hereby agree to deposit the following item in the digital repository maintained by Bangor University and/or in any other repository authorized for use by Bangor University.

Author Name: **Fahad Naif A Almutairi**

Title: **Effect of Chemically Modified Transport Layers on Photovoltaic Behavior of P3HT:IC₇₀BA-Based Organic Solar Cell.**

Supervisor/Department: **Dr. Mohammed Mabrook / Electronic Engineering**

Qualification/Degree obtained: **PhD**

This item is a product of my own research endeavors and is covered by the agreement below in which the item is referred to as “the Work”. It is identical in content to that deposited in the Library, subject to point 2 below.

Non-exclusive Rights

Rights granted to the digital repository through this agreement are entirely nonexclusive. I am free to publish the Work in its present version or future versions elsewhere.

I agree that Bangor University may electronically store, copy or translate the Work to any approved medium or format for the purpose of future preservation and accessibility. Bangor University is not under any obligation to reproduce or display the Work in the same formats or resolutions in which it was originally deposited.

Bangor University Digital Repository

I understand that work deposited in the digital repository will be accessible to a wide variety of people and institutions, including automated agents and search engines via the World Wide Web.

I understand that once the Work is deposited, the item and its metadata may be incorporated into public access catalogues or services, national databases of electronic theses and dissertations such as the British Library’s EThOS or any service provided by the National Library of Wales.

I understand that the Work may be made available via the National Library of Wales Online Electronic Theses Service under the declared terms and conditions of use (<http://www.llgc.org.uk/index.php?id=4676>). I agree that as part of this service the National Library of Wales may electronically store, copy or convert the Work to any approved medium or format for the purpose of future preservation and accessibility. The National Library of Wales is not under any obligation to reproduce or display the Work in the same formats or resolutions in which it was originally deposited.

Statement 1:

This thesis is the result of my own investigations, except the preparation of PAMAM dendrimers materials were performed in collaboration with the School of chemistry, Bangor University, UK.

Signed (candidate) Date

Statement 2:

I agree to submit my thesis (the Work) electronically via Bangor University's e-submission system, however I opt-out of the electronic deposit to the Bangor University (BU) Institutional Digital Repository, the British Library ETHOS system, and/or in any other repository authorized for use by Bangor University, due to lack of permissions for use of third party material.

In addition to the above I also agree to the following:

1. That I am the author or have the authority of the author(s) to make this agreement and do hereby give Bangor University the right to make available the Work in the way described above.
2. That the electronic copy of the Work deposited in the digital repository and covered by this agreement, is identical in content to the paper copy of the Work deposited in the Bangor University Library, subject to point 4 below.
3. That I have exercised reasonable care to ensure that the Work is original and, to the best of my knowledge, does not breach any laws – including those relating to defamation, libel and copyright.
4. That I have, in instances where the intellectual property of other authors or copyright holders is included in the Work, and where appropriate, gained explicit permission for the inclusion of that material in the Work, and in the electronic form of the Work as accessed through the open access digital
5. Repository, or that I have identified and removed that material for which adequate and appropriate permission has not been obtained and which will be inaccessible via the digital repository.
6. That Bangor University does not hold any obligation to take legal action on behalf of the Depositor, or other rights holders, in the event of a breach of intellectual property rights, or any other right, in the material deposited.
7. That I will indemnify and keep indemnified Bangor University and the National Library of Wales from and against any loss, liability, claim or damage, including without limitation any related legal fees and court costs (on a full indemnity bases), related to any breach by myself of any term of this agreement.

Signature: Date:

Contents

Abstract.....	i
Acknowledgements	iii
Chapter 1	1
Introduction	1
1.1 General background.....	1
1.2 Brief development history of organic solar cells	4
1.2.1 First generation solar cell	5
1.2.2 Second generation solar cell.....	6
1.2.3 Third generation solar cell.....	7
1.3 Literature review	8
1.4 Aim and objectives.....	11
1.5 Thesis outline.....	12
References.....	12
Chapter 2	15
Background and Theoretical Review	15
2.1 Introduction	16
2.2 Organic Semiconductors	17
2.3 Electron transport materials.....	20
2.4 Hole transport materials.....	22
2.5 Transparent conducting electrode	22
2.6 Top electrode	23
2.7 Buffer layers	24
2.8 Organic solar cells structure	25
2.8.1 Bulk Heterojunction (BHJ) organic solar cells	25
2.9 Basic operation principles of Organic solar cells.....	26

2.9.1 Light absorption and exciton generation.....	28
2.9.2 Exciton migration and dissociation	29
2.9.3 Charges transport and collection	30
2.9.4 Loss mechanism in organic solar cell.....	30
2.10 Electrical Characterisation of organic solar cells.....	31
2.10.1 Equivalent circuit diagram of organic solar cells	31
2.10.2 Current-voltage characterisation	32
2.10.2.1 Open-circuit voltage.....	34
2.10.2.2 Short-circuit current.....	34
2.10.2.3 Series and shunt resistance.....	34
2.10.2.4 Fill-factor.....	35
2.10.2.5 Origin of dark-current ideality factor.....	37
2.10.2.6 Power conversion efficiency	38
References.....	40
Chapter 3	47
Materials and Experimental Techniques	47
3.1 Introduction	47
3.2 Laboratory environment.....	47
3.3 Materials.....	48
3.3.1 Poly (3-hexylthiophene-2, 5-diyl) (P3HT).....	48
3.3.2 Indene-C70 Bisadduct (IC ₇₀ BA)	49
3.3.3 Poly(3,4-ethylenedioxythiophene) poly (styrenesulfonate) (PEDOT: PSS)	50
3.3.4 Lithium Floride (LiF).....	51
3.3.5 Graphene	53
3.4 Fabrication Methods.....	55
3.4.1 Spin Coating	55
3.4.2 Thermal Evaporation	56

3.4.3 Profilometer.....	57
3.5 Procedure of Fabrication.....	58
3.5.1 Substrate preparation	58
3.5.2 Spin coating of the hole transport layer	59
3.5.3 Preparation of the active layer solution.....	59
3.5.4 Spin coating of electron transport layer	59
3.5.5 Evaporation of buffer layer and top electrodes.....	60
3.6 Device characterization.....	60
3.6.1 Atomic Force Microscopy.....	60
3.6.2 Ultra-violet/visible Spectroscopy	61
3.6.3 Current-Voltage (<i>I-V</i>) Characterisation.....	61
References.....	64
Chapter 4	68
Optimisation of P3HT:IC70BA-based Organic Solar Cells.....	68
4.1 Introduction	68
4.2 P3HT:IC ₇₀ BA based OHJ solar cells with different solvents conditions.....	69
4.2.1 Fabrication process.....	69
4.2.2 Morphological analysis using AFM	70
4.2.3 Optical Absorption measurements	73
4.2.4 Electrical measurements.....	76
4.2.4.1 Diode measurements	76
4.2.4.2 Photovoltaic performance.....	80
4.3 IC ₇₀ BA-based devices under different concentration conditions.....	83
4.3.1 Fabrication process.....	83
4.3.2 Morphological analysis using AFM	83
4.3.3 Optical Absorption measurements	86
4.3.4 Electrical measurements.....	88

4.3.4.1 Diode measurements	88
4.3.4.2 Photovoltaic performance.....	92
4.4 IC ₇₀ BA-based devices under different annealing conditions.....	94
4.4.1 Fabrication process.....	94
4.4.2 Morphological analysis using AFM	95
4.4.3 Optical Absorption measurements	97
4.4.4 Electrical measurements.....	99
4.4.4.1 Diode measurements	99
4.4.4.2 Photovoltaic performance.....	102
4.5 IC ₇₀ BA-based devices under different annealing time conditions	104
4.5.1 Fabrication process.....	104
4.5.2 Morphological analysis using AFM	105
4.5.3 Optical Absorption measurements	108
4.5.4 Electrical measurements.....	109
4.5.4.1 Diode measurements	109
4.5.4.2 Photovoltaic performance.....	112
4.6 Using Lithium Fluoride (LiF) as electrons collecting buffer layer	115
4.6.1 Fabrication process.....	115
4.6.2 Morphological analysis using AFM	115
4.6.3 Optical Absorption measurements	117
4.6.4 Electrical measurements.....	118
4.6.4.1 Diode measurements	118
4.6.4.2 Photovoltaic performance.....	121
4.7 Summary	125
References:.....	127
Chapter 5	134

Improved OSC performance by modified hole transport layer using different metal salts	134
5.1 Introduction	134
5.2 Fabrication process.....	136
5.3 Morphological analysis using AFM.....	137
5.4 Optical Absorption measurements	141
5.5 Electrical measurements	145
5.5.1 Diode measurements.....	145
5.5.2 Photovoltaic measurements.....	150
5.6 Summary	154
References.....	155
Chapter 6	160
Effect of Graphene as an Electron Transport Layer.....	160
6.1 Introduction	160
6.2 Effect of Graphene as an electron transport layer.....	161
6.2.1 Different thickness conditions	161
6.2.1.1 Fabrication process	161
6.2.1.2 Morphological analysis using AFM.....	163
6.2.1.3 Optical Absorption measurements.....	166
6.2.1.4 Electrical measurements.....	168
6.2.1.4.1 Diode measurements	168
6.2.1.4.2 Photovoltaic performance	173
6.3 OSCs using graphene with chemical treatment conditions	176
6.3.1 Fabrication process.....	176
6.3.2 Morphological analysis using AFM	177
6.3.3 Optical Absorption measurements	178
6.3.4 Electrical measurements.....	180

6.3.4.1 Diode measurements	180
6.3.4.2 Photovoltaic performance.....	182
6.4 Summary	186
References.....	187
Chapter 7	191
Conclusions and Further Work	191
7.1 Conclusions.....	191
7.2 Further work	195

Abstract

Organic photovoltaic devices (OPVs) during the last decade have attracted a significant attention due to their simple processability and their advantages such as low costs and consider as an environmentally friendly and promising source of renewable energy. One of the main challenges faced by researchers in this field is how to improve the performance of the organic solar cells. In this thesis, a scientific approach has been used to optimize organic photovoltaic (OPV) devices and modify the hole transport layer (HTL) and electron transport layer (ETL). All devices in this work were prepared using Poly(3-hexylthiophene-2,5-diyl) (P3HT) as the donor and indene-C70 bisadduct (IC70BA) as the acceptor in the fabrication of the active layer of OPVs. Poly(3, 4 ethylenedioxythiophene):poly(styrenesulfonate) (PEDOT:PSS) was used as the hole transport layer, indium tin oxide (ITO) as anode and then aluminium (Al) was evaporated as the cathode. Optical, electrical, and morphological properties were investigated in all stages of these fabricated organic solar cells using different facilities such as UV visible spectrophotometer, atomic force microscopy (AFM) and current density-voltage (J-V) characterisation.

In the first part of this research, the optimisation of devices was carried out through investigating the use of different solvents, concentrations of active layer components, annealing temperatures, annealing time and the use of a buffer layer. For the solvents, three different solvents were used; chlorobenzene (CB), dichlorobenzene (DCB) and their co-solvent Mix (DCB:CB) and the results indicated that (DCB) showed the best PV behaviour with power conversion efficiency (PCE) of 2.8 %, short circuit current density (J_{sc}) of 17.04 mA.cm^{-2} , and open circuit voltage (V_{oc}) of 0.33V and fill factor (FF) of 55%. At the end, the final optimum structure was ITO/PEDOT:PSS/P3HT:IC70BA/LiF/Al with significant improvement in PCE of 5.5%, $V_{oc} = 0.79 \text{ V}$, FF of 56% and $J_{sc} = 12.5 \text{ mA.cm}^{-2}$.

In the second part aimed to improve OPV performance by modifying the hole transport layer using different metal salts, which are Copper Chloride (CuCl_2) and Lithium Chloride (LiCl). Each of salts was dissolved in a certain volume of deionized (DI) water, then mixed with accurate amount of PEDOT:PSS. While using PEDOT:PSS as a typical hole transport layer has shown PCE of 5.5%, the modified (HTL) by LiCl has increased to 18.4 %, with significant improvement in J_{sc} of 43.12 mA.cm^{-2} , $V_{oc} = 0.77 \text{ V}$ and FF of 55%.

In the third part, effect of Graphene as (ETL) has been studied. Two different solutions of graphene (normal one and chemically treated one) were used with different thicknesses and different concentrations. The highest results were for treated chemically, which were The PCE of 13.7%, J_{sc} of 50.08 mA.cm^{-2} , $V_{oc} = 0.61 \text{ V}$ and FF of 55%.

*Dedicated to my father's pure soul, my mother, my brothers, my sisters
and my family*

(Manal, Naif, Abdulrahman, Abdulaziz, Khalid, Faisal and Saud)

Acknowledgements

Firstly, I would like to thank God for everything; by whose grace, He has helped, and sustained me through from the beginning to the end of this program.

I am so indebted to my supervisor Dr. Mohammed Mabrook and deeply grateful for all his invaluable support, training, guidance and encouragement, and motivating enthusiasm. For his patience with me and believing in me, it is much appreciated. I could not have asked for a better supervisor and a mentor, I am appreciative, and I am proud to say that I have learnt from the best.

I would like to thank the Biocomposites Centre at Bangor University, represented by Dr. Ahmad Al-Dulaymi for the collaboration in preparing and chemical treatment of graphene solution used in this research.

Many thanks to Dr. Paul Sayers, Dr. Maysoon Ahmed, Dr. Thamraa Alshahrani, Amjad Alshawi and Ben Assinder for the help, and advice in the cleanroom facility at Bangor University. I want to acknowledge all the technical staff in the school of electronic engineering for all the support and assistance they have kindly provided in various capacities.

I would like to thank Shaqra university for the provision of a studentship and to Saudi cultural attaché in the UK for help and support.

I also acknowledge my family, for all their support and encouragement, I am very grateful for the blessing they have been in my life.

And for my friends, I am also thankful for all their prayerful support and encouragement that they have given me throughout the time of doing a PhD.

God bless everyone that has been involved in one way or the other in making this work a success.

Chapter 1

Introduction

1.1 General background

The energy consumption has been substantially increased since last several decades. The rapid increment of carbon dioxide (CO₂) concentrations in the environment is mainly due to the use of various conventional energy resources, i.e., fossil fuels. The use of these sources of energy results in different environmental concerns, including significant climate change, health issues, and global warming. The substantial rise of CO₂ emission in all around the world [1] is presented in Figure 1.1.

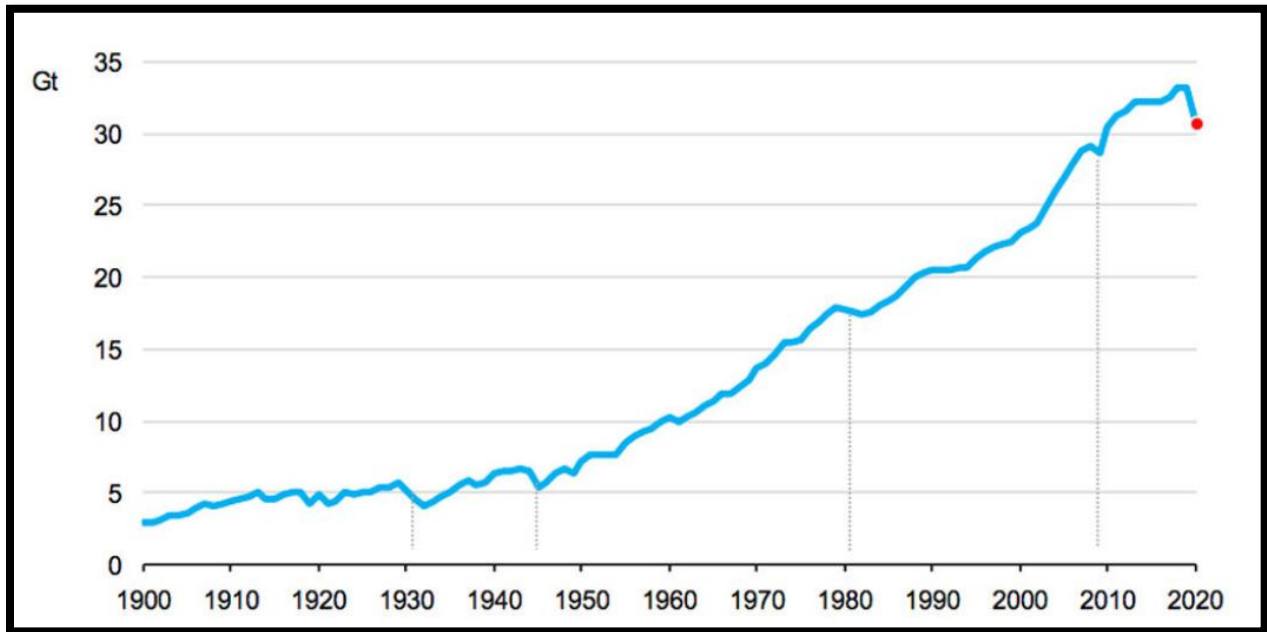


Figure 1.1: Significant growth in CO₂ global emission from last century [1].

The efficacy of nuclear energy supplies is also uncertain, due to the latest incident at the nuclear plants of Japan in March 2011. Thus, to satisfy existing and potential energy requirements, there is an immediate necessity to establish an environmentally sustainable and effective renewable energy sources [2]. Various sources of energy, such as solar, biomass, geothermal, and wind energy, represent the potential sources of renewable energy [3]. Solar energy is considered as the most efficient, reliable, environmentally friendly, and sustainable sources of energy [3]. Regularly, the sun energy coming on earth is approximately 1000 times greater than the daily use of the world. Nevertheless, the solar energy that is being used to fulfill the demands of the world is indeed minimal. There is still an immediate necessity for advanced technology that can convert sunlight into effective energy. One of the leading technologies for the conversion of the sun into electricity is photovoltaic (PV) cells. PV cells are strong electrical systems that work with the phenomenon of photovoltaic to directly transform light energy into electrical energy [4].

The direct transformation of solar light into the electricity inside photovoltaic cells is considered most effective ways of utilizing solar energy [5]. The photovoltaic action leads for the generation of electrical energy due to the exposure of light. The transmission of the photo generated electrons via material's excited energy levels towards the conduction energy band leads for an increase in voltage generation between the electrodes [2]. The first silicon-based PV cell was fabricated in 1954 and had shown the efficiency by 6 %. [6]. It is indeed a compelling method to transfer solar power into electrical power. However, the main disadvantage of these cells is their high manufacturing costs that require extraction of inorganic materials that are not easily accessible such as Ge, and the requirement of elevated processes temperatures. In the last 40 years, research development and experimentation work on organic solar cells has been increased significantly for a variety of reasons, such as the simplicity of manufacturing and extraction of lower cost, readily available organic materials, as well as the significant increase in energy conversion capacities [7]. Figure 1.2 displays the tested efficiency comparison for all the National Renewable Energy Laboratory (NREL) photovoltaic material systems.

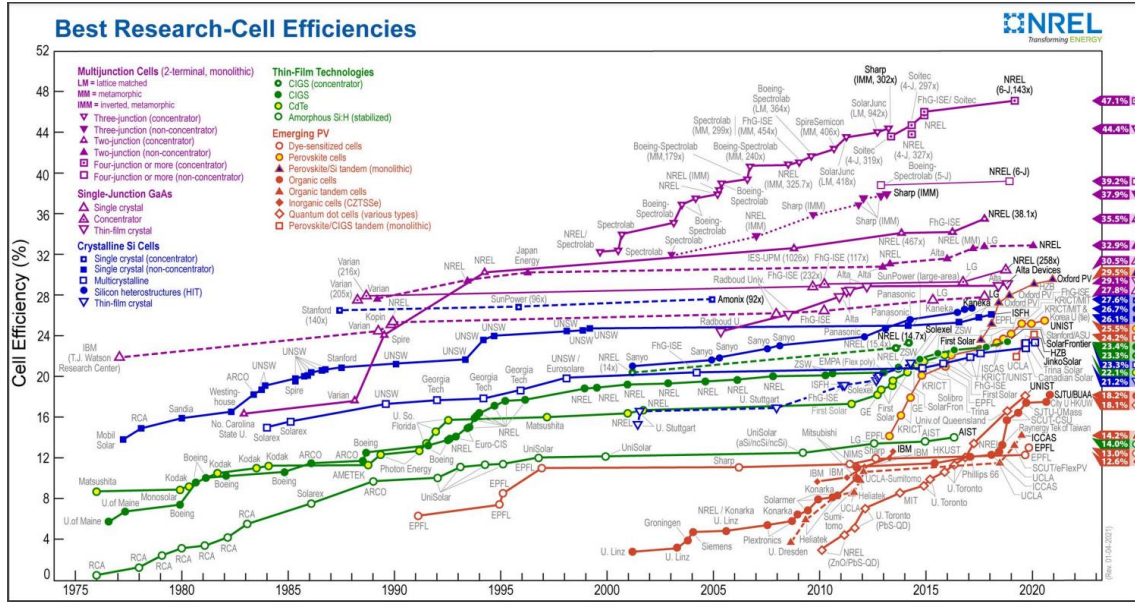


Figure 1.2: A comparison of verified recorded efficiencies for all PV material systems undertaken by NREL. The chart was downloaded 25th Jan 2021 [8].

Moreover, these materials have significantly attracted researchers related to the energy industry because they can be manufactured at low levels of temperatures and possess a higher value for the coefficient of absorption that enables the usage of thin films. The processing of such type of materials is rather flexible and thus allows flexibility for technological restriction and solubility to be modified. This has been further improved via the use of plastic substrates compared to other traditional silicon solar cells, rendering the system more effective. [9].

The Energy Information Administration of the US Government estimates that the world's consumption of energy would grow by more than 56% between 2010 and 2040. It is predicted that the bulk of this energy requirement would raise from emerging non-OECD (Organization for Economic Co-operation and Development) countries, as shown in the Figure 1.3.

Particularly in non-OECD nations, continuing growth is expected to contribute to higher demands of energy. Non-renewable sources of energy contaminate the environment and are likely to become far more expensive in the future because of their limited availability. In contrast, renewable sources of energy that are environmentally sustainable are infinitely accessible, and their costs decreased as their usage increases.

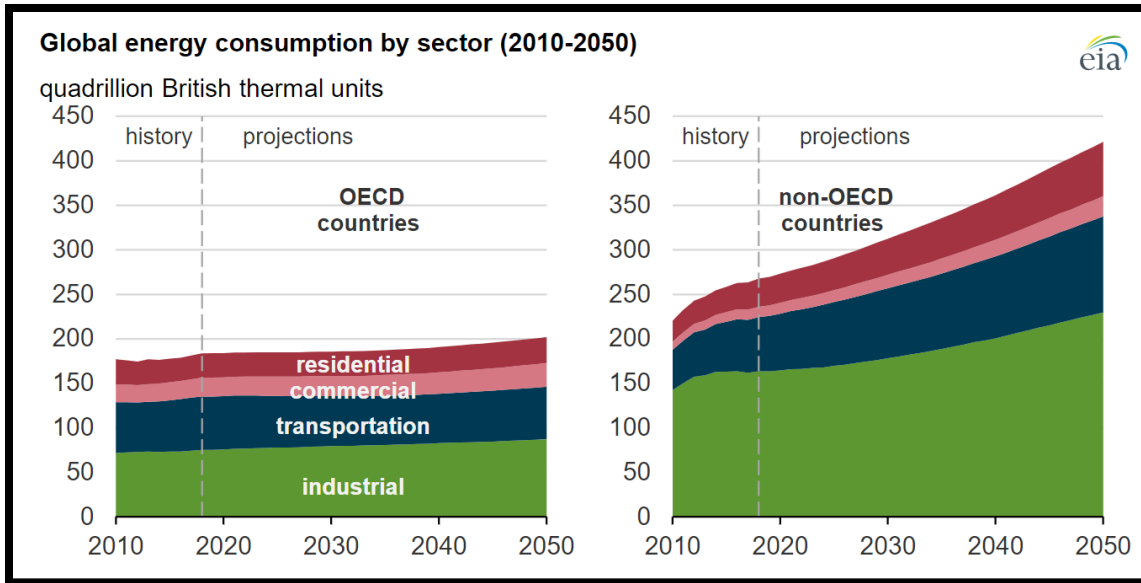


Figure 1.3: *The anticipated energy necessities of the world and the division between OECD and non-OECD countries [10].*

1.2 Brief development history of organic solar cells

Up to date, different types of solar cells have been classified as three different generations; the main different between these generations is basically the kind of materials used. The first one prepared by using crystalline silicon (Si) which is generally doped with Phosphorus (P) or Boron (B). The second generation of solar cell is based on semiconductor thin film technology; these include amorphous silicon (a-Si), polycrystalline silicon, cadmium telluride (CdTe) copper indium gallium selenide (CIGS) based solar cells. The third generation of which is based on a wide range of new materials. For instance, organic polymers, small molecules, nanotubes, quantum dots, silicon nanowires, and organic dyes [11].

Silicon (Si) solar cells dominate the PV market (92%) followed by cadmium telluride (CdTe, 5%), copper indium gallium selenide (CuInGaSe₂ or CIGS, 2%) and amorphous silicon (a-Si:H, ~1%). With thickness around 180 μm , Si wafer is the traditional material being used for module manufacturing and it has attained significant level of maturity at the industrial level. The production cost is a major concern for energy applications. About 50% of the cost of Si solar cells

production is due to Si substrate, and device processing and module processing accounts for 20% and 30% respectively [12].

1.2.1 First generation solar cell

In 1950 s, it was established the first-generation of solar cells which were based on crystalline Si. The advantages of these kinds of solar cells are stability, longer lifetime and higher efficiency. However, the manufacturing cost is one of the main issues with this generation. To produce this type of solar cell, highly pure Si is required and the processing costs too high, but and during the period 2010 to 2020, the silicon PV industry went through a period of significant changes, including a rapid decrease in manufacturing cost (more than -15% per year in average) and a continued increased in efficiency ($+2\%$ relative per year) and module power (typically $+5\text{ W}$ per year at the beginning of the decade, increasing much faster nowadays due to larger wafer sizes). The manufacturing cost reduction was driven by an increased collaboration between manufacturing partners [13].

According to Shockley-Queisser limitation, the highest efficiency for the material (such as Silicon) is found to be 32%. This is because the absorption of light by a material with such band gap corresponds to infrared light. In other words, photons of specific energies will power production, whereas other wavelengths which is not visible light such as radio waves and microwaves will not contribute [14]. Figure 1.4 shows the structure of the first generation solar cell based on crystalline silicon Si.

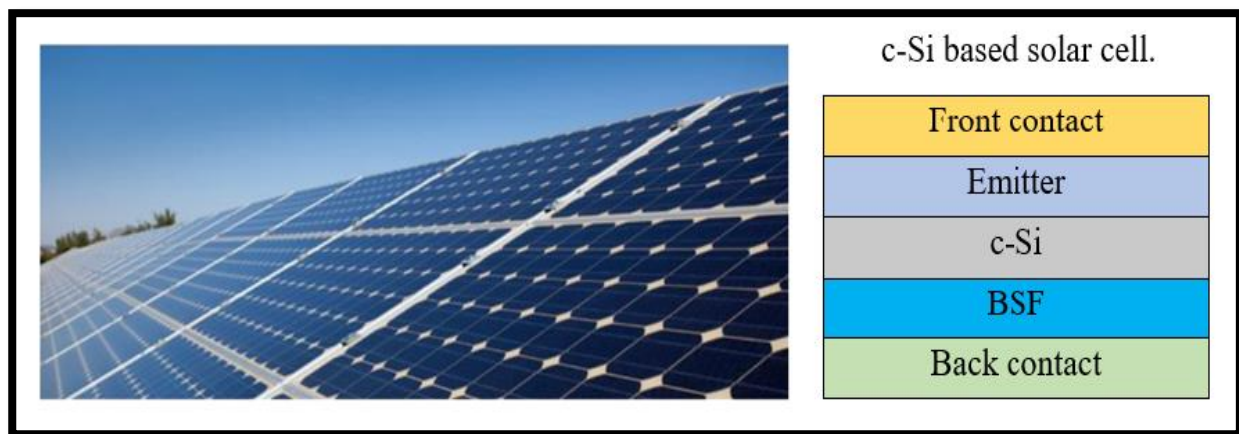


Figure 1.4: *First generation solar cell based on crystalline silicon Si.*

For crystalline-Si solar cells, the highest recorded efficiency was $25.6\pm0.5\%$ according to Panasonic HIT with an active area of 143.7 cm^2 ; this result has been certified by the Japanese National Institute of Advanced Industrial Science and Technology (NIST) [14]. Furthermore, an efficiency of $25.1\pm0.5\%$ have shown by smaller module crystalline-Si solar cells with an active area of 4.01 cm^2 which has been certified in Fraunhofer-Institut für Solare Energiesysteme (FhG-ISE) [14].

1.2.2 Second generation solar cell

To reduce the production cost of solar cells and accommodate new materials, a significant number of researches has been concentrated to improve and develop processes towards producing the second generation of solar cells. The latter covers III-V semiconductor cell technologies such as Gallium Arsenide (GaAs), thin film technology such as a-Si based thin film solar cells, Cadmium Telluride/Cadmium Sulfide (CdTe/CdS) solar cells and Copper Indium Gallium Selenide (CIGS) solar cells. a n-type layer of cadmium sulphide (CdS), and a p-type CdTe absorber layer. A good agreement between the simulation results and recent experimental data taken from literature has been achieved. The optimized design performs a short-circuit current density of 29.09 mA/cm^2 , an open-circuit voltage of 0.95 V , a fill-factor of 83.47% , and a conversion efficiency on the order of 23% under air mass 1.5 global spectrum (AM1.5G) with an incident irradiance of 1000 W.m^{-2} [15]. Moreover, the effects of layers thickness and doping on the photovoltaic cell parameters in copperindium-gallium-diselenide (CIGS) based solar cells, with a window layer (ZnO) and a buffer layer (CdS) have been investigated using solar cell capacitance simulator (SCAPS). The optimization has been made layer by layer and the results showed that the best structure must have a window layer (ZnO), a buffer layer (CdS) and an absorber layer (CIGS) that have thicknesses of 0.02 , 0.05 and $4\text{ }\mu\text{m}$, and doped with 10^{16} , 10^{16} and 10^{16} cm^{-3} , respectively. Cells with these features are found to give conversion efficiency of 25.9% [16]. A solar cell based on a CdTe thin film exhibited a world efficiency record of $(22.1 \pm 0.5)\%$, showing the following parameters measured under the global AM 1.5 spectrum (1000 W.m^{-2}) at $25\text{ }^\circ\text{C}$: $V_{oc} = 0.8872\text{ V}$, $J_{sc} = 31.69\text{ mA.cm}^{-2}$, fill factor (FF) = 0.785 over a designated illumination area of 0.4798 cm^2 [17]. Figure 1.5 shows the structure of the second generation solar cell based on GaAs, CdTe, CIGS and amorphous Si.

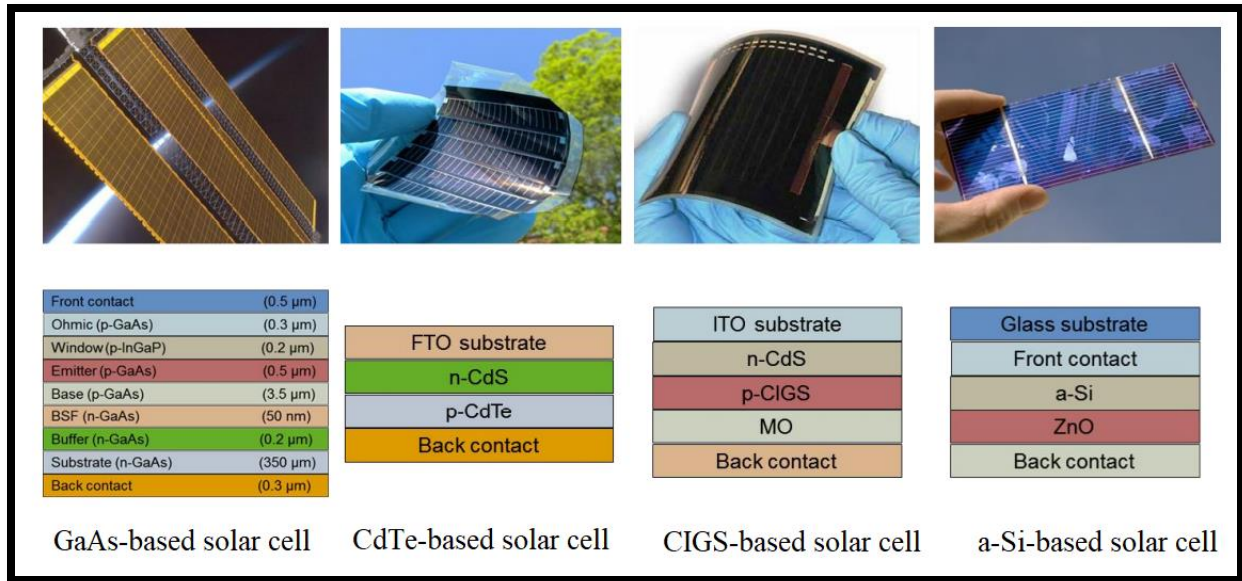


Figure 1.5: Second generation solar cell based on GaAs, CdTe, CIGS and amorphous Si.

1.2.3 Third generation solar cell

The solar cells of this generation is mainly based on new materials, which include conducting polymers, small molecules, nanotubes, quantum dots, silicon nanowires, and organic dyes [18]. The polymer or organic solar cells (OSCs) are mainly fabricated from thin films with a thickness of typically 100-200 nm of organic semiconductors (active layer) as shown in Figure1.6. Over the last two decades, a lot of different organic materials have been investigated to produce suitable layers for absorption which are: polymers, dyes and small-molecule as p-type semiconductor materials whereas n-type semiconductor materials are mostly carbon-based materials such as fullerene and its derivatives [19]. The advantages of organic materials such as their low-cost production as well as the viability of operating using flexible substrates, thus requiring less capital for investment, makes them with a significant competitive advantage over the previous two generations of solar cells [20]. OSCs are suitable for large manufacturing such as roll-to-roll printing process which potentially leads to low cost and large-scale flexible production [21]. Another advantage is ascribed to the versatile and diverse range of materials used, which provide a wide range of properties including tailored band gap and therefore a varied range of light harvesting efficiency and ability to cover a broad range of the solar spectrum [22]. On the other

hand, their efficiencies are much lower as compared to the use of inorganic materials and stability is considered as the main disadvantage for this generation of solar cells to compete with the conventional technology. The efficiency for organic solar cell increased steadily to over 18.2% in 2020 as shown in Figure 1.6.

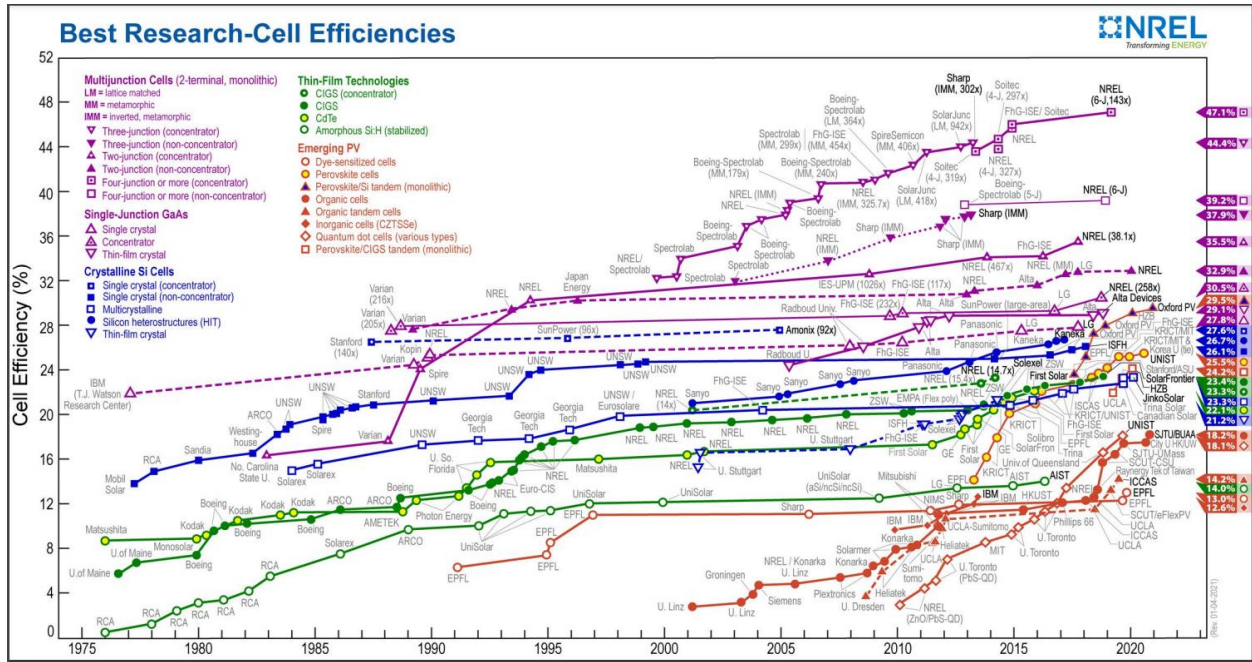


Figure 1.6: Research cells efficiencies for emerging PV from 1975 to 2020 from US National Renewable Energy Laboratory (NREL) [23].

1.3 Literature review

Guangjin et.al. (2011) [24] investigated the effects of various manufacturing conditions on organic photovoltaics OPVs device based on P3HT:IC₇₀BA, including the temperature of pre-thermal annealing, weight ratios, and active layer thickness. They observed that for devices having 188 nm active layer thickness of P3HT :IC₇₀BA (1:1, w:w), annealed at 150 ° C for 10 minutes had a power conversion efficiency (PCE) of 5.82 % with open circuit voltage of around 0.81 Volts, short circuit current (J_{sc}) of 11.37 mAcm⁻² and Full factor of about 64.0 % with AM1.5 G, 100 mW.cm⁻².

Guo et.al. (2012) [25] improved the PV efficiency of polymer-based solar cell (PSC) based on P3HT:IC₇₀BA via utilizing a 3 vol. % of solvent additives having high boiling point e.g., 1-Chloronaphthalene (CN). The configured PSCs have a strong power conversion capacity of 7.41%, an open circuit voltage of around 0.8 Volts, a *FF* of 75 % and J_{sc} of 4.35 mA.cm⁻².

Li et. al. (2012) [26] developed a bilayer polymer-based solar cell (PSC) focused on IC60BA as an acceptor and P3HT as a donor. The systems had a PCE of 5.12%, a J_{sc} of 8.21 mA per square cm, an *FF* of 70.4%, and an open circuit voltage of 0.88 V.

Kim et.al. (2013) [27] examined the effect of graphene oxide (GO) on organic solar cells based on P3HT:ICBA as a hole transfer substrate. They also have shown that GO is a robust possible substitute option for PEDOT: PSS and that GO has a higher energy conversion efficiency (PCE) of 3.70%, open circuit voltage of 0.9 Volts J_{sc} of 6.97 mA.cm⁻², and the *FF* of 63.7%.

Gartner et.al. (2014) [28] developed an organic based solar cell based on P3HT:ICBA utilizing MoO₃ and ZnO as an electron transport layer (ETL) and hole transport layer (HTL), they also examined that the usage of various solvents for the materials having active layer such as MeOH, EtOH, and DCB; as well as specific annealing temperatures like 100°C, 150°C, 180°C, and 200°C. The optimum conditions are there for the devices utilizing MeOH solvent and the temperature for the process of annealing is 200°C as the devices with these parameters displayed a PCE of 4.1%, an open circuit voltage of 0.78 Volts, a J_{sc} of 9.0 mA.cm⁻², and an *FF* of around 58%.

Jia et. al. (2014) [29] enhanced the effectiveness of P3HT:ICBA bulk heterojunction polymer based PSCs utilizing copper iodide (CuI) as film comprised of an anode buffer. The efficiency of energy conversion for such systems was 3.84 %, nearly 1.6 times greater as compared to the CuI-free reference system owing to the concurrently improved photocurrent (J_{sc}), *FF*, and open current-voltage. The buffer layer of CuI believes to modulate the Schottky barrier and create an ohmic connection at the interface of P3HT: ICBA/Au, that serves both as an electron block layer and transport layer.

Burak Kadem et. al. (2015) [30] studied the effects of metal chlorides such as LiCl, NaCl, CdCl₂ and CuCl₂ on optical transmittance, electrical conductivity as well as morphology of PEDOT:PSS films. Transmittance spectra of spun PEDOT:PSS layers were improved by more than 6% to a

maximum of 94% in LiCl doped PEDOT:PSS film. The surface of the PEDOT:PSS films has shown higher roughness associated with an increase in the electrical conductivity after doping with metal salts. The improvement in the physical properties of PEDOT:PSS as the hole transport layer proved to be key factors towards enhancing the P3HT:PCBM bulk heterojunction (BHJ) solar cells. These improvements include significantly improved power conversion efficiency with values as high as 6.82% associated with high fill factor (61%) and larger short circuit current density ($\sim 18 \text{ mA.cm}^{-2}$).

Zhou et. Al. (2015) [31] recorded the layered structure of mounted films of as anode layer at interface for P3HT/ICBA related OSCs. The existence of GO films enhanced the working mechanism of the ITO, contributing to more reliable communication between the ITO anode and active layer. The PSC has obtained an efficiency of 6.04 % with the optimal amount of deposition times.

M. Kadhem and B. A. Hasan (2016) [32] revealed a highly efficient polymer solar cells (PSCs) based on poly (3- hexylthiophene) (P3HT) and fullerene derivatives Indene-C70 Bisadduct (IC₇₀BA) by using Graphene (Gr) as electron collection layer (ECL) between the Al cathode and photoactive layer as a novel work. The efficiency η_e of the device with Gr buffer layer reaches 11.4% under the illumination of AM1.5G, 100 mW.cm^{-2} , in contrast with the 5.8% of the device without Gr buffer layer under the same experimental conditions. The results showed that Gr is a promising electron collection layer for PSCs.

G.A.Nemnes, et. al.(2017) [33] investigate a possible route for optimization of organic P3HT:ICBA photovoltaic cells. In order to ensure a more efficient charge separation and collection at the electrodes, two- and three-layer structures are produced, where additional P3HT and ICBA single layers are placed adjacent to the mixed layers. The open circuit voltage V_{oc} has enhanced from 0.3V for single layer to 0.8V for three layers.

Binrui Xu, et. al. (2018) [34] investigated the role of a functional solid additive, 2,3-dihydropyridine (DHP), in influencing the optoelectronic, morphological, structural and photovoltaic properties of bulk-heterojunction-based polymer solar cells (BHJ PSCs) fabricated using poly(3-hexylthiophene): indene-C60 bisadduct (P3HT:IC60BA) photoactive medium. A dramatic increase in the power conversion efficiency ($\sim 20\%$) was witnessed for the BHJ PSCs treated with DHP compared to the pristine devices.

Biswas, et. Al. (2020) [35] investigated the modification of hole transport layer (HTL) by preparing a series of PSS doped polyaniline (PANI) with synergic (around 90%) transmittance and work function value (within 5.09–5.16 eV) varying PSS concentrations to check the possible utility as HTM in a poly (3-hexylthiophene): [6,6]-indene-C60 bisadduct based organic photovoltaic (OPV) cell. Here, it is observed that, because of change in conductivity, the PV performance of those OPV devices is strongly dependent on the doping concentration of the HTM and, at optimized PSS concentration, PANI:PSS has higher conductivity. This facilitates better hole extraction efficiency into the PV device and results in higher short circuit current density (JSC). Therefore, the PANI:PSS-based OPV device with optimized PSS concentration exhibits same level of power conversion efficiency (PCE: $4.5 \pm 0.2\%$) as a PEDOT:PSS based OPV device.

1.4 Aim and objectives

1. P3HT:IC₇₀BA based OSCs manufacturing and characterization, using different fabrication conditions.
2. Evaluation of optimal conditions for the fabricated devices, including solvents, different concentrations of solvent, annealing temperature, annealing time and using lithium fluoride (LiF) as the electron transport layer .
3. Improve the efficiency of photovoltaic of fabricated OSCs with various interfacial layers.
4. Manufacture high quality OSCs utilizing the optimum process conditions.

Through this study, one type of OSCs, which is organic bulk heterojunction SCs (OBHJ) has been manufactured and characterized. Various kind of materials have been used in this study including indene-C70 bisadduct (IC₇₀BA) as an acceptor and Poly (3-hexylthiophene-2, 5-diyl) (P3HT) as a donor in the transport layer. The hole transport layer used in this research are Poly(3,4ethylenedioxythiophene):poly(styrenesulfonate) (PEDOT:PSS) , while lithium fluoride (LiF) as the electron transport layer. Cathode is of aluminum, while Indium the Tin Oxide (ITO) is acted as anode (whole injection layer). Moreover, the effects of thermal annealing, the transport layer thickness, and device efficiency were also examined. LiF, Graphene, and TiO₂ doped graphene as a new electron transport layers were also considered in this study.

1.5 Thesis outline

A general overview of energy resources and energy demand was discussed in the very first chapter. The history related to the invention of solar cells, the PV and its effects are briefly presented.

Chapter 2 provides an overview on OSCs with the concept of polymeric conjugated materials. This chapter explains the architectures of organic material based solar cells and their main components in the activity of organic solar cells: photon-coupling, exciton production, and light absorption, exciton migration, exciton dissociation, transfer of charges and electrode collection. The characterization of solar cell systems has also been present extensively.

Chapter 3 offers background on the materials, device configuration and the fabricated process with description of facilities used in this.

Chapter 4 mainly describes the results of the study, which represents the manufacturing & classification of organic bulk heterojunction (OBHJ) solar cells, using IC₇₀BA as an acceptor. Within this chapter, the discussion related to the various aspects has been presented, including, different solvents, different concentrations of the active layer, post-deposition annealing has been carried out at different temperatures, the annealing temperatures time, and the impact of LiF as electron transport layers on system activity, the electrical and optical properties parameters properties and morphology have been investigated.

In chapter 5, the work was on how to improve OSC performance by modifying the hole transport layer by using different metal salts; copper chloride (CuCl₂ 99.99%) and lithium chloride (LiCl 99.99%).

In chapter 6, the effect of graphene (Gr) as electron transport layer (ETL) has been investigated and the electrical and optical properties as well as the morphology of the thin films have been investigated. Finally, conclusion and future work are discussed in chapter 7.

References

- [1] “CarbonBrief clear on climate,” March. 21, 2020. Accessed on: Jan. 23, **2021**. [Online]. Available: <https://www.carbonbrief.org/iea-coronavirus-impact-on-co2-emissions-six-times-larger-than-financial-crisis>
- [2] P. A. Owusu and S. Asumadu-Sarkodie, “A review of renewable energy sources, sustainability issues and climate change mitigation,” *Cogent Eng.*, vol. 3, no. 1, **2016**.
- [3] P. C. Dastoor and W. J. Belcher, “How the West was Won? A History of Organic Photovoltaics,” *Substantia*, vol. 3, no. 2, pp. 99–110, **2019**.
- [4] H. Ziar, P. Manganiello, O. Isabella, and M. Zeman, “Photovoltaics: intelligent PV-based devices for energy and information applications,” *Energy Environ. Sci.*, **2021**.
- [5] D. Chapin, C. Fuller, G. Pearson, "A New Silicon pn Junction Photocell for Converting Solar Radiation into Electrical Power", *Journal of Applied Physics*, 25, pp. 676-677, (**1954**).
- [6] K. Kumar, “A History of the Solar Cell, in Patents,” *Finnegan J.*, vol. 3, pp. 8–15, **2020**.
- [7] T. Ibn-Mohammed *et al.*, “Perovskite solar cells: An integrated hybrid lifecycle assessment and review in comparison with other photovoltaic technologies,” *Renew. Sustain. Energy Rev.*, vol. 80, no. November 2015, pp. 1321–1344, **2017**.
- [8] National Renewable Energy Laboratory, “NREL_efficiencies_chart.pdf.” **2020**.
<https://www.nrel.gov/pv/cell-efficiency.html>
- [9] S. Xie *et al.*, “Recent progress in hybrid solar cells based on solution-processed organic and semiconductor nanocrystal: Perspectives on device design,” *Appl. Sci.*, vol. 10, no. 12, **2020**.
- [10] Independent Statistics & Analysis, U.S. Energy Administration
<https://www.eia.gov/todayinenergy/detail.php?id=41433>
- [11] A. Khatibi, F. Razi Astarai, and M. H. Ahmadi, “Generation and combination of the solar cells: A current model review,” *Energy Sci. Eng.*, vol. 7, no. 2, pp. 305–322, **2019**.
- [12] M. I. Hossain, W. Qarony, S. Ma, and L. Zeng, “Perovskite / Silicon Tandem Solar Cells : From Detailed Balance Limit Calculations to Photon Management,” *Nano-Micro Lett.*, vol. 11, no. 1, pp. 1–24, **2019**.
- [13] A. Luceño-s and A. Mar, “Materials for Photovoltaics: State of Art and Recent Developments,” vol. 20, no. 20, pp. 1–42, **2019**.
- [14] I. E. Tinedert, F. Pezzimenti, M. L. Megherbi, and A. Saadoune, “Optik Design and simulation of a high efficiency CdS / CdTe solar cell,” *Opt. - Int. J. Light Electron Opt.*, vol. 208, no. December 2019, pp. 112-142, **2020**.

- [15] B. Xu, G. Sai-Anand, A. I. Gopalan, Q. Qiao, and S. W. Kang, “Improving photovoltaic properties of P3HT:IC60BA through the incorporation of small molecules,” *Polymers (Basel)*, vol. 10, no. 2, pp. 1–10, **2018**.
- [16] A. Bosio, S. Pasini, and N. Romeo, “The history of photovoltaics with emphasis on CdTe solar cells and modules,” *Coatings*, vol. 10, no. 4, **2020**.
- [17] A. Luceño-s and A. Mar, “Materials for Photovoltaics: State of Art and Recent Developments,” **2019**.
- [18] Z. Ma, D. Liu, H. Ding, and X. Sheng, “Thin-Film III–V Single Junction and Multijunction Solar Cells and Their Integration onto Heterogeneous Substrates,” *Inorg. Flex. Optoelectron.*, pp. 177–207, **2019**.
- [19] G. M. Wilson et al., “The 2020 photovoltaic technologies roadmap,” *Appl. Phys.*, vol. 53, no. 493001, pp. 1- 47, **2020**.
- [20] S. Rao, A. Morankar, H. Verma, and P. Goswami, “Emerging Photovoltaics: Organic , Copper Zinc Tin Sulphide , and Perovskite-Based Solar Cells,” vol. 2016, **2016**.
- [21] R. Pradhan, P. Malhotra, G. Gupta, R. Singhal, G. D. Sharma, and A. Mishra, “Efficient Fullerene-Free Organic Solar Cells Using a Coumarin-Based Wide-Band-Gap Donor Material,” **2020**.
- [22] H. Ziar, P. Manganiello, O. Isabella, and M. Zeman, “Photovoltaics: intelligent PV-based devices for energy and information applications,” *Energy Environ. Sci.*, 2021.
- [23] National Renewable Energy Laboratory, “NREL_efficiencies_chart.pdf.” **2020**.
<https://www.nrel.gov/pv/assets/pdfs/cell-pv-eff-emergingpv.202001042.pdf>
- [24] Z. Guangjin, H. Youjun, P. Bo, L. Yongfang, "Effect of Device Fabrication Conditions on Photovoltaic Performance of Polymer Solar Cells Based on Poly(3-hexylthiophene) and Indene-C70 Bisadduct", *Chin. J. Chem.*, 30, pp. 19—22, (**2012**).
- [25] X. Guo, C. Cui, M. Zhang, L. Huo, Y. Huang, J. Hou, Y. Li, "High efficiency polymer solar cells based on poly(3-hexylthiophene)/indene-C70 bisadduct with solvent additive", *Energy Environ. Sci.*, 5, pp. 7943–7949, (**2012**).
- [26] Hui Li, YF. Li, J. Wang, "Optimizing performance of layer-by-layer processed polymer solar cells", *Appl. Phys. Lett.* 101, pp. 458-475, (**2012**).
- [27] H. Kim, A. Rashid, J. Jang, "High performance and stability of chemically modified graphene oxide organic solar cells", *Materials and processes for energy: communicating*

- current research and technological development, pp. 68-74, **(2013)**.
- [28] S. Gärtner, M. Christmann, S. Sankaran, H. Röhm, EM. Prinz, F. Penth, A. Pütz, A. Türel, B. Penth, B. Baumstümmler, A. Colsmann, "Eco-Friendly Fabrication of 4% Efficient Organic Solar Cells from Surfactant-Free P3HT:ICBA Nanoparticle Dispersions", *Adv. Mater.* 2014, DOI: 10.1002/adma., pp. 342-361, **(2014)**.
 - [29] X. Jia, L. Shen, Y. Liu, W. Yu, X. Gao, Y. Song, W. Guo, S. Ruan, W. Chen, "Performance improvement of inverted polymer solar cells thermally evaporating CuI as an anode buffer layer", *Synthetic Metals* 198, pp. 1–5, **(2014)**.
 - [30] B. Kadem, W. Cranton, and A. Hassan, "Metal salt modified PEDOT:PSS as anode buffer layer and its effect on power conversion efficiency of organic solar cells," *Org. Electron.*, vol. 24, pp. 73–79, **2015**.
 - [31] L. Zhou, D. Yang, W. Yu, J. Zhang, C. Li, "An efficient polymer solar cell using graphene oxide interface assembled via layer-by-layer deposition", *Organic Electronics*, 23, pp. 110–115, **(2015)**.
 - [32] M. Kadhem and B. A. Hasan, "11. 4 % efficiency of organic solar cells using Graphene electron collecting buffer layer as a novel work 11. 4 % efficiency of organic solar cells using Graphene electron collecting buffer layer as a novel work," no. November **2017, 2016**.
 - [33] G. A. Nemnes et al., "Applied Surface Science Optimization of the structural configuration of ICBA / P3HT photovoltaic cells," *Appl. Surf. Sci.*, vol. 424, pp. 264–268, **2017**.
 - [34] B. Xu, G. Sai-Anand, A. I. Gopalan, Q. Qiao, and S. W. Kang, "Improving photovoltaic properties of P3HT:IC60BA through the incorporation of small molecules," *Polymers (Basel)*, vol. 10, no. 2, pp. 1–10, **2018**.
 - [35] S. Biswas et al., "Decent efficiency improvement of organic photovoltaic cell with low acidic hole transport material by controlling doping concentration," *Appl. Surf. Sci.*, vol. 512, no. October 2019, pp. 1-8, **2020**.

Chapter 2

Background and Theoretical Review

2.1 Introduction

This chapter describes the entire functioning of device from the light absorption to the transportation of the charge carriers. Designs of heterojunction structure of photovoltaic (PV) cells will be examined. The model of energy band will also be explored under reverse and forward bias and short-circuit and open-circuit conditions. There will also be a discussion on the sources of semi conductive materials as well as conjugation and present in organic materials. Molecular and atomic processes, such as excitons in organic materials, will also be explained. An electronic circuit model will also be shown, with the appropriate electrical parameters defining the PV cell.

Figure 2.1 displays the schematics of a common organic solar cell comprising of a conductive and transparent electrode (generally anode of ITO) having transparent substructure, a blocking layer of electrons (PEDOT: PSS), an active layer of the organic polymer monolayer, (bulk heterojunction or bilayer) as well as a cathode (usually Ca, LiF and Alq3 / Al or Al). Light passes via translucent substructure and produces charge carriers in the active layer that flows to the corresponding electrodes. The descriptions of its internal operations are discussed in the subsequent sections.

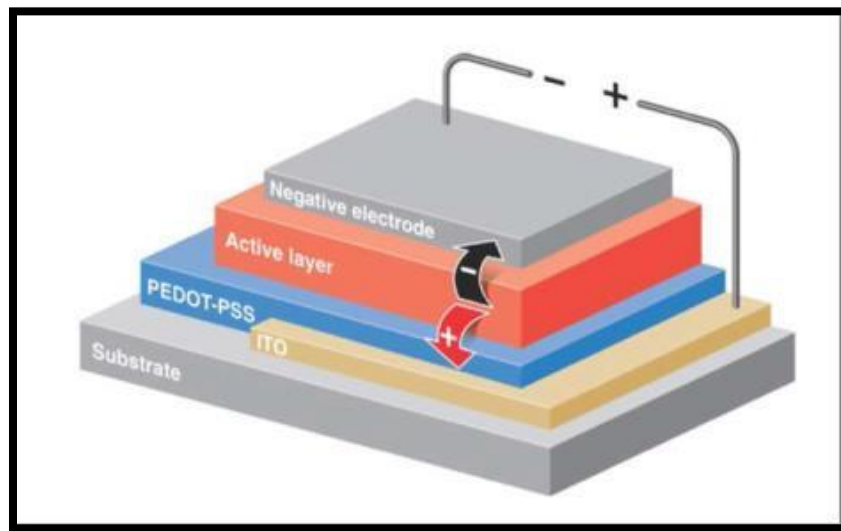


Figure 2.1: Representation of an organic photovoltaic cell [1].

2.2 Organic Semiconductors

One of the main promising materials for manufacturing low-cost solar cell modules are based on organic materials. Once the conductive polymers were identified in the 1980s, research towards organic materials for electronic devices such as transistors, solar cells and light-emitting diode commenced [2, 3].

Due to their chemical configurations, organic semiconductor materials are recognized as good conductive material compared to other available semiconductor materials. Several properties such as flexibility, conductivity and solubility can be obtained by chemical synthesis of organic semiconductors. Organic semiconductors are based on carbon atoms, while the electronic configuration in the ground state for the carbon atom is: $1s^2 2s^2 2p_x^1 2p_y^1$ that signifies that the orbital 1s possess two electrons, orbital 2s and orbital 2p has two electrons as well. It could be observed that the orbital s is highly loaded, and the orbital p possess two unpaired electrons, one in $2p_x$, one in $2p_z$ and $2p_z$ without electrons. This signifies that 1s contained core electrons, while the valence electrons are present in the $2s^2 2p^2$ orbitals [4-6]. Figure 2.2 displays the orbital forms for s orbitals, p orbitals (p_x , p_y , p_z) and respective variations.

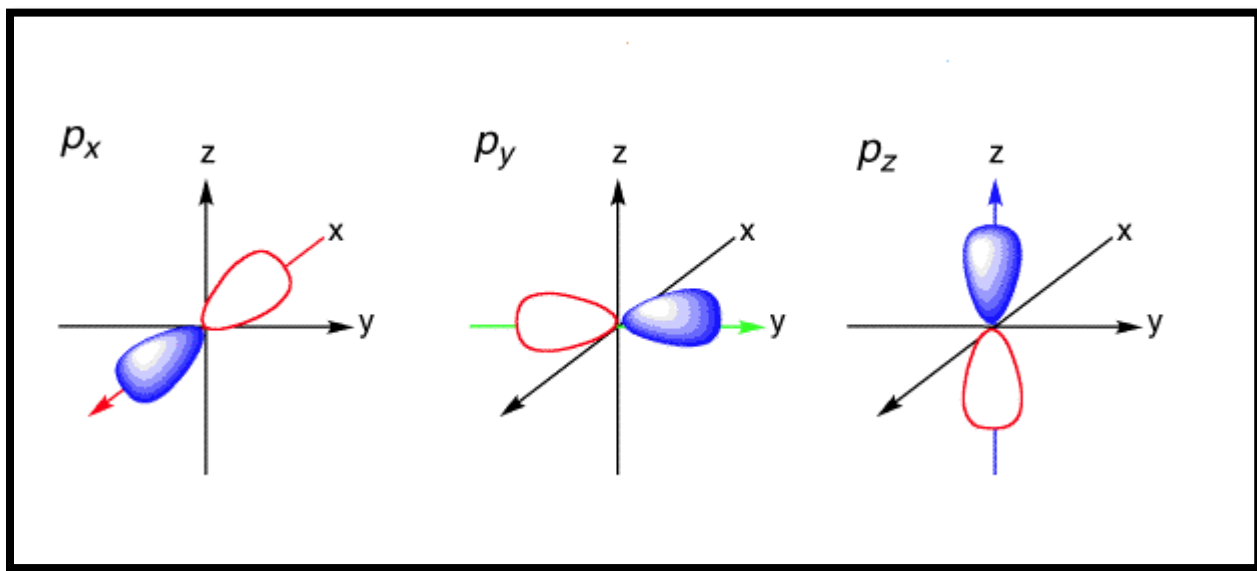


Figure 2.2: Orbital shapes and combination of s, p and z orbital (p_x , p_y and p_z) [7].

Nonetheless, hybridization among ($2s$ and $2p(x, y)$) orbitals renders $2p(z)$ uncharged, which is presented in Figure 2.3.

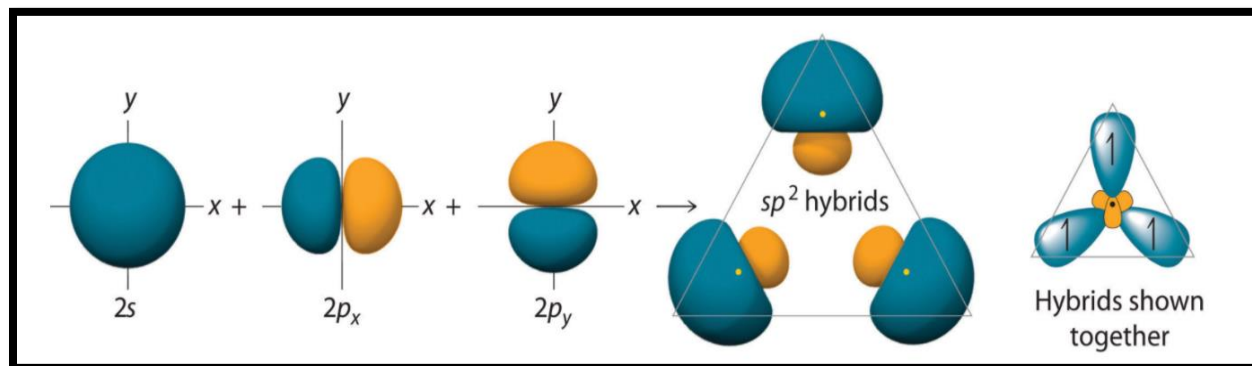


Figure 2.3: Hybridization among ($2s$ and $2p_{(x,y)}$) orbitals [7].

Two different types of bonds are generated as a result of hybridization; σ bonds are the single bonds among C-C and C-H atoms, for the localized electrons, while π bonds possess delocalized electrons. It is clear from sp^2 hybridizations in Figure 2.3, the 3 electrons of carbon form the σ bonds where such electrons are positioned. These hybrid orbitals were lying to one another at 120° . This arrangement leaves the fourth electron (unhybridized), which is delocalized, as seen in Figure 2.4 to produce the π bond. Electrons, such as hybridized carbon atoms sp^2 in case of conjugated polymers, can travel quickly through the chain of the polymer. Therefore, electrons are accountable for the organic semiconductor's electrical conductivity in these bonds [4, 6, 8]. The energy levels for the organic semiconductors are also represented by molecular orbitals that form π and σ bonds. The represented molecular bonding orbitals are the strongest molecular orbital have the highest energy levels, whereas π^* and σ^* , the denoted anti-bonding molecular orbitals are the lowest molecular orbitals having lowest energy levels. Such molecular orbits are comparable to the levels of energy bands in inorganic materials. Figure 2.5 illustrates the way energy gaps are generated in organic semiconductors [7].

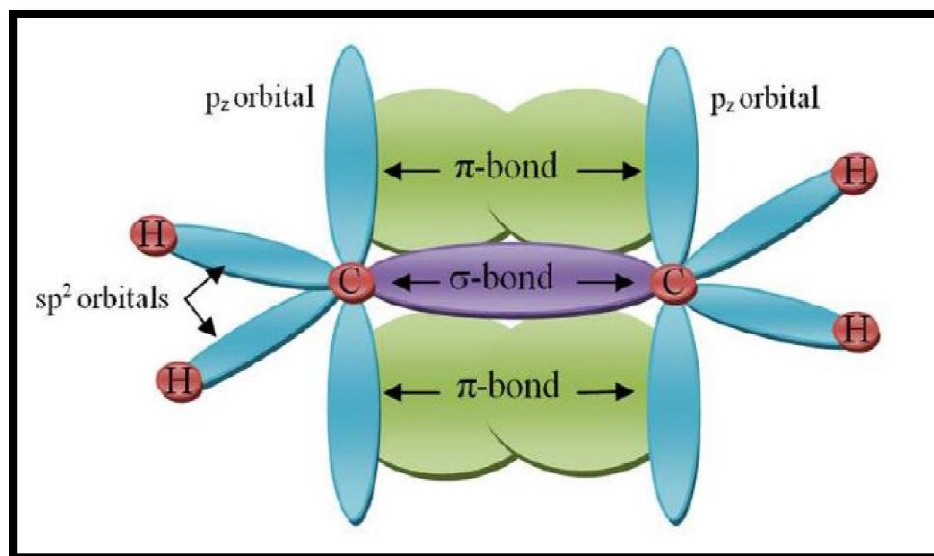


Figure 2.4: Schematic diagram of the orbitals and bonds for two sp^2 hybridized C atoms [7].

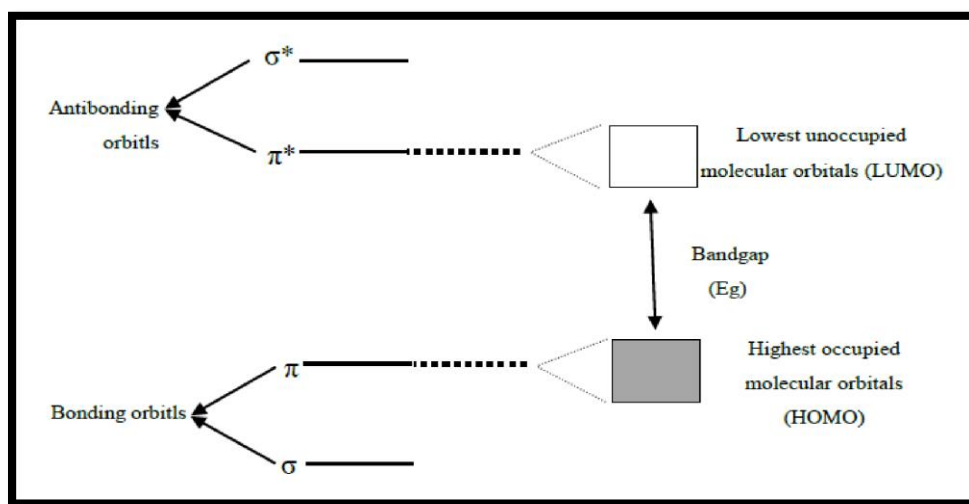


Figure 2.5: Energy levels present in organic semiconductors [7].

To generate the lowest unoccupied molecular orbital (LUMO) and the highest occupied molecular orbital (HOMO), the anti-bonding (π^*) molecular orbitals need to be joined with the π bonding molecular orbitals. The gap exists between LUMO/HOMO is the energy bandgap, on which the organic semiconductor conductivity depends. Thus, from Figure 2.5 Sigma (σ) bonds are excessively packed with the electrons wherever the π bonds are hollow. In comparison, the ability

of electrons to transfer from HOMO to LUMO decreases if the energy band difference is reduced as far as possible. Few organic semiconductors possess a low band gap of < 2 eV, indicating they are strong materials relative to some inorganic semiconductors that have a wide energy bandgap [4, 6, 8].

Organic semiconductors may be categorized into semiconductors consisting of polymers and the small molecules materials. The identification of doped polyacetylenes electrical conductivity was made 30 years ago that rendered the conjugated polymers an important field of study in electronic applications. Organic semiconductor polymers, involving optoelectronics, electrical conductivity, colour (emission and absorption), and photo-induced charging, are used in numerous electronic and optical devices such as organic field-effect transistors, organic PV cells, organic light-emitting diodes (OLEDs) and sensors [9-11]. The primary benefit of conjugated polymers is their ability to adjust the bandgap through adjustments in the synthesized materials, which could be used to cover larger surfaces. They incorporate the mechanical properties of polymers with the semiconductor and metal electronic properties. Conjugated polymers are very potential components in development for modern organic solar cells. Studies have created conjugated polymer synthesis and methods of deposition to obtain special electrical properties [12]. The highest recorded efficiency of the organic solar cells based on these sorts of materials was 11.4%. [13].

2.3 Electron transport materials

An ideal acceptor should have several properties such as good light harvesting, high electron mobility, stability under processing and operational conditions, low cost and simple to synthesis, which are combined to create an efficient component. Moreover, n-type materials are typically characterised by the low LUMO and can be modified to a lower value if needed, as well as low electron deficiency. Molecules which have low electron deficiency are more stable when exposed to water and oxygen [14]. Since 1985, C₆₀ received a great deal of attention as an electro active material due to many properties such as high degree of stability, high electron mobility and a limited solubility which leads to employ vacuum deposition [15]. A soluble version of C₆₀ namely methano-fullerene derivative Phenyl-C₆₁-butyric acid methyl ester (PC₆₁BM) was identified by Hummellen and his research group in 1995 [16]. They reported efficient separation of charges that resulted in a faster photoinduced electron transfer within the molecular structure. These findings

made PC₆₁BM widely used as the acceptor in most of the OPV devices. Furthermore, its spherical shape gives it an advantage enabling the transport of electrons in three dimensions. However, the main disadvantage of PC₆₁BM is the absorption inability in the visible light. To exceed this problem, a new material has been developed named PC₇₁BM (C70 analogue and PC₆₁BM). Due to the ability to absorb in the blue region of the solar spectrum, higher photocurrent and power conversion efficiency (PCE) in OPV cells have been achieved [17]. The knowledge of the resulting changes in the LUMO energy level has led to the synthesis of a variety of mono-bi- and tri adducts (as shown in Figure 2:6) and helped researchers achieve higher open circuit voltage (V_{OC}) in solar cells. For instance, Indene-C₆₀ bisadduct (IC₆₀BA) that has a LUMO level at 3.74 eV (0.17 eV up-shifted than that of PCBM) shows superior photovoltaic performance with 0.84 V V_{OC} and 6.48% power conversion efficiency (PCE) when used in P3HT-based OPVs as acceptor [18]. Indene-C₇₀ bisadduct (IC₇₀BA) has also been synthesized at a higher LUMO level of 3.72 eV (0.19 eV higher than that of PCBM). IC₇₀BA possesses good solubility in common organic solvents and stronger visible absorption [19].

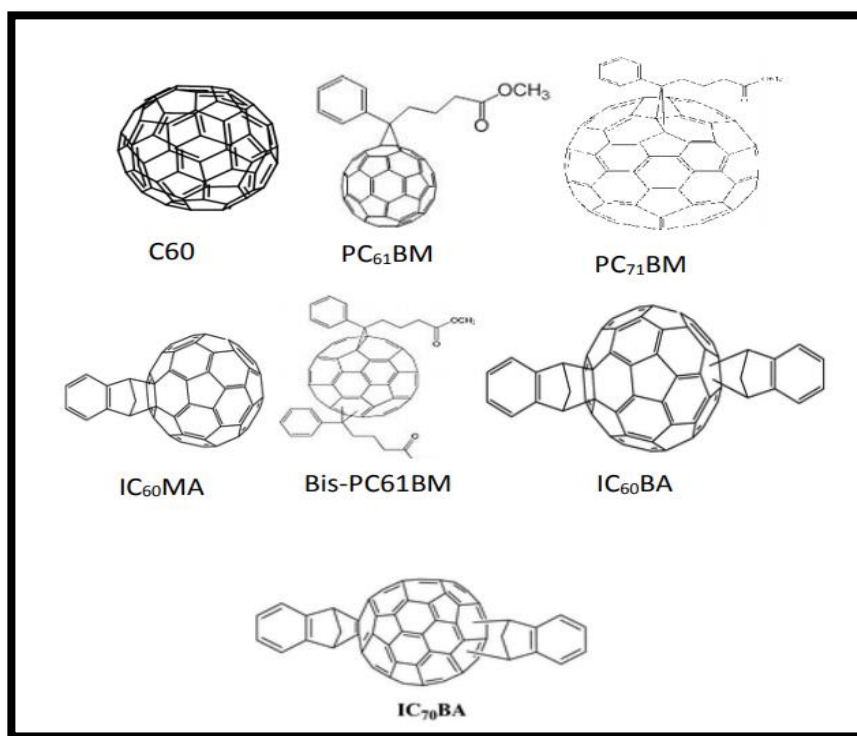


Figure 2.6: Chemical structures of relevant fullerene derivatives used as electron transport material in OPV [19].

2.4 Hole transport materials

The most promising p-type materials (hole transport) for application in OPV devices are conjugated donor polymers because they have the potential to combine their good films forming properties (suitable HOMO and LUMO levels, intensive light absorption and high hole mobilities) to achieve better electronic characteristics. Over the last few years, there has also been a significant rise in the number of publications and articles about new polymers [20]. The first bulk-heterojunction (BHJ) structures that were based on poly(phenylenevinylene) (PPV) were reported in 1995 including: poly[2-methoxy-5(2'-ethylhexyloxy)-1,4-phenylenevinylene] (MEH-PPV) and (poly[2-methoxy-5-(3,7-dimethyloctyloxy)]-1,4-phenylenevinylene (MDMO-PPV) [21]. When these poly-components were combined with fullerene acceptors, there was high PCEs reported of up to 3.3% [22].

However, the absorption edges for MEH-PPV and MDMO-PPV is 550 nm which almost equal to a band gap of 2.3 eV. Due to the big mismatch between their absorption spectra and the solar irradiation spectrum, organic solar cells based on these materials produced low output current density [23]. To tackle this scientific defect, p-type and polymer poly(3-hexylthiophene) (P3HT) was synthesised and reported to achieve approximately 5% PCE in the process of optimisation of organic solar cells. Number of factors affect the performance of the device based on P3HT as donor including processing conditions, molecular weight and regioregularity [24]. The low band gap (1.9 eV), broader absorption band and high hole mobility for P3HT helped to make the material very suitable for photovoltaic applications. By using P3HT as donor material blending with PCBM as acceptor, PCE of over 4% has been reported. The absorption band of P3HT/PCBM covers the range from 380 to 670 nm, which means that photons with energy between 2.0 and 3.3 eV can be absorbed by the active layer [25].

2.5 Transparent conducting electrode

Transparent conducting films which are thin, can achieve a large value of conductivity and maintain at the same time a transmission that is high within the visible range of the electromagnetic spectrum [26]. Today, the products of current commercial based on the n-doped metal oxide films that are referred to as transparent conducting oxides. These transparent films can be used in a wide

range of areas including transparent electrode materials in photovoltaic cells, touch-screen technology and flat panel displays e.g., liquid crystal displays (LCD), organic light emitting displays (OLED) and plasma screen displays [27].

In 1954 and by Rupprecht, Indium tin oxide (ITO) was discovered and considered as the first modern transparent conducting oxide (TCO) materials [28]. It is an n-type transparent semiconductor which has a wide band gap of approximately 4 eV. Nowadays as the technology that is growing dramatically, ITO plays a very important role in the industry of optics and electronics [29]

2.6 Top electrode

Cathode materials is supposed to be a metal of low work function to extract electrons through a strong electric field. Compared to the LUMOs of the materials act as the acceptor and materials for the extraction of electrons, top electrodes have lower energy. Most common metals have low work function used as cathode in OPV devices are calcium, magnesium, and aluminium. Because of its stability in air, aluminium is the most used cathode material among all the metals. However, V_{oc} does not depend on the working of the cathode which can support pinning of the Fermi level that are formed between the cathode and the active layer [30].

Due to interfacial integer charge transfer, the HOMO of acceptor material and LUMO of donor material become Fermi level (E_F -pinned) at the junction, and the energy level bending away from the interface on both sides occurs. This will form an interfacial dipole which results from the contact between the cathode and the active layer. The formation of dipoles results in reduction in the energy barriers exist between the Fermi levels and the LUMO level of the acceptor and this helps in transfer of electrons. The energy diagram for metal/semiconductor contact after interfacial dipole is formed is shown in Figure 2.7.

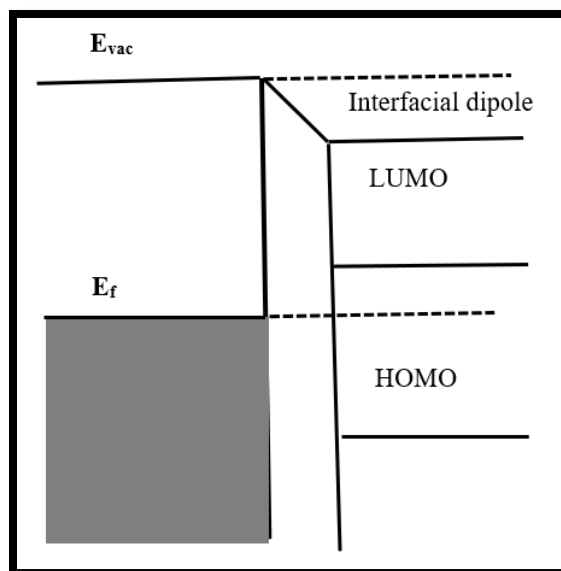


Figure 2.7: Energy diagram for metal/semiconductor contact after interfacial dipole is formed.

2.7 Buffer layers

The main problem faces organic solar cells is that the two electrodes touch both the donor polymer and the acceptor molecule and leads to the formation of acceptor electrons at an interface which is located very close to the anode. Therefore, and due the reduction of the working voltage of the device, if any of the electrons transferred to the anode, they will recombine very easily [31]. Also, this creates an electron blocking layer between the active layer blend and the anode that prevents the transfer of electrons in the acceptor to the anode. Same effect also occurs at the cathode, where holes may be produced in the HOMO of the polymer at a point close to the aluminium and the barrier between the Fermi level of the metal and the organic semiconductor LUMO is reduced. To tackle this, an electron transport layer (ETL) such as LiF can be inserted as well as poly (3,4-ethylenedioxythiophene), poly(styrenesulfonate) (PEDOT: PSS), which act as the hole transport layer, to achieve the buffer layers [32].

2.8 Organic solar cells structure

2.8.1 Bulk Heterojunction (BHJ) organic solar cells

The main idea stands behind a heterojunction is using two different materials have different electron affinities and different ionization potentials. At the interface and because of the strong resulted potentials, exciton dissociation may be aligned: material with the larger electron affinity will accept electron and the material with lower ionization potential will accept hole, as it is known, the differences in potential energy are larger than the exciton binding energy [33]. In an intimate way, the accepting materials and the donating are mixed to form an interpenetrating network that is three dimensional. Usually, the BHJ devices contain several components, one of them at least is a polymer semiconductor (usually is a conjugated polymer). Because of the continuous network is organized on a nanometre scale, this leads to a large area of interface which means every excitation created has ability to reach the interface. With higher short circuit current density (J_{sc}) the possibility of recombination is reduced. An excitation in the polymer phase is capable to transfer an electron from the polymer to the acceptor and this results in the formation of an interfacial charge transfer state which then relaxes thermally with an electron hole separation distance (thermalization length). The state of charge transfers able to germinate recombination either back to the zero-ground state or a triplet excitation. Otherwise, free charge carriers migrate towards the respective electrodes [34]. The size and bulkiness of the solubilizing components of the polymer backbone affect directly on the barrier that exists between the charges separation which can raise the energy level of charge transfer. A high interface area must be present and sufficient percolation pathways must be created to avoid any form of bimolecular recombination losses; the morphology has a substantial influence on the performance of the devices [35]. In addition to this, the organic materials and the electrodes interfaces are also decisive as well. The main aim of buffer layer is to avoid situations where the charge carriers reach the opposite electrodes and to maximise the V_{oc} as well [36]. Comparing to BHJ cells, bilayer solution processed require orthogonal solvent systems to avoid dissolve the underlying layer which make limitation of materials that can be used. In the BHJ devices, it is possible to deposit the active layer from one solution using different techniques such as: doctor blading methods and spin coating. The morphology of the bulk heterojunction can be also affected directly by the drying process [37]. In heterojunctions, the thermal annealing is widely used to alter the morphology and to enhance the separation phase

which affect the performance of the device [38]. To understand the morphology of the blend active layer and its influence, many techniques can be used such as: Transmission electron microscopy (TEM), Scanning electron microscopy (SEM) and Atomic force microscopy (AFM). The last one can gain high resolution information for the topography of the surface and the distribution of acceptor a donor. Figure 2.8 shows the structure of an organic bulk heterojunction (BHJ) solar cell as well as the energy band diagram of the cell, which shows the differences between HOMO and LUMO levels between acceptor and donor materials.

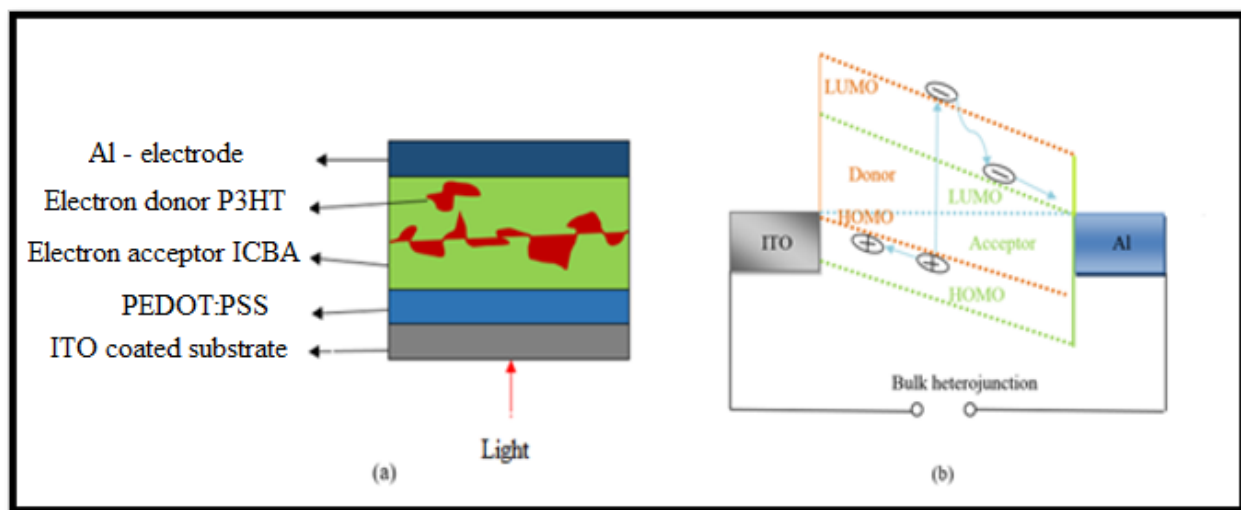


Figure 2.8: *a) Device structure of an organic bulk heterojunction (BHJ) solar cell; b) energy band diagram of a BHJ cell.*

2.9 Basic operation principles of Organic solar cells

In a visual context, Figure 2.9 demonstrates the operational and loss mechanisms of the organic solar cells at various levels, from absorbing light to charges collection. The operational steps of the organic photovoltaic (OPV) will be discussed in subsequent sections.

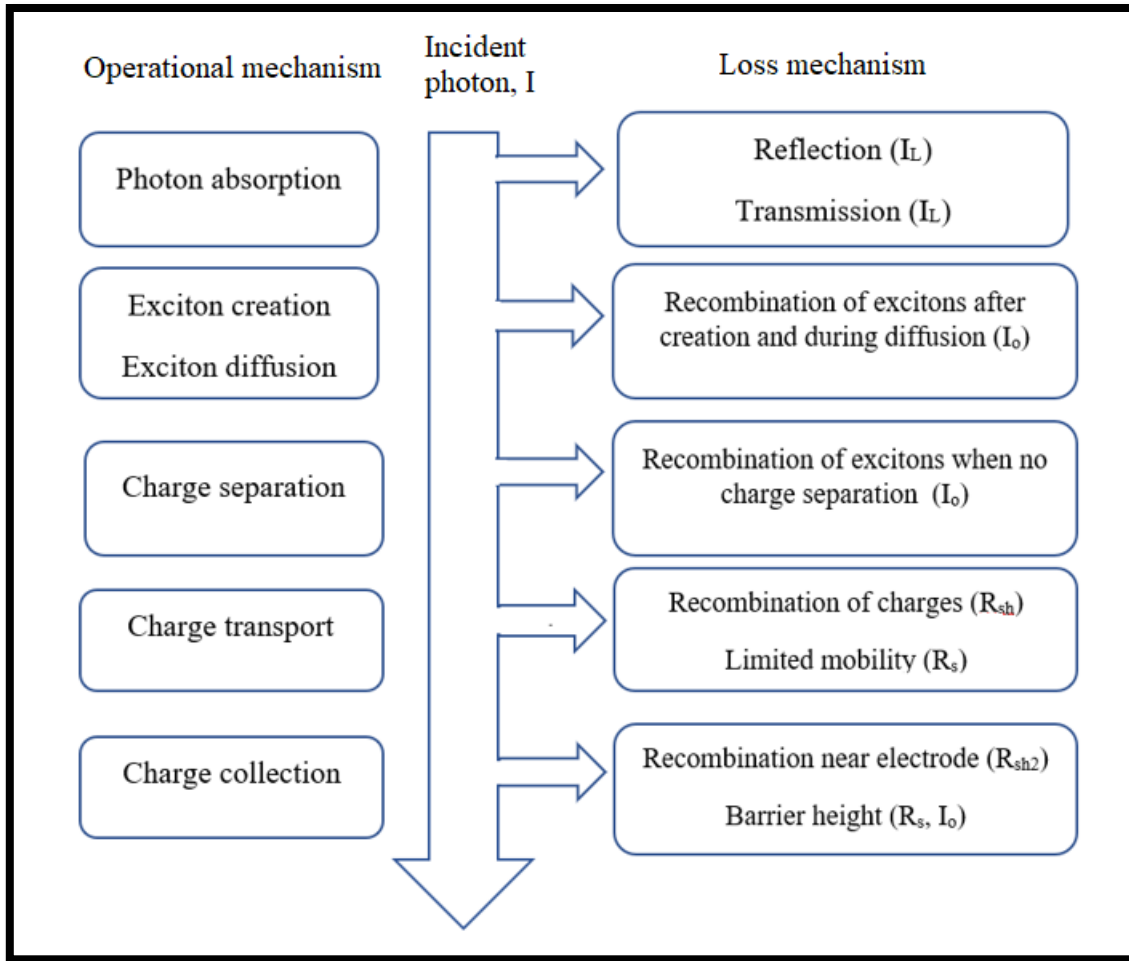


Figure 2.9: Loss mechanism and operational steps in organic solar cell from [39].

In inorganic semiconductors, the photons are converted directly into carriers of direct charge and the carriers collected at the appropriate electrodes. While in organic photovoltaic devices, a pair of hole and electron (exciton) formed through the excitation of molecule by photon [40]. The diffusion length of these excitons is about 5-15 nm and then decay either in a radiative way or non-radiative way. The generation's process of power from organic photovoltaic devices can be divided into several stages. 1) The absorption of incident photons, this relies on the range of absorption spectrum of material. These photons which have energies in this range will be absorbed otherwise will transmits (photons with high frequencies) and some of the will reflect (photons with low frequencies). (2) Generation of excitons by the absorption of a photon. (3) The exciton diffuses to the heterojunction. (4) Due to the energy dissociation occurs at the D-A interface, the charge

carriers are separated and can be transported and collected at the appropriate electrodes. Figure 2.10 shows these stages and more information further illustrated in the relevant next sections.

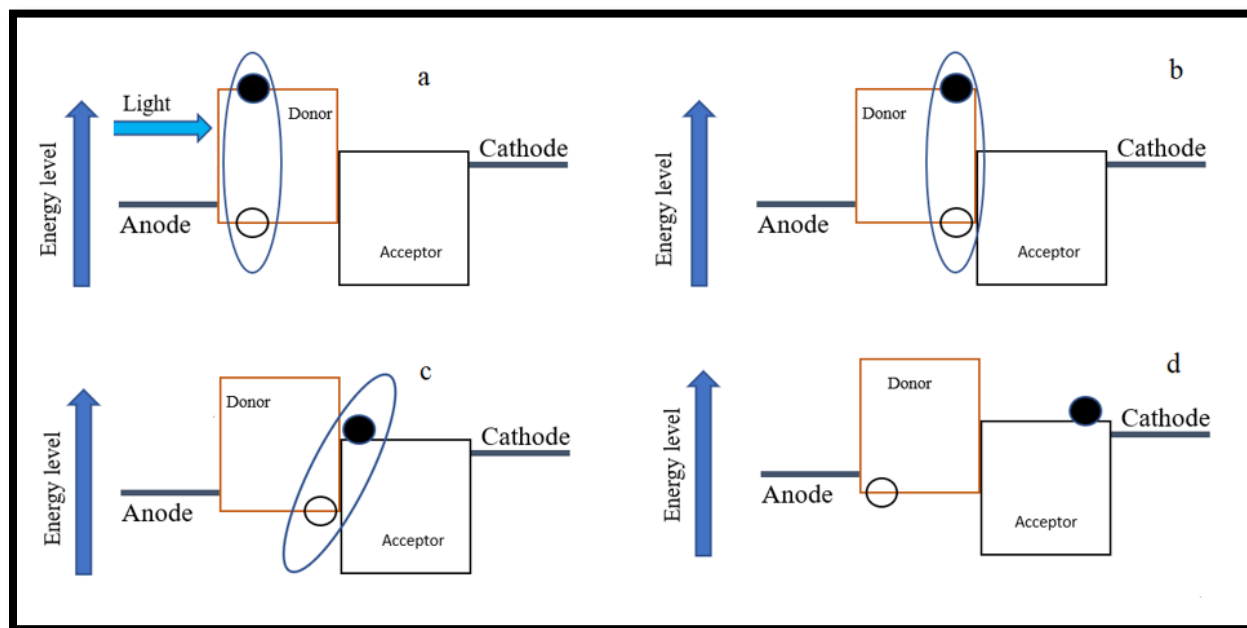


Figure 2.10: a) A photon is absorbed, exciting an electron from the HOMO of donor to its LUMO. b) The bound pair of electron-hole diffuses towards interface of donor-acceptor. c) Provided that the LUMO offset is higher than the exciton Coulombic binding energy, the electron is passed from the donor LUMO to the acceptor LUMO. d) The splitting of the poorly attached hole and electron into free-charge carriers that are then deposited at their respective electrodes.

2.9.1 Light absorption and exciton generation

The absorption process in organic semiconductors usually occurs when a photon that have an energy equal to or greater than the bandgap of the semiconductor material absorbed. This photon has ability to free an electron from the HOMO to the LUMO leaving behind a vacant space in the previous level, which is called a hole. The hole, then, form a coulombic attraction with an electron which is referred to as exciton state [41]. Figure 2.11 shows exciton binding energy.

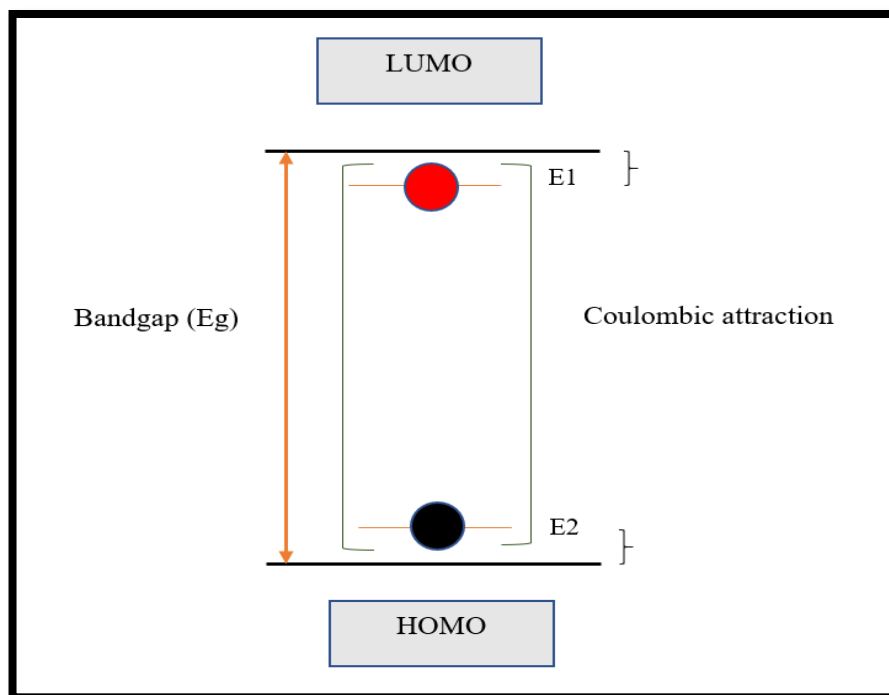


Figure 2.11: *Exciton binding energy.*

2.9.2 Exciton migration and dissociation

The dissociating possibility of an exciton is normally made available by the creation of a heterojunction between two organic semiconductors whereby the second semiconductor is selected so that the electron results from the exciton can drop into the second semiconductor. This releases the energy difference between the LUMO and the HOMO, therefore breaking the bound states. Dissociation only occurs when the excitons from the donor where $\Delta\text{LUMO} > E_B$ (binding energy in the donor) and for the excitons from the acceptor, $\Delta\text{HOMO} > E_B$ (acceptor). This method of dissociation requires that the excitation reaches the interface between the two semiconductors. As exciton has no charge, any external electric field cannot control the exciton and therefore cannot be used to help the dissociation to be achieved or drive the exciton towards an interface. However, for excitons to reach the interface this can only be accomplished through the hopping process by transfer of energy to adjacent molecules [42]. Generally, the mobility of excitons is in the range of 10 nm, and this is called the exciton diffusion length. The lifetime of exciton is very small, in the range of few picoseconds if not separated the excitons will recombine. Thus, exciton diffusion length (and lifetime) plays an important role in the performance of organic solar cells [43].

2.9.3 Charges transport and collection

After the generation of the free charges have been established at the interface, it is required that they reach the external circuit in an OPV device, as electrons can be transported through the electron acceptor material and holes can be transported through the electron donor material. Recently, there have been some developments in the modification of the electrodes by using ultra-thin internal layers such as metal oxides like LiF to give a perfect match to the energy levels of the organic semiconductors [44]. This can be achieved through using an electron transporter layer (ETL) on the acceptor side with a work function less than the LUMO level of the acceptor to ease the collection of electrons from the acceptor. Furthermore, a hole transporter layer (HTL) can be used on the donor side with a work function higher than the HOMO level of the donor to ease the collection of the electron from the donor [45].

2.9.4 Loss mechanism in organic solar cell

The significant energy loss in OSCs is mainly due to the complex photovoltaic structure and photovoltaic process. As it is known, strongly bounded electron-hole pairs are generated in organic molecules after the absorption of photons [46]. To realize the dissociation of these generated excitons into free charge carriers, the heterojunction structure with donor/ acceptor (D/A) interfaces are generally used for the photovoltaic modules in photovoltaic devices. So, when excitons arrive at (donor/acceptor) D/A interfaces, the energy offset ΔE (defined as the difference of lowest unoccupied molecular orbital [LUMO] energy levels or highest occupied molecular orbital [HOMO] energy levels between D and A materials) can provide a driving force to help excitons overcome the binding energy. In actual applications, to harvest more excitons at D/A interfaces, the photovoltaic structures are designed as the bulk heterojunction (BHJ) structure, where the domain sizes of the D and/or A materials need to be smaller than the length of exciton migration (10–20 nm) [47]. In addition, to keep high-efficient charge transport and extraction, the structure of interpenetrating network of D and/or A materials with appropriate aggregation sizes is needed [48].

In fact, all the photovoltaic steps shown in Figure 2.10 can result in energy loss, such as the relaxation loss during the exciton photogeneration and migration processes due to the high-energy

vibrations of the carbon backbones in organic molecules [49]. However, in most of the recent works, the energy loss in OSCs is commonly defined as the difference between the lowest photogenerated exciton energy of the D or A material and the open-circuit voltage energy (V_{oc}) [50]. It means that the energy loss in PVs is mainly ascribed to the charge transfer, separation and transport processes, during which diverse charge recombination pathways actually play crucial roles. In terms of the device physics, the PCE of a PV is proportional to its (V_{oc}) (J_{sc}), and (FF) [51]. Hence, reducing the energy loss in PVs requires us to maximize the value of V_{oc} without sacrificing the values of J_{sc} and (FF). In the last few years, focusing on such a topic, great advances have been made and several insightful review articles have successively summarized these progresses and prospected the future research directions from different perspectives [52].

2.10 Electrical Characterisation of organic solar cells

2.10.1 Equivalent circuit diagram of organic solar cells

Understanding the electrical model of a solar cell is very important before the discussion of the electrical properties of organic solar cells. It can be modelled by a diode parallel with a current source in an ideal case, but practically a series and a shunt resistance (R_s and R_{sh} , respectively) should be included in the model. The series resistor R_s reflects free migration or movement of charge carriers in the transport medium and the shunt resistor R_{sh} represents the recombination of charge carriers around the dissociation area. Figure 2.12 shows the typical equivalent circuit for solar cell, ideally $R_s = 0$ and $R_{sh} = \infty$ [53].

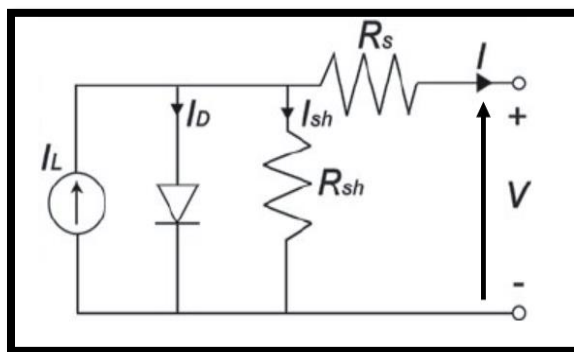


Figure 2.12: *Equivalent circuit diagram of organic solar cells.*

In the circuit diagram, the current source (I_l) represents the produced current from the incident light and the diode explains the nonlinearity of the I - V curve. It is only when the series resistor (R_s) drops down to zero that the circuit I - V characteristic represents the ideal diode, and the shunt resistor (R_{sh}) moves to infinity. The conductivity of material (thickness of the proactive layer and impurity concentrations) is usually responsible for series resistor in solar cells as it comes from the charge carrier recombination at the surface of the junction. The value of shunt resistance can be calculated from the reverse bias of the I - V where the current change linearly with bias voltage. Whereas the serial resistance can be calculated from the slop of the I - V under high forwarded bias voltage ($V > V_{oc}$). Increasing the R_s lower the short circuit current (J_{sc}) and decrease the fill factor of the solar cells while decreasing R_{sh} affect the V_{oc} [54].

2.10.2 Current-voltage characterisation

For most workable inorganic and organic solar cells, characteristics of the current density as a function of voltage (J - V) take the shape of exponential response of a diode with low current in reverse bias and high current in forward bias when carried out under dark condition. When light is directed on a device, photocurrent in the cell is builds up as well as the diode characteristic. The J - V characteristics of the device and also the photocurrent term, J_{ph} is described by the Shockley equation:

$$J = J_0 [\exp (eV / \eta k_B T) - 1] - J_{ph} \quad 2.1$$

Where J is the current density, J_0 is the reverse saturation current density of the diode, e the elementary charge, V is the applied voltage, η is the ideality factor, k is the Boltzmann constant and T is temperature. Indeed, the photocurrent depends on the applied voltage and similarly the lighting affects the diode characteristics. Figure 2.13 shows the J - V plot for a typical solar cell in the dark and under illumination. The photovoltaic performance parameters are open-circuit voltage (V_{oc}), short-circuit current density (J_{sc}), fill factor (FF), and power conversion efficiency (PCE).

In figures 2.13 and 2.14 the effect of series resistance and shunt resistance on the curve of photovoltaic device behaviour. It is noticed that when the shunt resistance (R_{sh}) has high values,

the curve tends to be ideal while quite the opposite for series resistance (R_s). Low values for (R_s) lead to ideal curve and high fill factor (FF).

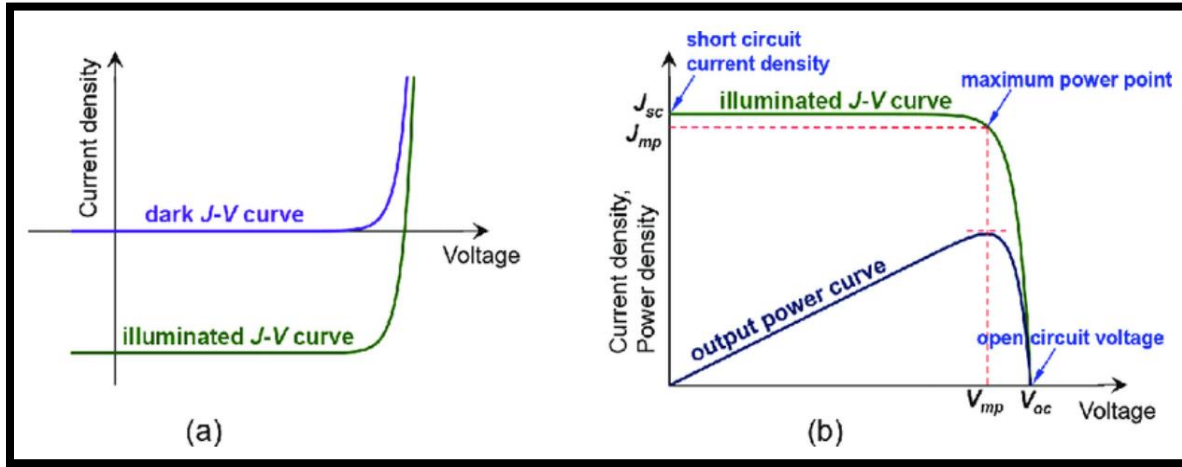


Figure 2.13: Dark and illuminated J-V curves of a silicon solar cell (a); a typical representation of an illuminated J-V curve as well as output power density curve as a function of voltage (b), including indication of the short-circuit point $(0, J_{sc})$, the open-circuit point $(V_{oc}, 0)$, as well as the maximum power point (V_{mp}, J_{mp}) .

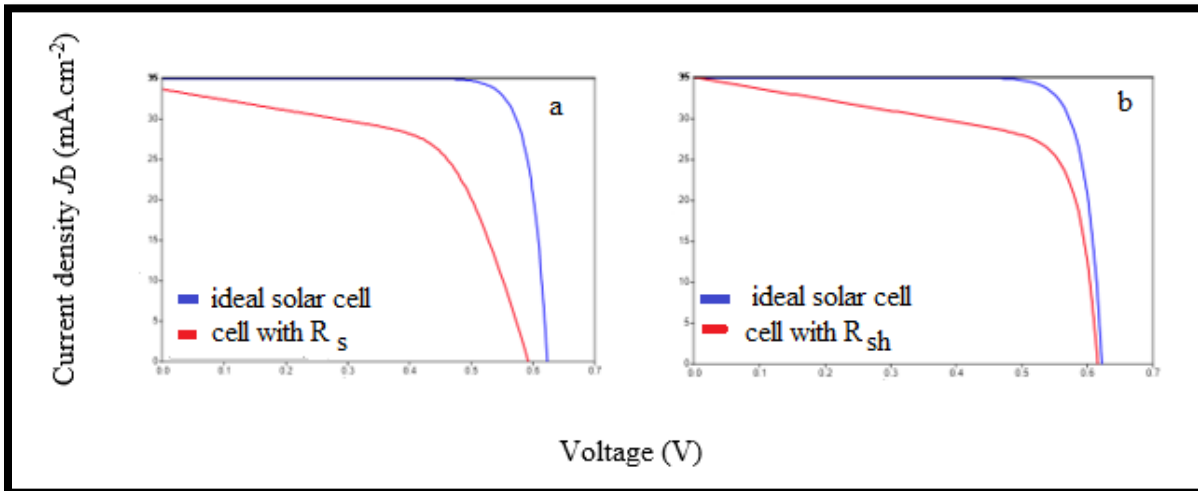


Figure 2.14: a) effect of the series resistance R_s on the shape of a J-V curve. b) effect of the shunt resistance R_{sh} on the shape of a J-V curve.

2.10.2.1 Open-circuit voltage

Excitons are formed mostly in the organic solar cell as light is being absorbed by organic based active layer and they are divided into electrons and holes inside the active layer at the interface of donor/acceptor. These charge carriers compelled to migrate under the force of electric field to their corresponding electrode, whereas they supply power to an open load. [55-57]. The carriers that are being generated will converge on both of the electrodes within the open circuit conditions and stable lighting, generating a variable voltage that cancels out all the built-in potential (V_{bi}). On that point, no current exists within the system as the generation of charge carriers and recombination rates are perfectly balanced. The device is therefore under the state of quasi-equilibrium as well as the difference in voltage among the anode and cathode reflects V_{oc} . The value of V_{oc} represents the ultimate output voltage given by a solar cell. [58-60]. Because of the alignment in energy level, a clear relationship occurs among V_{oc} , V_{bi} and the Fermi level (E_f).

2.10.2.2 Short-circuit current

When the $V=0$, then the current density value represents the J_{sc} short-circuit current density. Throughout this case, no power is produced, however the J_{sc} marks the start of the power production. In functional appliances, the density of photocurrent would be equal to the J_{sc} . For the convention indications used here, J_{sc} is actually negative, however evaluations of various J_{sc} values would be mostly about its magnitude and regard this as a positive number. A high J_{sc} , for example, leads to a high J_{ph} . [61].

2.10.2.3 Series and shunt resistance

Shunt resistance (R_{sh}) and Series resistance (R_s) are considered the most powerful parameters that directly effects the behaviour of solar cells. the R_{sh} is related to the quality of the films, such as traps and pinholes, while, the R_s is a sum of the bulk resistance of various layers in devices and the contact resistance between them [62]. From the other side, in dark conditions where the photocurrent is zero, (R_{sh}) reflects the cell leaks. When R_{sh} approaches to infinity the shunt current (saturation current) reaches zero, as it is a parasitic current, that is desirable. In the high current region, the total current

is much higher than the reverse saturation current ($I \gg I_0$) which can be described through following formula [63]:

$$J \frac{dV}{dI} = JR_s + \frac{nKT}{q} \quad (2.2)$$

R_s may be derived through the slope using the above equation at the high current area of the plot of $I (dV/dI)$ vs. I , as seen in Figure 2.15. Furthermore, via slope the identification of (R_s) and (R_{sh}) from the illuminated J - V curves can be made.

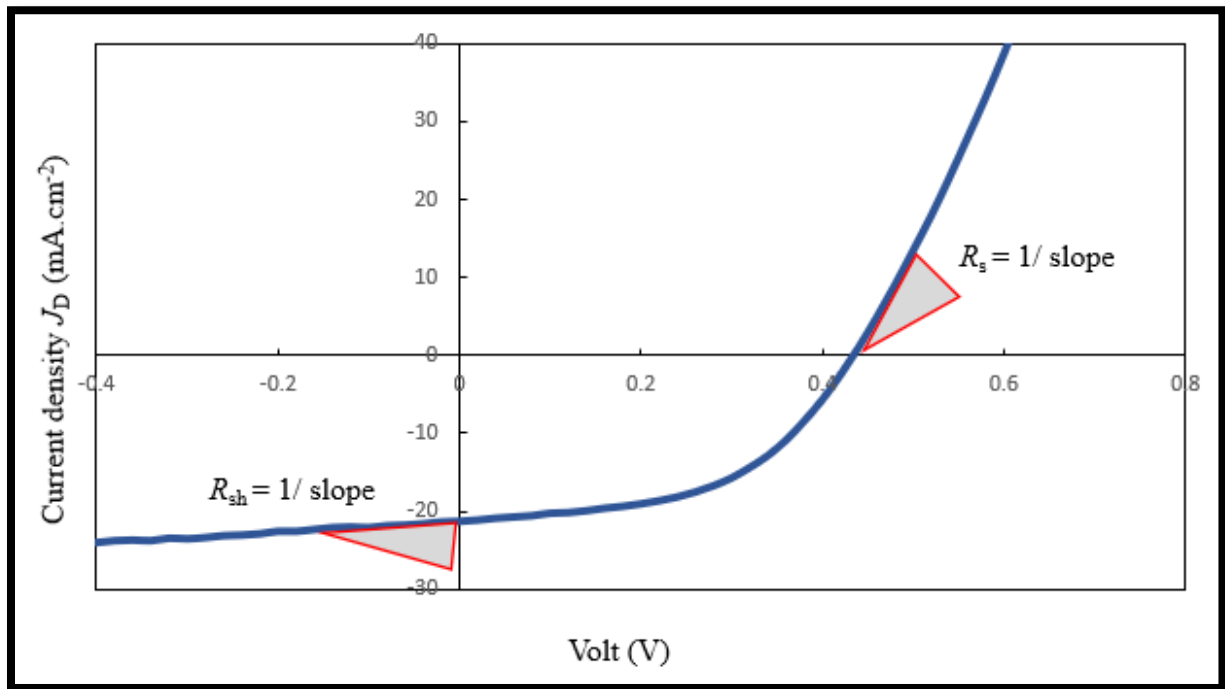


Figure 2.15: Determination of (R_s) and (R_{sh}) from the J - V curves.

2.10.2.4 Fill-factor

The solar cell fill factor (FF) has previously been shown to be a crucial parameter that defines the maximum power (P_{max}) derived in accordance with J_{sc} and V_{oc} .

$$FF = \frac{J_{max} \times V_{max}}{J_{sc} \times V_{oc}} \quad (2.3)$$

Graphically, as seen in Figure 2.16, FF is spread over a larger rectangular region in the J - V curve. In particular, FF shows how photo-generated carriers have an ideal level of 100 % are derived from solar cell devices (see Figure 2.16 (a)). It is well established that the FF reflects the effectiveness of the charge carrier selection before recombining within the cell, which generally relies on the mobility of charge carriers and the recombination rate [63]. The highest FF values recorded for inorganic solar cells are approximately 90 %, whereas the FF value is usually between 50 and 70 % in OSCs [64,65]. Among many other aspects, the fill factor is calculated primarily by (R_{sh}) and (R_s) of the solar cell. The solar cell's series resistance largely stems from the passage of charge carriers via the device as well as the resistance that arises at the interaction between the active layer and the electrodes, and also the resistance difference between two electrodes respectively. The influence of R_s on the FF is important as the incredibly high R_s values contribute to a decrease in J_{sc} . In order to stop leakage current and lower R_s , a high FF needs substantial (R_{sh}) (refer Figure 2.5 (b)) [66]. For higher R_s and R_{sh} , as seen in Figure 2.15, the FF is decreased as in Figure 2.15 (c). Whereas in the case of low R_s and R_{sh} , the effect of FF is seen in Figure 2.16. (d).

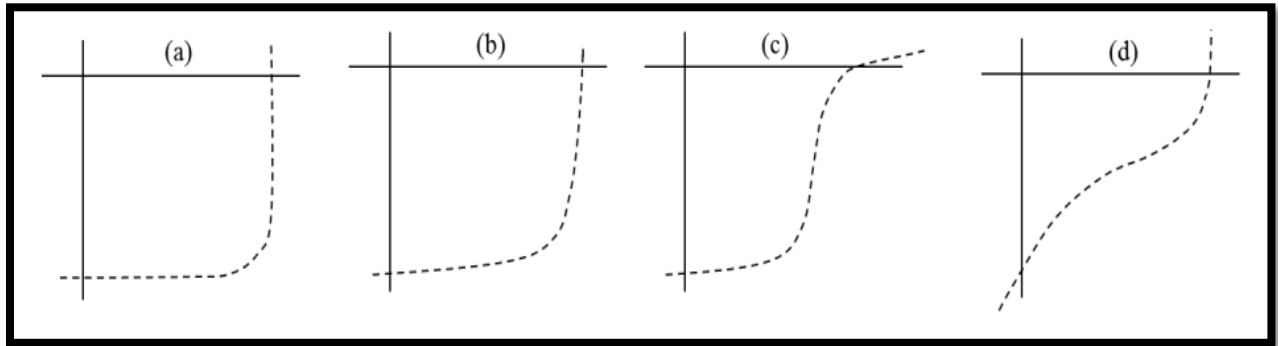


Figure 2.16: J - V characteristics of a solar cell with different FF ; (a) ideal FF , (b) FF with high R_{sh} and low R_s , (c) FF with high R_s and high R_{sh} , (d) FF with low R_{sh} and high R_s .

In OSCs, FF and device performance improvements could occur only if the photo-generated carriers were processed without the recombination loss. Solar cell FF is therefore limited to both holes and electrons by the carrier diffusion length (L_d); which can be described in the equation [67]:

$$L_d = \mu\tau E \quad (2.4)$$

where μ is the mobility of the charge carrier, τ represents the lifetime of the carrier recombination and E represents electrical field. Because of the poor mobility of carriers in case of organic materials as well as the higher incidence of recombination that impedes the efficient collection of photo generated charge carriers in OSCs, it is important to establish a strategy to solve this problem.

2.10.2.5 Origin of dark-current ideality factor

Researchers found that the recombination of carriers in bulk-heterojunction solar cell (BHJ) is considered as the main reasons that reduced the efficiency of the solar cell. Therefore, the understanding of the mechanism behind the carrier recombination becomes very crucial. It is believed that reducing the recombination can further increase the power conversion efficiency (PCE) of solution processed BHJ organic solar cells [68]. The diode ideality factor has been used as a useful tool for the investigation that indicates the effects of traps on carrier recombination in the photovoltaic device [69]. In 1952, Shockley and Read [70] first reported a method with ideal diode solar cell current–voltage equation and single exponential diode model to analyse the efficiencies of solar cells. The ideal solar cell current–voltage equation is listed as follows:

$$J = J_L - J_o \left[\exp\left(\frac{qV}{nK_B T}\right) - 1 \right] \quad (2.5)$$

where J_L is the light current density, J_o is the carrier recombination current density (also called saturation current density), q is the elementary charge, V is the applied voltage, K is the Boltzmann constant, T is the operating temperature in Kelvin scale, and n is the diode ideality factor. In this model, the ideal photovoltaic device is assumed to precisely follow the solar cell current–voltage equation and the diode ideality factor n acts as an indicator that can describe the difference between the practical device and the ideal [71]. Generally, the ideality factor's value of the diode ranges from 1 to 2. The value of $n = 1$, that is an ideal ideality factor, in contrast, the more n value increase

is indicates that there are traps involved in a carrier recombination mechanism in solar cells [72]. Thus, the diode ideality factor is an important parameter that can describe the electrical behaviour of photovoltaic devices. There are various methods to calculate the diode ideality factor based on different theories [73]. In this research, the ideality factor will be determined by using the most common method that is based on the dark current density–voltage (J – V) curve [74]. In this method, the parasitic resistances are ignored. The ideal solar cell current–voltage equation in the dark can be written as

$$J_{dark} = J_0 \left[\exp\left(\frac{qV}{nK_B T}\right) - 1 \right] \quad (2.6)$$

Where J_{dark} is the dark current density, J_0 is the carrier recombination current density, and V is the applied bias voltage. By using the J – V characteristics in the dark, the diode ideality factor n can be calculated from the slope in the exponential region of the curve. The diode ideality factor extracted from the J – V curve can be represented as follows [72]:

$$n = \left(\frac{K_B T}{q} \frac{\partial \ln J}{\partial V} \right)^{-1} \quad (2.7)$$

It can be independently obtained from the slope of the exponential regime of dark J – V characteristics on a semi-logarithmic plot.

2.10.2.6 Power conversion efficiency

The most important performance parameter of a solar cell is the amount of power conversion efficiency (PCE), or in some literature defined as η . This parameter defines the percentage of transformation of light power into output power. It is calculated as the ratio between the generated maximum power generated by the solar cell and the power of the incident light.

$$PCE = \frac{J_{max} \times V_{max}}{P_{light}} \times 100 = \frac{FF \times J_{sc} \times V_{oc}}{P_{light}} \times 100 \quad (2.8)$$

It is clear from the *PCE* equation that three main parameters, FF , J_{SC} and V_{OC} have direct effect on the *PCE* of solar cells. Moreover, the light source spectrum and its power are major factors for determining *PCE*, due to the limitation of absorption of wavelengths and the conversion of photons to electrons within solar cells. A standard spectrum is picked for working out *PCE* to effectively draw comparisons between different solar cells [75].

References

- [1] A. K. Singh, "Organic photovoltaics using novel pentacene derivatives," Northeastern University Boston, **2013**.
- [2] M. S. AlSalhi, J. Alam, L. A. Dass, and M. Raja, "Recent advances in conjugated polymers for light emitting devices," *International Journal of Molecular Sciences*, vol. 12, no. 3, pp. 2036-2054, **2011**.
- [3] N. Belghiti, M. Bennani, M. Hamidi, S. Bouzzine, and M. Bouachrine, "New compounds based on anthracene for organic solar cells applications," *Mater. Env. Sci*, vol. 5, p. 2191, **2014**.
- [4] V. Coropceanu, J. Cornil, D. A. da Silva Filho, Y. Olivier, R. Silbey, and J.-L. Brédas, "Charge transport in organic semiconductors," *Chemical reviews*, vol. 107, no. 4, pp. 926-952, **2007**.
- [5] E. Orgiu *et al.*, "Conductivity in organic semiconductors hybridized with the vacuum field," *Nature Materials*, vol. 14, no. 11, pp. 1123-1129, **2015**.
- [6] M. Terrones, "Science and technology of the twenty-first century: synthesis, properties, and applications of carbon nanotubes," *Annual review of materials research*, vol. 33, no. 1, pp. 419-501, **2003**.
- [7] T. M. Alshahrani. B. University. (**2016**). Fabrication and Charactrasation of PAMAM-Based Organic Photovoltics.
- [8] A. Alias, Z. Zabidi, A. Ali, M. Harun, and M. Yahya, "Optical characterization and properties of polymeric materials for optoelectronic and photonic applications," *International Journal of Applied Science and Technology*, vol. 3, no. 5, **2013**.
- [9] S. Cataldo and B. Pignataro, "Polymeric thin films for organic electronics: properties and adaptive structures," *Materials*, vol. 6, no. 3, pp. 1159-1190, **2013**.
- [10] S. Mohd-Nasir, M. Sulaiman, N. Ahmad-Ludin, M. Ibrahim, K. Sopian, and M. Mat-Teridi, "Review of polymer, dye-sensitized, and hybrid solar cells," *International Journal of Photoenergy*, vol. 2014, **2014**.
- [11] M. H. Harun, E. Saion, A. Kassim, N. Yahya, and E. Mahmud, "Conjugated conducting polymers: A brief overview," *UCSI Academic Journal: Journal for the Advancement of Science & Arts*, vol. 2, pp. 63-68, **2007**.

- [12] M. C. Scharber and N. S. Sariciftci, "Efficiency of bulk-heterojunction organic solar cells," *Progress in polymer science*, vol. 38, no. 12, pp. 1929-1940, **2013**.
- [13] M. Kadhem and B. A. Hasan, "11 . 4 % efficiency of organic solar cells using Graphene electron collecting buffer layer as a novel work 11 . 4 % efficiency of organic solar cells using Graphene electron collecting buffer layer as a novel work," no. December 2019, **2018**.
- [14] J. Anthony, A. Facchetti, M. Heeney, S. Marder and X. Zhan. "n-Type Organic Semiconductors in Organic Electronics", *Advanced Materials*, Vol.22 (34), pp. 3876–3892, **2010**.
- [15] P. Peumans and S. Forrest. "Very-high-efficiency double-heterostructure copper phthalocyanine/C₆₀photovoltaic cells", *Applied physics letters*, Vol. 79(1), pp.126-128, **2001**.
- [16] J. Hummelen, B. Knight, F. LePeq, F. Wudl, J. Yao and C. Wilkins. "Preparation and characterization of fulleroid and methanofullerene derivatives", *Journal of Organic Chemistry*, Vol. 60(3). pp. 532–538, **1995**.
- [17] M. Wienk, J. Kroon, W. Verhees, J. Knol, J. Hummelen, P. Hal and R. Janssen. "Efficient Methano[70]fullerene/MDMO-PPV Bulk Heterojunction Photovoltaic Cells", *Angewandte Chemie International Edition*, Vol. 42(29), pp. 3371–3375, **2003**.
- [18] A. C. Mayer, S. R. Scully, B. E. Hardin, M. W. Rowell, and M. D. McGehee, "Polymer-based solar cells," *Materials today*, vol. 10, no. 11, pp. 28-33, **2007**.
- [19] W. C. Choy, *Organic solar cells: materials and device physics*. Springer, **2012**.
- [20] C. J. Brabec *et al.*, "Tracing photoinduced electron transfer process in conjugated polymer/fullerene bulk heterojunctions in real time," *Chemical Physics Letters*, vol. 340, no. 3-4, pp. 232-236, **2001**.
- [21] S. Günes, H. Neugebauer, and N. S. Sariciftci, "Conjugated polymer-based organic solar cells," *Chemical reviews*, vol. 107, no. 4, pp. 1324-1338, **2007**.
- [22] T. Kietzke, "Recent advances in organic solar cells," *Advances in OptoElectronics*, vol. 2007, **2007**.
- [23] L. J. Koster, E. Smits, V. Mihailetschi, and P. Blom, "Device model for the operation of polymer/fullerene bulk heterojunction solar cells," *Physical Review B*, vol. 72, no. 8, p. 085205, **2005**.

- [24] C. J. Brabec *et al.*, "Origin of the open circuit voltage of plastic solar cells," *Advanced Functional Materials*, vol. 11, no. 5, pp. 374-380, **2001**.
- [25] I. D. Parker, "Carrier tunneling and device characteristics in polymer light-emitting diodes," *Journal of Applied Physics*, vol. 75, no. 3, pp. 1656-1666, **1994**.
- [26] M. C. Scharber *et al.*, "Design rules for donors in bulk-heterojunction solar cells—Towards 10% energy-conversion efficiency," *Advanced materials*, vol. 18, no. 6, pp. 789-794, 2006.
- [27] V. Mihailetschi, P. Blom, J. Hummelen, and M. Rispens, "Cathode dependence of the open-circuit voltage of polymer: fullerene bulk heterojunction solar cells," *Journal of Applied Physics*, vol. 94, no. 10, pp. 6849-6854, **2003**.
- [28] C. J. Brabec, S. E. Shaheen, C. Winder, N. S. Sariciftci, and P. Denk, "Effect of LiF/metal electrodes on the performance of plastic solar cells," *Applied physics letters*, vol. 80, no. 7, pp. 1288-1290, **2002**.
- [29] A. Hayakawa, O. Yoshikawa, T. Fujieda, K. Uehara, and S. Yoshikawa, "High performance polythiophene/fullerene bulk-heterojunction solar cell with a TiO_x hole blocking layer," *Applied Physics Letters*, vol. 90, no. 16, p. 163517, **2007**.
- [30] C. Waldauf *et al.*, "Highly efficient inverted organic photovoltaics using solution based titanium oxide as electron selective contact," *Applied Physics Letters*, vol. 89, no. 23, p. 233517, **2006**.
- [31] T. Kuwabara, T. Nakayama, K. Uozumi, T. Yamaguchi, and K. Takahashi, "Highly durable inverted-type organic solar cell using amorphous titanium oxide as electron collection electrode inserted between ITO and organic layer," *Solar Energy Materials and Solar Cells*, vol. 92, no. 11, pp. 1476-1482, **2008**.
- [32] K. Keis, E. Magnusson, H. Lindström, S.-E. Lindquist, and A. Hagfeldt, "A 5% efficient photoelectrochemical solar cell based on nanostructured ZnO electrodes," *Solar energy materials and solar cells*, vol. 73, no. 1, pp. 51-58, **2002**.
- [33] A. Kyaw, X. Sun, C. Jiang, G. Lo, D. Zhao, and D. Kwong, "An inverted organic solar cell employing a sol-gel derived ZnO electron selective layer and thermal evaporated MoO₃ hole selective layer," *Applied Physics Letters*, vol. 93, no. 22, p. 221107, **2008**.
- [34] H. Schmidt, H. Flügge, T. Winkler, T. Bülow, T. Riedl, and W. Kowalsky, "Efficient semitransparent inverted organic solar cells with indium tin oxide top electrode," *Applied Physics Letters*, vol. 94, no. 24, p. 163, **2009**.

- [35] S. Han, W. S. Shin, M. Seo, D. Gupta, S.-J. Moon, and S. Yoo, "Improving performance of organic solar cells using amorphous tungsten oxides as an interfacial buffer layer on transparent anodes," *Organic Electronics*, vol. 10, no. 5, pp. 791-797, **2009**.
- [36] C. Y. Jiang, X. W. Sun, A. K. K. Kyaw, and Y. N. Li, "Low work function metal modified ITO as cathode for inverted polymer solar cells," *Solar Energy Materials and Solar Cells*, vol. 94, no. 10, pp. 1618-1621, **2010**.
- [37] A. Gadisa, M. Svensson, M. R. Andersson, and O. Inganäs, "Correlation between oxidation potential and open-circuit voltage of composite solar cells based on blends of polythiophenes/fullerene derivative," *Applied Physics Letters*, vol. 84, no. 9, pp. 1609-1611, **2004**.
- [38] K. Vandewal *et al.*, "Varying polymer crystallinity in nanofiber poly (3-alkylthiophene): PCBM solar cells: Influence on charge-transfer state energy and open-circuit voltage," *Applied Physics Letters*, vol. 95, no. 12, p. 256, **2009**.
- [39] E. Bundgaard and F. C. Krebs, "Low band gap polymers for organic photovoltaics," *Solar Energy Materials and Solar Cells*, vol. 91, no. 11, pp. 954-985, **2007**.
- [40] L. Dou *et al.*, "Tandem polymer solar cells featuring a spectrally matched low-bandgap polymer," *Nature Photonics*, vol. 6, no. 3, pp. 180-185, **2012**.
- [41] P. G. Nicholson and F. A. Castro, "Organic photovoltaics: principles and techniques for nanometre scale characterization," *Nanotechnology*, vol. 21, no. 49, p. 492001, **2010**.
- [42] C. W. Tang, "Two-layer organic photovoltaic cell," *Applied physics letters*, vol. 48, no. 2, pp. 183-185, **1986**.
- [43] J. E. Slota, X. He, and W. T. Huck, "Controlling nanoscale morphology in polymer photovoltaic devices," *Nano Today*, vol. 5, no. 3, pp. 231-242, **2010**.
- [44] R. Steim, F. R. Kogler, and C. J. Brabec, "Interface materials for organic solar cells," *Journal of Materials Chemistry*, vol. 20, no. 13, pp. 2499-2512, **2010**.
- [45] K. Hong, S. Y. Yang, C. Yang, S. H. Kim, D. Choi, and C. E. Park, "Reducing the contact resistance in organic thin-film transistors by introducing a PEDOT: PSS hole-injection layer," *Organic electronics*, vol. 9, no. 5, pp. 864-868, **2008**.
- [46] Y. Cao *et al.*, "Dye-sensitized solar cells with a high absorptivity ruthenium sensitizer featuring a 2-(hexylthio)thiophene conjugated bipyridine," *J. Phys. Chem. C*, vol. 113, no. 15, pp. 6290–6297, **2009**.

- [47] R. Meng, Y. Li, C. Li, K. Gao, S. Yin, and L. Wang, "Exciton transport in π -conjugated polymers with conjugation defects," *Phys. Chem. Chem. Phys.*, vol. 19, no. 36, pp. 24971–24978, **2017**.
- [48] X. Jiao, L. Ye, and H. Ade, "Quantitative Morphology–Performance Correlations in Organic Solar Cells: Insights from Soft X-Ray Scattering," *Adv. Energy Mater.*, vol. 7, no. 18, pp. 1–22, **2017**.
- [49] R. Meng *et al.*, "Exciton intrachain transport induced by interchain packing configurations in conjugated polymers," *Phys. Chem. Chem. Phys.*, vol. 17, no. 28, pp. 18600–18605, **2015**.
- [50] S. M. Menke, N. A. Ran, G. C. Bazan, and R. H. Friend, "Understanding Energy Loss in Organic Solar Cells: Toward a New Efficiency Regime," *Joule*, vol. 2, no. 1, pp. 25–35, **2018**.
- [51] Y. Ji, L. Xu, X. Hao, and K. Gao, "Energy Loss in Organic Solar Cells: Mechanisms, Strategies, and Prospects," *Sol. RRL*, vol. 4, no. 7, pp. 1–17, **2020**.
- [52] Z. Zhou *et al.*, "Subtle Molecular Tailoring Induces Significant Morphology Optimization Enabling over 16% Efficiency Organic Solar Cells with Efficient Charge Generation," *Adv. Mater.*, vol. 32, no. 4, pp. 1–8, **2020**.
- [53] B. Friedel *et al.*, "Effects of layer thickness and annealing of PEDOT: PSS layers in organic photodetectors," *Macromolecules*, vol. 42, no. 17, pp. 6741–6747, **2009**.
- [54] S. Timpanaro, M. Kemerink, F. Touwslager, M. De Kok, and S. Schrader, "Morphology and conductivity of PEDOT/PSS films studied by scanning–tunneling microscopy," *Chemical Physics Letters*, vol. 394, no. 4–6, pp. 339–343, **2004**.
- [55] J. Huang, P. F. Miller, J. C. de Mello, A. J. de Mello, and D. D. Bradley, "Influence of thermal treatment on the conductivity and morphology of PEDOT/PSS films," *Synthetic Metals*, vol. 139, no. 3, pp. 569–572, **2003**.
- [56] D. Wakizaka, T. Fushimi, H. Ohkita, and S. Ito, "Hole transport in conducting ultrathin films of PEDOT/PSS prepared by layer-by-layer deposition technique," *Polymer*, vol. 45, no. 25, pp. 8561–8565, **2004**.
- [57] F. Zhang, A. Vollmer, J. Zhang, Z. Xu, J. Rabe, and N. Koch, "Energy level alignment and morphology of interfaces between molecular and polymeric organic semiconductors," *Organic Electronics*, vol. 8, no. 5, pp. 606–614, **2007**.

- [58] F. C. Krebs, S. A. Gevorgyan, and J. Alstrup, "A roll-to-roll process to flexible polymer solar cells: model studies, manufacture and operational stability studies," *Journal of Materials Chemistry*, vol. 19, no. 30, pp. 5442-5451, **2009**.
- [59] F. C. Krebs, "All solution roll-to-roll processed polymer solar cells free from indium-tin-oxide and vacuum coating steps," *Organic Electronics*, vol. 10, no. 5, pp. 761-768, **2009**.
- [60] S. Ciná *et al.*, "P-135: Efficient Electron Injection from PEDOT-PSS into a Graded-n-doped Electron Transporting Layer in an Inverted OLED Structure," in *SID Symposium Digest of Technical Papers*, **2005**, vol. 36, no. 1: Wiley Online Library, pp. 819-821.
- [61] Y.-C. Tseng, A. U. Mane, J. W. Elam, and S. B. Darling, "Ultrathin molybdenum oxide anode buffer layer for organic photovoltaic cells formed using atomic layer deposition," *Solar energy materials and solar cells*, vol. 99, pp. 235-239, **2012**.
- [62] M. D. Irwin, D. B. Buchholz, A. W. Hains, R. P. Chang, and T. J. Marks, "p-Type semiconducting nickel oxide as an efficiency-enhancing anode interfacial layer in polymer bulk-heterojunction solar cells," *Proceedings of the National Academy of Sciences*, vol. 105, no. 8, pp. 2783-2787, **2008**.
- [63] I. Hancox *et al.*, "Optimization of a high work function solution processed vanadium oxide hole-extracting layer for small molecule and polymer organic photovoltaic cells," *The Journal of Physical Chemistry C*, vol. 117, no. 1, pp. 49-57, **2013**.
- [64] J. Meyer, S. Hamwi, M. Kröger, W. Kowalsky, T. Riedl, and A. Kahn, "Transition metal oxides for organic electronics: energetics, device physics and applications," *Advanced materials*, vol. 24, no. 40, pp. 5408-5427, **2012**.
- [65] K. X. Steirer *et al.*, "Solution deposited NiO thin-films as hole transport layers in organic photovoltaics," *Organic Electronics*, vol. 11, no. 8, pp. 1414-1418, **2010**.
- [66] I. S. Oh, G. M. Kim, S. H. Han, and S. Y. Oh, "PEDOT: PSS-free organic photovoltaic cells using tungsten oxides as buffer layer on anodes," *Electronic Materials Letters*, vol. 9, no. 4, pp. 375-379, **2013**.
- [67] R. Roesch, K.-R. Eberhardt, S. Engmann, G. Gobsch, and H. Hoppe, "Polymer solar cells with enhanced lifetime by improved electrode stability and sealing," *Solar energy materials and solar cells*, vol. 117, pp. 59-66, **2013**.

- [68] L. Duan et al., "Relationship between the diode ideality factor and the carrier recombination resistance in organic solar cells," *IEEE J. Photovoltaics*, vol. 8, no. 6, pp. 1701–1709, **2018**.
- [69] Y. Zhu et al., "Improving the charge carrier transport and suppressing recombination of soluble squaraine-based solar cells via parallel-like structure," *Materials (Basel)*, vol. 11, no. 5, **2018**.
- [70] W. S. and W. T. Read, "Statistics of the recombinations of holes and electrons," *Phys. Rev.*, vol. 87, no. 5, pp. 835–842, **1952**.
- [71] H. Bayhan and M. Bayhan, "A simple approach to determine the solar cell diode ideality factor under illumination," *Sol. Energy*, vol. 85, no. 5, pp. 769–775, **2011**.
- [72] C. M. Amaral Da Luz, P. Dos Santos Vicente, F. L. Tofoli, and E. M. Vicente, "Influence of series and shunt resistances in the ideality factor of photovoltaic modules," *2016 12th IEEE Int. Conf. Ind. Appl. INDUSCON 2016*, no. 2, pp. 1–6, **2017**.
- [73] S. A. Hawks, G. Li, Y. Yang, and R. A. Street, "Band tail recombination in polymer: Fullerene organic solar cells," *J. Appl. Phys.*, vol. 116, no. 7, **2014**.
- [74] S. Yan et al., "Effects of solvent additives on trap-assisted recombination in P3HT:ICBA based polymer solar cells," *Phys. Status Solidi Appl. Mater. Sci.*, vol. 212, no. 10, pp. 2169–2173, **2015**.
- [75] F.-C. Chen, J.-L. Wu, K.-H. Hsieh, W.-C. Chen, and S.-W. Lee, "Polymer photovoltaic devices with highly transparent cathodes," *Organic electronics*, vol. 9, no. 6, pp. 1132–1135, **2008**.

Chapter 3

Materials and Experimental Techniques

3.1 Introduction

The techniques and experimental methods used in this study are discussed in this chapter. Organic solar cells processing and most characterizations, including atomic force microscopy (AFM) and current-voltage (*I-V*) experiments, are carried out at the School of Computer Science and Electronic Engineering, Bangor University. Ultra-Violet/Visible (UV/VIS) spectrophotometer measurements were carried out at the School of Chemistry, Bangor University. Techniques and materials used for fabrication of organic solar cell are described in the first part of this chapter. All fabrication processes were carried out in a class 1000 clean room and glovebox to minimize atmospheric contamination. The second part of the chapter focused on the equipment used for studying the morphology and electrical properties and of the fabricated organic solar cells.

3.2 Laboratory environment

Materials and the preparations for tests were performed in a cleanroom of class 1000. It involved preparing of mixtures, cleaning of the substrates, and deposition of poly(3,4-ethylenedioxythiophene) polystyrene sulfonate (PEDOT:PSS). Cells were produced in a nitrogen-glovebox that preserved concentrations of oxygen and water as small as 0 ppm and eliminate solvent vapors. A Control of Substances Hazardous to the Health (COSHH) evaluation forms were filled out to describe the risks of the materials used and the measures of emergency for the period of the trial as a preparation for the practical work. Hazardous chemicals include Decon 90, Propanol, Acetone, PEDOT: PSS, P3HT, ICBA, Chlorobenzene, Titanium, Gr, HCl, and Al.

ITO coated substrate (2.5 cm x 2.5 cm), poly(3-hexylthiophene) (P3HT) as a donor and indene- C_{70} bisadduct (IC₇₀BA) as an acceptor (P3HT:IC₇₀BA) blend or bilayer as an active layer, poly (3, 4-ethylenedioxythiophene) polystyrene sulfonic acid (PEDOT: PSS) as a hole transport layer, Lithium fluoride (LiF) or graphene (Gr) precursor as an electron transport layer, and Al (Aluminum) as an electrode are the necessary materials for producing the OPV cells. Figure 3.1 displays a diagram of the systems at the top view.

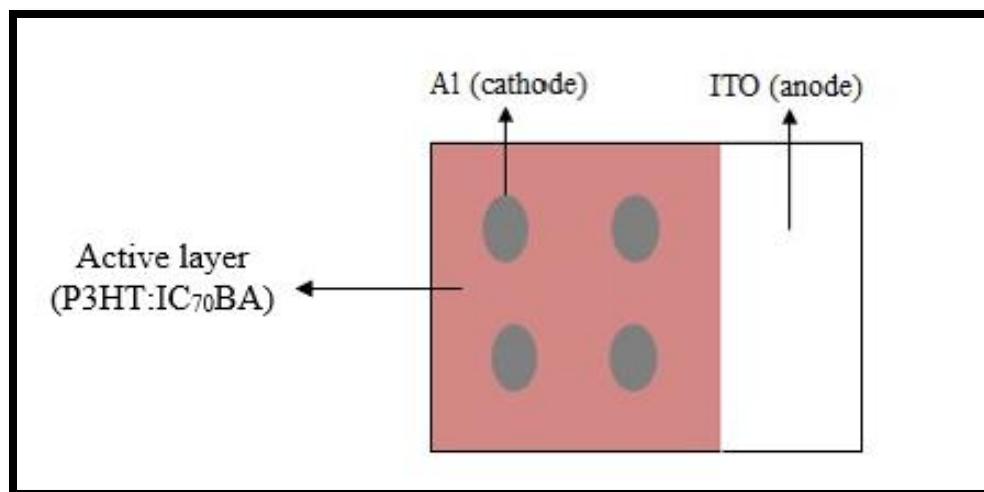


Figure 3.1: *Top view of the OPV cells diagram.*

3.3 Materials

Poly(3-hexylthiophene-2,5-diyl) (P3HT), graphene (Gr) and Lithium fluoride (LiF) were purchased from Sigma Aldrich. PEDOT:PSS solution (CLEVIOS AL 4083) was obtained from Heraeus, and indene-C₇₀ bisadduct (IC₇₀BA) IC₇₀BA was purchased from Solaris Chem Inc.

3.3.1 Poly (3-hexylthiophene-2,5-diyl) (P3HT)

Regio-regular poly (3-hexylthiophene) (P3HT) has been used as a light-absorber as well as an electron hole/donor transporter. Regio-regular means that a unit of 3-hexylthiophene in the chain of a particular polymer is aligned in such orientation that the residue group C₆H₁₃ is either head-to-head (HH) or head to tail (HT) [1, 2]. These characteristics make the polymer better organized during deposition, which means the mobility of the product is significantly increased [3, 4]. Figure 3.2 shows the material's chemical structure.

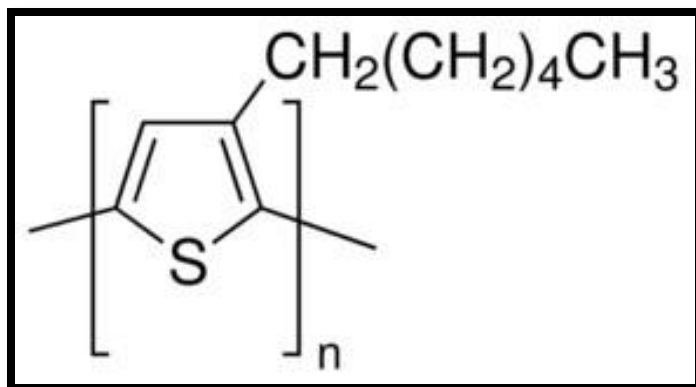


Figure 3.2: Chemical structure of P3HT.

The electrical and optical properties of P₃HT were used to measure the bandgap of the material and found to be around 1.9 eV, while the Lowest Unoccupied Molecular Orbital (LUMO) and the Highest Occupied Molecular Orbital (HOMO) are at 3.2 and 5.1 eV, respectively [1,5]. Generally, a thin film of P3HT serves as a donor to an electron-acceptor in photo-excitation and has strong hole mobility. The film comprises a mobility of around $10^{-3} \text{ cm}^2 \text{ V}^{-1} \text{ s}^{-1}$ in small, badly structured films. The P3HT has an optical absorption peak of 550 nm wavelength, and a broad absorption range of 400 to 650 nm, a rich area of energy concerning the solar spectrum at 1.5 AM (refers to exactly two standard terrestrial solar spectral irradiance spectra) [6-8].

3.3.2 Indene-C70 Bisadduct (IC₇₀BA)

To further optimize the efficiency of P3HT-based systems, new derivatives of fullerene containing high energy levels of LUMO were manufactured for the application as acceptors in P3HT-based OSCs [9-11]. Zhao, Guangjin et al. identified a number of acceptors of indene-fullerene adducts, namely indene-C₆₀ bisadduct (ICBA) [12,13], indene-C₇₀ bisadduct (IC₇₀BA) [13] and [6,6]-phenyl-C₆₁-butyric acid methyl ester (PCBM) indene addition [14]. IC₇₀BA and ICBA have higher energy levels of LUMO -3.74 and -3.72 eV, respectively, that are greater than those of [6,6]-Phenyl-C₇₀-butyric acid methyl ester (PC₇₀BM) and PCBM. In addition, they have gained significant attention due to their electroactive properties. They act as electron acceptor that has high electron mobility and accepts up to six electrons when in solution [12,14]. The higher levels of LUMO energy of these fullerene derivatives resulted in higher (V_{oc}) and better power

conversion efficiency (PCE) of the OSCs dependent on P3HT [13, 15]. The PCE of OSCs based on P3HT:ICBA exceeded 6.5 %, the highest recorded values reported for P3HT-based OSCs [12], and OSCs based on P3HT:IC₇₀BA exhibited a PCE of 5.64% [13]. Figure 3.3 displays the chemical structure for the C₇₀-based fullerene derivative. PCBM is the most widely used acceptor in OPV and due to its spherical shape, it offers advantage over other planar semiconductors because 3D electron transport is possible in it. However, the main drawback is the weak absorption of visible light. To overcome this problem, a C₇₀ analogue of it was developed to have a higher photocurrent in OPV devices as it had a stronger absorption in the solar spectrum blue region [16].

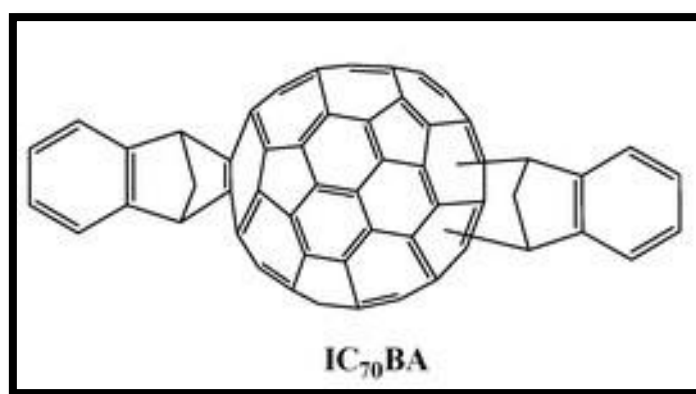


Figure 3.3: Chemical structures of IC₇₀BA fullerene derivative used in OPV devices[13].

3.3.3 Poly(3,4-ethylenedioxythiophene) poly (styrenesulfonate) (PEDOT: PSS)

This material has been extensively used in organic electronics due to its characteristics in the conduction of hole. This was formerly used as an active barrier among the dielectric material and the gate electrode in transistors, buffers, or electrode [16-18]. It has many advantages, including mechanical flexibility, high transparency, and reliable thermal stability. Due to these characteristics, it was used as anode buffer layer in the OSCs [19, 20]. It is among the finest hole conduction buffers since it possesses a high ionization potential that closely correlates to the feature of ITO, whereas its electron affinity is around 2.2 eV [21]. It is a polymer with two ionomers of a single component. The first part (PEDOT) is a polythiophene polymer bearing positive charge, and the other portion (PSS) is a polymer holding negative charge of sodium

polystyrene sulfonate. The PEDOT:PSS mixture is being used to enhance the contact of ITO-anode [22, 23]. The chemical composition of PEDOT-PSS can be seen in Figure 3.4.

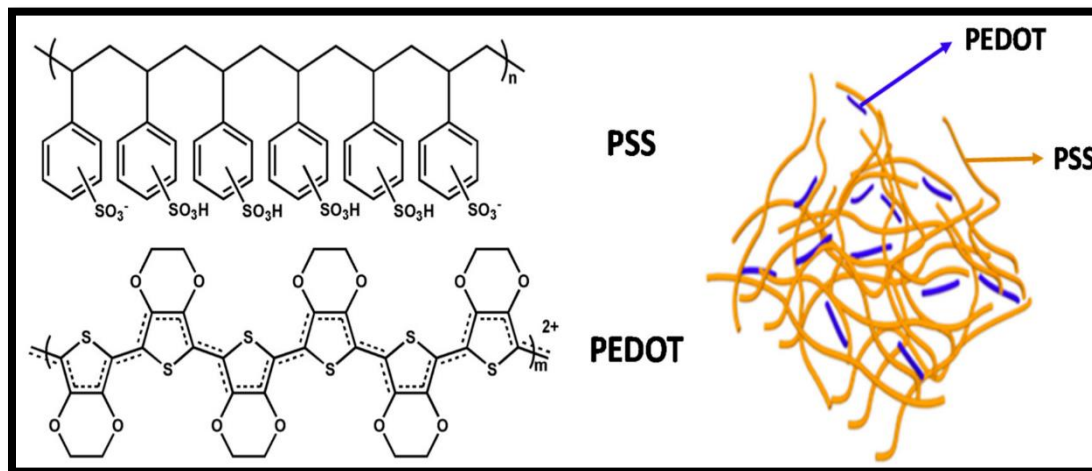


Figure 3.4: *PEDOT, PSS and PEDOT: PSS structures.*

3.3.4 Lithium Fluoride (LiF)

Lithium fluoride (LiF) is one of the commonly utilized electrode material in both inorganic and organic solar cells owing to attractive features like considerably high conduction energy band, that is higher than 10 eV, and various other attractive features such as high stability and ease in processability [24]. Thermal evaporation deposition is the excessively utilized technique for the deposition of LiF. Lithium fluoride is typically used as a thin layer to act as good electron transfer layer (ETL) to effectively improve the efficiency of OSCs. It was observed that a thin layer of lithium fluoride on aluminum-based electrode drastically improve the electron injection. Lithium fluoride in its vapor form consists of three forms i.e. monomers, dimmers and trimers [25]. It is colorless solid in nature that undergo transitions to white color by decreasing its crystal size. Figure 3.5 represents the formation of lithium fluoride compound from its structural atoms in which electron from the outer most orbital of the Li atom being transferred to the outer most orbital of the F atom. This bonding resulted in the formation of lithium fluoride compound.

Lithium fluoride is being used as a thin interfacial layer in organic solar cells as the interlayer structure of LiF decreases the barrier resistance between the aluminum electrode and active layer

in organic solar cells and decreases the overall resistance in charge transfer. Addition of LiF layer avoids the forming of trap states owing to the oxidation reaction that takes place on the interface of the metal aluminum. A thin LiF layer (nearly 15 angstroms) also increases (FF) of the device by forming a buffer layer of ohmic contact in organic solar cell [26].

Lithium fluoride reduces the barrier height of cathode and ensures smooth transfers ejection of electrons. Various researches revealed the lowering of the highest occupied molecular orbital (HOMO) which is possible by the deposition of LiF prior to the deposition of Al [27].

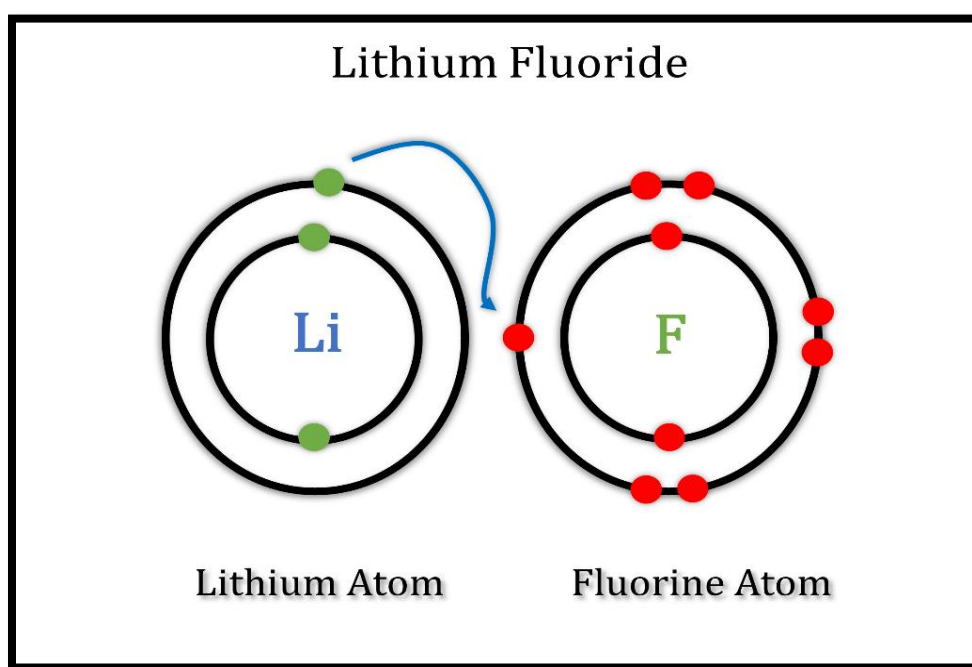


Figure 3.5: *Formation of lithium fluoride compound from its structural atoms.*

From the above information, it is expected that the LiF layer is responsible for the protection of other layers underneath when evaporation of metal is required as the top takes electrode. Less diffusion of metal (such as aluminum) will take place in the film which may lead to a higher conducting channel followed by charge recombination which results in the decrease of fill factor. The method of deposition of lithium fluoride on the other hand is very expensive which is one of the biggest limitations of using lithium fluoride [28]. However, owing to the wide range of band gap and improved surface chemistry, LiF appears to be an attractive interfacial layer material as

well as an excellent emitter layer. LiF is also utilized as an emitter that also supported to acquire high efficiency with solar cells based on silicon heterojunction. LiF is also useful as an inter-layer material to decrease the resistance in series and also to shunt leakage. LiF is also favorable for the improvement in optical features of solar cells [29]. It is widely recognized that those materials which have low work function properties are usually favored for establishing a small barrier height towards the electron transportation. The highest value for fill factor was noted for the devices with 2 nm LiF interfacial layer thickness. By further increasing the LiF interfacial layer thickness, the fill factor value remained same or increased gradually. The short circuit current density (J_{sc}) value was observed to decrease when the LiF interfacial layer thickness was increased from 2 to 40 nm. A much wider band gap was observed for the LiF electron selective carrier layer (3.9 eV) which ensured the low absorption of light and less optical losses on the upper side of the cell. All these findings predicted various electrical features and optical properties of LiF that are advantageous in utilization of lithium fluoride as a selective carrier layer to acquire various optronic features and alignment of band gap [30].

3.3.5 Graphene

Graphene has received remarkable interest since it was formed in 2004 because of its valuable material properties including high stability of charges, accessibility, flexibility, and electrical mechanical strength. It is also predicted that graphene plays a significant function as a transparent and conductive electrode in the next-generation of electronic devices. A zero-overlap semimetal (with both holes and electrons as charge carriers) with very high electrical conductivity is considered as one of the most useful properties of graphene. It has 5 electrons; 4 in the outer shell and 2 in the inner shell. Each atom of the four outer shell electrons is connected to three other atoms by two-dimensional plane leaving one free electron for electronic conduction. The pi (π) electrons are highly mobile ones and be above and below the graphene sheet. The orbitals of pi electrons are overlap and helps to enhance carbon bonds in graphene. Principally, the bonding and anti-bonding of these pi orbitals are formed the electronic properties of graphene [31].

The Dirac point in graphene, electrons and holes have zero effective mass, that what combined research over the last 50 years has proved. This is due to the relation of energy-movement is linear for low energies near the six individual corners of the Brillouin zone. The six corners of the Brillouin zone are known as the Dirac points and the electrons and holes are known as Dirac fermions, or Graphinos. Generally, electronic conductivity is actually quite low due to zero density of states at the Dirac points. to create a material that is potentially better at conducting electricity than graphene, the Fermi level can be changed by doping (with electrons or holes) [32].

Tests have approved that the electronic mobility of graphene is very high, with previously reported results above $15,000 \text{ cm}^2 \cdot \text{V}^{-1} \cdot \text{s}^{-1}$ and theoretically potential limits of $200,000 \text{ cm}^2 \cdot \text{V}^{-1} \cdot \text{s}^{-1}$ (limited by the scattering of graphene's acoustic photons). It is said due to lack of mass, graphene electrons behave very much like photons in their mobility. These charge carriers are able to travel micrometres distances without scattering; this phenomenon is known as ballistic transport. Figure 3.6 shows the Graphene monolayer and Graphite crystal [33].

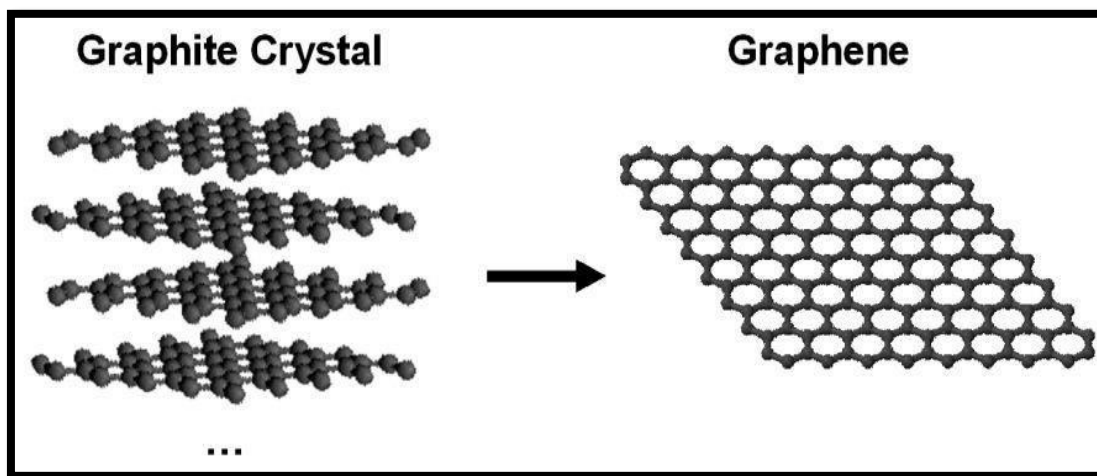


Figure 3.6: *Monolayer Graphene and Graphite crystal [33].*

3.4 Fabrication Methods

3.4.1 Spin Coating

The most popular deposition method is the spin coating process, which produces a simple, thin and durable film over a substrate. This is commonly used in organic light emitting diode (OLED) for the organic insulators, photoresist, and active materials deposition. It operates via a dispenser to drop the solution onto the substrate mounted on the spin coater's vacuumed tray, and then operate the spin coater to produce a thin film on the surface of the substrate. The theory of action of the spin coater is shown in Figure 3.7.

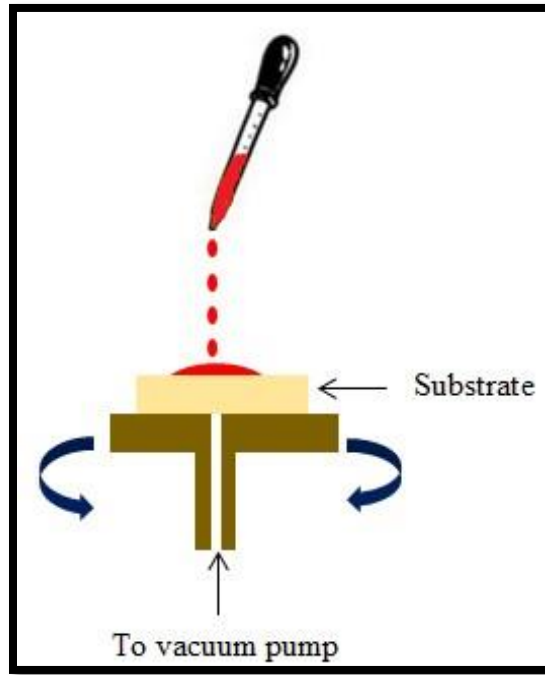


Figure 3.7: Operational procedure of Spin coater.

Thin films of organic materials may be created utilizing spin coating with thicknesses varying from nanometers to micrometers. The theoretical model for the spin coating method which governs the relationship among the thickness of the spun film (t), the solution's viscosity coefficient (η), material density (ρ), spinning angular velocity (ϑ) and spinning period (ω) is [34]:

$$t = (\eta / (4\pi \rho \vartheta^2))^{1/2} \omega^{-1/2} \quad (3.1)$$

Certain considerations, including the rate of drying (temperature/minute), pressure, surface tension, viscosity, etc. often control the final film thickness. Nevertheless, the spin speed is the spin process's most critical consideration for deciding the final thickness of the film. Figure 3.8 shows an example of the correlation between the film thickness of a photoresist substance and the speed of spinning [35]. The graph reveals that the high thickness is obtained by operating the spin coater at a lower speed while maintaining low thickness for higher speeds.

3.4.2 Thermal Evaporation

Mini-spectros system of Kurt J. Lesker as shown in Figure 3.8 was used to conduct the actual vapor deposition of the metal (Al cathode) and LiF via thermal evaporation. The electrical energy has been used for heating a filament that heated the deposition content to the extent of evaporation. A shadow mask has been used to establish a thin film design in which the vapor content in this design creates a thin film on the substrate surface. This method was carried out at very high vacuum rates enabling removal of film impurities. To avoid interaction among the vaporized materials and the environment, low pressures of around 10^{-6} mbar were used. Quartz crystal sensor (QCS) has been used to measure the film thickness and the Sigma device used to manage the processes of film deposition.

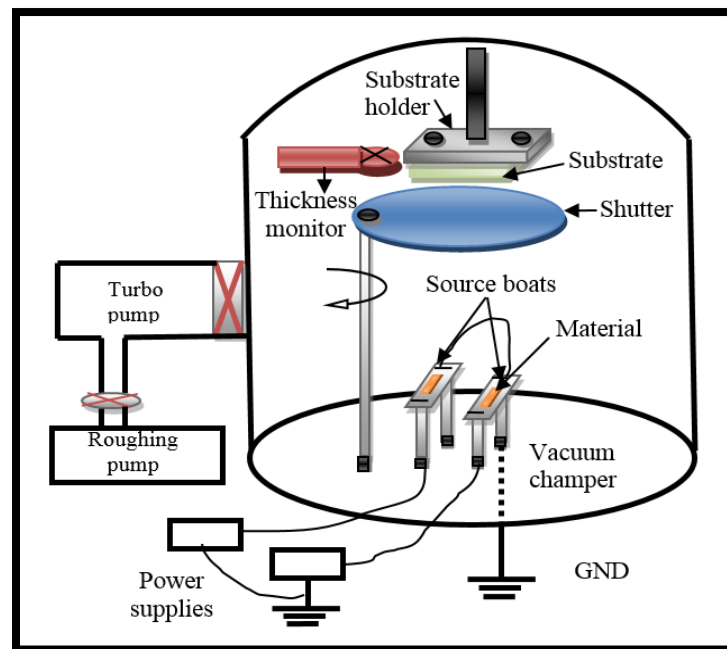


Fig 3.8: Kurt Lesker mini-spectros system diagram

3.4.3 Profilometer

The Dektak XT shown in Figure 3.9 is a 2D contact profilometer used to provide quantitative information about step heights and surface roughness for thin and thick films measurements. By Vision 64 application software, the information is collected and analysed. A diamond stylus is moved vertically in contact with the sample and then moved laterally across the sample for specified contact force at a specified distance. A profilometer can measure small surface variations in vertical stylus displacement as a function of position. Generally, profilometer can measure small vertical features ranging in height from ~ 10 nm to ~ 1 mm. The height position of the diamond stylus allows it to generate an analogy signal which is converted into a digital signal, stored, analysed, and then displayed on the computer display. The diamond stylus radius ranges from 20 nm to $50\text{ }\mu\text{m}$, and the horizontal resolution is controlled by data signal sampling rate and the scan speed. The stylus tracking force can range from less than ~ 1 to ~ 50 milligrams.



Figure 3.9: *Dektak XT within an environmental enclosure.*

3.5 Procedure of Fabrication

In this research, the general structure for fabricated devices will be as shown in Figure 3:10.

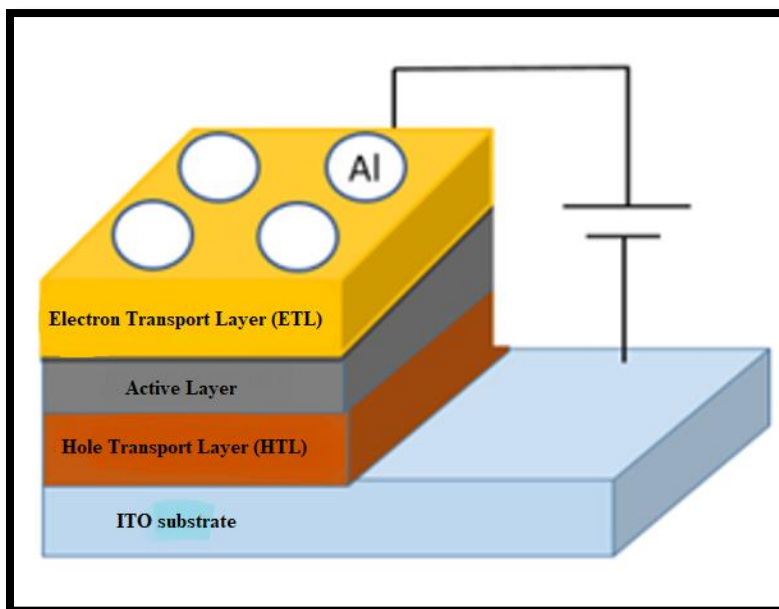


Figure 3.10: *cross section of fabricated devices.*

3.5.1 Substrate preparation

The substrates of pre-patterned ITO electrodes on glass were cut into small pieces with dimensions of 2.5 cm x 2.5 cm which can produce four devices each through a shadow mask. The cleaning of substrates started with soap, warm water and deionised water, then were placed on a cleanroom wipes inside the fume hood. The substrates were dried gently through nitrogen gun to remove the solvent and any remaining residue and were placed on another clean cleanroom wipes. The substrates were arranged in a specially designed substrates holder, then placed in acetone filled beaker so that the acetone level is above the substrates. After that, the beaker was placed in ultrasonic bath for 10 minutes. Then, the substrates were removed from the holder with a clean tweezers and blow-dried with compressed nitrogen. Previous steps were repeated but this time using isopropanol instead of acetone. Followed with UV-ozone treatment for 20 minutes.

3.5.2 Spin coating of the hole transport layer

In this process, the EMS spin coater model 4000 was used. Conducting poly (3, 4-ethylenedioxylenethiophene)-polystyrene sulfonic acid (PEDOT:PSS) was spin-cast at 4000 rpm from aqueous solution for 40 second, after passing through a 0.45 μm filter, to produce a thin film with approximate thickness of 40 nm. The film was subjected to drying for 30 minutes at 150 $^{\circ}\text{C}$ in air.

3.5.3 Preparation of the active layer solution

The solution of the active layers was prepared by dissolving donor material P3HT and acceptor material IC₇₀BA in one glass vial at certain amount of the solvent, which changes depends on the experiment condition. The solvents are chlorobenzene (CB), dichlorobenzene (DCB) and mix of both to provide different concentrations of active layer solution. The vial was placed inside ultrasonic bath at a temperature of 50 $^{\circ}\text{C}$ for 30 minutes to increase the solubility of the solution. After that, the vials were placed on a hot plate at 40 $^{\circ}\text{C}$ in the glovebox with a magnetic stirrer, dissolving for at least 24 hours. Finally, the solution was syringed through a 0.2 μm PTFE filter into a second clean vial to remove any un-dissolved particles. Then, the solution was spin-cast at 600 rpm for 60 second with expected thickness ~ 100 nm on top of the PEDOT layer.

3.5.4 Spin coating of electron transport layer

Two different concentrations of graphene 10 mg and 20 mg were dissolved in 10 mL of deionized (DI) water. Each of the solutions was in a glass vial and the vials were placed inside ultrasonic bath at a temperature of 45 $^{\circ}\text{C}$ for 24 hours. Finally, the solution was syringed through a 0.45 μm PTFE filter into a second clean vial to remove any un-dissolved particles. Then, the solutions were spin-cast at different speeds (100 rpm, 4000 rpm and 7000 rpm) for 60 second with different thickness on the top of the active layer (P3HT:IC₇₀BA).

3.5.5 Evaporation of buffer layer and top electrodes

Lithium fluoride (LiF) which represents the buffer layer and aluminium electrodes were thermally evaporated using the Kurt. J. Lesker deposition system at rate of 0.1 \AA.s^{-1} , 1 \AA.s^{-1} , respectively through a shadow mask at a base pressure of 10^{-6} mbar. The deposition thickness of LiF is about 0.75 nm and the aluminium electrodes was ~ 100 nm. The active area of the complete devices is 0.125 cm^2 . Devices were tested under AM 1.5 illumination with intensity of 100 mW/cm^2 simulator at room temperature. Figure 3.11 represents the final of fabricated device.

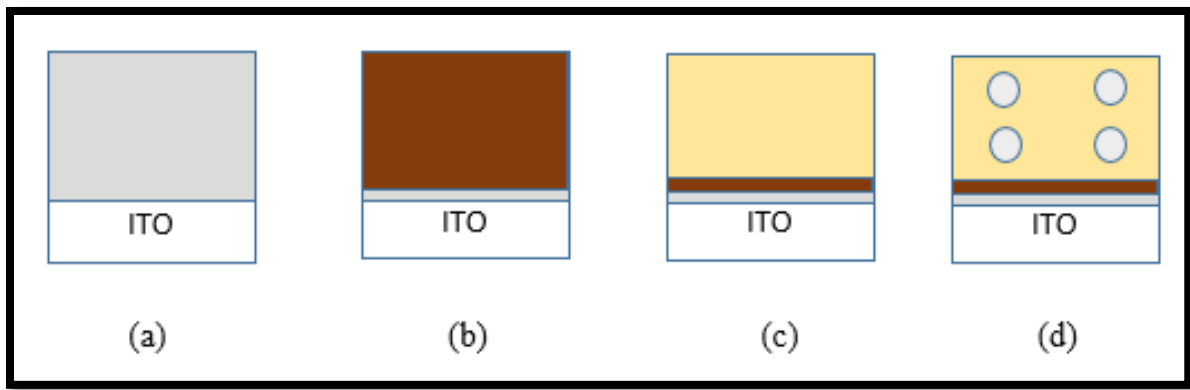


Figure 3.11: *device preparation process: a) ITO glass (25mm×25mm) with PEDOT:PSS deposited b) active layer deposited on top of the PEDOT:PSS c) LiF deposited on top of active layer d) Al deposited through shadow mask on top of the LiF.*

3.6 Device characterization

3.6.1 Atomic Force Microscopy

To study the surface morphology of thin films, researchers used atomic force microscopy (AFM) which is a high-resolution scanning probe microscopic technique. In 1985, Binnig, Quate and Gerber developed this technique to study materials and take high resolution images of sample surfaces. The technique is employed for many analyzing proposals such as magnetic forces, repulsive forces, and lateral friction forces. However, digital instrument nasoscope AFM was used to analyze the surface properties of the device layers in this study.

To obtain images in AFM technique, a sharp probe is used to scan the sample surface while analyzing the interactions of the sample with the tip. The scanning process involves the placement of a sharp microscope cantilever tip close to the sample's surface and the distance between the tip and the surface is adjusted in order to keep the cantilever deflection constant and small deflections will cause it to bend upwards. The bending's measurement is carried out using a laser spot reflected to sensor following which an image of the surface can be obtained at atomic level resolution. Generally, AFM measurement depends on the interaction between tip and sample surface and it is of two types, one is the contact mode where the tip touches the sample surface and the other is the non-contact mode where the tip only stays near the surface without contact. Vibrations are induced on the tip and these are monitored using a laser.

3.6.2 Ultra-violet/visible Spectroscopy

UV-visible spectroscopy (UV-vis) has been implemented to characterize the radiation absorption as a function of the wavelength for the active OPV layers. The device used for this characterization was a spectrophotometer 4800 Ocean Optics UV-Vis (300 to 900 nm) installed under a Newport Xenon arc lamp of class AAA (AM1.5 G range, 100 mW.cm⁻²) rating. To determine a residual absorption range, a measurement of a light source as well as glass substrate is mutually employed as a reference. The disparity determined the absorption spectrum of a system among the experimental spectra and the background.

3.6.3 Current-Voltage (*I-V*) Characterisation

A vacuum system used for the organic solar cells electric characterization. The system was designed with low vacuum system (10⁻³ torr) contained a steel chamber connected to a rotary pump. Inside the chamber, the substrate holder mounted in copper stage opposite to the light window where the substrate holder dimensions is 2.5 cm x 2.5 cm and the light source is a tungsten halogen lamp (50W) focused through a window onto the substrate (anode). Researchers have mostly used the tungsten lamp in the solar cell field although it has a slight difference with the AM 1.5 solar simulator, thus providing a reasonable light for comparison. The intensity of the light falling on the device could be varied from ~1 to 200 mW/cm² by moving the light source toward or away from the test sample. The light intensity was measured using a light intensity meter. A

light intensity equivalent to AM1.5 radiation from the halogen lamp was set using an AM1.5 calibrated Si photodiode (Thorlabs SM1PD2A). Figure 3.12 and Figure 3.13 show the schematic design of the measurement setup and a picture of the system.

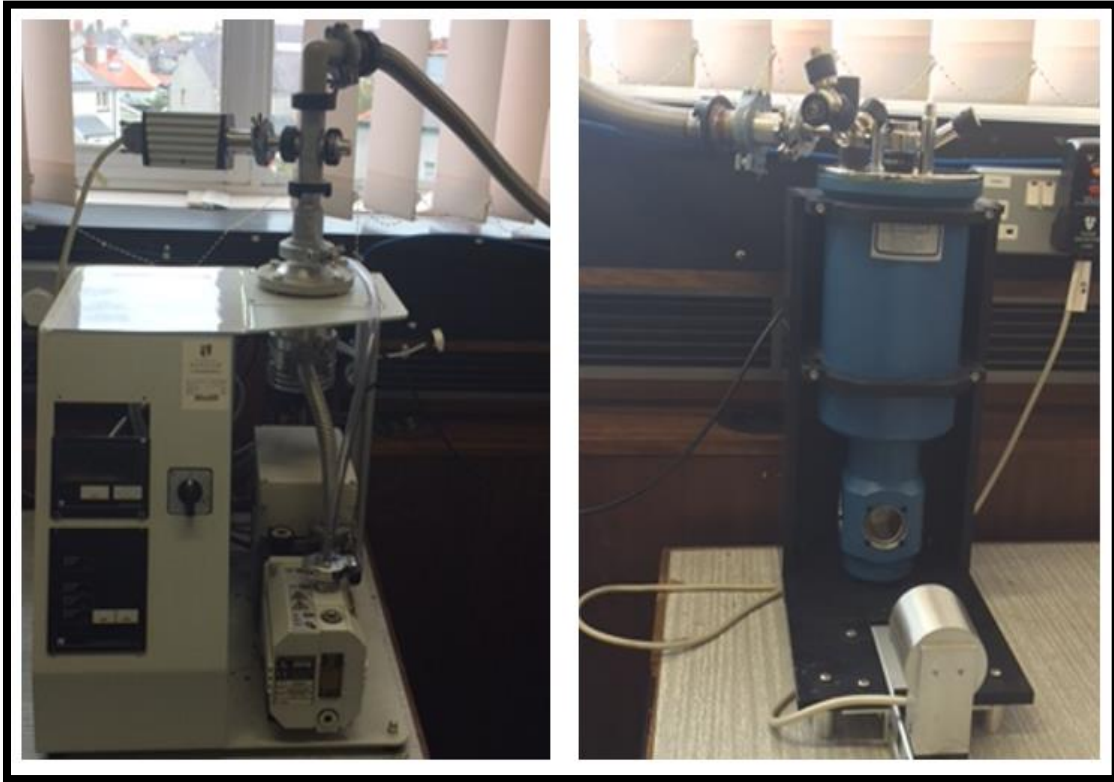


Figure 3.12: *a picture of Vacuum system setup.*

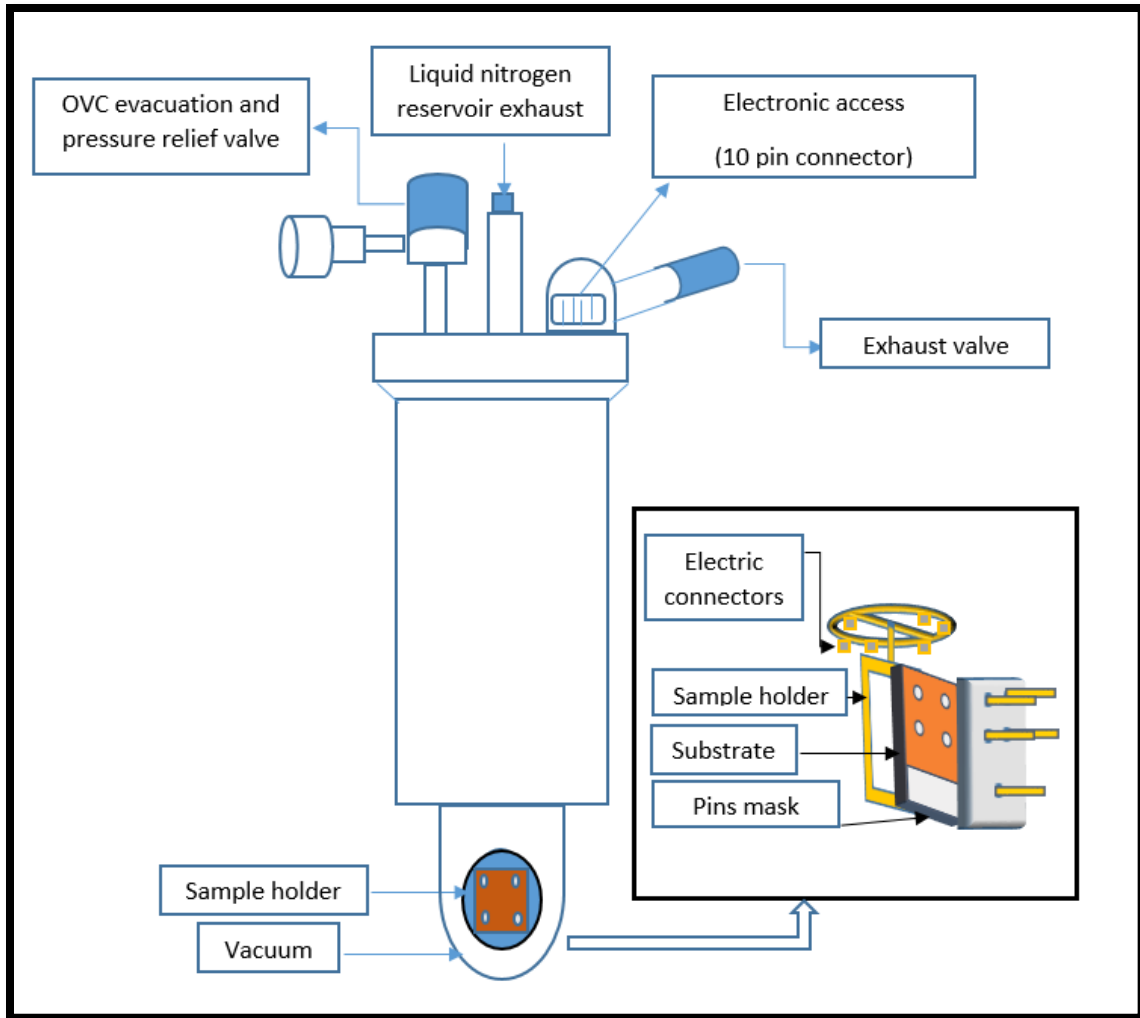


Figure 3.13: *Schematic diagram of the designed vacuum system.*

References

- [1] D. Chirvase, Z. Chiguvare, M. Knipper, J. Parisi, V. Dyakonov, and J. Hummelen, "Electrical and optical design and characterisation of regioregular poly (3-hexylthiophene-2, 5diyl)/fullerene-based heterojunction polymer solar cells," *Synthetic Metals*, vol. 138, no. 1-2, pp. 299-304, **2003**.
- [2] G. Li, V. Shrotriya, Y. Yao, J. Huang, and Y. Yang, "Manipulating regioregular poly (3-hexylthiophene):[6, 6]-phenyl-C 61-butyric acid methyl ester blends—route towards high efficiency polymer solar cells," *Journal of Materials Chemistry*, vol. 17, no. 30, pp. 3126-3140, **2007**.
- [3] D. Chirvase, J. Parisi, J. C. Hummelen, and V. Dyakonov, "Influence of nanomorphology on the photovoltaic action of polymer–fullerene composites," *Nanotechnology*, vol. 15, no. 9, p. 1317, **2004**.
- [4] D. Chirvase, Z. Chiguvare, M. Knipper, J. Parisi, V. Dyakonov, and J. Hummelen, "Temperature dependent characteristics of poly (3 hexylthiophene)-fullerene based heterojunction organic solar cells," *Journal of Applied Physics*, vol. 93, no. 6, pp. 3376-3383, **2003**.
- [5] J. You, L. Dou, Z. Hong, G. Li, and Y. Yang, "Recent trends in polymer tandem solar cells research," *Progress in polymer science*, vol. 38, no. 12, pp. 1909-1928, **2013**.
- [6] G. Kalonga, G. Chinyama, M. Munyati, and M. Maaza, "Characterization and optimization of poly (3-hexylthiophene-2, 5-diyl)(P3HT) and [6, 6] phenyl-C61-butyric acid methyl ester (PCBM) blends for optical absorption," *Journal of Chemical Engineering and Materials Science*, vol. 4, no. 7, pp. 93-102, **2013**.
- [7] J.-S. Huang *et al.*, "Polymer bulk heterojunction solar cells employing Förster resonance energy transfer," *Nature Photonics*, vol. 7, no. 6, pp. 479-485, **2013**.
- [8] B. J. Moon *et al.*, "Enhanced photovoltaic performance of inverted polymer solar cells utilizing versatile chemically functionalized ZnO@ graphene quantum dot monolayer," *Nano Energy*, vol. 20, pp. 221-232, **2016**.
- [9] M. Lenes, S. W. Shelton, A. B. Sieval, D. F. Kronholm, J. C. Hummelen, and P. W. Blom, "Electron trapping in higher adduct fullerene-based solar cells," *Advanced Functional Materials*, vol. 19, no. 18, pp. 3002-3007, **2009**.

- [10] R. B. Ross *et al.*, "Endohedral fullerenes for organic photovoltaic devices," *Nature materials*, vol. 8, no. 3, pp. 208-212, **2009**.
- [11] Y. He and Y. Li, "Fullerene derivative acceptors for high performance polymer solar cells," *Physical chemistry chemical physics*, vol. 13, no. 6, pp. 1970-1983, **2011**.
- [12] G. Zhao, Y. He, and Y. Li, "6.5% efficiency of polymer solar cells based on poly (3-hexylthiophene) and indene-C60 bisadduct by device optimization," *Advanced Materials*, vol. 22, no. 39, pp. 4355-4358, **2010**.
- [13] Y. He, G. Zhao, B. Peng, and Y. Li, "High-yield synthesis and electrochemical and photovoltaic properties of indene-C70 bisadduct," *Advanced Functional Materials*, vol. 20, no. 19, pp. 3383-3389, **2010**.
- [14] Y. He, B. Peng, G. Zhao, Y. Zou, and Y. Li, "Indene addition of [6, 6]-phenyl-C61-butyric acid methyl ester for high-performance acceptor in polymer solar cells," *The Journal of Physical Chemistry C*, vol. 115, no. 10, pp. 4340-4344, **2011**.
- [15] Y. He, H.-Y. Chen, J. Hou, and Y. Li, "Indene– C60 bisadduct: a new acceptor for high-performance polymer solar cells," *Journal of the American Chemical Society*, vol. 132, no. 4, pp. 1377-1382, **2010**.
- [16] A. Guerrero *et al.*, "How the charge-neutrality level of interface states controls energy level alignment in cathode contacts of organic bulk-heterojunction solar cells," *ACS nano*, vol. 6, no. 4, pp. 3453-3460, **2012**.
- [17] F.-C. Chen, C.-W. Chu, J. He, Y. Yang, and J.-L. Lin, "Organic thin-film transistors with nanocomposite dielectric gate insulator," *Applied physics letters*, vol. 85, no. 15, pp. 3295-3297, **2004**.
- [18] D. Khodagholy *et al.*, "In vivo recordings of brain activity using organic transistors," *Nature communications*, vol. 4, no. 1, pp. 1-7, **2013**.
- [19] J. N. Haddock, X. Zhang, B. Domercq, and B. Kippelen, "Fullerene based n-type organic thin-film transistors," *Organic Electronics*, vol. 6, no. 4, pp. 182-187, **2005**.
- [20] I. Cruz-Cruz, A. C. Tavares, M. Reyes-Reyes, R. López-Sandoval, and I. A. Hümmelgen, "Interfacial insertion of a poly (3, 4-ethylenedioxythiophene): poly (styrenesulfonate) layer between the poly (3-hexyl thiophene) semiconductor and cross-linked poly (vinyl alcohol) insulator layer in organic field-effect transistors," *Journal of Physics D: Applied Physics*, vol. 47, no. 7, p. 075102, **2014**.

- [21] Z. Su, L. Wang, Y. Li, H. Zhao, B. Chu, and W. Li, "Ultraviolet-ozone-treated PEDOT: PSS as anode buffer layer for organic solar cells," *Nanoscale research letters*, vol. 7, no. 1, p. 465, **2012**.
- [22] Y.-K. Han *et al.*, "Improved performance of polymer solar cells featuring one-dimensional PEDOT nanorods in a modified buffer layer," *Journal of The Electrochemical Society*, vol. 158, no. 3, p. K88, **2011**.
- [23] A. Bello, M. Giannetto, G. Mori, R. Seeber, F. Terzi, and C. Zanardi, "Optimization of the DPV potential waveform for determination of ascorbic acid on PEDOT-modified electrodes," *Sensors and Actuators B: Chemical*, vol. 121, no. 2, pp. 430-435, **2007**.
- [24] P. Wang, S. M. Zakeeruddin, J.-E. Moser, and M. Grätzel, "A new ionic liquid electrolyte enhances the conversion efficiency of dye-sensitized solar cells," *The Journal of Physical Chemistry B*, vol. 107, no. 48, pp. 13280-13285, **2003**.
- [25] J. Maçaira, L. Andrade, and A. Mendes, "Review on nanostructured photoelectrodes for next generation dye-sensitized solar cells," *Renewable and Sustainable Energy Reviews*, vol. 27, pp. 334-349, **2013**.
- [26] Y. M. Kim, Y. W. Park, J. H. Choi, J. K. Kim, and B. K. Ju, "Efficient organic light-emitting diodes by insertion a thin lithium fluoride layer with conventional structure," *Journal of Information Display*, vol. 7, no. 2, pp. 26-30, **2006**.
- [27] M.-S. Kim, "Understanding Organic Photovoltaic Cells: Electrode, Nanostructure, Reliability, and Performance," **2009**.
- [28] E. Singh and H. S. Nalwa, "Stability of graphene-based heterojunction solar cells," *Rsc Advances*, vol. 5, no. 90, pp. 73575-73600, **2015**.
- [29] J. Bullock *et al.*, "Lithium fluoride based electron contacts for high efficiency n-type crystalline silicon solar cells," *Advanced Energy Materials*, vol. 6, no. 14, p. 1600241, **2016**.
- [30] F. Mohd Zain, "Limitation of lithium fluoride (LiF) properties for passivation layer in organic solar cells application," Universiti Tun Hussein Onn Malaysia, **2014**.
- [31] M. Q. Khokhar *et al.*, "Simulation of Silicon Heterojunction Solar Cells for High Efficiency with Lithium Fluoride Electron Carrier Selective Layer," *Energies*, vol. 13, no. 7, p. 1635, **2020**.

- [32] A. K. Geim and K. S. Novoselov, "The rise of graphene," in *Nanoscience and technology: a collection of reviews from nature journals*: World Scientific, **2010**, pp. 11-19.
- [33] A. K. Geim, "Graphene: status and prospects," *science*, vol. 324, no. 5934, pp. 1530-1534, **2009**.
- [34] J. K. Wassei and R. B. Kaner, "Graphene, a promising transparent conductor," *Materials today*, vol. 13, no. 3, pp. 52-59, **2010**.
- [35] K. S. Novoselov *et al.*, "Electric field effect in atomically thin carbon films. science 306," **2004**.

Chapter 4

Optimisation of P3HT:IC70BA-based Organic Solar Cells

4.1 Introduction

In organic solar cells world, heterojunction cells can be fabricated in two different structures: bilayer heterojunction and bulk- heterojunction structure. The main issues considered in the later approach is the blend morphology and structures which affect the performance of the organic solar cells (OSCs). These properties can be significantly influenced by the used solvents [1,2]. Organic bulk-heterojunction solar cell (OBHJ), particularly solution-processed solar cells, received more attention in the last few decades due to their advantages of low-cost fabrication process, flexibility, lightweight and possibility of application in a large area [3]. The active layer of OBHJ commonly contain mixed of soluble acceptor and donor polymers to gain a large interface area between donor and acceptor for effective charge separation. However, the nanometre-scale network structure of OBHJ is the key for high efficiency solar cells where the dissociation of charge carriers can occur anywhere in the bulk and transfer to appropriate electrodes [4].

In this chapter, the fabrication and characterisation of organic bulk heterojunction solar cells based on indene-C70 bisadduct (IC₇₀BA) as the acceptor material and Poly(3-hexylthiophene-2,5-diyl) (P3HT) as the donor material are investigated. The first part of this research was based on employing different solvents and their cosolvent to prepare the P3HT: IC₇₀BA blends as the active layers of the studied OSCs. The used solvents are chlorobenzene (CB), dichlorobenzene (DCB) and their co-solvent Mix (DCB:CB) to control the morphology of P3HT:IC₇₀BA by controlling the film formation process [5]. Moreover, the best solvent processed device was used as a reference device to prepare different concentrations of P3HT:IC₇₀BA to study the effect of material concentration on the electrical and optical properties of the OSCs. Post-deposition annealing has been carried out at different temperatures 150 °C, 175 °C and 200 °C for 10 minutes following the deposition of the active layer to study the effect of post-deposition annealing on the device's performance. Furthermore, annealing duration have been investigated for five different times (10, 20, 30, 40 and 50 minutes) to study annealing time influence on the electrical and optical properties parameters of the devices. Additionally, a thin film of lithium fluoride (LiF) has been used as the

electron transport layer (ETL). A thin film of LiF layer of about 7.5 nm thickness was deposited between the active layer and the top electrode (Al) by thermal evaporation. Further to the initial heat treatment, all the prepared devices have been subjected to another annealing treatment inside the nitrogen glove box at 150 °C for 10 minutes after the deposition of the top contact (Al) and left to cool down for 15 minutes. The electrical properties of all devices were investigated in the dark and under illumination with a halogen lamp. The experimental details, surface morphology and optical characteristics of each of these seven devices are also presented and discussed in this chapter.

4.2 P3HT:IC₇₀BA based OHJ solar cells with different solvents conditions

4.2.1 Fabrication process

Pre-patterned ITO coated glass substrates were washed in acetone, 2-isopropanol and deionised (DI) water for 10 minutes each in an ultrasonic bath, respectively, and then dried with nitrogen gas after each step and kept under vacuum in a vacuum desiccator. All cleaned substrates were treated with O₂ plasma treatment for 20 minutes. Poly(3,4-ethylenedioxythiophene) poly(styrenesulfonate) (PEDOT:PSS) layer was spin-coated on the ITO coated glass substrates at 4000 rpm spin speed for 40 seconds to produce thin film with almost 40 nm thickness, followed by annealing on a hot plate at 150 °C in ambient air for 30 minutes. Thin-film of P3HT:IC₇₀BA active layer in the weight ratios of 1:1 and a concentration of 20 mg/ml have been dissolved in different organic solvents. The solvents used are CB, DCB and their co-solvent DCB:CB. The solutions were stirred for 16 hours at 45°C followed by filtering the P3HT:IC₇₀BA solution through a PTFE filter with a pore size of 0.45 µm. All the P3HT:IC₇₀BA active layers have been spin-coated inside a nitrogen-filled glove box with fixed spin speeds of 600 rpm for 60 seconds to produce similar active layer thickness ~ 100 nm and annealed inside the nitrogen-filled glove box at 150 °C for 20 minutes. All layers thickness was measured by a profilometer to ensure same thickness for all devices. To end the device fabrication, a top contact of aluminium (Al) was then thermally evaporated with a thickness of 100 nm through a shadow mask with an active area of 0.125 cm². This process was carried out under a vacuum of about 10⁻⁶ mbar (~10⁻⁴ Pa), at a deposition rate of 1 nm/sec. Both film thickness and deposition rate were monitored using a quartz crystal thickness

monitor. Figure 4.1 shows the schematic diagram of P3HT:IC₇₀BA-based OBHJ with all the layers used in this chapter.

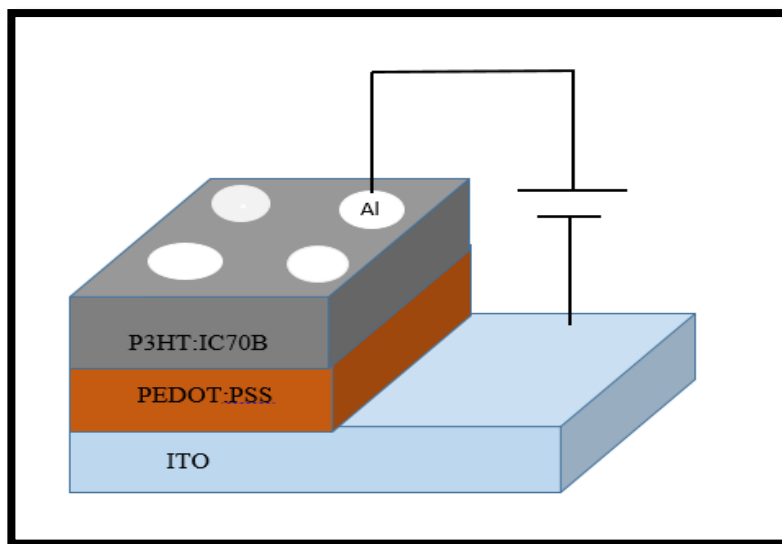


Figure 4.1: Schematic diagram of P3HT:IC₇₀BA devices.

4.2.2 Morphological analysis using AFM

It is important to study the surface morphology of the active layer in OBHJ solar cell to understand the effect of the microstructure of the active layer on the photovoltaic properties. It was reported that surface morphology plays a crucial role in the percolation pathways for transport of both charges and photogenerated excitons. Atomic force microscopy (AFM) is used to study donor: acceptor surface structure and how electrical performance characteristics affected by the morphology of the devices [5-7]. Optical images were taken to the fluorescent P3HT and IC₇₀BA active layer blend on top of ITO/PEDOT:PSS substrate to examine the coating uniformity and quality of the active layer blend. Figure 4.2 shows the variation in the surface morphology of P3HT: IC₇₀BA BHJ films prepared using different chlorinated solvents. As shown from the AFM optical images in Fig. 4.2, the P3HT and IC₇₀BA blends spread smoothly without any substrate-solution incompatibility problems such as separated islands in the film. Therefore, Figure 4.2 shows that the ITO/PEDOT:PSS substrate is a suitable substrate that active blend can be spin-coated smoothly.

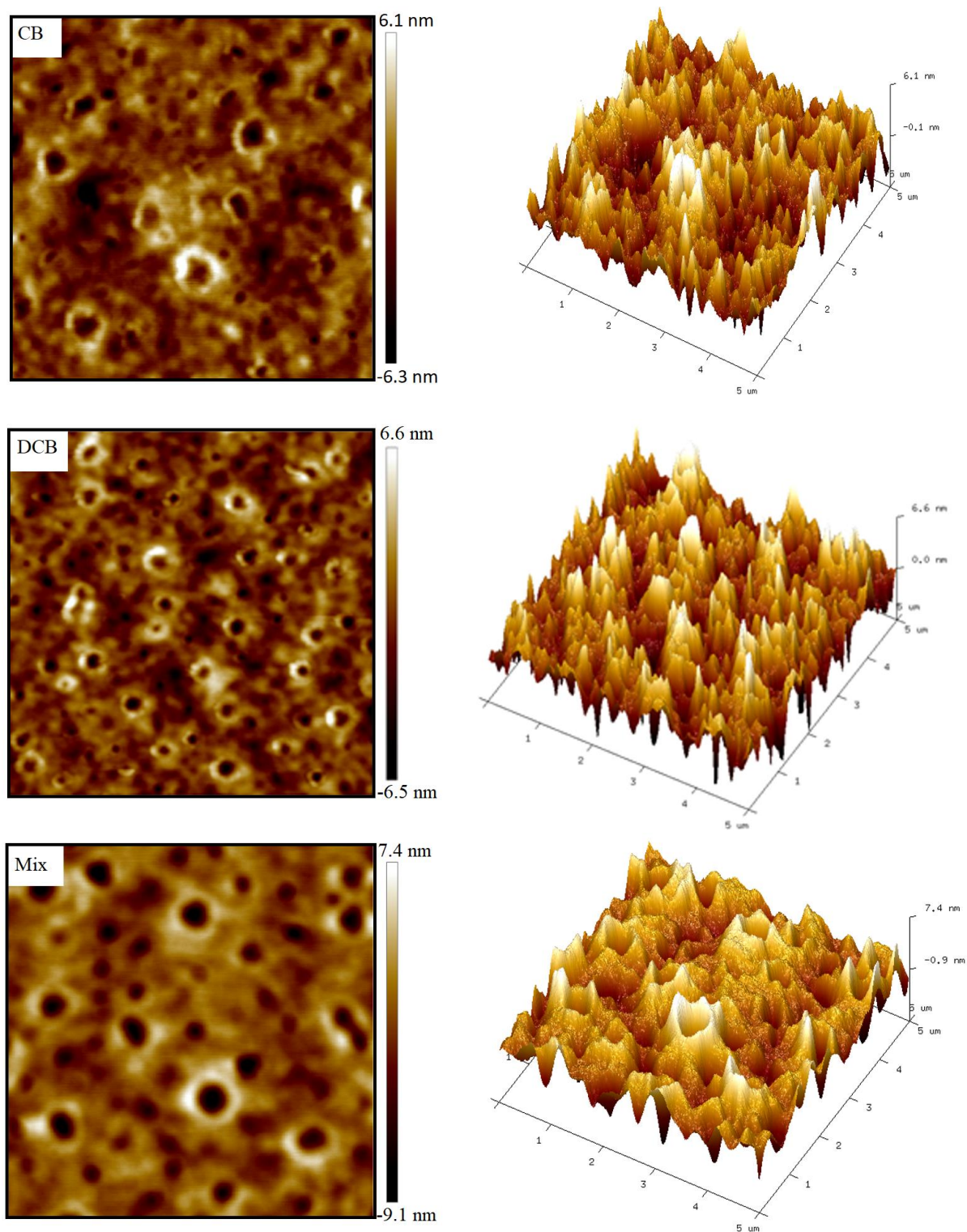


Figure 4.2: 2D and 3D (5 $\mu\text{m} \times 5 \mu\text{m}$) AFM images and phase analysis of the *P3HT:IC₇₀BA* blends prepared by different solvents.

The DCB-based film has revealed a smooth surface with rms roughness of 1.23 nm correlating with noticeable pinholes. On the other hand, CB and Mix(CB:DCB) based films have demonstrated higher surface roughness with rms values of 1.75 nm and 2.15 nm, respectively as shown in Table 4.1. The brighter regions are associated with the IC₇₀BA domains while the darker regions are related to the P3HT domains [8]. The surface morphology provides different interface properties between the P3HT:IC₇₀BA and the Al contact such as the variation in the metal/organic interface due to the surface morphology variation with different energy level alignments for both P3HT and IC₇₀BA concerning Al contact.

Solvent	Roughness (nm)
CB	1.75
DCB	1.23
Mix (CB: DCB)	2.15

Table 4.1: *Roughness for P3HT:IC₇₀BA based OPVs according different solvents.*

The improvement in the interpenetrating network could facilitate charge carrier transport and hence improved solar cell performance. The phase analysis has revealed a better phase separation between P3HT and IC₇₀BA within the P3HT: IC₇₀BA blends in the co-solvents-based films compared to the mono-solvents based films. The darker region is higher in the case of co-solvents based films, which suggests that the phase separation has become less, resulting in improved dissociation rate of the photo-generated excitons [9]. An illustration of the different distributions of IC₇₀BA within P3HT main matrix has been demonstrated in Figure 4.3, which leads to three different domain sizes within the final blend. In the case of small domain size (Figure 4.3(a)) where the IC₇₀BA domains are not linked with each other, higher charge carriers recombination is thought to occur. In large domain size as shown in Figure 4.3(b), there is a scarcity of interface areas within the BHJ, which results in low excitons separation. A critical balance between the two domains is necessary to have moderate domain size as shown in Figure 4.3(c). This is advantageous for higher

charge dissociation and improved network for charge transport [10]. Therefore, it is worthwhile mentioning that: (a) Small domains with many interfaces: Large charge generation yield (high short circuit current (J_{sc})) but non-efficient charge transport (low Fill factor (FF)) due to high recombination rate, (b) Excessively large domains with a lower interface area between the donor and acceptor: low charge generation yield (low J_{sc}) but good charge transport (high FF), and (c) Intermediate domain size with an optimised interface area: large charge generation yield (high J_{sc}) and good charge transport (high FF). In the current study, it has been shown that the DCB solvent-based films have exhibited the best morphology as compared to the CB and Mix solvents.

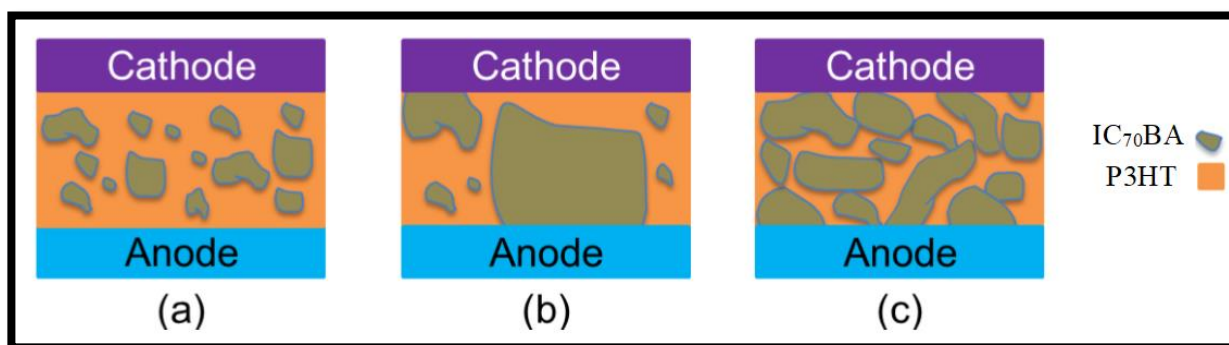


Figure 4.3: *Different domain size for P3HT: IC₇₀BA blends; (a) small, (b) large and (c) intermediate domain size [11].*

4.2.3 Optical Absorption measurements

The optical bandgap E_g in organic materials is defined as the difference between the lowest unoccupied molecular orbital (LUMO) and the highest occupied molecular orbital (HOMO) of the absorber material [12-14]. The bandgap measurement is very important in semiconductor materials as it determines the portion of the spectrum the PV cell absorbs. 4 eV bandgap value determines whether the material is a semiconductor (less than 4 eV) or an insulator (more than 4 eV) [15,16]. The majority of solar radiation reaches the earth with combination wavelengths with energy greater than the bandgap of silicon. Solar cells will absorb this energy, but the difference in energy is converted into heat rather than electrical energy [17]. There is an inverse relationship between the energy E of the photon and the wavelength of light λ as follow:

$$E = \frac{hc}{\lambda} \quad (4.1)$$

where h is Planck's constant ($h = 6.626 \times 10^{-34} \text{ J}\cdot\text{s}$) and c is the speed of light ($c = 2.998 \times 10^8 \text{ m}\cdot\text{s}^{-1}$). In terms of wavelength, in nanometres (nm), and energy (E) in electron volts (eV), can be expressed for light by the following equation:

$$E = \frac{1240}{\lambda (\text{nm})} \quad (4.2)$$

The energy bandgap can be calculated from Figure 4.4, where the intercept of the linear part with x-axis gives the optical bandgap. Accordingly, the optical energy band gap values were obtained by extrapolating the linear part of the curves in Figure 4.4 and tabulated in Table 4.2. In the visible light spectrum (400 nm to 800 nm), the energy of photons areas from nearly 1.55 eV to 3.1 eV, the corresponding wavelengths of these energies are 750 nm and 400 nm, respectively. These wavelengths match the red and violet ends of the spectrum of visible light. Therefore, the absorption property, particularly the absorption in the visible region, is very important for the photovoltaic (PV) materials [18-19]. Low bandgap materials ($E_g < 2 \text{ eV}$) are interesting materials in the application of solar cells as their absorption spectra cover from the visible to the near-infrared region. For that reason, semiconductors with bandgap $< 2 \text{ eV}$ have great chance to form an efficient solar cell [20]. Figure 4.4 shows the effect of different solvents on the UV-Vis absorption spectra for the thin films of P3HT:IC₇₀BA. For CB, the absorption edge at 738 nm where the bandgap at this point is about 1.68 eV, with peak absorption at 496 nm (2.50 eV). However, DCB absorption edge at 713 nm where the bandgap at this point 1.74 eV, with peak absorption at 485 nm (2.55 eV). The DCB:CB demonstrated the UV-V spectrum with an absorption edge at 681 nm where the bandgap at this point is about 1.8 eV and peak absorption at 506 nm (2.45 eV). The amount of generated charge in an organic solar cell is proportional to the absorption of light, and therefore the absorption properties affect the improvement the power conversion efficiency (PCE).

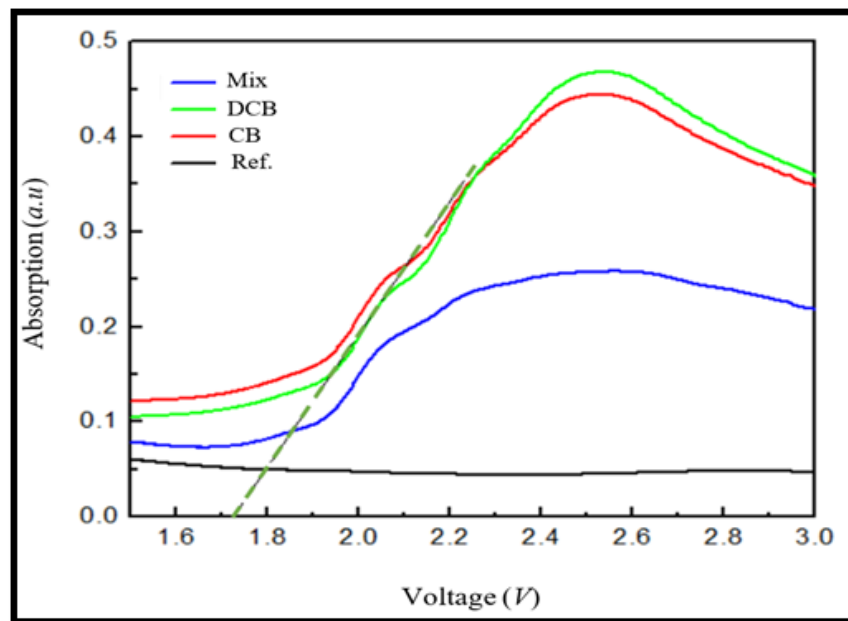


Figure 4.4: *The optical absorption of the P3HT:IC₇₀BA based OBHJ solar cells under different solvents conditions.*

As Figure 4.4 shows, absorption intensity above 490 nm associated with the use of DCB is stronger than that of CB and DCB:CB, in which this result would lead to the improvement of the short circuit current (J_{sc}). Absorption spectra for the P3HT:IC₇₀BA blend from DCB led to increased ordering and crystallinity than CD and DCB:CB based films. Table 4.2 represents the values of bandgaps for three different devices.

Solvent	Bandgap (eV)
CB	1.68
DCB	1.74
Mix (CB: DCB)	1.80

Table 4.2: *The variation of P3HT:IC₇₀BA blend optical bandgaps with different solvents.*

4.2.4 Electrical measurements

4.2.4.1 Diode measurements

The electrical characteristics of the studied devices were measured under illumination and dark conditions using current density–voltage (J - V) measurements. The latter can provide useful information about the diode parameters.

The series (R_s) and shunt (R_{sh}) resistances of the diodes fabricated using different solvents have been estimated using the dark J - V characteristics as was described in chapter 2. The series resistance can be obtained by calculating the inverse of the slope of the J - V curve at the open-circuit voltage and the shunt resistance could be determined from the inverse of the slope of the J - V curve at the short circuit condition $V = 0$. The DCB-based device has exhibited low R_s (7.6 Ω) compared to co-solvents-based device DCB:CB and CB-based device (8.8 Ω) and (10.7 Ω), respectively, as shown in Table 4.3. The main reason for this high series resistance is attributed to the clear presence of pinholes. However, improved contact properties between the active layer and the back (Al) electrode will result in lower series resistance due to the stronger interfacial adhesion [21]. Under dark condition, the devices displayed good rectifying characteristics as current stayed at almost 0 A from -1V and turned on at 0.4 V for the mix and CB-based devices; and 0.6 V for DCB-based device as shown in Figure 4.5. This non-linear behaviour indicates that the very low current from -1 V up to 0.4 V reflects the lack of carriers in the structure and thus a non-conducting behaviour.

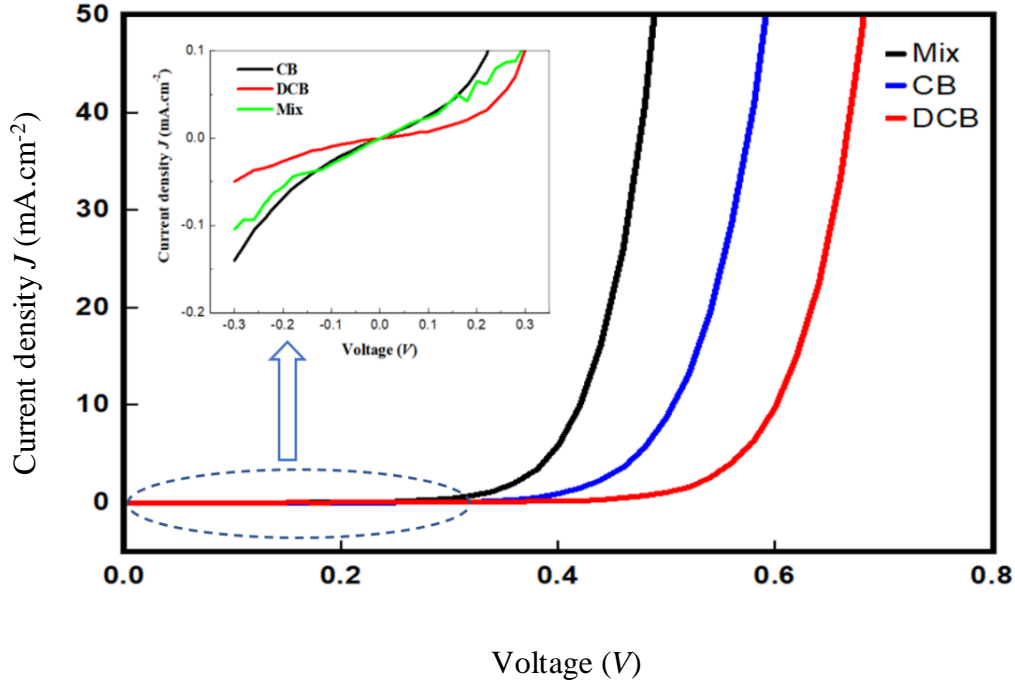


Figure 4.5: Dark J - V characteristics of devices fabricated using different solvents. The inset figure shows the leakage current.

For shunt resistances, from Figure 4.5, it is clear that CB-based device has the highest leakage current as shown in inset figure in Figure 4.5, with the lowest value of R_{sh} (3.878 k Ω) followed by Mix (DCB:CB)-based device with (12.6 k Ω) and the DCB-based device with (30 k Ω), respectively. This is also reflected in the R_s values, where DCB-based device has the lowest R_s value. Such a large variation in the leakage current of organic solar cells is not uncommon and is known to be affected by substrate cleaning procedures, film thickness, electrode interlayers, and film deposition techniques [22-23]. Shunt resistance is also shown to be reduced by the aid of using high boiling point solvents to process the active layer [23].

Parasitic Resistances		
Solvent	Shunt resistance (kΩ)	Series resistance (Ω)
CB	3.878	10.7
DCB	30	7.6
Mix (DCB:CB)	12.6	8.8

Table 4.3: *Diodes parasitic resistances for different solvents.*

The ideality factor is an indicator that help to describe the difference between the practical and ideal devices, contains critical data on the recombination and transport processes in organic solar cells. It can be independently obtained from the slope of the exponential regime of dark J – V characteristics on a semi-logarithmic plot as in Figure 4.6. In general, the ideality factor n can be estimated from:

$$n = \frac{q}{K_B T} \left[\frac{dV}{d \ln(J_D)} \right] \quad (4.3)$$

where J_D is the (current density) in the dark, V the applied voltage, q the elementary charge, K_B Boltzmann's constant, T temperature, and n is the ideality factor.

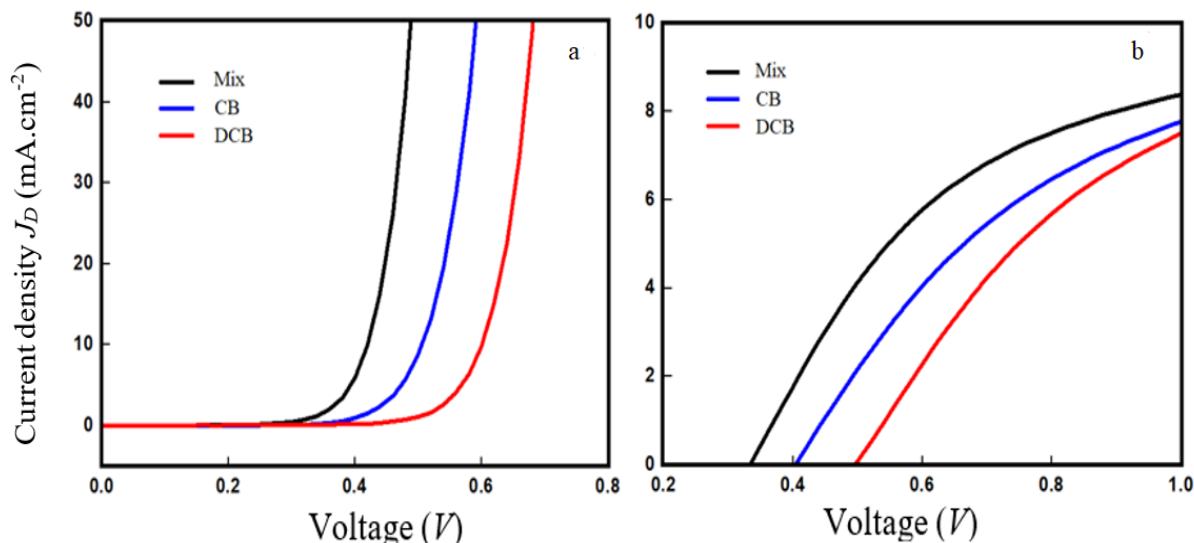


Figure 4.6: (a) J - V characteristics of the OBHJ solar cells under the dark. (b) Variation of $\ln(J_D)$ versus the bias voltage with different solvents films for P3HT:IC₇₀BA OSC devices.

The ideality factors for the CB-based device and DCB:CB-based device are found to be 2 and 1.9 respectively, which suggests a high recombination rate in such devices. This high value might be attributed to the morphological disorder of these devices which shows clear pinholes and interrupted networks. Using high boiling point solvents has resulted in a decreased recombination rate as demonstrated by the decreasing ideality factor to reach 1.5 in DCB-based devices. Table 4.4 shows the value of ideality factors of the three devices.

Device	Ideality factor (n)
CB	2
DCB	1.5
Mix (DCB:CB)	1.9

Table 4.4: Ideality factors for diode devices.

This enhancement has been attributed to the improved distribution of IC₇₀BA within P3HT matrix and thus improved film morphology which facilitate the charge carriers transportation by creating percolation pathways for both charges (electrons and holes) and hence a decrease in the recombination rate [10].

4.2.4.2 Photovoltaic performance

To investigate the photovoltaic behaviour of P3HT:IC₇₀BA-based organic solar cells, the electrical properties have been investigated under illumination. Different solvents and their co-solvents were used to control the active layer morphology and structure has resulted in different photovoltaic performances. The $J-V$ characteristics of the fabricated devices were tested under 100 mW.cm⁻². AM 1.5 G illumination for different P3HT-IC₇₀BA solvents as shown in Figure 4.7; with device performance parameters are given in Table 4.5.

The CB-based device has exhibited the poorest performance with $PCE = 1.5\%$, $FF = 45\%$, $J_{sc} = 10.3 \text{ mA.cm}^{-2}$ and $V_{oc} = 0.33\text{V}$ correlating with the high series resistance and the low shunt resistance. The highest performance was observed for OSCs processed using DCB with $PCE = 2.8\%$, $FF = 55\%$, $J_{sc} = 17.04 \text{ mA.cm}^{-2}$ and $V_{oc} = 0.33\text{V}$ associated with the high shunt resistance as well as low series resistance. For the co-solvent (DCB:CB), the photovoltaic characteristics showed a performance of $PCE = 1.86\%$, $FF = 50\%$, $J_{sc} = 11.8 \text{ mA.cm}^{-2}$ and $V_{oc} = 0.31\text{V}$. Table 4.5 summarised the PV parameters for P3HT: IC₇₀BA -based devices prepared using different solvents. The efficiency values were obtained by extrapolating the peaks of the curves in Figure 4.8, representing the output power as a function of applied voltage for the region between 0 V and V_{oc} .

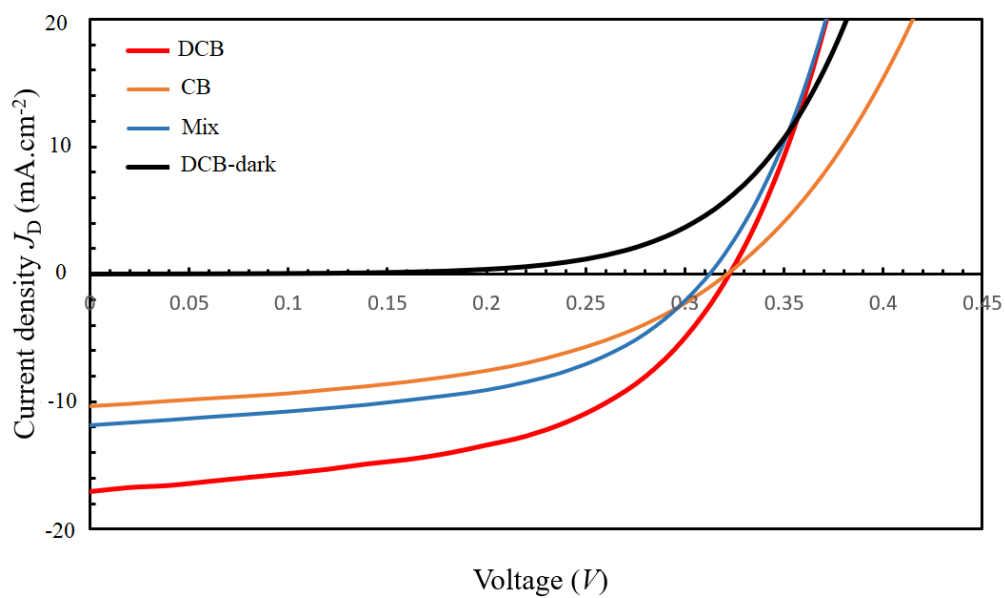


Figure 4.7: *J-V characteristics for P3HT:IC₇₀BA-based devices under AM 1.5 solar simulator source of 100 mW.cm⁻² using different solvents.*

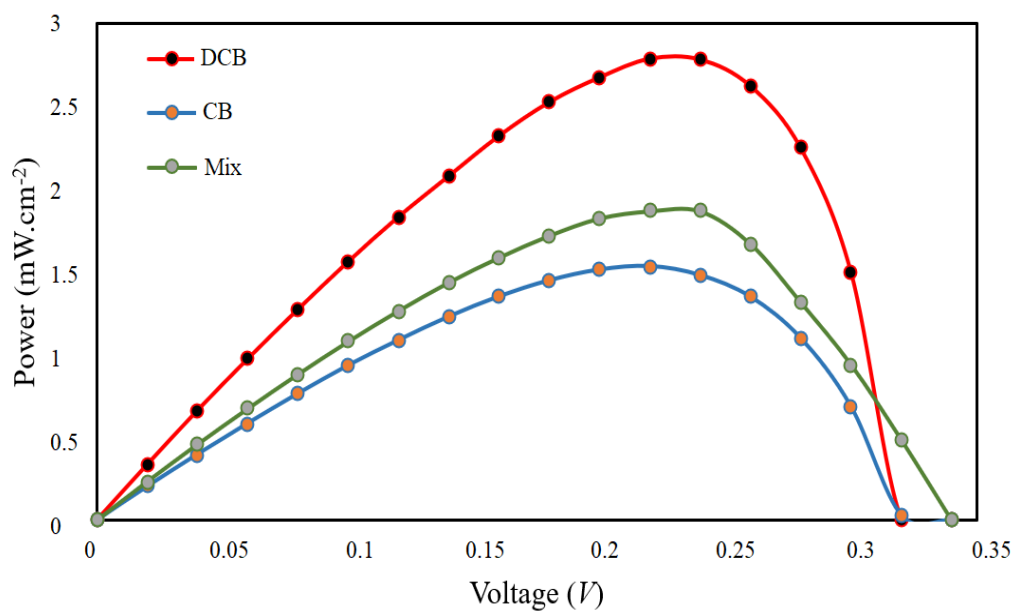


Figure 4.8: *Power curve of IC₇₀BA-based devices at different P3HT:IC₇₀BA solvents.*

Solvents	J_{sc} (mA.cm ⁻²)	V_{oc} (V)	FF (%)	PCE (%)	R_{sh} (Ω)	R_s (Ω)
CB	10.3	0.33	45	1.5	870	8.5
DCB	17.04	0.33	55	2.8	952	7
Mix (DCB:CB)	11.8	0.31	50	1.86	769	8.8

Table 4.5: The J-V characteristics for the P3HT: IC₇₀BA based devices under illumination.

The clear increase in the FF for devices based on DCB is attributed to the enhancement of the device resistance, both series and shunt resistances (7 Ω and 952 Ω) respectively. The increase in J_{sc} could be related to the higher charge carrier mobility as well as the lower recombination rate leading to high FF . The creation of a shunt path has enhanced the shunt resistance and decreased device leakage current [8]. The enhancement in the DCB-based morphology and the reduced recombination rate compared to CB-based and co-solvent DCB:CB devices can also be attributed to the reduction in pinholes in the active layer service resulting in a higher value of FF . The use of DCB solvent to process the OSCs has also increased the measured current of these devices; the increase in J_{sc} has been ascribed to the increase in the charge carriers mobility and the electrical conductivity due to the improved layer structure and the good interpenetrating network. V_{oc} , on the other hand, has almost unchanged for the fabricated devices; V_{oc} is mainly determined by the difference between the HOMO of the donor and the LUMO of the acceptor [8]. The obvious increase in J_{sc} in DCB-based devices has resulted in improved PCE by almost double from devices produced using CB.

Improved OSC performance could only take place once the photo-generated carriers are extracted with lower recombination loss; hence the fill factor of the solar cell is limited by the carriers diffusion length (L_d) according to the following relation [24]:

$$L_d = \mu\tau E \quad (4.4)$$

where τ is the carrier recombination lifetime and E is the electrical field. Therefore, to prevent charge recombination L_d must be higher than the active layer thickness; higher mobility or thinner

active layer is very important for charge carrier extraction. PCE and other performance parameters were found to increase with decreasing the active layer thickness until reaching an optimum thickness of almost 100 nm (all devices were measured through profilometer with thickness in the range of 100 nm). Devices with active layer thickness larger than 100 nm have demonstrated a deteriorated performance compared to those with the optimum film thickness. In general, PCE of organic solar cells is limited by two factors: low carrier mobility and short exciton diffusion lengths [25]. The current density was found to decrease when the photoactive layer thickness increased. The increase in the series resistance could be the main reason for the decreased FF in thicker films-based devices as well as the devices with the active layer thickness below 95 nm [26].

In summary, it is clear from the optical, electrical and surface morphology results indicate that the device performance depends strongly on the solvent used for the active layer. By comparing the efficiencies of the devices, it can be seen that the optimum solvent to enhance the performance of OBHJ solar cells based on P3HT:IC₇₀BA is DCB due to the high ordered molecules in the active layer. The device with DCB solvent resulted in lower energy band gap, high FF and high-efficiency PCE which provides a favourable pathway for exciton separation and charge-carrier transport.

4.3 IC₇₀BA-based devices under different concentration conditions

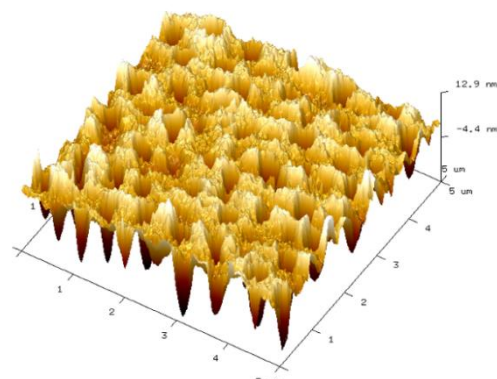
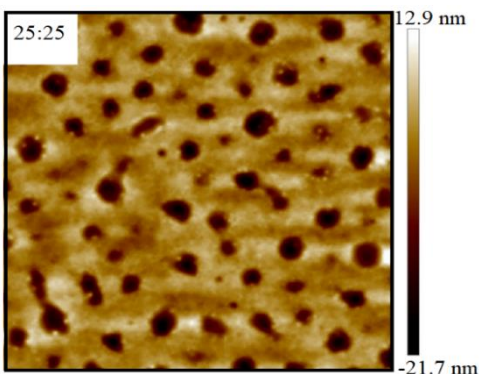
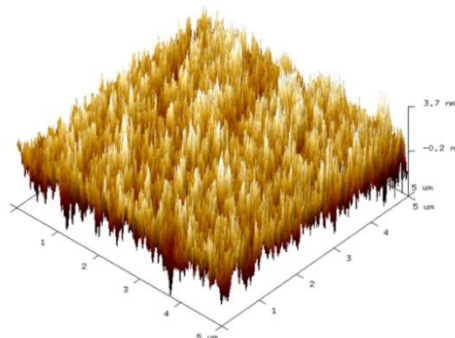
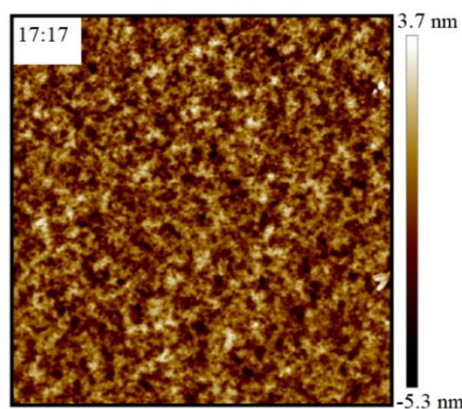
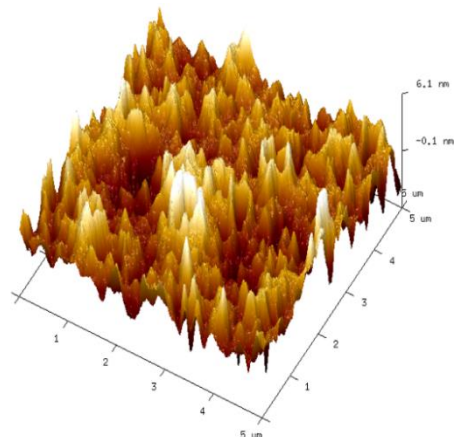
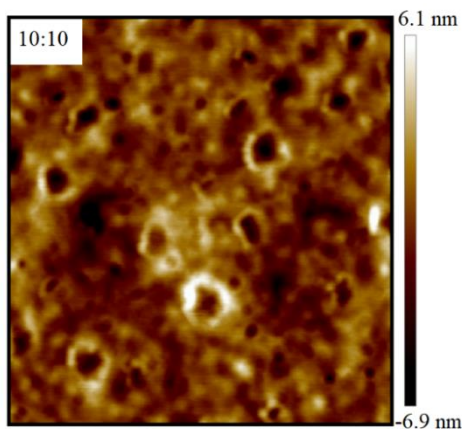
4.3.1 Fabrication process

The device structure in this section is similar to the structure in Figure 4.1 with the fabrication procedure explained in the previous section (different solvents effect). To investigate the effect of the weight ratio of the active layer on the photovoltaic properties, the active layer P3HT:IC₇₀BA was fabricated with different weight ratios of 10:10, 17:17, 25:25, 15:20 and 20:15 (mg/mL) in DCB as the solvent. These ratios have been chosen based on the latest studies as discussed in the Literature Review.

4.3.2 Morphological analysis using AFM

The variation in the surface morphology of P3HT:IC₇₀BA films as a function of different concentrations has been carried out using AFM technique. AFM images in the Figure 4.9 shows

the active layer at different concentrations. The images show that the roughness gradually increased as concentration of P3HT:IC₇₀BA increased. Roughness were 1.23 nm, 1.24 nm, 3.41 nm, 1.50 nm, and 1.55 nm for devices with ratios of 10:10, 17:17, 25:25, 15:20 and 20:15 (mg/mL), respectively as listed in Table 4.6. In the previously reported studies regarding surface morphology [27], the rough surface was mentioned as the self-organization signature of the polymer. As can be noticed, the smoothest specimens were in devices with concentrations of (10:10) and (17:17).



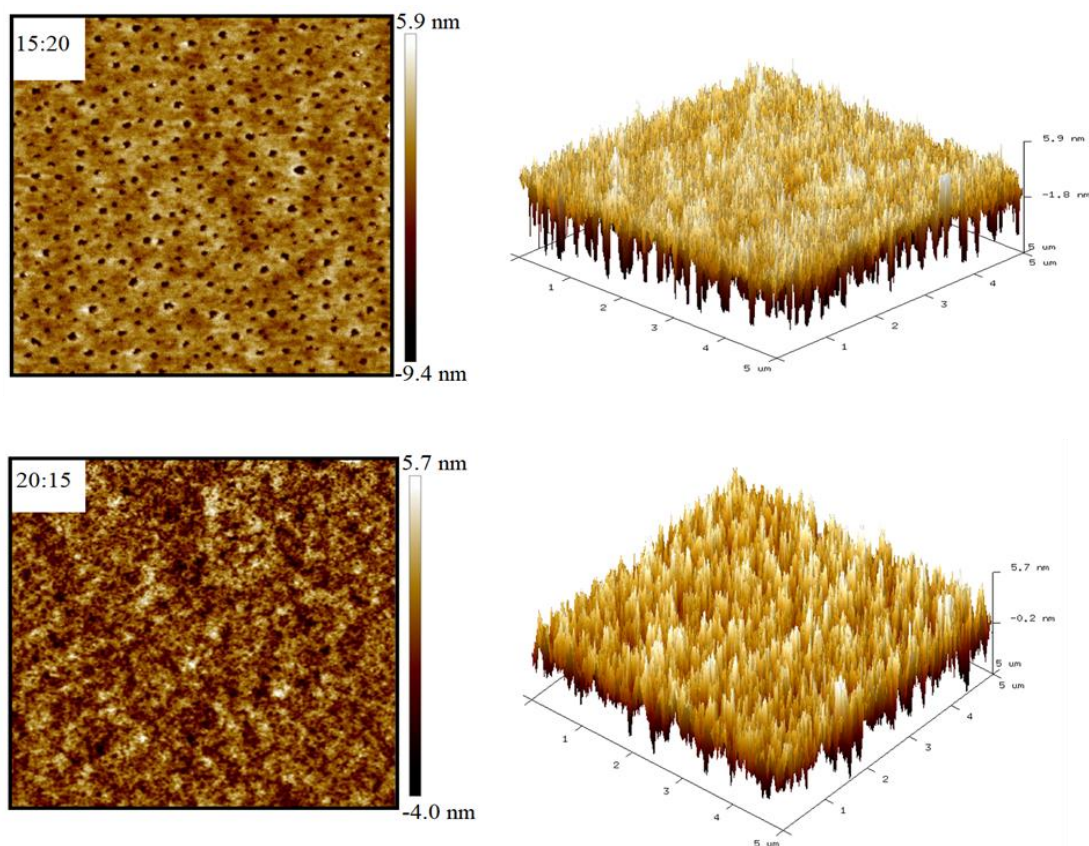


Figure 4.9: 2D and 3D ($5\mu\text{m}\times 5\mu\text{m}$) AFM images and phase analysis of the P3HT:IC₇₀BA blends prepared by different concentrations.

These results imply that the increased smoothness of the surface yields increased (i) interfacial contact between the P3HT:IC₇₀BA layer and Al layer, and (ii) separation of photo-generated electron and hole pairs at the P3HT:IC₇₀BA interface. However, the higher surface roughness may indicate non-uniform coverage, which may in turn affect the interface resistance. The improved performance of the device is attributed to the improvement in the morphology of the electron and hole separation in the photoactive layer [28].

The trend of RMS roughness reaches a minimum for all devices except device with concentration of (25:25) composition which exhibited higher roughness than others by more than double. Overall roughness of less than 1.55 nm suggests a fine morphology in all blends. This confirms that a moderate morphological development takes place in annealed vacuum-deposited blends like

polymer-fullerene systems. Table 4.6 has listed values of roughness for devices under different concentrations condition. The domains observed in the phase image of the devices with concentration of (10:10), (25:25) and (15:20) blends range from an average size of ~10-15 nm at low concentration content to larger ~25-30 nm for the highest concentration as shown in Figure 4.9. The optimal reported domain size (10~20 nm) of P3HT for the improved exciton dissociation [29]. Generally, the smaller domain size is critical for efficient exciton diffusion in BHJ OSCs. However, efficient charge transport requires a high conductivity of the donor material. Therefore, for crystalline donor polymers such as P3HT, high crystallinity and aggregation are desired.

Concentration (mg/mL)	Roughness (nm)
10:10	1.23
17:17	1.24
25:25	3.41
15:20	1.50
20:15	1.55

Table 4.6: *Roughness for P3HT:IC₇₀BA based OPVs according different concentrations.*

4.3.3 Optical Absorption measurements

UV-Vis spectra of devices made with different concentrations (10:10, 17:17, 25:25, 15:20 and 20:15 mg/mL) are shown in Figure 4.10. The lowest concentration absorption edge at 713 nm where the bandgap at this point 1.74 eV, with peak absorption at 485 nm (2.55 eV). However, the highest concentration absorption edge at 652 nm where the bandgap at this point was estimated to be 1.9 eV, with peak absorption at 460 nm (2.7 eV). The other three devices with concentrations (17:17, 15:20 and 20:15) demonstrated the same UV-Vis spectrum with almost same peak absorption at 500 nm (2.50 eV) where the bandgaps are 1.8 eV, 1.8 eV and 1.84 eV, respectively.

No significant change in the peak position has been observed for all the P3HT:IC₇₀BA active layers. Moreover, using different concentrations blend has resulted in different absorption peak position.

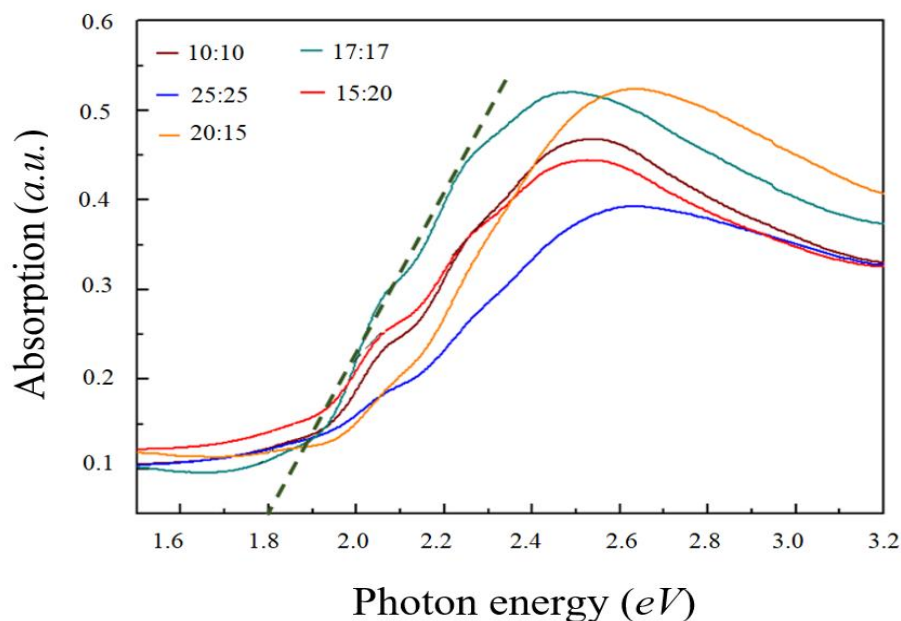


Figure 4.10: *The optical absorption of the P3HT:IC₇₀BA based OBHJ solar cells under different solvents concentrations.*

Table 4.7 shows bandgaps for P3HT:IC₇₀BA with respect to different concentrations. Nicolaidis and co-workers have stated that an increase of about 13% in generated photocurrent could be attributed to light absorption by the fullerene molecules within the P3HT:IC₇₀BA blends [30]. As concentration increased, the molarity of solution increased which effect negatively the conduction of electrons, which results in reducing electron transfer between P3HT and IC₇₀BA. However, at low concentration, this means that the photogenerated current due to light absorption by the fullerene component needs to be taken into account in the performance of OSCs systems [31].

Concentration (mg/mL)	Bandgap (eV)
10:10	1.74
17:17	1.80
25:25	1.90
15:20	1.84
20:15	1.80

Table 4.7: Bandgaps for P3HT:IC₇₀BA based OPVs according to different concentrations.

4.3.4 Electrical measurements

4.3.4.1 Diode measurements

The dark J - V measurements were carried out to determine the various electronic parameters of the studied OSC devices, including shunt resistance, series resistance and ideality factor. Figure 4. 11 represents the J - V characteristic of the fabricated devices under dark condition. Modifying the active layer concentration has resulted generally in decreasing the series resistance in comparison to the reference device with concentration (10:10) as demonstrated in Table 4.8. As an example, using the device with the concentration of (17:17) has reduced the R_s value significantly by about 50% ($R_s = 4 \Omega$) compare to the reference device which has $R_s = 7.6 \Omega$, whereas the series resistance for the device which has the highest concentration (25:25) has remained almost the same with ($R_s = 8 \Omega$) compare to the reference device. For other two other devices with concentrations of (15:20) and (20:15), R_s has shown improvement for both devices by 21% and 27%, respectively.

Regarding shunt resistances, using the device with a concentration of (17:17) has doubled R_{sh} to reach 60 k Ω compare to the reference device of $R_{sh} = 30$ k Ω , whereas the resistance for the device with concentration of (25:25) has dropped to the lowest value ($R_{sh} = 1.2$ k Ω) compare to the reference. For the other two devices with concentrations of (15:20) and (20:15), R_{sh} has shown a large reduction for both devices by almost 85%.

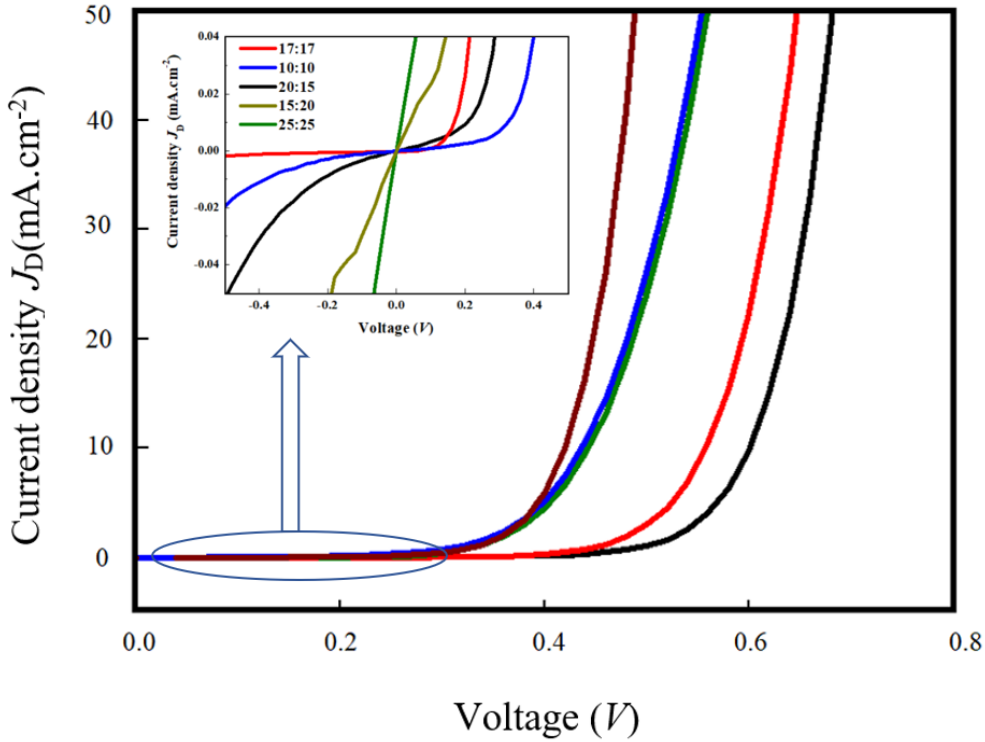


Figure 4.11: Dark J - V behaviours for devices fabricated with different concentrations. The insert figure represents leakage current.

In a practical device, R_s mostly comes from the bulk resistance of the active layer or the contact resistance between the active layer and the top Al electrode. Incompatible band alignment can lead to a large R_s value, causing a dramatic decrease in the values of FF and PCE . In OPV systems, a transparent conducting electrode of ITO is widely chosen as the device electrode. Furthermore, the conductivity of ITO is good enough for laboratory-scale devices, however, it may not be adequate for large scale devices. Therefore, when fabricating large scale OPV devices, the R_s caused by the limited conductivity of ITO must be taken into consideration [32].

In a similar fashion as previous devices, at low positive voltages, the J - V curve performs close to a straight line. It is beneficial to avoid the conditions leading to the decreased in R_{sh} to obtain the high value of FF . In OPVs, due to their distinctive BHJ structure that both donor and acceptor materials have contacts with the same carrier collection electrode, one additional pathway for leakage current comes from the bimolecular recombination near the interface between the active

layer and electrode. This extra pathway for leakage current must be reduced or eliminated [33]. Table 4.8 shows parasitic resistances for devices under different concentrations condition.

Parasitic Resistances		
Concentration	Shunt resistance (k Ω)	Series resistance (Ω)
10:10	30	7.6
17:17	60	4
25:25	1.200	8
15:20	3.700	6
20:15	4	5.5

Table 4.8: *Diodes parasitic resistances for different P3HT:IC₇₀BA concentration.*

To investigate the recombination under dark condition, the diode ideality factor n is extracted from the dark J - V curve in Figure 4.12(b) using equation (4.1). Under high voltage (>0.4 V) for the (25:25), (15:20) and (20:15)-based devices and (>0.5 V) for the (17:17)-based device and (>0.6 V) for (10:10)-based device, most of the current density is influenced by the parasitic effects raised by shunt resistance and series resistance [34-36]. The values of ideality factors are responsible for the reduced slope of dark J - V curves due to the series resistance and shunt resistance. For the (17:17) concentration-based device, the value of the minimum diode ideality factor is found as 1.35, while for the (25:25) concentration-based devices, the value of diode ideality factor is the maximum and be found 1.9. For the (10:10), (15:20) and (20:15)-based devices, the value of diode ideality factors are 1.5, 1.6 and 1.45, respectively as demonstrated in Table 4.9.

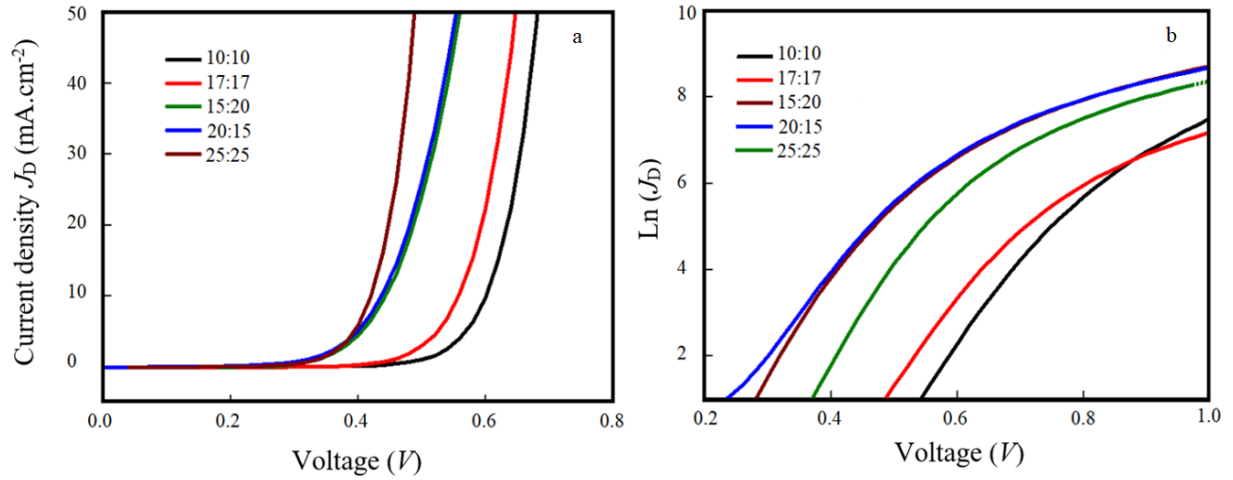


Figure 4.12: (a) J - V characteristics of the OBHJ solar cells under the dark. (b) Variation of $\ln(J_D)$ versus the bias voltage with different concentrations for P3HT:IC₇₀BA OPV devices.

Device concentration	Ideality factor (n)
10:10	1.5
17:17	1.35
25:25	1.9
15:20	1.6
20:15	1.45

Table 4:9: Ideality factors for diode devices.

It is also easy to understand that good ideality factor will prevent the recombination process to occur. When the diode ideality factor equalling to unity ($n = 1$) usually means that there is no trapping of charge carriers, and bimolecular recombination dominates the recombination in a device. With the diode ideality factor increasing, the trap-assisted recombination also grows in the space-charge region of photodevices. For bulk-heterojunction organic solar cells, the typically reported diode ideality factor value is in the range of 1.3–2.0, which is coherent with the results of this study [37-38].

4.3.4.2 Photovoltaic performance

To validate the efficiency of P3HT:IC₇₀BA blend system, current density-voltage (J - V) curves were recorded under AM 1.5 G illumination at $100 \text{ mW}\cdot\text{cm}^{-2}$ and the parameters PCE , J_{sc} , V_{oc} , FF , R_{sh} and R_s of different concentrations are shown in Figure 4.13 and listed in Table 4.10, respectively. The (10:10) device exhibited a $PCE = 2.8\%$, with $V_{oc} = 0.33 \text{ V}$, $J_{sc} = 17.04 \text{ mA}\cdot\text{cm}^{-2}$, $FF = 55\%$, $R_s = 7 \Omega$ and $R_{sh} = 952 \Omega$. By increasing the concentration of P3HT:IC₇₀BA to be 17:17, V_{oc} and PCE were significantly improved by 40% and 25%, respectively. The value of R_s showed a clear improvement as reduced 57%, while R_{sh} increased from 952Ω to be 1200Ω . The FF , however, nearly maintained the same value compared to the (10:10) device. The efficiency values were obtained by extrapolating the peaks of the output power curves in Figure 4.14.

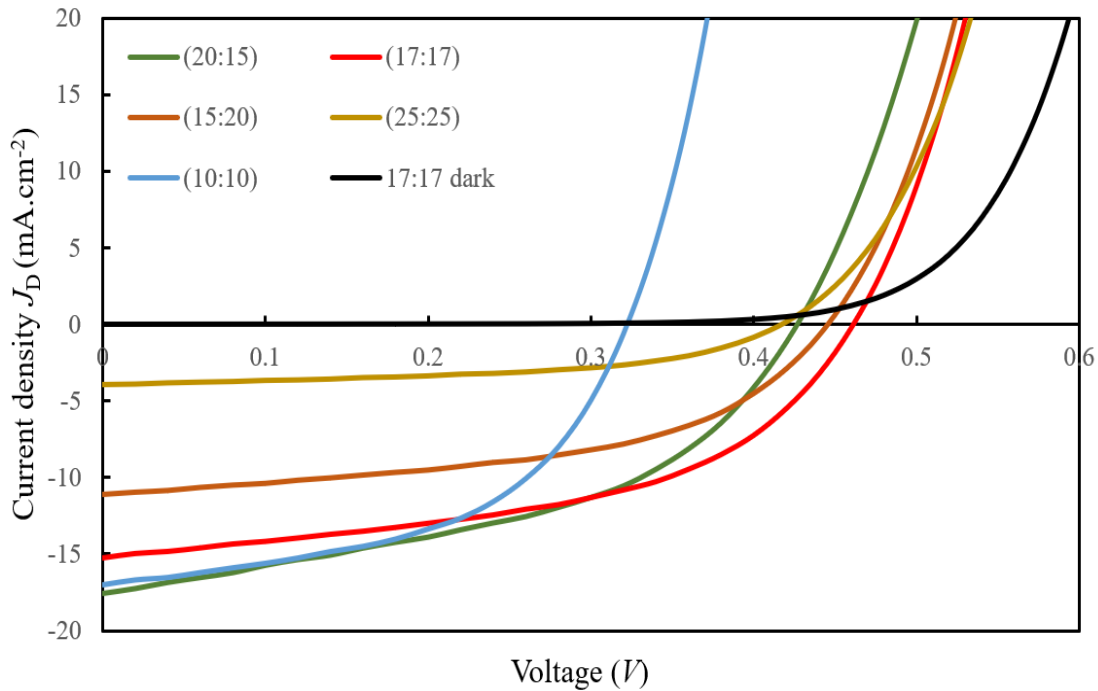


Figure 4.13: J - V characteristics for P3HT:IC₇₀BA-based devices under AM 1.5 solar simulator source of $100 \text{ mW}\cdot\text{cm}^{-2}$ using different concentrations.

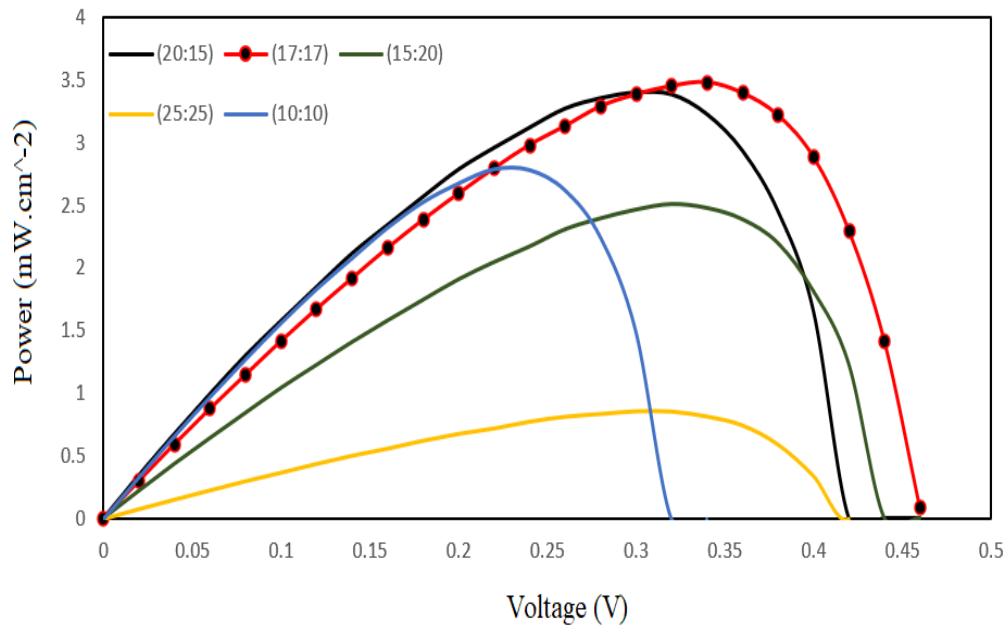


Figure 4.14: Power curve of IC₇₀BA bulk device at different P3HT:IC₇₀BA concentrations.

Concentration	J_{sc} (mA.cm ⁻²)	V_{oc} (V)	FF (%)	PCE (%)	R_{sh} (Ω)	R_s (Ω)
10:10	17.04	0.33	55	2.8	952	7
17:17	15	0.46	55	3.5	1200	3
25:25	4	0.42	40	1.86	255	22
15:20	11	0.44	44	2.5	728	15
20:15	19	0.43	42	3.3	500	12

Table 4.10: The J-V characteristics for the P3HT: IC₇₀BA based devices under illumination.

The trend of the device performance changes when the P3HT:IC₇₀BA blend concentration changes as shown in Figure 4.13 and Figure 4.14. When the P3HT to IC₇₀BA concentration was 10:10, a J_{sc} of 17.04 mA/cm² and full factor of 55% was obtained which consequently yielded the PCE of 2.8 %. The value of V_{oc} was greatly enhanced by 40% to 0.46 V for devices with the polymer to IC₇₀BA concentration of 17:17, compared to device concentration of (10:10), where electron and

hole have a lower concentration. A *PCE* of 3.5% for this device was achieved. As it is known, electrons have more mobility than holes in semiconductor materials and therefore increasing the ratio between donor material (P3HT) and acceptor material (IC₇₀BA) leads to increase in molar mass of compound which creates more excitons. However, by reference to optical properties and roughness measurements for the device with concentration of (25:25), increasing the IC₇₀BA weight ratio (25:25), reduces the photon absorption efficiency (as the polymer absorbs more light in the visible range than fullerene), resulting in an imbalance of charge transport in the device, which increases the value of the bandgap. This leads to the low amount of excitons, it can be noticed that at higher fullerene-to-polymer concentration, a larger domain size (high value of roughness) of fullerene can be formed which make trapping for electrons [39]. As results of the above, devices with (25:25) concentration produced the lowest (J_{sc}). Also, the same phenomenon occurred when the P3HT content increases to concentration of (15:20), $J_{sc} = 11 \text{ mW.cm}^{-2}$ and *PCE* 2.5%. Further increase in the P3HT weight ratio (20:15) increased the $J_{sc} = 19 \text{ mW.cm}^{-2}$ due to decrease recombination which reduces the device performance. This study demonstrates that at a concentration of 17:17 is the optimum concentration which prevents generated charges from becoming trapped within isolated domains. Moreover, excessive increasing in IC₇₀BA concentration (15:20) result in higher recombination rate and reduce device performance. Thus, Optimization of the composite concentration detects the important role played by morphology and bandgap for the transport properties of P3HT:IC₇₀BA bulk heterojunction based solar cells [40-42].

4.4 IC₇₀BA-based devices under different annealing conditions

4.4.1 Fabrication process

The device structure in this section is similar to the structure in Figure 4.1 with the fabrication procedure explained in the previous section (different solvents effect). The active layer for these devices was prepared by spin coating the blend solution of P3HT: IC₇₀BA (concentration of 17:17 mg/mL) with a spin coating 600 rpm for 60 seconds. Thermal annealing was performed at different temperatures (150 °C, 175 °C and 200 °C) for 20 minutes before the vacuum deposition of the metal electrodes (pre-thermal annealing). Finally, post-annealing was carried out for all devices for 20 minutes at 150 °C.

4.4.2 Morphological analysis using AFM

To understand the morphological changes that occur in the active layer due to thermal annealing, AFM images of the active layer surface before and after annealing at different temperatures were studied. The tapping-mode AFM images in Figure 4.15 shows the variation in OBHJ active layer morphology after annealing at different temperatures. The surface at 150°C thermal annealing is amorphous and very smooth with rms roughness of 1.23 nm. This smooth layer prevents charge carriers from trapping in the interface between the active layer and the metal electrodes. After undergoing thermal treatment at 175°C for 20 minutes, the rms roughness becomes 1.90 nm. Further increase in temperature to 200 °C resulted in more aggregate and rougher (2.53 nm) surface compared to the film treated at 150 °C. The high agglomeration of the active film guide to a negative impact on the OBHJ performance as the donor:accepter (D:A) interface area reduces the ability to separate excitons. From the AFM images, the annealing at 150 °C results in good mixing structures with a moderate agglomeration which gives large and connected grains. Thus, the change in annealing conditions significantly modify the nature of the underlying active layer morphology, and the morphology is correlated to the cell performance [43]. The values of roughness's for devices are listed in Table 4.11.

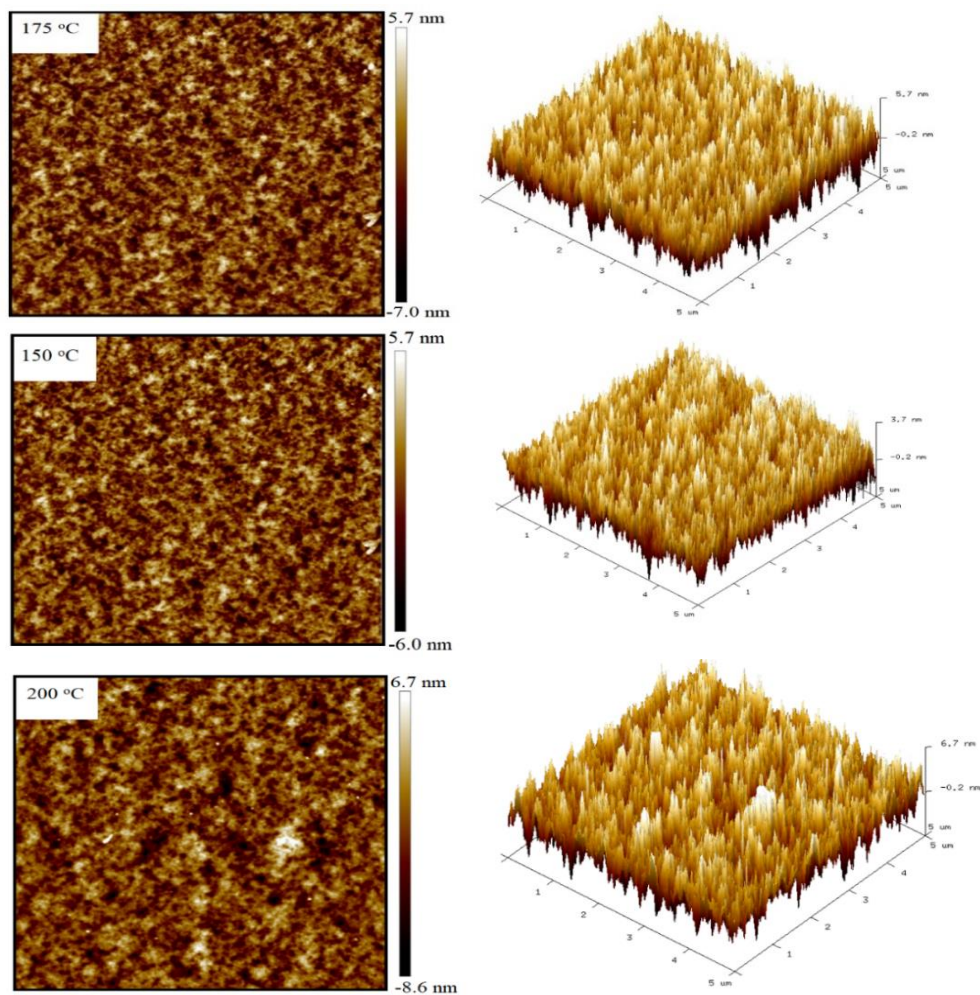


Figure 4.15: 2D and 3D ($5\mu\text{m}\times 5\mu\text{m}$) AFM images and phase analysis of the *P3HT:IC₇₀BA* blends prepared by different annealing temperature.

Temperature (°C)	Roughness (nm)
150	1.23
175	1.90
200	2.53

Table 4.11: Roughness for *P3HT:IC₇₀BA* based OPVs according different temperature annealing.

4.4.3 Optical Absorption measurements

Figure 4.16 shows the effect of thermal annealing on the *UV-Vis* absorption spectra for the thin films of P3HT:IC₇₀BA annealed at different temperature. The change in the peak and edge absorption wavelength with the different annealing temperature may be attributed to the enhancement of the crystallinity of P3HT domains and the degree of the aggregation of IC₇₀BA molecules in the blend film. For annealing temperature film at 150 °C, the wavelength of the absorption peak (λ_{max}) is 477 nm (2.6 eV). At annealing temperature higher than that required for complete reordered molecules film (at 175 °C) the (λ_{max}) is remain at 477 nm (2.6 eV) but the absorption intensity lower than the absorption in the film at 150 °C. Further increase of the annealing temperature to 200 °C results in reducing the absorption peak (λ_{max}) to 496 nm (2.5 eV). These changes are attributed to an increase in internal order, as the polymer chains move more freely with higher temperatures [31]. These changes indicate that thermal annealing significantly affected the molecular order of P3HT and the connectivity of IC₇₀BA crystallites as the thermal annealing induces a thermodynamic alteration of the photoactive layer. This causes a rearrangement of donor and acceptor phases, an increase in crystallinity of the P3HT and an improved absorption profile [44-46].

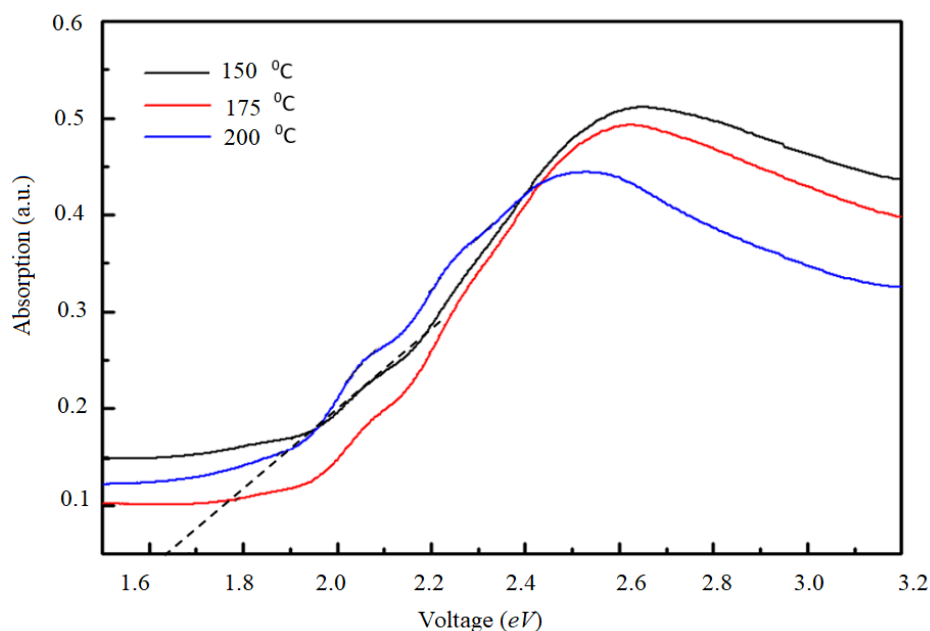


Figure 4.16: *The optical absorption of the IC₇₀BA based OBHJ solar cells under different annealing temperature.*

Table 4.12 shows that small changes in thermal annealing temperature resulted in significant changes to the bandgap and provide a direct method for tuning the bandgap in P3HT:IC₇₀BA devices. At 150 °C, the bandgap was 1.68 eV, whereas annealing increased to temperature 175 °C, the bandgap of the blend increased to 1.80 eV. Moreover, increasing annealing temperature to 200 °C resulted in increasing the bandgap to be 1.83 eV. This is considered as a barrier for electrons to be excited from the valance band to the conduction band in semiconductors. Hence, the heat treatment of the blend at the optimal temperature (150 °C) causes an increase in the energy width of the localized state thereby reducing the optical energy gap [47] and increase the number of excitons created due to light absorption. In summary, it is clear from the optical and surface morphology results indicate that the device performance depends strongly on the thermal annealing temperature. By comparing the efficiencies of the devices, the optimum annealing temperature to enhance the performance of OBHJ solar cells based on P3HT:IC₇₀BA is 150 °C due to the high ordered molecules in the active layer. Annealing at 150 °C resulted in lower energy bandgap and a moderate agglomeration grains size, which provides a favourable pathway for exciton separation and charge-carrier transport.

Temperature (°C)	Bandgap (eV)
150	1.68
175	1.80
200	1.83

Table 4.12: *The variation of P3HT:IC₇₀BA blend optical bandgaps with different annealing temperatures.*

4.4.4 Electrical measurements

4.4.4.1 Diode measurements

The dark $J-V$ characteristics as shown in Figure 4.17 were measured to further study the effect of different annealing temperature on series and shunt resistance of devices. Large shunt resistance and small series resistance is beneficial to obtaining higher FF [33]. At the reverse bias region of the dark $J-V$ curves, the current is mainly limited by the shunt resistance due to leakage current [23]. As the annealing temperature increases, the shunt resistances decrease and then increases in the series resistances of the dark $J-V$ curves as shown in Table 4.13. The R_s is a sum of the bulk resistance of various layers in devices and the contact resistance between them, while the R_{sh} is related to the quality of the films, such as traps and pinholes [48]. Larger R_s , which may be attributed to an inefficient contact between blend film and modified electrodes and to a larger roughness. Compared with the ($T= 150\text{ }^{\circ}C$)-based devices, $R_{sh}= 60\text{ k}\Omega$, while ($T= 175\text{ }^{\circ}C$) and ($T= 200\text{ }^{\circ}C$)-based devices exhibits a larger leakage current, which would decrease the shunt resistance by 86% and 96% ($8.3\text{ k}\Omega$ and $2.6\text{ k}\Omega$, respectively). Such large variation in the leakage current of organic solar cells is not uncommon and is known to be affected by substrate cleaning procedures, film thickness, electrode interlayers, and film deposition techniques which is evidenced by the roughness of the AFM diagram shown in Figure 4.15. At high positive voltages region of the dark $J-V$ curves, the dark current is mainly controlled by series resistance [49]. For series resistances, the ($T= 200\text{ }^{\circ}C$)-based device has the highest R_s followed by the ($T= 175\text{ }^{\circ}C$)-based device and the ($T= 150\text{ }^{\circ}C$)-based device which have $R_s= 8\text{ }\Omega$ and $4\text{ }\Omega$, respectively.

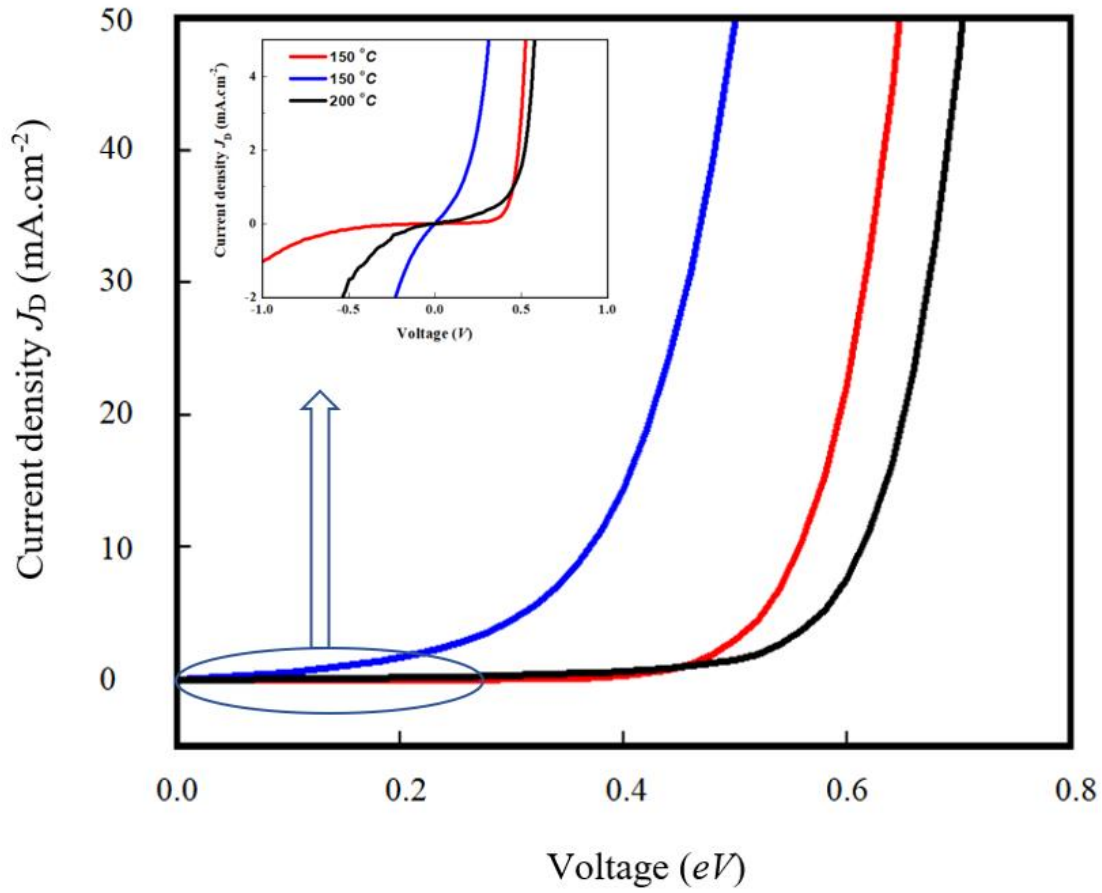


Figure 4.17: Diode behaviours for different annealing temperature devices. The insert figure represents leakage current.

Parasitic Resistances		
Temperature (°C)	Shunt resistance (kΩ)	Series resistance (Ω)
150	60	4
175	8.3	8
200	2.6	11

Table 4.13: Diodes parasitic resistances for different temperatures.

As a method to investigate the recombination in the dark, the diode ideality factor n is extracted from the dark J - V curve in Figure 4.18. Under high voltage bias (>0.3 V) for the $T = 175$ °C, (>0.5 V) for $T = 150$ °C and (>0.6 V) for $T = 200$ °C-based device in the exponential region, most of the current density is influenced by the parasitic effects raised by series resistance and shunt resistance [50-51]. For the $T = 150$ °C-based device, the value of the diode ideality factor is found in the range of 1.2, while for the devices annealed at $T = 175$ °C the value of the diode ideality factor is found to be 1.5. For devices annealed at $T = 200$ °C, the value of the diode ideality factor is 1.79 as listed in Table 4.14.

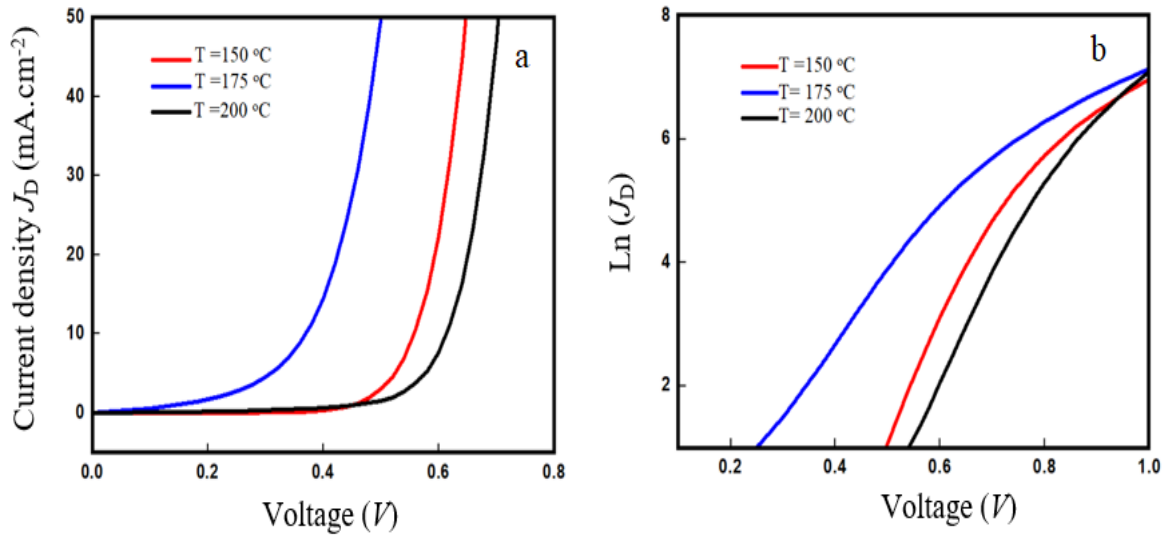


Figure 4.18: *a) J - V characteristics of the OBHJ solar cells under the dark. (b) Variation of $\ln(J_D)$ versus the bias voltage with different annealing temperature films for P3HT:IC₇₀BA OPV devices.*

Different temperature-based device ($^{\circ}\text{C}$)	Ideality Factor (n)
150	1.2
175	1.5
200	1.79

Table 4.14: Ideality factors for diode devices.

4.4.4.2 Photovoltaic performance

The J – V curves of the OBHJ solar cells with different thermal annealing under the illumination of 100 mW.cm^{-2} white light is shown in Figure 4.19 (Figure 4.20 represents the output electric power as a function of applied voltage used to estimate the maximum power). Data for the OBHJ solar cells performance are summarized in Table 4.15. For shunt resistance, significant decrease with increasing thermal annealing, which negatively affects the performance of devices, is evidenced in Table 4.15. The OBHJ solar cells with thermal annealing at 150°C exhibited a PCE of 3.5% with $J_{sc}=15 \text{ mW.cm}^{-2}$, V_{oc} is 0.46 V and FF of 51% with a semi-flat curve. As the heat-treatment temperature was increased, the R_{sh} , R_s and FF parameters were decreased. It is the variation of the optoelectrical and physical properties of the photoactive layer due to heat treatments influences the device performance significantly where the optimum annealing temperature is 150°C for 20 minutes. That depends on the degree of the aggregation of IC₇₀BA molecules in the blend film with thermal annealing to provide interpenetrating networks for charge-carrier transport and the degree of the enhancement of the crystallinity of P3HT domains [38]. Efficient OBHJ solar cells can be obtained by enhancing the connectivity of IC₇₀BA and P3HT crystallinity. It is believed that the main process affects the photoactive layer performance due to thermal annealing is the IC₇₀BA aggregation and diffusion to the P3HT order structure [52]. The output power for the device annealed at 150°C increased more than 33% compared to the device annealed at 200°C . For shunt resistances, R_{sh} at 200°C decreased by more than 70% compared to R_{sh} at 150°C , while series resistance showed increased in value as the annealing temperature been raised.

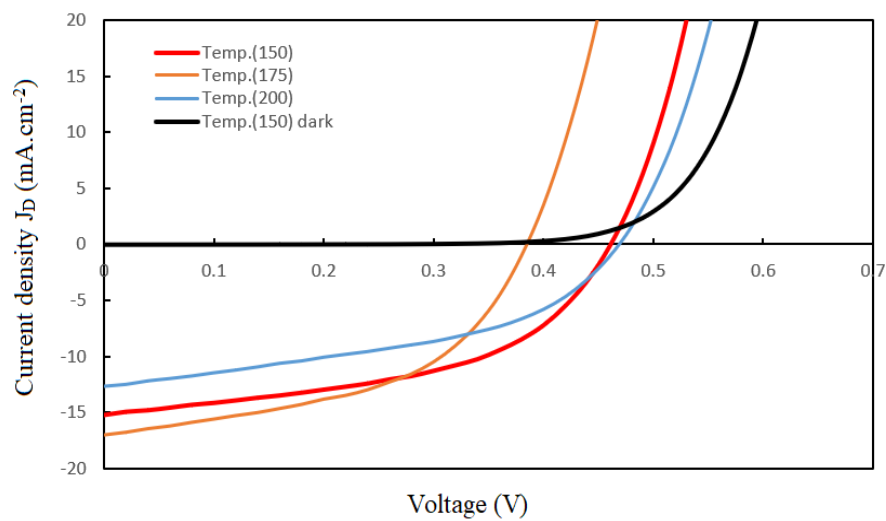


Figure 4.19: *J-V characteristics for P3HT:IC₇₀BA-based devices under AM 1.5 solar simulator source of 100 mW.cm⁻² using different annealing temperature.*

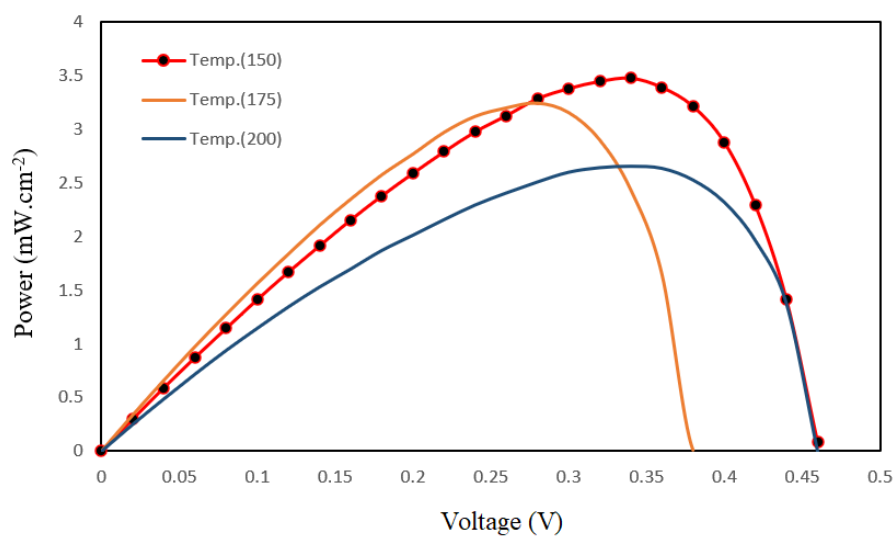


Figure 4.20: *Power curve of IC₇₀BA bulk device at different annealing temperature.*

Annealing temperature (°C)	J_{sc} (mA.cm ⁻²)	Voc (V)	FF (%)	PCE (%)	R_{sh} (Ω)	R_s (Ω)
150	15	0.46	51	3.5	1200	3
175	17	0.39	48	3.2	286	4.5
200	12.6	0.47	45	2.7	333	4

Table 4.15: The J-V characteristics for the P3HT: IC₇₀BA based devices under illumination.

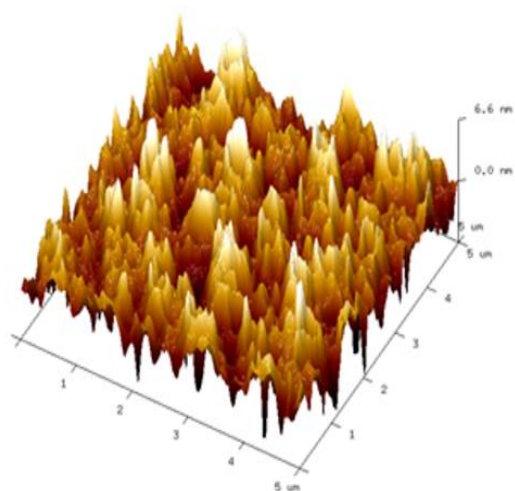
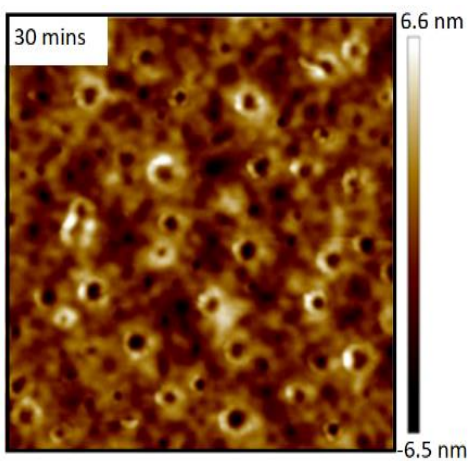
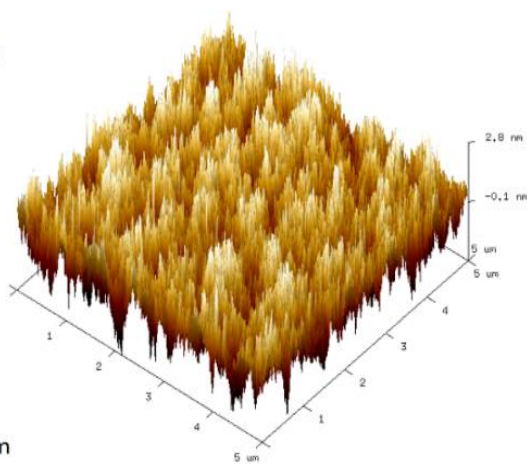
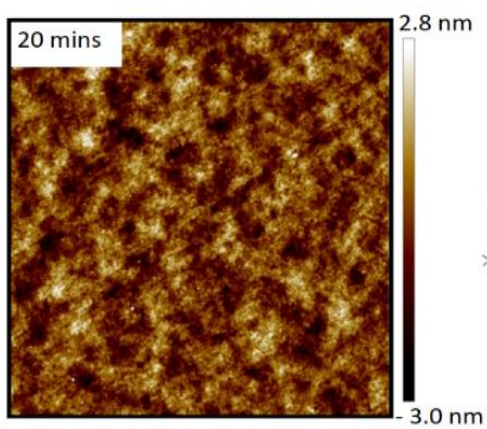
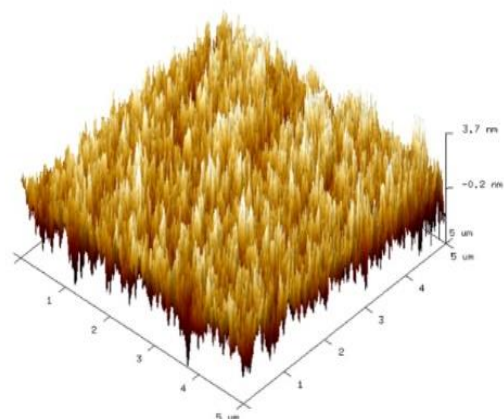
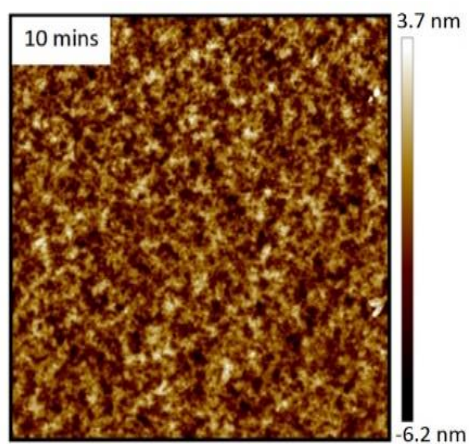
4.5 IC₇₀BA-based devices under different annealing time conditions

4.5.1 Fabrication process

P3HT:IC₇₀BA-based OBHJ devices were fabricated using a pre-patterned ITO-coated glass substrate. Before the use, the substrate was cleaned in ultrasonic using 20% Decon90, deionized water, isopropanol, and acetone in the cleanroom, and later dried with N₂ compressor. All cleaned substrates were treated with O₂ plasma treatment for 20 minutes. The solution for hole transporter PEDOT:PSS was spin-coated at 4000 rpm for 40 seconds onto the cleaned substrates and annealed at 150 °C for 30 minutes. The photoactive layer P3HT:IC₇₀BA (1:1) weight/weight (w/w) dissolved in DCB with a concentration of 34 mg/ml (17:17) was spin-coated at 600 rpm for 60 seconds in the glove box and subsequently annealed at 150°C for different annealing times 10, 20, 30, 40 and 50 minutes. To complete the device, 100 nm thick Al was thermally evaporated at rate 1Å/s through a shadow mask at a base pressure of 10⁻⁶ mbar. The active area of the complete devices is 0.125 cm². Devices were tested under AM 1.5 illumination with an intensity of 100 mW.cm⁻² at room temperature.

4.5.2 Morphological analysis using AFM

The surface morphology for devices annealed at different annealing times were examined using tapping-mode atomic force microscope (AFM). The tapping-mode AFM images are illustrated in Figure 4.21. Variation in the morphology values of active layer after different annealing times as listed in Table 4.16. The surface morphology for devices treated with thermal annealing for 20 minutes showed enhanced properties as the surface roughness decreased more than 35% compared to the roughness of device annealed for 10 minutes. In contrast, increasing annealing time beyond 20 minutes resulted in a clear increase in surface roughness and therefore works as an impediment for excitons leading to high recombination process. The increase in surface roughness arises from self-assembled P3HT and IC₇₀BA domains due to possible molecular-level interactions between IC₇₀BA and solvent [53]. Moreover, these films exhibited more pinholes compared to devices annealed for 20 minutes, this may cause leakage current that reduces the fill factor and overall power conversion efficiency (PCE) of the OSCs [54]. With long temperature thermal-annealing, polymer crystallization size becomes large in the active layer, thus increasing the overall surface roughness of the films.



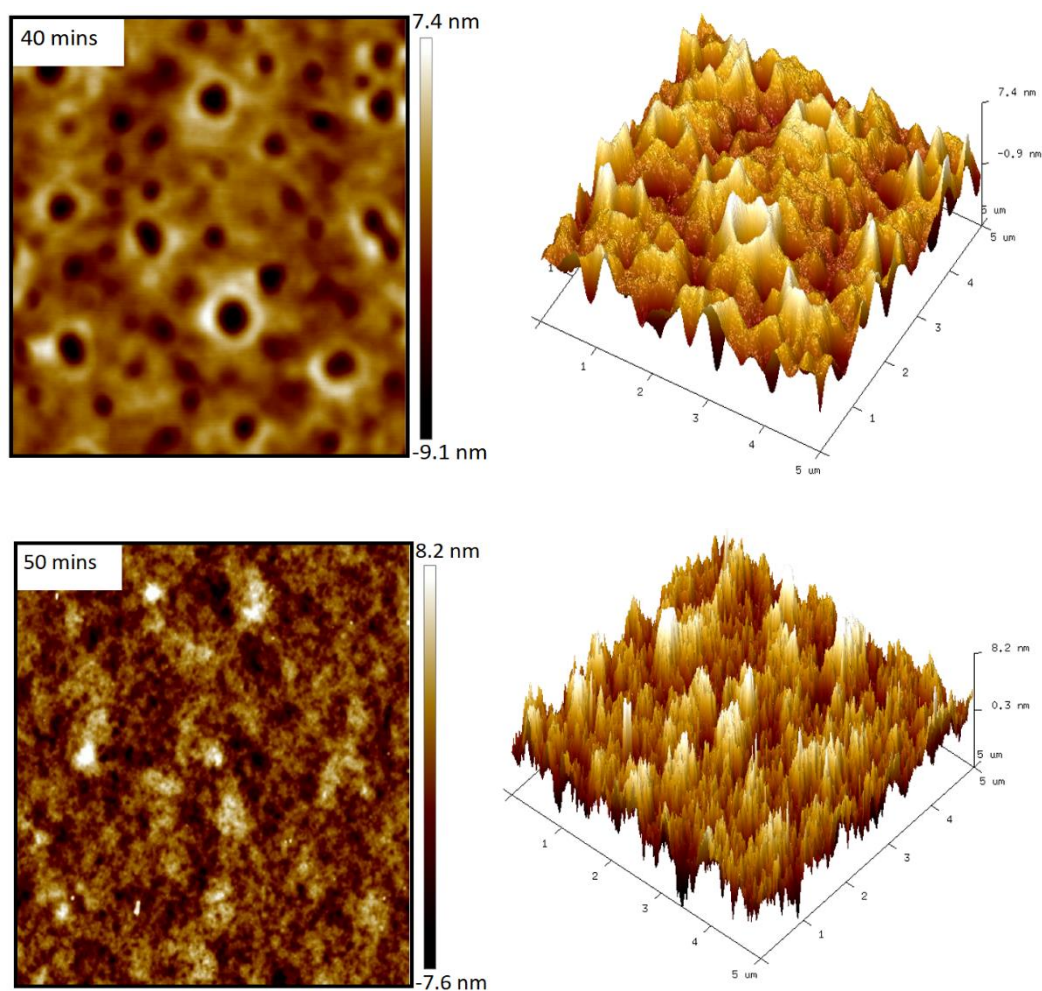


Figure 4.21: 2D and 3D ($5\mu\text{m} \times 5\mu\text{m}$) AFM images and phase analysis of the P3HT:IC₇₀BA blends prepared by different annealing times.

Annealing time (mins)	Roughness (nm)
10	1.23
20	0.87
30	1.33
40	4.63
50	4.71

Table 4.16: Roughness for P3HT:IC₇₀BA based OPVs according different annealing time.

4.5.3 Optical Absorption measurements

Starting with 10- and 20-minutes annealing time, the energy band gap was calculated from Figure 4.22 and predicted in Table 4.17. It can be noticed that changes in thermal annealing time resulted in changes to the bandgap and provide another direct method for tuning the bandgap in P3HT:IC₇₀BA device structure. For both annealing time the energy band gap showed almost similar values which are 1.74 eV and 1.76 eV, respectively. While increasing the duration of post-annealing further (more than 20 minutes) increase in the bandgap as shown in Table 4.17. This behaviour may be attributed to the decomposition of the blend structure at longer annealing time. Generally, P3HT:IC₇₀BA film annealed for 20 minutes showed the highest absorption peak as shown in Figure 4.22, with a peak wavelength of 500 nm which was attributed to improved chain ordering of the P3HT molecules within the active layer and the enhanced exciton dissociation efficiency at the donor/acceptor interface [54].

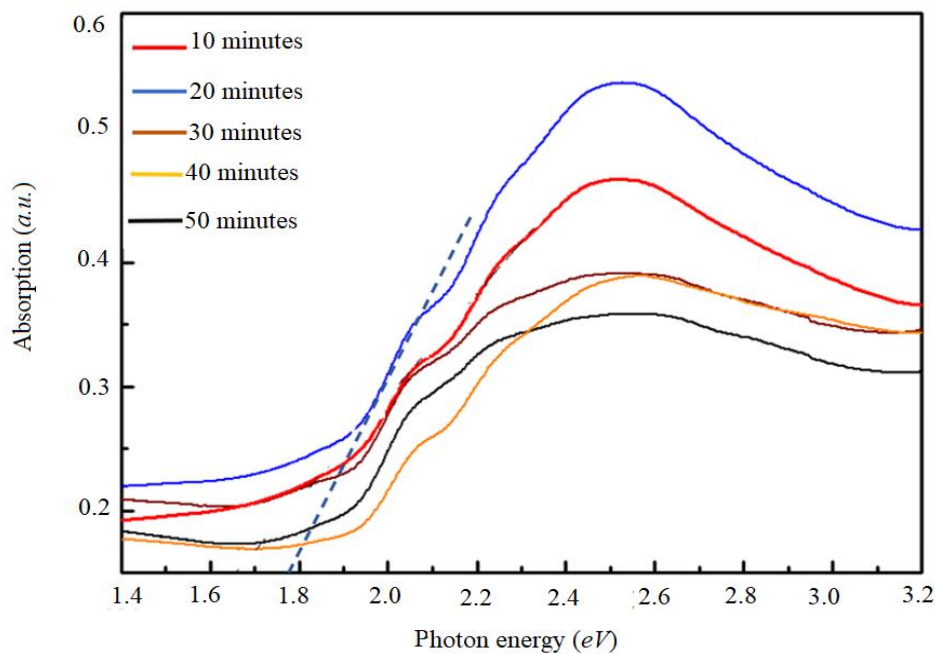


Figure 4.22: *The optical absorption of the IC₇₀BA based OBHJ solar cells under different annealing times.*

Annealing time (<i>minutes.</i>)	Bandgap (<i>eV</i>)
10	1.74
20	1.76
30	1.80
40	1.90
50	1.89

Table 4.17: Bandgaps for P3HT:IC70BA based OPVs according to different annealing time.

4.5.4 Electrical measurements

4.5.4.1 Diode measurements

The R_{sh} and R_s of the OSCs produced using different thermal annealing times have been estimated using the dark J - V characteristics in Figure 4.23. Device annealed for 20 minutes has exhibited the lowest R_s with a value of $2\ \Omega$ compared to the rest of the devices annealed at different times as shown in Table 4.18 and Figure 4.23. The main reason for these high series resistances could be attributed to the larger roughness and presence of pinholes. A high series resistance results in low FF and therefore reduced solar cell efficiency; improved contact properties between the active layer and the top (Al) electrode will result in low series resistance due to the stronger interfacial adhesion [55]. Shunt resistance is also calculated as listed in Table 4.18. For 20 minutes annealing, the device has the highest value with $R_{sh} = 75\ k\Omega$, which prevents current leakage through pinholes and traps or current leakage from the edge of cells. The value of resistance associated with devices annealed for 20 minutes represents the optimal conditions for device fabrication. By increasing thermal annealing time more than 20 mins, R_{sh} showed a significant decrease by more than 97%, 92% and 92% for devices annealed for 30, 40 and 50 minutes, respectively. These low values can be related to low-quality films and more charge carrier recombination [48].

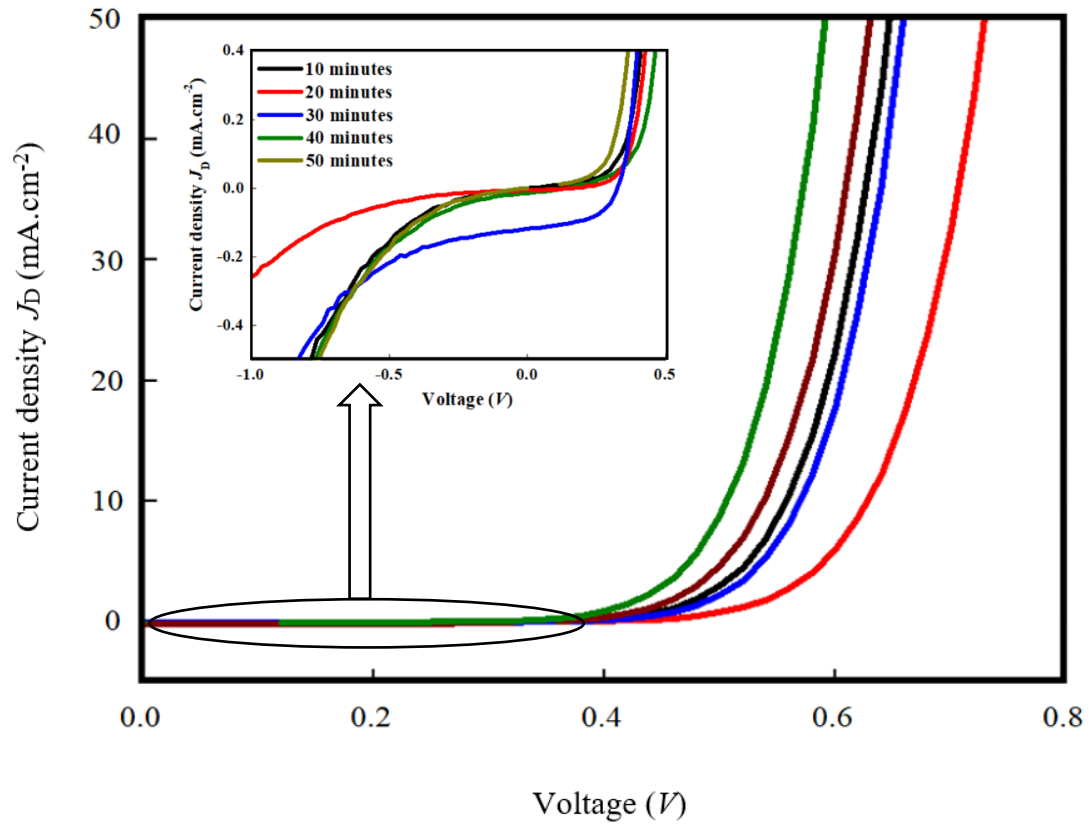


Figure 4.23: Diode behaviors for different annealing times. The insert figure represents leakage current.

Parasitic Resistances		
Annealing time (minutes.)	Shunt resistance (k Ω)	Series resistance (Ω)
10	60	4
20	75	2
30	2	12
40	6	9
50	6	7

Table 4.18: Diodes parasitic resistances for different P3HT:IC₇₀BA annealing times.

To illustrate the impact of the trap on recombination, the ideality factors of the OSCs were calculated from Figure 4.24. The ideality factor from the dark current density–voltage curve is defined as real and important parameter which can be used to decide whether the p-n junction device behaves closely to the ideal diode [56]. The ideality factor is close to 1 for an ideal trap-free device, while it approaches 2 for the case with the deep and dominant recombination induced by the trap [57]. The results are shown in Figure 4.24 and summarized in Table 4.19. Using different thermal annealing times has resulted with different rectification; the device annealed for 20 minutes has shown close to unity ideality factor, this is attributed to the improved distribution of IC₇₀BA within P3HT matrix and thus improved film morphology which facilitates the charge carriers transportation by creating percolation pathways for both charges and hence a decrease in the recombination rate [55]. For long thermal annealing times (30, 40 and 50 minutes), the ideality factors are found to be 1.35, 1.73 and 1.96, respectively which suggests high recombination rate in such devices. This high value might be attributed to the morphological disorder of the devices which show clear pinholes and interrupted networks [55].

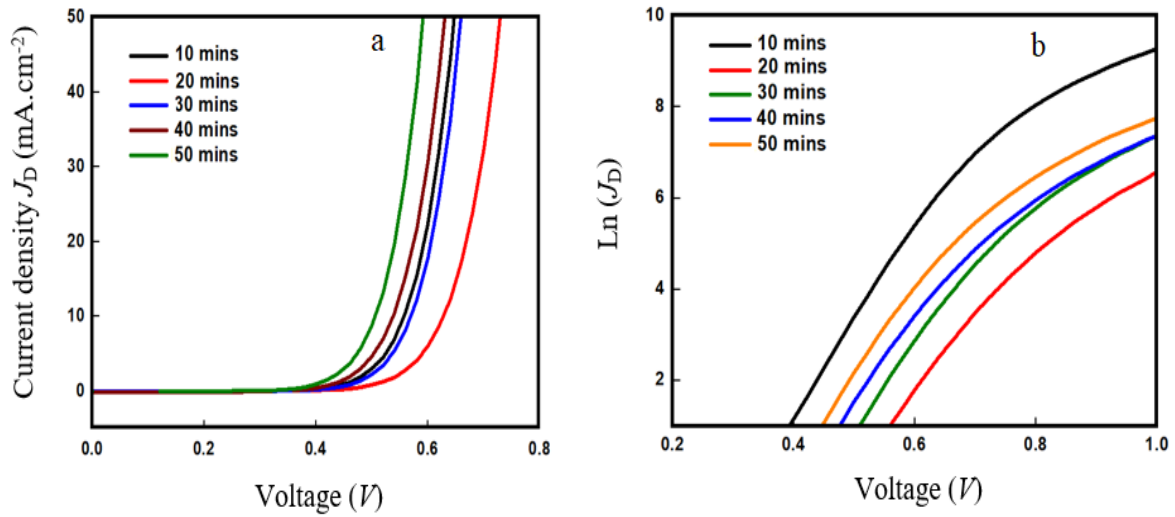


Figure 4.24: (a) J - V characteristics of the OBHJ solar cells under the dark. (b) Variation of $\ln(J_D)$ versus the bias voltage with different annealing times for P3HT:IC₇₀BA OPV devices.

Annealing Time (minutes.)	Ideality Factor (n)
10	1.20
20	1.05
30	1.35
40	1.73
50	1.96

Table 4.19: Ideality factors for different annealing times.

4.5.4.2 Photovoltaic performance

J – V curves of the devices tested under 100 mW.cm^{-2} AM 1.5 G illumination for different annealing times are shown in Figure 4.25 and device performance parameters are listed in Table 4:20. The trend of the device performance change when the annealing times change (see Figure 4.25 and Figure 4.26). When the annealing time was 50 minutes, a J_{SC} of 4 mA/cm^2 and FF of 51% were obtained which consequently yielded a PCE of 0.9 %. This attribute to surface roughness and the large difference between the mobilities of electrons and the holes, then space charge effects due to unbalanced mobilities results in a low current density [39]. J_{sc} was significantly enhanced to 21.3 mA.cm^{-2} for the device annealed for 20 minutes, where electron and hole transport are balanced resulting in much improved value of PCE 4.7%. This is ascribed to the increase in the charge carriers' mobility and the electrical conductivity due to the improved layer structure and good interpenetrating network. When the thermal annealing time was further increased to 30 minutes, the FF started to decrease by almost 30% and reached a value of 38% resulted in PCE of 3.9%. In this case, shunt resistance and series resistance played a critical role, high R_s and low R_{sh} compared to device annealed for 20 minutes. Similar phenomenon occurred when the device annealed for 40 minutes, $J_{SC} = 8 \text{ mA.cm}^{-2}$ and PCE 1.8% with low $R_{sh}=700 \Omega$ and high $R_s=9 \Omega$. It is clear that device performance weakens with the increase of the annealing time for more than 20 minutes. Devices annealed for 10 mins showed decreased value of $J_{sc} = 15 \text{ mA.cm}^{-2}$ due to increase in recombination which reduces the device performance. V_{oc} , on the other hand, has slightly changed

for the fabricated devices; V_{oc} is mainly determined by the difference between the HOMO of the donor and the LUMO of the acceptor [58]. However, increasing the annealing times reduces the photon absorption efficiency (as the polymer absorbs more light in the visible range than fullerene), resulting in an imbalance of charge transport in the device, which decreases the device performance.

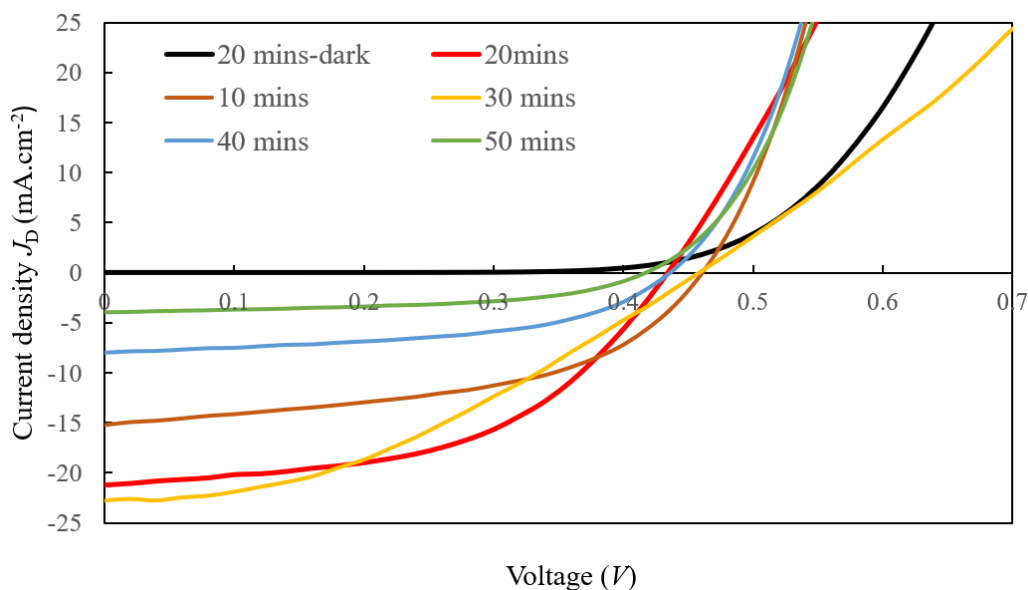


Figure 4.25: *J-V characteristics for P3HT:IC₇₀BA-based devices under AM 1.5 solar simulator source of 100 mW.cm⁻² using different annealing times.*

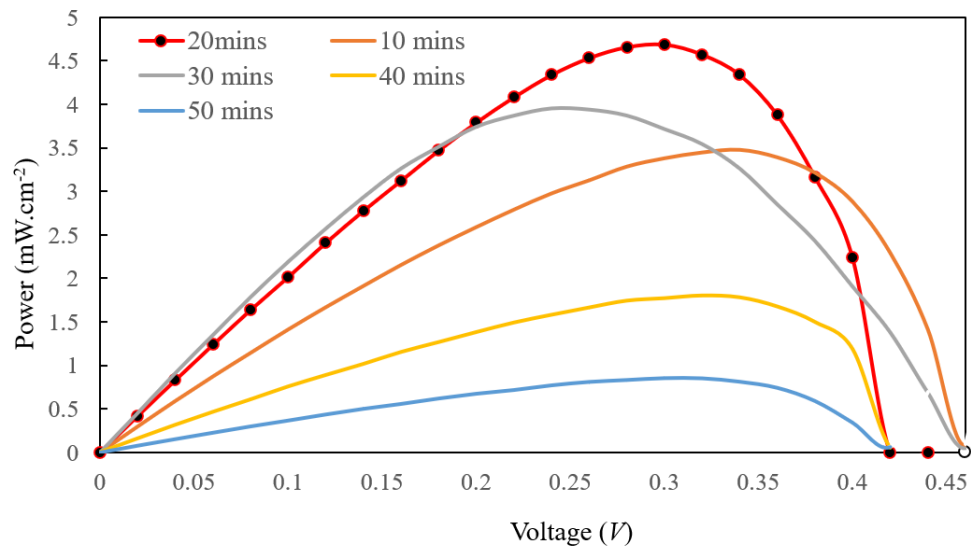


Figure 4.26: Power curve of $IC_{70}BA$ bulk device at different annealing times.

Annealing time (minutes.)	J_{sc} ($mA.cm^{-2}$)	V_{oc} (V)	FF (%)	PCE (%)	R_{sh} (Ω)	R_s (Ω)
10	15	0.46	51	3.5	1200	3
20	21.3	0.43	53	4.7	3000	3
30	22.8	0.45	38	3.9	600	15
40	8	0.43	52	1.8	700	9
50	4	0.41	51	0.9	1000	6

Table 4.20: The J-V characteristics for the $P3HT: IC_{70}BA$ based devices under illumination for different annealing time.

4.6 Using Lithium Fluoride (LiF) as electrons collecting buffer layer

4.6.1 Fabrication process

The device is fabricated in a similar structure as described for the device in section 4.5 with annealing time of 20 minutes. To complete the device, 0.75 nm thick of LiF was thermally evaporated at evaporation rate 0.1 Å/s and 100 nm thick Al was thermally evaporated at rate 1 Å/s through a shadow mask at a base pressure of 10^{-6} mbar. The active area of the completed devices is 0.125 cm². Devices were tested under AM 1.5 illumination with an intensity of 100 mW.cm⁻² at room temperature. Figure 4.27 shows the schematic diagram of P3HT:IC70BA based OBHJ with all the layers used in this experiment.

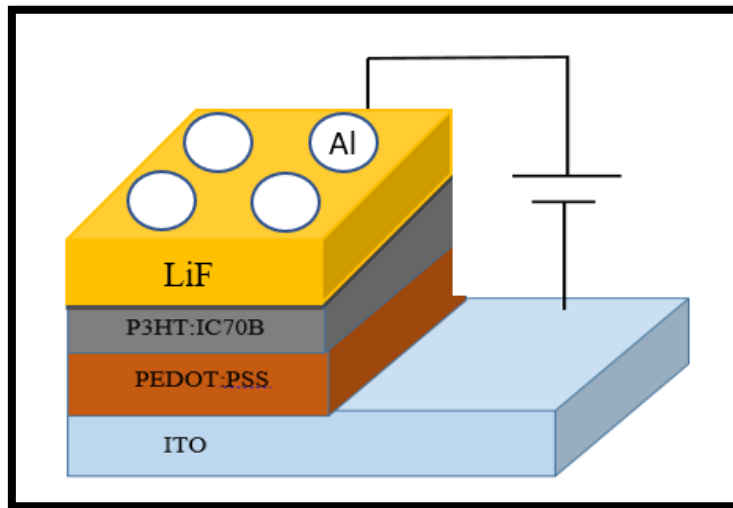


Figure 4.27: Schematic diagram of P3HT:IC₇₀BA devices.

4.6.2 Morphological analysis using AFM

To find out the reasons leading to high *FF* for the LiF-based OSCs, AFM measurements were performed to examine the surface morphology of the LiF layer on P3HT:IC₇₀BA surface. Figure 4.28 shows the phase images, recorded by tapping mode AFM of the P3HT:IC₇₀BA films without LiF and with LiF (0.75 nm) layer deposited on top of the active layer (image size 5 μm × 5 μm). The pristine P3HT:IC₇₀BA film exhibits a very smooth surface with a low

roughness of 0.87 nm. After depositing 0.75 nm thick LiF on top, the rms roughness increases to 1.68 nm. Figure 4.28 shows there is a significant difference in rms roughness between without LiF layer and with LiF layer and the surface morphologies of these two films are very different. The P3HT:IC₇₀BA/LiF film shows larger aggregates (spherical shape) as compared to pristine P3HT:IC₇₀BA, which can also be observed in their phase images, a similar behaviour was observed by other researchers [59]. Therefore, some intermixing occurs at the P3HT:IC₇₀BA /LiF interface, which results in the good V_{oc} and high FF as will be demonstrated in this section. Also, the increase in surface roughness arises from self-assembled P3HT and IC₇₀BA domains due to possible molecular-level interactions with LiF and solvent annealing.

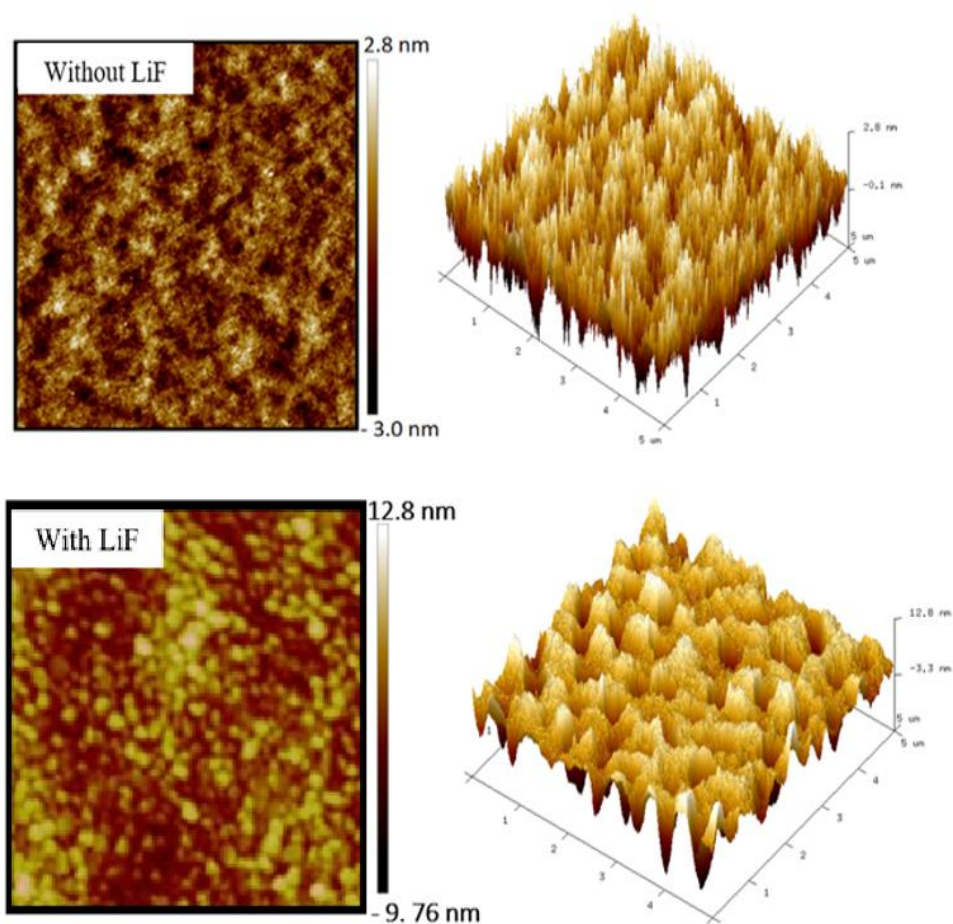


Figure 4.28: 2D and 3D ($5\mu\text{m} \times 5\mu\text{m}$) AFM images and phase analysis of the P3HT:IC₇₀BA blends with and without LiF.

Device	Roughness (nm)
Without LiF	0.87
With LiF	1.68

Table 4.21: *Roughness for P3HT:IC₇₀BA based OPVs with and without LiF.*

4.6.3 Optical Absorption measurements

UV-Vis spectra of thin-films with and without LiF are shown in Figure 4.29. The pristine P3HT:IC₇₀BA film absorption edge at 704 nm where the bandgap at this point is 1.76 eV, with peak absorption at 496 nm (2.50 eV). However, the P3HT:IC₇₀BA/LiF absorption edge at 680 nm where the bandgap at this point is 1.82 eV, with peak absorption at 500 nm (2.48 eV). No significant change in the peak position has been observed for both devices. Table 4.22 shows bandgaps for P3HT:IC₇₀BA based OPVs and P3HT:IC₇₀BA/LiF. It is clear from Figure 4.29 that the absorption intensity for devices with deposited LiF thin film is much higher than absorption intensity for devices without LiF layer, this shows that the emission only comes from the LiF [60]. Compared with the active layer without LiF, the absorption peak of annealed films did not shift, only the intensity of absorption peak changed. The peak intensity is determined by the structural order of the LiF and the active layer film.

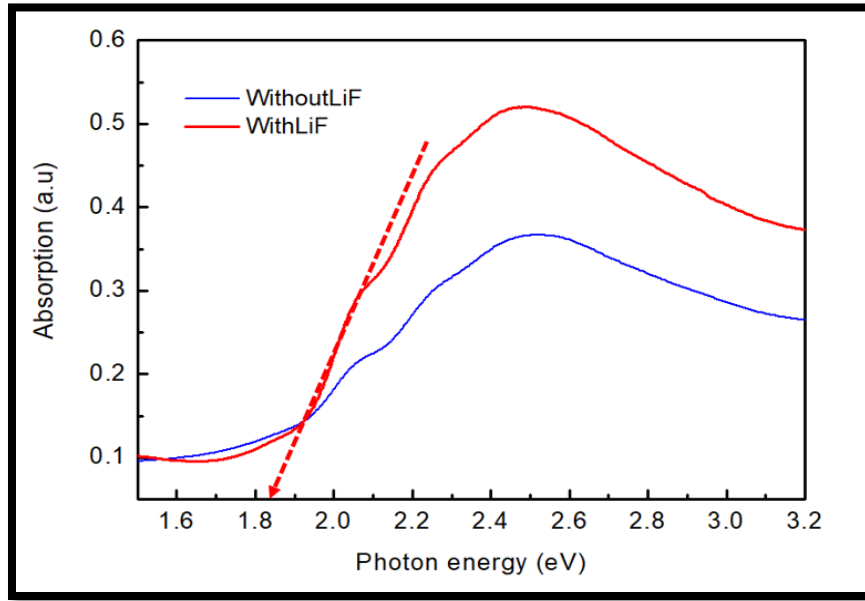


Figure 4.29: The optical absorption of the IC₇₀BA based OBHJ with and without LiF layer.

Device	Bandgap (eV)
Without LiF	1.76
With LiF	1.82

Table 4.22: The variation of P3HT:IC₇₀BA blend optical bandgaps with and without LiF.

4.6.4 Electrical measurements

4.6.4.1 Diode measurements

Figure 4.30 displays the dark current density vs voltage curve for both devices without and with LiF. It is obvious to observe that the device without LiF has a much lower leakage current when under the reverse bias. The low shunt resistance indicates the high leakage current and also indicates the higher charge carrier recombination in the device [61-62]. The small dark leakage current of the fresh device is also responsible for its higher V_{oc} [50,63]. Shunt resistance and series

resistances are calculated as listed in Table 4.23. For R_{sh} , LiF-based device showed better value compared to the device without LiF layer, which is 90 k Ω and 75 k Ω , respectively. On the other hand, related to R_s values, LiF device showed a double value of R_s compared to the device without LiF layer, this is attributed to high roughness of LiF device.

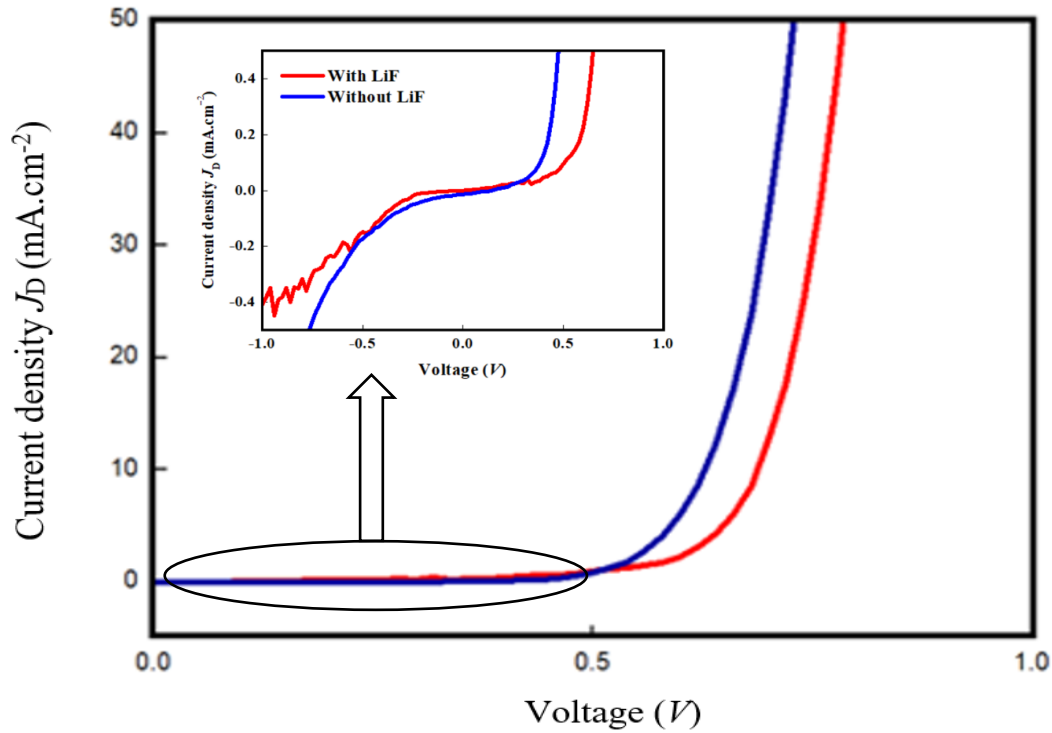


Figure 4.30: Diode behaviours for non LiF layer and with LiF layer. The insert figure represents leakage current.

Parasitic Resistances		
Devices	Shunt resistance (k Ω)	Series resistance (Ω)
Without LiF	75	2
With LiF	90	4

Table 4.23: Diodes parasitic resistances for P3HT:IC₇₀BA device with and without LiF.

For the ideality factor (n), a deviation of n from unity was observed because of trap-assisted recombination. This result likely to be consistent with the observation of n larger than unity in dark-current measurements. Consequently, an ideality factor greater than unity in organic solar cells is often used as evidence for a dominant trap assisted recombination process [64]. In this section, it is demonstrated that in organic solar cells with trap-free transport, the dark ideality factor is determined by the transport dominating carrier in the blend, Recently, it is demonstrated that the ideality factor often deviates from unity even in single-carrier diodes of a single material, where recombination is completely absent. This deviation from unity was caused by a small number of deeply trapped carriers which are not in thermal equilibrium with free carriers in the transport sites. Finally, it is demonstrated that the ideality factor of the dark current is dominated by the fastest transporting material in the blend. Consequently, a dark ideality factor deviating from unity can be used as an indication for the presence of trap-assisted recombination in an organic solar cell [65]. Table 4:24 shows the value of ideality factors in the dark for both devices. J-V characteristics of the OBHJ solar cells under the dark. (B) Variation of $\ln(J_D)$ versus the bias voltage with and without LiF layer are shown in Figure 4:31.

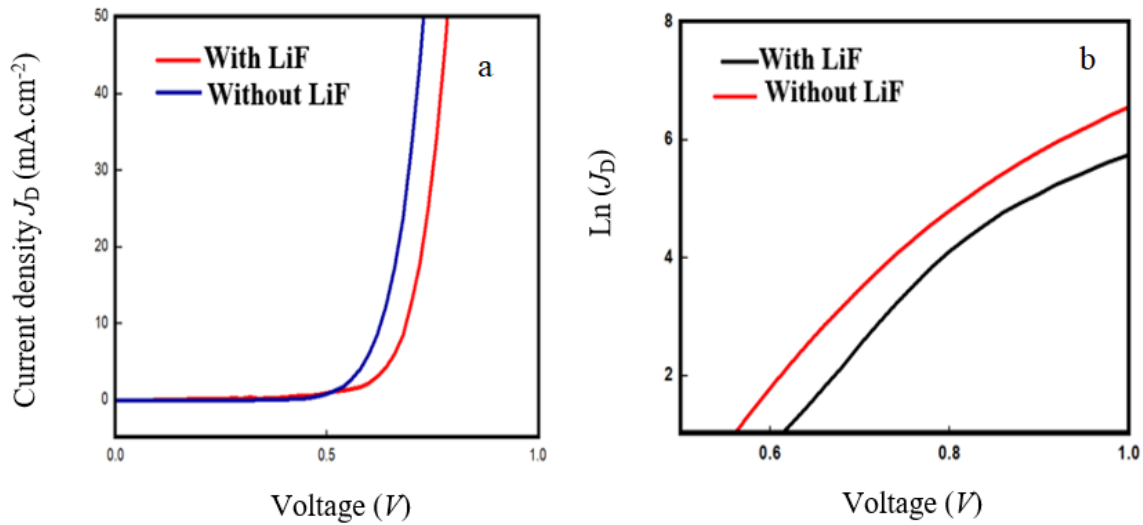


Figure 4:31: a) J-V characteristics of the OBHJ solar cells under the dark. b) Variation of $\ln(J_D)$ versus the bias voltage with and without LiF layer.

Device	Ideality factor (n)
Without LiF	1.05
With LiF	1.9

Table 4.24: *Ideality factors for diode devices.*

4.6.4.2 Photovoltaic performance

Lithium fluoride (LiF) is widely used as the interfacial layer between the electron transport layer (ETL) and metal back contact as electron collecting layer, and to improve the device performance. The fill factor (FF) of solar cells could be improved from 53% to around 56% just by depositing 0.75 nm LiF before Aluminium (Al) evaporation. Implying the energy mismatch between cathode and electron transporting layer is compensated by the formation of dipoles with LiF insertion layer. It is also expected that the LiF layer protects the layers underneath when the (Al) is evaporated, resulting in less Al diffuses into the film which may be responsible for forming high conducting channels leading to recombination [66]. However, it is still in a debate the exact operation mechanism of these buffers or ultrathin layers. Forming a tunnelling junction to increase built-in electric field, an interfacial dipole layer to shift the work function of electrodes, or to protect the active layer from damage is considered the underlying reason for using LiF [67]. OSCs using no LiF and 0.75 nm LiF were fabricated with the following structures: ITO/PEDOT:PSS/P3HT:IC₇₀BA/LiF (0 and 0.75 nm)/Al. The current density–voltage (J – V) characteristics for both cells under 100 mW/cm² are shown in Figure 4.34. Their main extracted performance parameters, V_{oc} , (J_{sc}), (FF) and PCE which are obtained through the peaks of curves in Figure 4.35, all parameters are summarized in Table 4.24. It is distinguished that the device efficiency is enhanced by 15% by the insertion of 0.75 nm LiF layer. The V_{oc} of 0.43 V and 0.79 V for both OSCs with 0 and 0.75 nm LiF are significantly different. Table 4.24 also showed J_{sc} of 21.2 mA.cm⁻² and FF of 53% for the OSC with no LiF and J_{sc} of 12.5 mA.cm⁻² and FF of 56% for

the OSC with LiF layer. Finally, the overall PCE for the cell with LiF (5.55%) is much improved compared to that without LiF (4.7%) due to the clearly improved V_{oc} .

The series resistance was decreased to $0.5\ \Omega$ compared to $3\ \Omega$ for devices with no LiF, and then the FF of the OSCs has improved because of the insulating nature of thin LiF buffer layer. When electrons come to the interface of polymer/LiF, many of them can pass through the LiF layer by tunneling. Because the thickness of LiF is only 0.75 nm, the tunnelling efficiency of electrons is so high that only a few electrons cannot pass through LiF layer. A build-in electric field pointing from Al to polymer will be formed inside the polymer/LiF/Al system. The build-in field can push the electrons passing through the buffer layer. So, the V_{oc} of the cells could also be increased, which increased almost by 100% compared with no LiF device. Also, the evaporation of Al electrode needs a high temperature [68], and the Al atoms have very high energy and would destroy the polymer active layers during the evaporation process. Some Al atoms embedding into the polymer active layer may create recombination centres, resulting in many excitons and carriers recombine in these centres. So, the pre-evaporated LiF buffer layer can prevent the Al atoms from directly bombarding the polymer active layer. Moreover, in the cell without the cathode buffer layer, there exists a kind of bonds near the interface of polymer/Al. These bonds also can cause serious recombination of excitons and carriers. When a LiF cathode buffer layer is introduced, it can isolate the metallic cathode from the polymer active layers. Then, nearly no bonds will be formed, the quality of the interface has been improved, and the recombination probability of the excitons has been reduced [69].

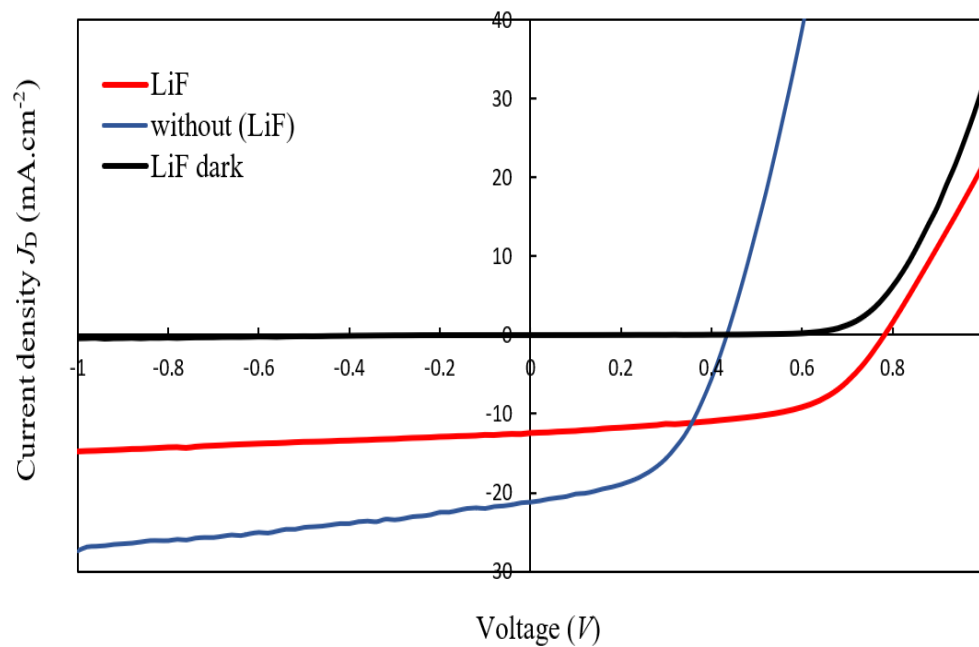


Figure 4.32: *J-V characteristics for P3HT:IC₇₀BA-based devices under AM 1.5 solar simulator source of 100 mW.cm⁻² with and without LiF.*

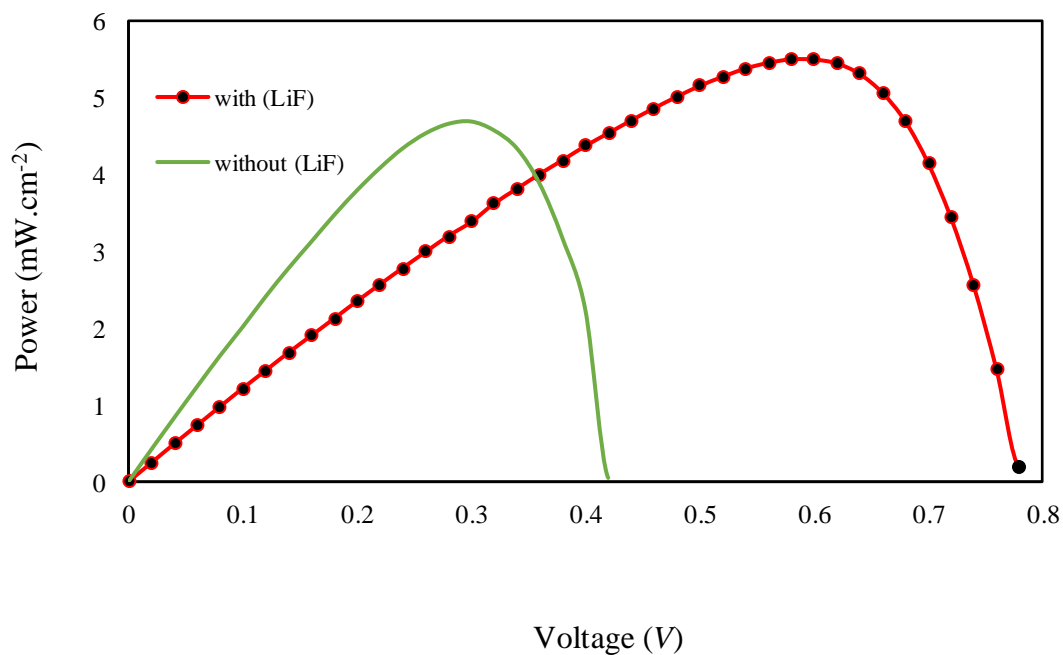


Figure 4.33: *Power curve of IC₇₀BA bulk device with and without LiF layer.*

Device	J_{sc} (mA.cm ⁻²)	V_{oc} (V)	FF (%)	PCE (%)	R_{sh} (Ω)	R_s (Ω)
Without LiF	21.2	0.43	53	4.7	3000	3
With LiF	12.5	0.79	56	5.5	2500	1.5

Table 4.25: *The J-V characteristics for the P3HT: IC₇₀BA based devices under illumination for different annealing time.*

4.7 Summary

Different strategies were carried out in order to improve the performance of P3HT:IC₇₀BA-based solar cells; these are employing different solvents and their co-solvents, preparing different active layer concentrations, selecting the optimum annealing temperature, selecting the optimum post-annealing treatments for the optimum combined devices and finally, investigating the influence of LiF as buffer layer. Firstly, the morphology and crystallinity of polymer blends have presented significant improvement when using DCB solvent. OSCs devices produced with DCB solvent has demonstrated a noticeable increase in photovoltaic performance with improved PCE from 1.5% in the CB-based device to 2.8% in DCB-based device. Using the optimum solvent (DCB), P3HT:IC₇₀BA solar cells were fabricated with different active layer concentrations. The PV performance was evaluated for these devices as a function of the active layer concentration and a maximum *PCE* of 3.5% was recorded for the devices with 17:17 mg/mL active layer concentration. In addition, OSCs with different annealing temperature have been investigated using the optimum solvent (DCB) and the optimum active layer concentration (17:17mg/mL). The main purpose was to improve the current density. Optimum device performance was associated with 150 °C as *PCE* of 3.5% and *FF* of 51% have been obtained for such annealing temperature with *J*_{sc} and *V*_{oc} of 15 mA.cm⁻² and 0.46V, respectively. The effect of post- annealing time at 150 °C (at different times in the range 10 *minutes* - 50 *minutes*) was also been investigated using the above-mentioned parameters. The annealing time has shown to result in significant impact on the morphology of the BHJ films. Samples with annealing for 20 minutes have exhibited significantly improved PV performance with *PCE* reaching 4.7%, and *FF* approaching 53%. Furthermore, the influence of using LiF as electron collecting buffer layer has been investigated and showed significant results with high *PCE* of 5.5% which is similar to what the manufacturer indicated and a remarkable improvement in the open-circuit voltage from 0.43V to 0.79V. All parameters values for devices under previous conditions are summarized in Table 4.21.

Electrical properties									
Devices	Dark		Light		J_{sc} (mA.cm ⁻²)	V_{oc} (V)	FF (%)	η (%)	Ideality factor n
	R_{sh} (Ω)	R_s (Ω)	R_{sh} (Ω)	R_s (Ω)					
Different Solvents									
CB	3878	10.7	870	8.5	10.3	0.33	45	1.5	2
DCB	30000	7.6	952	7	17.04	0.33	55	2.8	1.5
Mix	12600	8.8	769	8.8	11.8	0.31	50	1.86	1.9
Different Concentrations									
10:10	30000	7.6	952	8	17.04	0.33	55	2.8	1.5
17:17	60000	4	1200	3	15	0.46	49	3.5	1.35
25:25	1200	8	255	22	4	0.42	40	0.85	1.9
15:20	3700	6	728	15	11	0.44	44	2.5	1.6
20:15	4000	5.5	500	12	19	0.43	42	3.3	1.45
Different Annealing Temperatures									
150	60000	4	1200	3	15	0.46	51	3.5	1.2
175	8300	7	286	4.5	17	0.39	48	3.2	1.5
200	2600	11	333	4	12.6	0.47	45	2.7	1.79
Different Annealing Times									
10	60000	4	1200	3	15	0.46	51	3.5	1.2
20	75000	2	3000	3	21.2	0.43	53	4.7	1.05
30	2000	12	600	15	22.8	0.45	38	3.9	1.35
40	6000	9	700	9	8	0.43	52	1.8	1.73
50	6000	7	1000	6	4	0.41	51	0.9	1.96
The Buffer Layer									
LiF	120000	4	2500	1.3	12.5	0.79	56	5.5	1.9

Figure 4.35: Power curve of IC₇₀BA bulk device with and without LiF layer.

References:

- [1] V. D. Mihailetschi *et al.*, “Origin of the enhanced performance in poly(3-hexylthiophene): [6,6]-phenyl C61-butyric acid methyl ester solar cells upon slow drying of the active layer,” *Appl. Phys. Lett.*, vol. 89, no. 1, pp. 6–9, **2006**.
- [2] F. Zhang *et al.*, “Influence of solvent mixing on the morphology and performance of solar cells based on polyfluorene copolymer/fullerene blends,” *Adv. Funct. Mater.*, vol. 16, no. 5, pp. 667–674, **2006**.
- [3] T. L. Benanti and D. Venkataraman, “Organic solar cells: An overview focusing on active layer morphology,” *Photosynth. Res.*, vol. 87, no. 1, pp. 73–81, **2006**.
- [4] T. M. Alshahrani, “Advanced Materials for Organic Solar Cells : Influence of Generation and pH on PAMAM-Based Devices By,” Bangor University, **2016**.
- [5] Y. Sun, J. G. Liu, Y. Ding, and Y. C. Han, “Controlling the surface composition of PCBM in P3HT/PCBM blend films by using mixed solvents with different evaporation rates,” *Chinese J. Polym. Sci. (English Ed.)*, vol. 31, no. 7, pp. 1029–1037, **2013**.
- [6] I. Botiz and N. Stingelin, “Influence of molecular conformations and microstructure on the optoelectronic properties of conjugated polymers,” *Materials (Basel)*, vol. 7, no. 3, pp. 2273–2300, **2014**.
- [7] C. Musumeci, A. Liscio, V. Palermo, and P. Samorì, “Electronic characterization of supramolecular materials at the nanoscale by Conductive Atomic Force and Kelvin Probe Force microscopies,” *Mater. Today*, vol. 17, no. 10, pp. 504–517, **2014**.
- [8] E. A. Parlak, “The blend ratio effect on the photovoltaic performance and stability of poly (3-hexylthiophene):[6,6]-phenyl-C 61 butyric acid methyl ester (PCBM) and poly(3-octylthiophene):PCBM solar cells,” *Sol. Energy Mater. Sol. Cells*, vol. 100, pp. 174–184, **2012**.
- [9] R. Bkakri, O. E. Kusmartseva, F. V. Kusmartsev, M. Song, and A. Bouazizi, “Degree of phase separation effects on the charge transfer properties of P3HT:Graphene nanocomposites,” *J. Lumin.*, vol. 161, pp. 264–270, **2015**.
- [10] I. Etxebarria, J. Ajuria, and R. Pacios, “Solution-processable polymeric solar cells: A review on materials, strategies and cell architectures to overcome 10%,” *Org. Electron.*, vol. 19, pp. 34–60, **2015**.

- [11] B. Y. Kadem, "P3HT:PCBM-based organic solar cells: optimisation of active layer nanostructure and interface properties," Sheffield Hallam University, **2017**.
- [12] J. Roncali, "Molecular Engineering of the Band Gap of p -Conjugated Systems : Facing Technological Applications," pp. 1761–1775, **2007**.
- [13] B. Minnaert and M. Burgelman, "Efficiency Potential of Organic Bulk Heterojunction Solar Cells," pp. 741–748, **2007**.
- [14] J. Lu, Y. Yao, P. M. Shenai, and Y. Zhao, "of low band gap polymers by tuning the structure," vol. 1, pp. 9541–9551, **2015**.
- [15] J. M. Nunzi, "Organic photovoltaic materials and devices," *Comptes Rendus Phys.*, vol. 3, no. 4, pp. 523–542, **2002**.
- [16] V. Coropceanu, J. Cornil, D. A. da Silva Filho, Y. Olivier, R. Silbey, and J. L. Brédas, "Charge transport in organic semiconductors," *Chem. Rev.*, vol. 107, no. 4, pp. 926–952, **2007**.
- [17] G. Sadashivappa and N. P. Sharvari, "Nanoantenna – A Review," *Int. J. Renew. Energy Techilogy Res.*, vol. 4, no. 1, pp. 1–9, **2015**.
- [18] S. Naz, S. K. Durrani, M. Mehmood, and M. Nadeem, "Hydrothermal synthesis, structural and impedance studies of nanocrystalline zinc chromite spinel oxide material Studies of nanocrystalline zinc chromite spinel oxide material," *J. Saudi Chem. Soc.*, vol. 20, no. 5, pp. 585–593, **2016**.
- [19] S. Calnan, "Applications of oxide coatings in photovoltaic devices," *Coatings*, vol. 4, no. 1, pp. 162–202, **2014**.
- [20] R. Das and S. Pandey, "Comparison of Optical Properties of Bulk and Nano Crystalline Thin Films of CdS Using Different Precursors," *Int. J. Mater. Sci.*, vol. 1, no. March, pp. 35–40, **2011**.
- [21] Y. Shen, K. Li, N. Majumdar, J. C. Campbell, and M. C. Gupta, "Bulk and contact resistance in P3HT:PCBM heterojunction solar cells," *Sol. Energy Mater. Sol. Cells*, vol. 95, no. 8, pp. 2314–2317, **2011**.
- [22] Y. Zhou, T. M. Khan, J. W. Shim, A. Dindar, C. Fuentes-Hernandez, and B. Kippelen, "All-plastic solar cells with a high photovoltaic dynamic range," *J. Mater. Chem. A*, vol. 2, no. 10, pp. 3492–3497, **2014**.

- [23] C. M. Proctor and T. Q. Nguyen, “Effect of leakage current and shunt resistance on the light intensity dependence of organic solar cells,” *Appl. Phys. Lett.*, vol. 106, no. 8, **2015**.
- [24] W. Ma, C. Yang, X. Gong, K. Lee, and A. J. Heeger, “Thermally stable, efficient polymer solar cells with nanoscale control of the interpenetrating network morphology,” *Adv. Funct. Mater.*, vol. 15, no. 10, pp. 1617–1622, **2005**.
- [25] G. Li, V. Shrotriya, Y. Yao, and Y. Yang, “Investigation of annealing effects and film thickness dependence of polymer solar cells based on poly(3-hexylthiophene),” *J. Appl. Phys.*, vol. 98, no. 4, pp. 1–6, **2005**.
- [26] A. Guerrero *et al.*, “How the Charge-Neutrality Level of Interface States Controls Energy Level Alignment in Cathode Contacts of Organic Bulk-Heterojunction Solar Cells,” *ACS Nano*, vol. 6, no. 4, pp. 3453–3460, Apr. **2012**.
- [27] Y. Yang, “High-efficiency solution processable self-organization of polymer blends,” vol. 4, no. November, pp. 2–6, **2005**.
- [28] M. Thambidurai *et al.*, “Enhanced photovoltaic performance of inverted organic solar cells with In-doped ZnO as an electron extraction layer,” *Renew. Energy*, vol. 66, pp. 433–442, **2014**.
- [29] B. Kim, B. Ma, V. R. Donuru, H. Liu, and J. M. J. Fréchet, “Bodipy-backboned polymers as electron donor in bulk heterojunction solar cells,” *Chem. Commun.*, vol. 46, no. 23, pp. 4148–4150, **2010**.
- [30] N. C. Nicolaidis, B. S. Routley, J. L. Holdsworth, W. J. Belcher, X. Zhou, and P. C. Dastoor, “Fullerene contribution to photocurrent generation in organic photovoltaic cells,” *J. Phys. Chem. C*, vol. 115, no. 15, pp. 7801–7805, **2011**.
- [31] F. Zhang *et al.*, “Influence of PC60BM or PC70BM as electron acceptor on the performance of polymer solar cells,” *Sol. Energy Mater. Sol. Cells*, vol. 97, pp. 71–77, **2012**.
- [32] B. Y. Finck and B. J. Schwartz, “Understanding the origin of the S-curve in conjugated polymer/fullerene photovoltaics from drift-diffusion simulations,” *Appl. Phys. Lett.*, vol. 103, no. 5, pp. 1–4, **2013**.
- [33] M. H. Jao, H. C. Liao, and W. F. Su, “Achieving a high fill factor for organic solar cells,” *J. Mater. Chem. A*, vol. 4, no. 16, pp. 5784–5801, **2016**.

- [34] T. Kirchartz, F. Deledalle, P. S. Tuladhar, J. R. Durrant, and J. Nelson, “On the Differences between Dark and Light Ideality Factor in Polymer: Fullerene Solar Cells BT - The Journal of Physical Chemistry Letters,” *J. Phys. Chem. Lett.*, vol. 4, no. 14, pp. 2371–2376, **2013**.
- [35] G. A. H. Wetzelaer, M. Kuik, M. Lenes, and P. W. M. Blom, “Origin of the dark-current ideality factor in polymer:fullerene bulk heterojunction solar cells,” *Appl. Phys. Lett.*, vol. 99, no. 15, pp. 5–8, **2011**.
- [36] W. Tress, M. Yavari, K. Domanski, and P. Yadav, “Correction: Interpretation and evolution of open-circuit voltage, recombination, ideality factor and subgap defect states during reversible light-soaking and irreversible degradation of perovskite solar cells (Energy and Environmental Science (2018) 11 (1,” *Energy Environ. Sci.*, vol. 11, no. 3, p. 715, **2018**.
- [37] T. Kirchartz, B. E. Pieters, J. Kirkpatrick, U. Rau, and J. Nelson, “Recombination via tail states in polythiophene:fullerene solar cells,” *Phys. Rev. B - Condens. Matter Mater. Phys.*, vol. 83, no. 11, pp. 1–13, **2011**.
- [38] C. Deibel and A. Wagenpfahl, “Comment on ‘Interface state recombination in organic solar cells,’” *Phys. Rev. B - Condens. Matter Mater. Phys.*, vol. 82, no. 20, **2010**.
- [39] D. Bartsaghi *et al.*, “Competition between recombination and extraction of free charges determines the fill factor of organic solar cells,” *Nat. Commun.*, vol. 6, no. May, pp. 2–11, **2015**.
- [40] N. Abu-Zahra and M. Algazzar, “Effect of crystallinity on the performance of P3HT/PC70BM/n-dodecylthiol polymer solar cells,” *J. Sol. Energy Eng. Trans. ASME*, vol. 136, no. 2, **2014**.
- [41] D. Ghoneim, K. H. Marzouk, N. A. Mohsen, and A. M. A. Mahmoud, “Chalcogenide Letters EFFECT OF ANNEALING ON THE ELECTRICAL AND OPTICAL PROPERTIES OF Cu₅Ga₃₃Te₆₂ THIN FILM,” vol. 7, no. 5, pp. 307–316, **2010**.
- [42] J. A. Bartelt *et al.*, “The importance of fullerene percolation in the mixed regions of polymer-fullerene bulk heterojunction solar cells,” *Adv. Energy Mater.*, vol. 3, no. 3, pp. 364–374, **2013**.
- [43] H. Bronstein *et al.*, “Thieno[3,2- b]thiophene-diketopyrrolopyrrole-containing polymers for high-performance organic field-effect transistors and organic photovoltaic devices,” *J. Am. Chem. Soc.*, vol. 133, no. 10, pp. 3272–3275, **2011**.

- [44] M. T. Dang and J. D. Wuest, “Using volatile additives to alter the morphology and performance of active layers in thin-film molecular photovoltaic devices incorporating bulk heterojunctions,” *Chem. Soc. Rev.*, vol. 42, no. 23, pp. 9105–9126, **2013**.
- [45] X. Fan, S. Li, S. Guo, and G. Fang, “Understanding the phase separation evolution in efficient P3HT:IC 70BA-based bulk-heterojunction polymer solar cells,” *J. Phys. D: Appl. Phys.*, vol. 46, no. 5, **2013**.
- [46] V. Turkovic *et al.*, “Multiple stress degradation analysis of the active layer in organic photovoltaics,” *Sol. Energy Mater. Sol. Cells*, vol. 120, no. PART B, pp. 654–668, **2014**.
- [47] Y. Y. Lai, Y. J. Cheng, and C. S. Hsu, “Applications of functional fullerene materials in polymer solar cells,” *Energy Environ. Sci.*, vol. 7, no. 6, pp. 1866–1883, **2014**.
- [48] Y. Zhu *et al.*, “Improving the charge carrier transport and suppressing recombination of soluble squaraine-based solar cells via parallel-like structure,” *Materials (Basel)*, vol. 11, no. 5, **2018**.
- [49] N. Li, B. E. Lassiter, R. R. Lunt, G. Wei, and S. R. Forrest, “Open circuit voltage enhancement due to reduced dark current in small molecule photovoltaic cells,” *Appl. Phys. Lett.*, vol. 94, no. 2, pp. 29–31, **2009**.
- [50] L. Duan *et al.*, “Relationship between the diode ideality factor and the carrier recombination resistance in organic solar cells,” *IEEE J. Photovoltaics*, vol. 8, no. 6, pp. 1701–1709, 2018.
- [51] W. Tress *et al.*, “Interpretation and evolution of open-circuit voltage, recombination, ideality factor and subgap defect states during reversible light-soaking and irreversible degradation of perovskite solar cells,” *Energy Environ. Sci.*, vol. 11, no. 1, pp. 151–165, **2018**.
- [52] B. Ray, P. R. Nair, and M. A. Alam, “Annealing dependent performance of organic bulk-heterojunction solar cells: A theoretical perspective,” *Sol. Energy Mater. Sol. Cells*, vol. 95, no. 12, pp. 3287–3294, **2011**.
- [53] B. Xu, G. Sai-Anand, A. I. Gopalan, Q. Qiao, and S. W. Kang, “Improving photovoltaic properties of P3HT:IC60BA through the incorporation of small molecules,” *Polymers (Basel)*, vol. 10, no. 2, pp. 1–10, **2018**.
- [54] B. Kadem and A. Hassan, “The Effect of Fullerene Derivatives Ratio on P3HT-based Organic Solar Cells The effect of fullerene derivatives ratio on P3HT-based organic solar cells,” pp. 439–445, **2015**.

- [55] Y. Shen, K. Li, N. Majumdar, J. C. Campbell, and M. C. Gupta, “Solar Energy Materials & Solar Cells Bulk and contact resistance in P3HT : PCBM heterojunction solar cells,” *Sol. Energy Mater. Sol. Cells*, vol. 95, no. 8, pp. 2314–2317, **2011**.
- [56] H. Bayhan and M. Bayhan, “A simple approach to determine the solar cell diode ideality factor under illumination,” *Sol. Energy*, vol. 85, no. 5, pp. 769–775, **2011**.
- [57] L. Lv *et al.*, “Self-assembled TiO₂ nanorods as electron extraction layer for high-performance inverted polymer solar cells,” *Chem. Mater.*, vol. 27, no. 1, pp. 44–52, **2015**.
- [58] H. W. Ro *et al.*, “Poly(3-hexylthiophene) and [6,6]-phenyl-C 61-butyric acid methyl ester mixing in organic solar cells,” *Macromolecules*, vol. 45, no. 16, pp. 6587–6599, **2012**.
- [59] X. Liu, L. J. Guo, and Y. Zheng, “5-nm LiF as an Efficient Cathode Buffer Layer in Polymer Solar Cells Through Simply Introducing a C60 Interlayer,” *Nanoscale Res. Lett.*, vol. 12, pp. 1–7, **2017**.
- [60] X. Jing, D. Zhenbo, L. Chunjun, X. Denghui, X. Ying, and G. Dong, “Effect of LiF buffer layer on the performance of organic electroluminescent devices,” *Phys. E Low-Dimensional Syst. Nanostructures*, vol. 28, no. 3, pp. 323–327, **2005**.
- [61] A. Mahmud *et al.*, “Solar Energy Materials and Solar Cells,” vol. 167, no. April, pp. 70–86, **2017**.
- [62] D. Huang, Y. Li, Z. Xu, S. Zhao, and J. Zhao, “Enhanced performance and morphological evolution of PTB7 : PC 71 BM polymer solar cells by using solvent mixtures with different additives,” pp. 8053–8060, **2015**.
- [63] L. Duan and A. Uddin, “Progress in Stability of Organic Solar Cells,” vol. 1903259, 2020.
- [64] E. L. Meyer, “Extraction of Saturation Current and Ideality Factor from Measuring Voc and Isc of Photovoltaic Modules,” *Int. J. Photoenergy*, vol. 2017, **2017**.
- [65] G. A. H. Wetzelaer, M. Kuik, M. Lenes, and P. W. M. Blom, “Origin of the dark-current ideality factor in polymer:fullerene bulk heterojunction solar cells,” *Appl. Phys. Lett.*, vol. 99, no. 15, **2011**.
- [66] H. Hu *et al.*, “Highly Efficient Reproducible Perovskite Solar Cells Prepared by Low-Temperature Processing,” no. April, **2016**.
- [67] F. Cheng *et al.*, “Solar Energy Materials & Solar Cells Enhancing the performance of P3HT : ICBA based polymer solar cells using LiF as electron collecting buffer layer and UV – ozone treated MoO₃ as hole collecting buffer layer,” *Sol. Energy Mater. Sol. Cells*,

- vol. 110, pp. 63–68, **2013**.
- [68] J. C. Phys, “First-principles theoretical study of interfaces : Origin of the interfacial dipole,” vol. 244704, no. February 2008, **2010**.
- [69] M. J. Å, K. Norrman, and F. C. Krebs, “Stability / degradation of polymer solar cells,” vol. 92, pp. 686–714, **2008**.

Chapter 5

Improved OSC performance by modified hole transport layer using different metal salts

5.1 Introduction

Despite the ongoing technological developments humankind experienced during the past decades, the challenge of energy shortages and environmental pollution seem to be two of the most predominant challenges humanity has faced. Alternative energy sources are highly required, due to the humankind's continuously increasing demand for energy. Although conventional energy sources are continuously satisfying the ongoing demand, such conventional sources contribute negatively towards the environment. As a result, solar cells have been the focus in many intensive studies as an alternative energy source that could satisfy humanity's request for energy, whilst being environmentally friendly. Thus, over the past years, remarkable progress has been witnessed in both solar energy's market growth and experimental research [1- 4].

Despite providing a lower power conversion energy (PCE), organic solar cells (OSCs) during the past two decades have received global attention, due of their potential benefits [5-7]. Such benefits include low cost, mechanically flexible, lightweight and being compatibility to be processed using roll-to-roll printing [8]. Excellent photovoltaic materials used in OSCs are indene-C70 bisadduct (IC₇₀BA) and poly(3-hexylthiophene) (P3HT), where both materials can theoretically gain a high fill factor (*FF*) and high open-circuit voltage (*V_{oc}*) [9-11].

One of the most commonly known conductive polymer is Poly(3,4-ethylenedioxythiophene):poly(styrenesulfonate) which abbreviated as PEDOT:PSS [12]. The importance of this material is due to its visible range optical transparency, high mechanical flexibility, work function, tunnelable electrical conductivity cost-effectiveness etc., which allowed PEDOT:PSS to be used for the fabrication of (OSCs), displays, transistors, and various sensing electronics, including biosensors, pressure, temperature, humidity and strain sensors [13-14]. The electrical conductivity (σ) of PEDOT:PSS films is known to be not more than 1.0 S.cm⁻¹ [15-17]. However, dramatically improved electrical conductivity values reaching 4000 S.cm⁻¹ can be

obtained, utilizing modified films of PEDOT:PSS through the doping of polar solvents, [18] strong acids, and ionic liquids [19-21].

In OSCs, an interface layer referred to as the Hole Transport Layer (HTL), is inserted between the anode electrode and the active layer, to improve the extraction and collection of charge carriers, in addition to enhancing the device's stability and performance [22]. Due to its aforementioned properties, PEDOT:PSS is one of the commonly used materials in replacing inorganic HTLs. Additionally, spin coating deposition of PEDOT:PSS dispersed in water can produce highly conductive transparent films with ease, allowing low sheet resistance films [23]. It is actively used in plastic electronic applications such as OLEDs, flexible photovoltaic (PVs) devices, memories, and sensors [22].

To improve the performance of PV devices, it is necessary to intentionally dope the materials used [24-25]. Such improvements are important for space charge layer generation in p-n junctions and for tunneling contacts with efficient carrier injection [26-27]. Various studies have demonstrated multiple achievements with efficiency improvements [28-29]. The number of charge carriers could also be increased (both holes and electrons), allowing a higher conductivity, which is crucial in lowering contact losses [30-31]. Up to now, there have been several actions that can successfully modify the properties of a PEDOT:PSS layer, which involves the use of various organic solvents. Such solvents are dimethylsulfoxide, ethanol, tetra-hydrofuran and acetonitrile, which have effectively demonstrated improvement in the conductivity of PEDOT:PSS layers [32]. An alternative method was studied by Ouyang, where the effect of different salts on PEDOT:PSS was investigated. This study showed that metal salts employed as dopants within aqueous PEDOT:PSS effectively enhanced the conductivity, which is due to metal ions binding to the PSS anions of the PEDOT:PSS layer. Thus, this study investigates the impact of metal salts on PEDOT:PSS, in order to improve the properties of PEDOT:PSS for an enhanced performance in HTL.

5.2 Fabrication process

PEDOT:PSS (conductive grade-483095 purchased from Aldrich) were mixed with different metal salts; Copper Chloride (CuCl_2 99.99%) and Lithium Chloride (LiCl 99.99%) (Sigma Aldrich) as powder. To prepare the salts aqueous solutions, 2 mg of each metal salt was added to 6 ml of deionized (DI) water separately. In order to examine the role of dopant concentration, different salt concentrations were added to 1 ml of PEDOT:PSS, separately. For example, 0.1, 0.2 and 0.4 ml of LiCl were added to 1 ml of PEDOT:PSS to prepare LiCl 0.1, LiCl 0.2 and LiCl 0.4 solutions, respectively. The solutions were then sonicated for 30 minutes before mixing with PEDOT:PSS to remove any aggregates. The final solutions were also sonicated for 45 minutes to ensure good dispersion and complete solubility of the salts.

The organic photovoltaic devices depicted schematically in Figure 5.1, were fabricated by spin coating of doped PEDOT-PSS onto clean ITO-coated glass substrates. The substrates were thoroughly cleaned using DI water, acetone, and iso-propanol for 10 minutes each in an ultrasonic bath, respectively, and then dried with dry N_2 gas. All cleaned substrates were treated with O_2 plasma treatment for 20 minutes. Doped PEDOT:PSS was spin-coated at a spin speed of 4000 rpm for 40 seconds and annealed on a hot plate at 150°C for 30 minutes in ambient air. P3HT:IC₇₀BA active layer (17 mg.ml^{-1}) was dissolved in dichlorobenzene (DCB) with the ratio 1:1. The active layer was spin-coated with a spin speed of 600 rpm inside a nitrogen-filled glove box, followed by annealing inside the glove box at 150°C for 20 minutes. The active layer thickness was estimated to be 100 nm using Dektak Stylus Profilometer. Then, the samples were immediately placed in the evaporator to deposit Lithium Fluoride (LiF) with thickness equals 0.75 nm. A top contact of Aluminium (Al) was thermally evaporated through a shadow mask with a thickness of 100 nm. The deposited Al electrode area defines the active area of the devices as 0.125 cm^2 . All the devices were subjected to further heat treatment inside the glove box at 150°C for 20 minutes and left to cool down for 30 minutes before measurements were carried out.

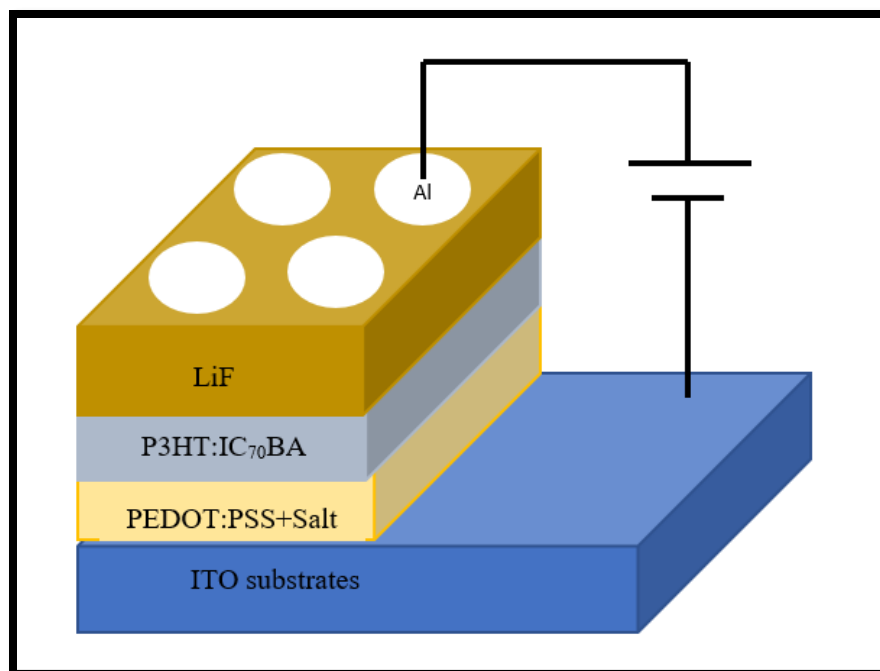


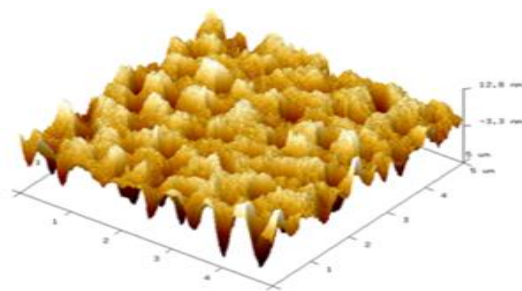
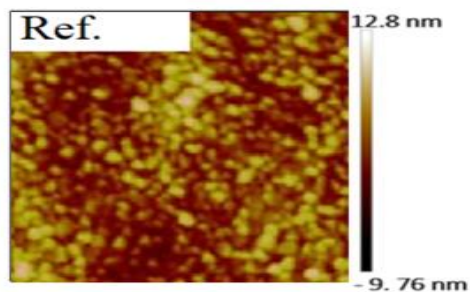
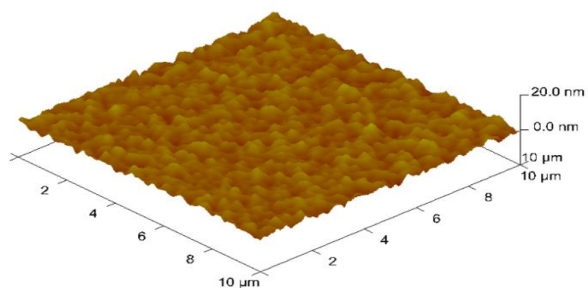
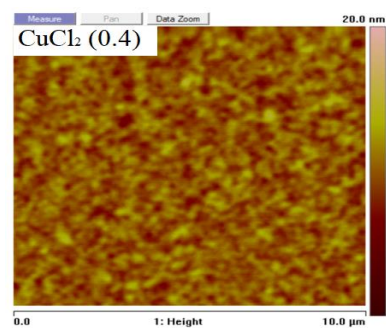
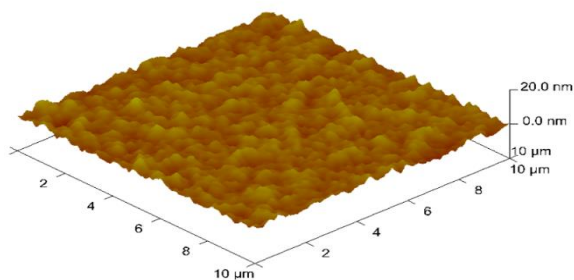
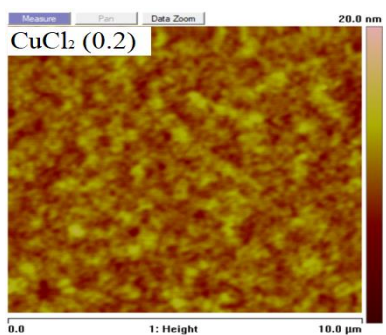
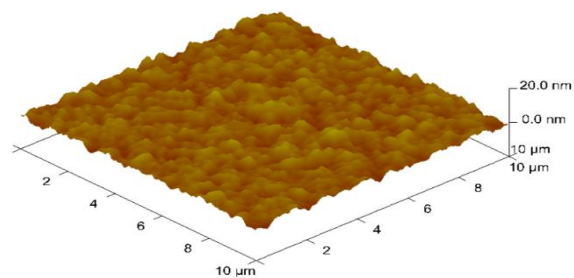
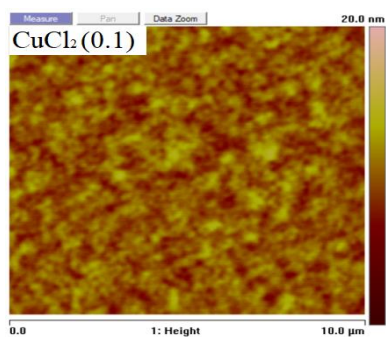
Figure 5.1: *Structural formula of P3HT:IC₇₀BA photovoltaic device.*

5.3 Morphological analysis using AFM

The morphology of the PEDOT:PSS films treated with different metal salts in aqueous solution forms were investigated using AFM techniques. The characterization of surface roughness parameters is very powerful for many essential problems, such as contact deformation, fraction, tightness etc., [33]. Figure 5.2 shows the AFM images of the PEDOT:PSS films treated with different metal salts in aqueous solution forms. As can be seen, an increase in the ratio of different metal salts led to a decrease in surface roughness. It has been noticed that the correlation between the surface pore size with the surface roughness is direct. For example, the smaller surface pore size is the smoother sample roughness and vice versa [34]. It may be suggested that the metal salts with small diameters fill the gaps or holes between the protrusions of blended polymer and thus reduce the roughness of the film surface and get a good surface quality. Furthermore, the height of the grain size of the films was decreased with increasing the ratios of metal salts blended with PEDOT:PSS. This result reveals that the surface of films has a low surface roughness feature. The doped films have exhibited smooth morphologies compared to the pure PEDOT:PSS film. To investigate the effect of higher concentrations of metal salts impurities on the surface morphology

of PEDOT:PSS layer, devices with aqueous solutions with higher concentrations of the two group of salts, LiCl (0.1, 0.2 and 0.4) and CuCl₂ (0.1, 0.2 and 0.4) devices were examined as shown in Figure 5.2. Phase separation between the conductive site (PEDOT) and the insulating site (PSS) might have occurred within the PEDOT:PSS layer which results in separating both domains thus leading to a change in the PEDOT:PSS morphology [35]. The films have exhibited smoother surface with increased LiCl and CuCl₂ solution concentrations. The device with pure PEDOT:PSS film has exhibited smooth surface with rms roughness of 1.68 nm while smoother surface morphologies of 1.18 nm, 1.09 nm, and 1.08 nm for LiCl device (0.1, 0.2 and 0.4, respectively). For CuCl₂ devices (0.1, 0.2 and 0.4) group, the roughness was 1.06 nm, 1.05 nm, and 1.00 nm, respectively as listed in Table 5.1.

Generally, the brighter regions observed in the AFM image for the pure PEDOT:PSS (reference device) could be associated with the PEDOT whereas the darker regions are related to the less conductive PSS regions [36]. This improvement in the surface roughness may be ascribed to the increase in grain size after metal chloride treatment. Therefore, an improvement in the light scattering might be ascribed to such surface roughness which is thought to improve the light-harvesting by the active layer as well as decreasing the contact resistance of the interfacial layer, hence increasing the short circuit current density (J_{sc}).



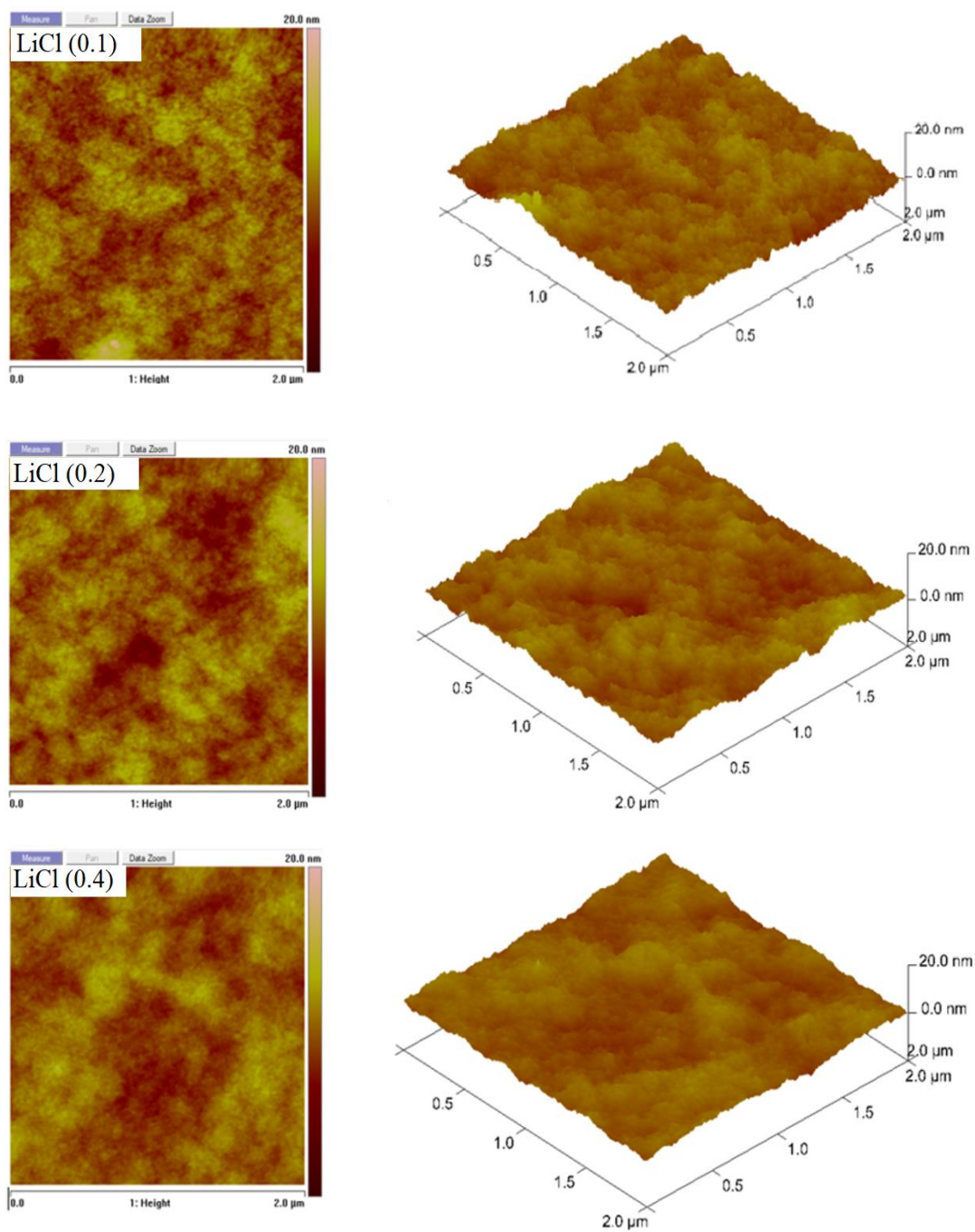


Figure 5.2: 2D and 3D AFM images and phase analysis of the *P3HT:IC₇₀BA* blends prepared by different *PEDOT:PSS* deposited by different salts concentrations.

Annealing time	Roughness (nm)
Pure PEDOT:PSS	1.68
PEDOT:PSS+LiCl (0.1)	1.18
PEDOT:PSS+LiCl (0.2)	1.09
PEDOT:PSS+LiCl (0.4)	1.08
PEDOT:PSS+CuCl ₂ (0.1)	1.06
PEDOT:PSS+CuCl ₂ (0.2)	1.05
PEDOT:PSS+CuCl ₂ (0.4)	1.00

Table 5.1: *Roughness for P3HT:IC₇₀BA based OPVs according to pure, LiCl and CuCl₂ aqueous solution treated PEDOT:PSS layers.*

5.4 Optical Absorption measurements

The UV-Vis absorption spectrum of the P3HT:IC₇₀BA based OPVs for the pure, LiCl and CuCl₂ aqueous solution treated PEDOT:PSS thin films are shown in Figure 5.3. Figure 5.3(a) presents the UV-Vis spectrum of CuCl₂ group compared to the pristine sample. At the lowest concentration of CuCl₂ (0.1), the absorption edge around 805 nm where the bandgap at this point is 1.54 eV. The peak absorption at 590 nm (2.1 eV), which has the highest absorption intensity. On the other hand, the absorption intensity decreased for CuCl₂ (0.2) device. For this thin film, the absorption edge was around 795 nm (1.56 eV) with a peak absorption as same as CuCl₂ (0.1) device at 590 nm (2.1 eV). Finally, for the highest concentration of CuCl₂ (0.4) devices, the absorption edge of was around 775 nm where the bandgap at this point 1.60 eV. The peak absorption at 590 nm (2.1 eV), has the lowest absorption intensity of these thin films group.

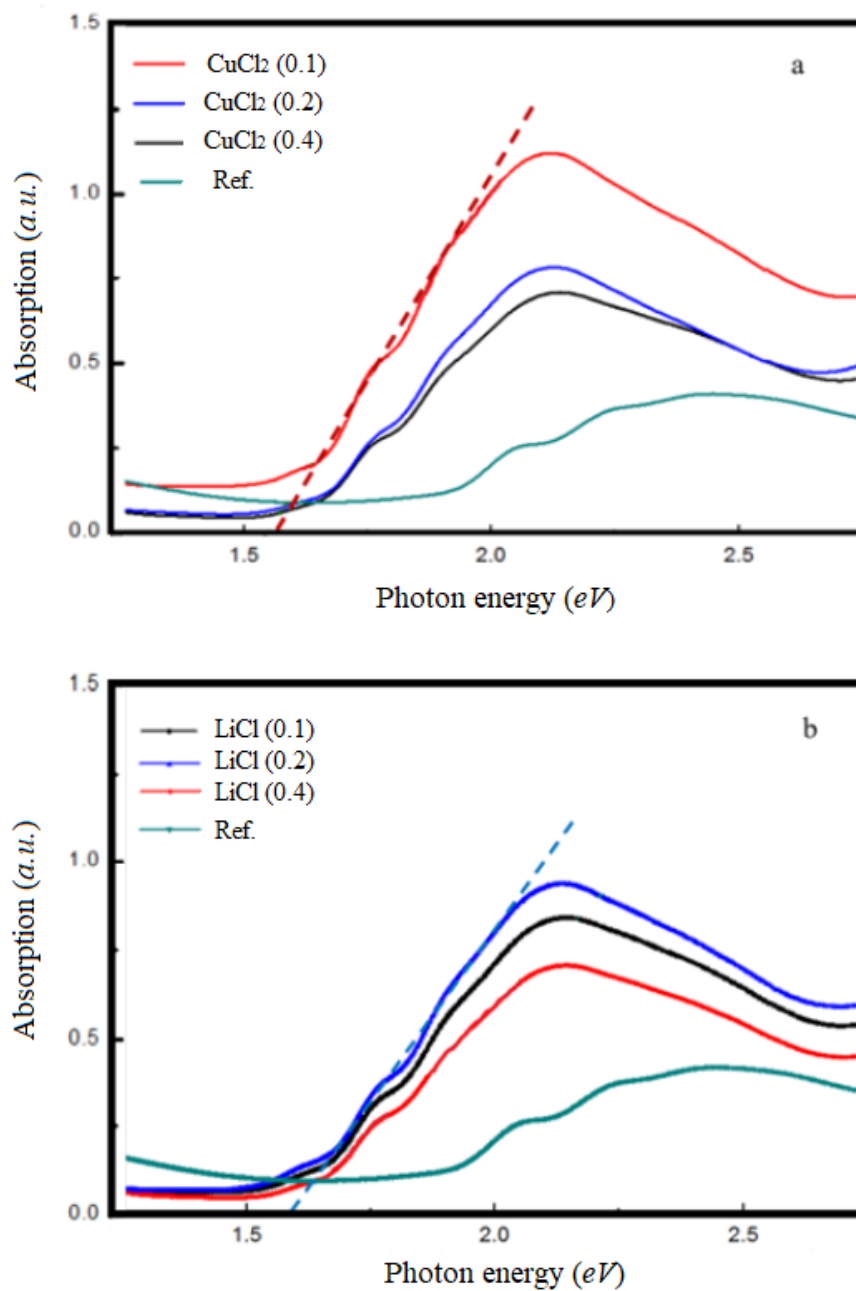


Figure 5.3: Absorption spectra of PEDOT:PSS films on treatment with different concentrations of (A) CuCl₂ and (B) LiCl.

For the LiCl devices and as shown in Figure 5.3 (b), the highest absorption intensity is for LiCl (0.2) device with the absorption edge around 805 nm where the bandgap at this point is 1.54 eV. The peak absorption at 590 nm (2.1 eV). However, the absorption intensity decreased to be the lowest for the highest concentration of LiCl salt which is LiCl (0.4) device. For this thin film, the absorption edge was around 790 nm, with a bandgap of (1.57 eV) and with a peak absorption at 590 nm (2.1 eV). Finally, the lowest concentration of LiCl devices is LiCl (0.1) device, the absorption edge of which is around 800 nm where the bandgap at this point 1.55 eV. The peak absorption at 590 nm (2.1 eV), which has the lowest absorption intensity of these thin films group. The values of bandgaps are listed in Table 5.2.

The absorption spectra of metal salts treated PEDOT:PSS films have exhibited higher absorption as compared to pure PEDOT:PSS films. In both groups, the metal chloride treated PEDOT:PSS layers have been found to have a great benefit for solar cells specifically for materials employed as a window layer. The maximum absorption of pure PEDOT:PSS film was in within the wavelength range (400–650 nm), while absorption of salts treated-PEDOT:PSS films has increased for both groups of salts. Moreover, a decrease in the salt's concentration has led to further improvement in the absorption of thin films. It has been reported that PEDOT:PSS layer has higher absorption coefficient in the NIR region of the spectra, while has a small absorption coefficient in the UV and visible regions [37].

The roughness of ITO/PEDOT:PSS-salts doped surface influences light scattering; therefore, it may contribute in longer light propagation pathway within the P3HT:IC₇₀BA active layer and this may result in light trapping. Generally, light trapping occurs due to total internal absorption, surface plasmon and reflection [38]. Increasing the optical path length of a device which has 100 nm thickness by light trapping encourages the light to bounce forth and back within the cell about 50 times [39]. The light scattering and trapping within the complete device is thought to assist in increasing the current density through enhancing light-harvesting efficiency and thus improving the device efficiency, but when the surface has a high value of roughness, this results to be an obstacle of light propagation [40]. It has been reported that the roughness of the absorber layer assists the light scattering [41]. This is thought to contribute to increasing the absorption and therefore the current density, which results in improvement of OPVs performance. It has also been verified that when the polymer/fullerene active layer incorporated into a complete device which

incorporates charge transport layers on both sides of the device and an anti-reflection layer, the total absorption might be further improved by minimizing reflection losses. To enhance light propagation through the device, it could be through the reflected light from the randomly textured organometallic/metal electrode (LiF/Al) to the P3HT:IC₇₀BA active layer, where the reflected light exhibits lengthy optical path [42].

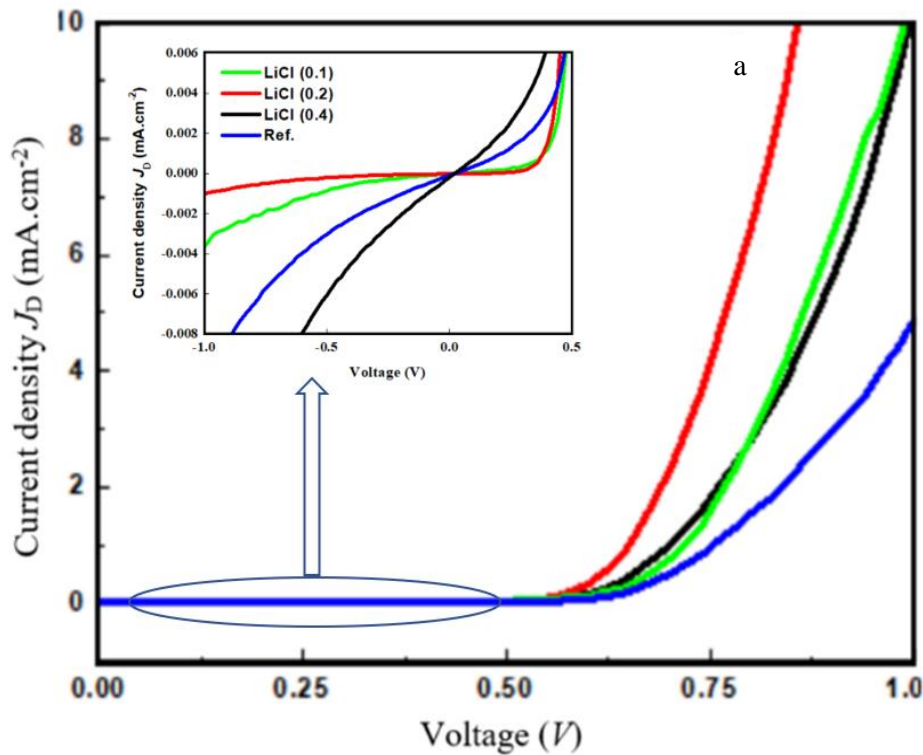
Device	Bandgap (eV)
Pure PEDOT:PSS	1.82
PEDOT:PSS+CuCl ₂ (0.1)	1.54
PEDOT:PSS+CuCl ₂ (0.2)	1.56
PEDOT:PSS+CuCl ₂ (0.4)	1.60
PEDOT:PSS+LiCl (0.1)	1.55
PEDOT:PSS+LiCl (0.2)	1.54
PEDOT:PSS+LiCl (0.4)	1.57

Table 5.2: Bandgaps for P3HT:IC₇₀BA based OPVs according to pure, LiCl and CuCl₂ treated PEDOT:PSS layers.

5.5 Electrical measurements

5.5.1 Diode measurements

Doping of PEDOT:PSS layer with different metal salts has resulted in huge decreasing of the R_s by about > 99%. The improvement in both R_s and R_{sh} could be a key factor among others towards achieving efficient electrode properties and therefore better device performance [43]. The dark J - V measurements, as shown in Figure 5.4 were carried out to determine the various electronic parameters of the studied OSC devices, including shunt resistance, series resistance and ideality factor. Modifying the hole transport layer has resulted in significant improvement in both series and shunt resistances, except for LiCl(0.4) and CuCl₂(0.4) devices, in comparison to the reference device with pure PEDOT:PSS as demonstrated in Table 5.3. As an example, devices doped with LiCl (0.2) has reduced the R_s significantly by more than 666% ($R_s = 0.006\Omega$ compare to the reference device which has $R_s = 4\Omega$). Same trend of the series resistances for all concentrations of both groups of metal salts has remained almost the same within the range ($R_s = 0.02\Omega \sim 0.006\Omega$) compare to the reference.



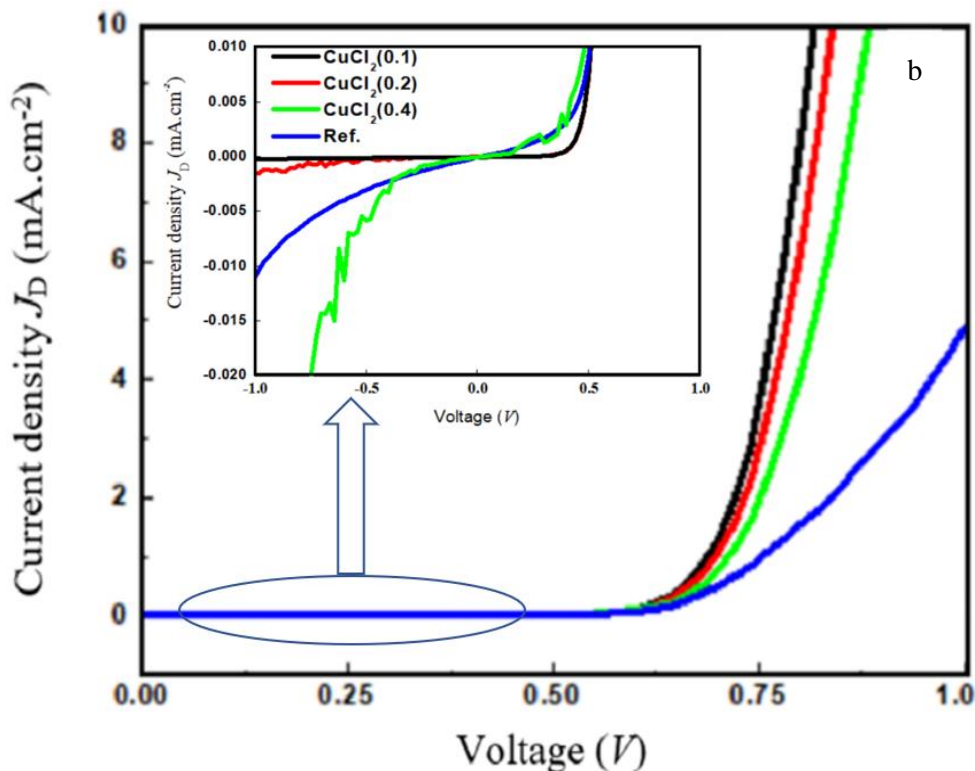


Figure 5.4: (a) J - V characteristics of the OBHJ solar cells under the dark for LiCl group devices. (b) J - V characteristics of the OBHJ solar cells under the dark for CuCl₂ group devices. Inset figures show the leakage current.

Regarding to shunt resistances, most devices show higher values compare to pure one. For instance, LiCl (0.2) device has the highest shunt resistance for all devices which is higher by more than 455% in comparison to pure device. For CuCl₂ devices, device with concentration of (0.1) has shown the highest value with 300% higher than pure one as demonstrated in Table 5.3.

Apparently to have a high FF , the R_s is expected to be as small as possible. In a practical device, R_s mostly comes from the bulk resistance of the active layer or from the contact resistance between the active layer and electrode. Incompatible band alignment can lead to a large R_s value, causing a dramatic decrease in the FF and PCE . The improved conductivity of PEDOT:PSS through doped metal salts has influenced these values of resistances.

It is beneficial to avoid the conditions leading to a decreased R_{sh} to obtain a high FF value. In most photovoltaic devices, high values of shunt resistance lead to prevent current leakage through pin holes and traps or current leakage from the edge of cells. In OPVs, due to their distinctive BHJ structure that both donor and acceptor materials have contacts with the same carrier collection electrode, one additional pathway for current leakage comes from the bimolecular recombination near the interface between the active layer and electrode. This extra pathway for current leakage must be reduced or eliminated in the OPV device [44].

Parasitic Resistances		
Device	Shunt resistance ($k\Omega$)	Series resistance (Ω)
Pure PEDOT:PSS	90	4
PEDOT:PSS+LiCl (0.1)	185	0.02
PEDOT:PSS+LiCl (0.2)	500	0.006
PEDOT:PSS+LiCl (0.4)	85	0.04
PEDOT:PSS+CuCl ₂ (0.1)	285	0.004
PEDOT:PSS+CuCl ₂ (0.2)	200	0.005
PEDOT:PSS+CuCl ₂ (0.4)	75	0.006

Table 5.3: *Diodes parasitic resistances for different solvents.*

As mentioned in chapter 2, the ideality factor is an indicator could describe the difference between the practical device and ideal device, contains critical data on the recombination and transport processes in organic solar cells. It can be independently obtained either from the slope of the exponential regime of dark J - V characteristics on a semi-logarithmic plot as it in Figure 5.5. To extract the ideality factors, the reference device has shown an ideality factor of 1.90, which has decreased using both groups of salts LiCl and CuCl₂ as an HTL. This decrease in device ideality factor is assigned to a lower recombination rate within the device. However, the lower recombination rate may be ascribed to effective charge collection from the selective electrodes by

employing efficient hole transport layers [45] and thought to contribute to the higher fill factor of the examined devices [43]. It is well known that the efficiency of charge collection before they recombine inside the active layer of the cell is represented by the solar cell FF , which in turn depends on the charge carrier recombination rate, the built in potential and the charge carrier's mobility [45]. Moreover, using different metal salts has further reduced the ideality factor to reach a value as low as 1.60 in the CuCl_2 (0.4) doped PEDOT:PSS-based device. Further decrease in the recombination rate was observed when HTL electrode has been modified with CuCl_2 (0.1) and LiCl (0.2); the ideality factor has reached a value of 1.54 which suggests that efficient charge collection has occurred within the complete device as the recombination rate has reduced and therefore high solar cell parameters are expected. It was reported that many non-interactive interfaces could form between the organic layer and the metal interface, which therefore allow the injection barrier to follow Schottky-Mott limitation [46]. The ideality factors for metal salts-doped PEDOT:PSS-based device has shown lower value compared to pure PEDOT:PSS, which suggests low recombination rate in such devices. These low values might be attributed to the low roughness and R_s values of these devices which shows clear. Table 5.4 shows the ideality factors values for both groups of devices.

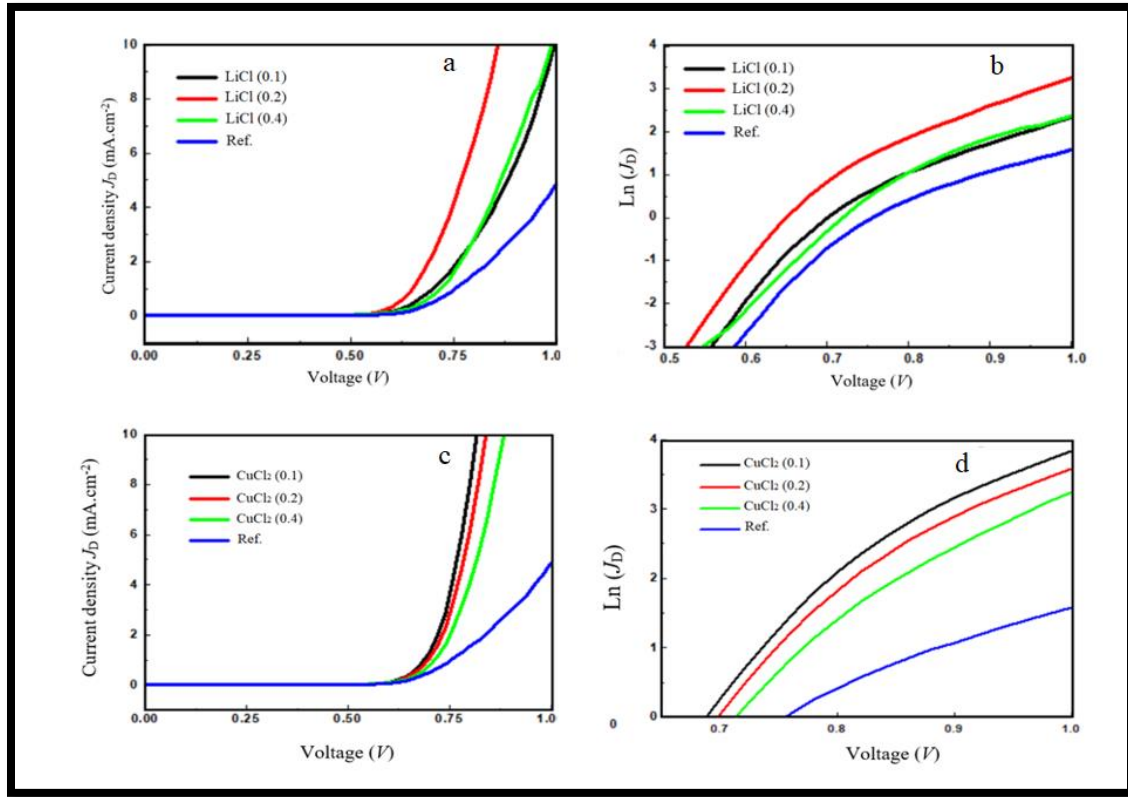


Figure 5.5: a) J - V characteristics of the OBHJ solar cells under the dark for LiCl group. b) Variation of $\ln(J_D)$ versus the bias voltage with pure PEDOT:PSS and with PEDOT:PSS+LiCl. c) J - V characteristics of the OBHJ solar cells under the dark for CuCl₂ group. d) Variation of $\ln(J_D)$ versus the bias voltage with pure PEDOT:PSS and with PEDOT:PSS+ CuCl₂.

Device	Ideality factor (n)
Pure PEDOT:PSS	1.90
PEDOT:PSS+LiCl (0.1)	1.54
PEDOT:PSS+LiCl (0.2)	1.55
PEDOT:PSS+LiCl (0.4)	1.57
PEDOT:PSS+CuCl ₂ (0.1)	1.54
PEDOT:PSS+CuCl ₂ (0.2)	1.56
PEDOT:PSS+CuCl ₂ (0.4)	1.60

Table 5.4: Ideality factors for diode devices.

5.5.2 Photovoltaic measurements

To determine the PV properties of P3HT:IC₇₀BA-based solar cells, *J-V* characteristics has been carried out under illumination in order which has undergone different groups of salts modifications, as discussed in the previous sections. Figures 5.6 (a) and 5.7(a) show the *J-V* curves of the investigated OSCs with different metal salts treated-PEDOT:PSS layers. The efficiency of devices can be obtained from the peak power curve of devices as shown in Figure 5.6(b) and Figure 5.7(b). Devices with untreated PEDOT:PSS layer (pure) have exhibited lower PV performance with $V_{oc}=0.79$ V, $J_{sc}=12.4$ mA.cm⁻², $FF=56\%$ and PCE of 5.5%. These are in line with values frequently reported in the literature [46]. However, devices having PEDOT:PSS layers doped with both groups of metal salt have demonstrated significant improvement in all PV parameters except some values of series resistances and the results summarized in Table 5.5. The highest PCE of 18.4 % and J_{sc} of 43.1 mA.cm⁻² were achieved when PEDOT:PSS layer was doped with LiCl (0.2) metal salt as shown in Figure 5.8 (b). The device FF has demonstrated slight change for all devices treated with metal salts, whereas V_{oc} in the region of 0.80 ± 0.03 V was recorded for those devices.

When the PEDOT:PSS layers were doped with the CuCl₂ metal salts with different concentrations, the highest of PCE and J_{sc} of the studied OSC devices have reached values of about 17.11% and 35.12 mA.cm⁻², respectively as shown in Figure 5.8 (a). Once again, V_{oc} and FF have remained unchanged for all metal salts studied in this work (see Table 5:5). The substantial increase in J_{sc} could be ascribed to the improved electrical conductivity of PEDOT:PSS layers as a result of metal salt treatment while the enhanced PCE could be associated with the increased film absorption and surface roughness, as discussed earlier. V_{oc} maintained its value since it is mainly determined by the difference between the lower unoccupied molecular orbital of the acceptor (LUMO acceptor) and the donor's higher occupied molecular orbital (HOMO donor) [47]. Furthermore, the metal salt treatment of PEDOT:PSS layers seems to solve the wetting problem between the active layer, which is hydrophobic in nature and the hydrophilic PEDOT:PSS [48].

For CuCl₂ devices, PCE as high as 12.65% associated with $FF=60\%$, J_{sc} of 25.36 mA.cm⁻², $V_{oc}=0.83$ V (the highest value recorded for V_{oc} for all devices), $R_{sh}=10$ k Ω and $R_s=3.28$ Ω have been recorded for CuCl₂ (0.2) devices. Treatment of PEDOT:PSS with CuCl₂ (0.4) has shown the lowest parameter's values for PCE , J_{sc} and R_s of both groups of meatal salts. The highest

concentration of CuCl_2 (0.4) has recorded a PCE of 7.10%, J_{sc} = 15.63 mA.cm^{-2} , V_{oc} = 0.79 V, FF = 58%, R_{sh} =10 $\text{k}\Omega$ and R_s = 4.4 Ω . Nevertheless, it showed significant improvement compare to fabricated device with pure PEDOT:PSS. Regarding devices which treated PEDOT:PSS with LiCl metal salt, concentrations of LiCl(0.1) and LiCl (0.4) have almost the same values for most parameters. For PCE , they recorded 12.77% and 12.72% , for J_{sc} , 31.36 and 35.76 mA.cm^{-2} and for R_{sh} , 15 and 13 $\text{k}\Omega$, respectively. While recorded same value for V_{oc} which is 0.79 V and R_s =2.1 and 4.0 Ω , respectively.

It was found that the optimization of the PEDOT:PSS layer with different treatment is one of the keys processing conditions to achieve good device performance [49-51]. It has been revealed that by adding organic compounds such as ionic liquids, high boiling point polar organic solvents and surfactants or using post-treatment of PEDOT:PSS films with organic compounds, including high-boiling point polar solvents, salts, co-solvents, organic and inorganic acids, the electrical conductivity of pure PEDOT:PSS prepared from its aqueous solution can be significantly improved [52]. As it can be noticed, the modification of hole transport layer in P3HT:IC₇₀BA-based OSC has revealed an improvement in the cells PCE as compared to device without treated HTL as shown in Figure 5.6 and Figure 5.7, with PCE reaching 5.5%, J_{sc} of 12.4 mA.cm^{-2} , FF of 55% and V_{oc} of 0.63V (see Table 5.5). The improvement of FF in both groups of metal salts has indicated a good resistances R_s and R_{sh} in the devices, which may be attributed to the acceptable molding between HTL and the active layer

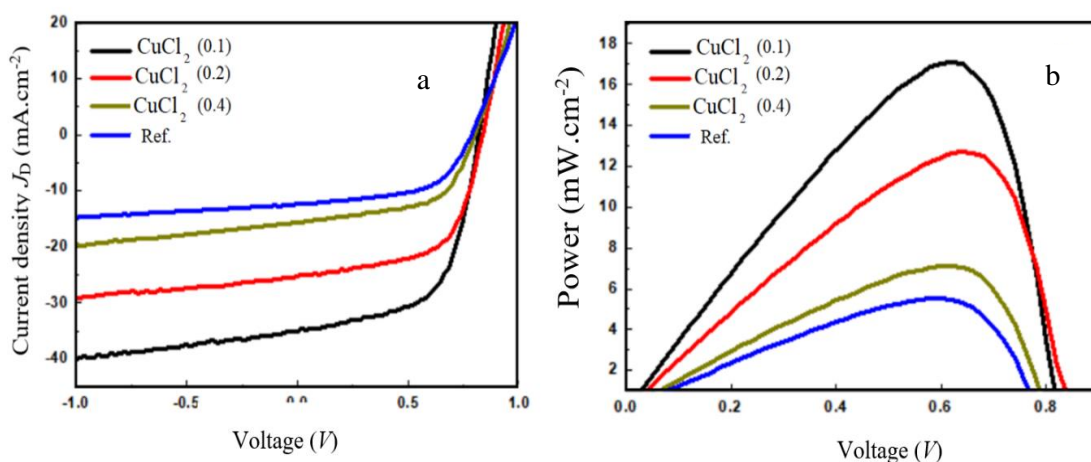


Figure 5.6: a) J - V characteristics of the for the P3HT:IC₇₀BA based devices without and with CuCl_2 metal salts treated-PEDOT:PSS layers. b) Power curves of IC₇₀BA bulk device with pure PEDOT:PSS and with PEDOT:PSS+ CuCl_2 .

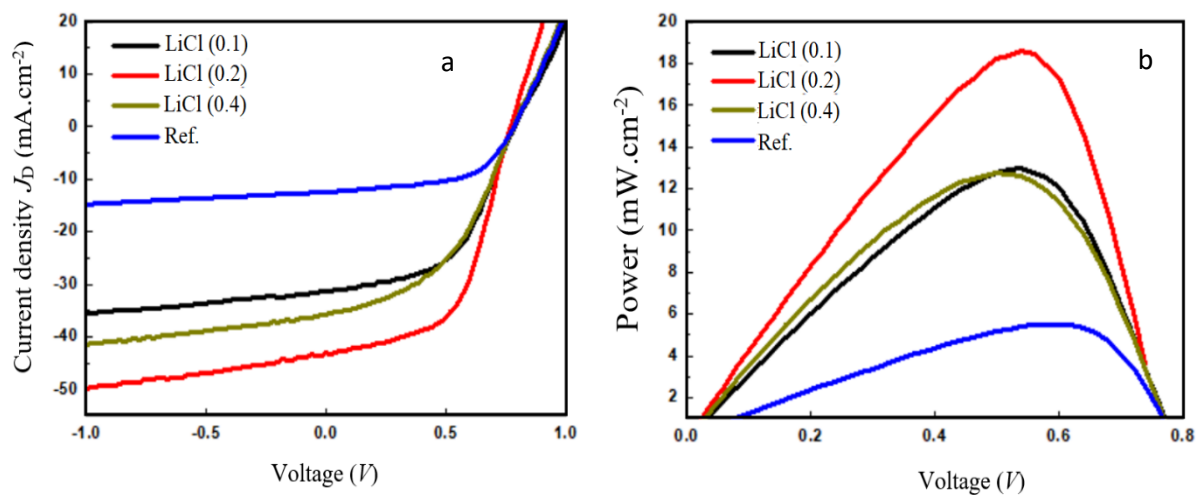


Figure 5.7: a) J - V characteristics for $P3HT: IC_{70}BA$ based devices without and with $LiCl$ metal salts treated- $PEDOT:PSS$ layers b) Power curves of $IC_{70}BA$ bulk device with pure $PEDOT:PSS$ and with $PEDOT:PSS+LiCl$.

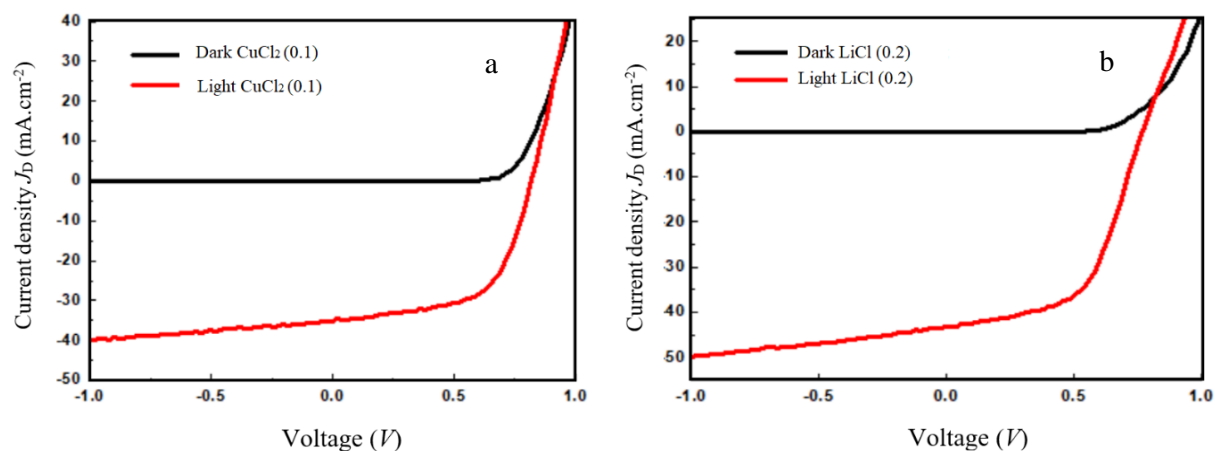


Figure 5.8: J - V characteristics of the for the $P3HT: IC_{70}BA$ based devices with a) $CuCl_2$ (0.1). b) $LiCl$ (0.2) metal salts treated- $PEDOT:PSS$ layers.

Device	J_{sc} (mA.cm ⁻²)	V_{oc} (V)	FF %	η %	R_{sh} (k Ω)	R_s (Ω)
Pure PEDOT:PSS	12.432	0.79	56	5.5	2.5	1.5
PEDOT:PSS+CuCl ₂ (0.1)	35.12	0.81	60	17.11	13	1.5
PEDOT:PSS+CuCl ₂ (0.2)	25.36	0.83	60	12.65	10	3.28
PEDOT:PSS+CuCl ₂ (0.4)	15.63	0.79	58	7.10	10	4.4
PEDOT:PSS+LiCl (0.1)	31.36	0.79	52	12.77	15	2.1
PEDOT:PSS+LiCl (0.2)	43.12	0.77	55	18.4	20	1.3
PEDOT:PSS+LiCl (0.4)	35.76	0.79	45	12.72	13	4.0

Table 5.5: The J-V characteristics for the P3HT: IC₇₀BA based devices without and with different metal salts treated-PEDOT:PSS layers.

5.6 Summary

This chapter aimed to investigate the effect of different metal salts treated-PEDOT:PSS layers on the performance of organic heterojunction solar cells. It was observed that metal salts influenced significantly the OHJ solar cells efficiency. Using PEDOT:PSS as a typical hole transport layer has shown *PCE* of 5.5%, this value has increased to 18.4 % and 17.11%, which are of the highest reported parameters for OSCs using P3HT:IC₇₀BA blend, for LiCl(0.2) device and CuCl₂(0.1) device, respectively as shown in Figure 5.8. The doped devices have shown remarkable improvement for both shunt R_{sh} and series R_s resistances in the dark and under illumination. The highest R_{sh} is recorded by LiCl (0.2) in the dark ($R_{sh} = 500 \text{ k}\Omega$) and for CuCl₂(0.1) device, the $R_{sh} = 285 \text{ k}\Omega$. For series resistances, both of salts group recorded significant improvement under the dark. Moreover, both resistances were enhanced as well with using treated PEDOT:PSS.

Generally, all parameters were improved by using both metal salts group. For example, current density has raised to 43 mA.cm^{-2} compared to reference device without modifying the PEDOT:PSS layer which is $J_{sc} = 12.43 \text{ mA.cm}^{-2}$. For open circuit voltage V_{oc} , a slight improvement and in most devices remained the same, and same trend for fill factors *FF*. Finally, surface roughness and ideality factors showed notable improvement.

References

- [1] C. Liu *et al.*, “Improving the charge carrier transport of organic solar cells by incorporating a deep energy level molecule,” *Phys. Chem. Chem. Phys.*, vol. 19, no. 1, pp. 245–250, **2017**.
- [2] Y. He, J. Quan, and G. Ouyang, “The atomistic origin of interface confinement and enhanced conversion efficiency in Si nanowire solar cells,” *Phys. Chem. Chem. Phys.*, vol. 18, no. 10, pp. 7001–7006, **2016**.
- [3] W. Ma, C. Yang, X. Gong, K. Lee, and A. J. Heeger, “Thermally stable, efficient polymer solar cells with nanoscale control of the interpenetrating network morphology,” *Adv. Funct. Mater.*, vol. 15, no. 10, pp. 1617–1622, **2005**.
- [4] K. Lee, J. Lee, B. A. Mazor, and S. R. Forrest, “Transforming the cost of solar-to-electrical energy conversion: Integrating thin-film GaAs solar cells with non-tracking mini-concentrators,” *Light Sci. Appl.*, vol. 4, no. February, pp. 1–7, **2015**.
- [5] S. Chatterjee, Y. Ie, and Y. Aso, “Naphtho[1,2- c:5,6- c']bis[1,2,5]thiadiazole-Based Nonfullerene Acceptors: Effect of Substituents on the Thiophene Unit on Properties and Photovoltaic Characteristics,” *ACS Omega*, vol. 3, no. 5, pp. 5814–5824, **2018**.
- [6] S. Günes, H. Neugebauer, and N. S. Sariciftci, “Conjugated polymer-based organic solar cells,” *Chem. Rev.*, vol. 107, no. 4, pp. 1324–1338, **2007**.
- [7] B. G. Dennler, M. C. Scharber, and C. J. Brabec, “Polymer - Fullerene Bulk - Heterojunction Solar Polymer-Fullerene Bulk-Heterojunction Solar Cells,” *Adv. Mater.*, vol. 21, pp. 1323–1338, **2015**.
- [8] G. Yu, J. Gao, J. C. Hummelen, F. Wudl, and A. J. Heeger, “Polymer Photovoltaic Cells: Enhanced Efficiencies via a Network of Internal Donor-Acceptor Heterojunctions,” *Science (80-.)*, vol. 270, no. 5243, pp. 1789–1791, **1995**.
- [9] B. Xu, G. Sai-Anand, A. I. Gopalan, Q. Qiao, and S. W. Kang, “Improving photovoltaic properties of P3HT:IC60BA through the incorporation of small molecules,” *Polymers (Basel)*, vol. 10, no. 2, pp. 1–10, **2018**.
- [10] S. Gärtner *et al.*, “Eco-Friendly Fabrication of 4% Efficient Organic Solar Cells from Surfactant-Free P3HT:ICBA Nanoparticle Dispersions,” *Adv. Mater.*, vol. 26, no. 38, pp. 6653–6657, **2014**.
- [11] Y. He *et al.*, “The role of Au nanorods in highly efficient inverted low bandgap polymer solar cells,” *Appl. Phys. Lett.*, vol. 105, no. 22, pp. 1–6, **2014**.

- [12] X. Fan *et al.*, “PEDOT:PSS for Flexible and Stretchable Electronics: Modifications, Strategies, and Applications,” *Adv. Sci.*, vol. 1900813, p. 1900813, **2019**.
- [13] C. Liao, M. Zhang, L. Niu, Z. Zheng, and F. Yan, “Highly selective and sensitive glucose sensors based on organic electrochemical transistors with graphene-modified gate electrodes,” *J. Mater. Chem. B*, vol. 1, no. 31, pp. 3820–3829, **2013**.
- [14] X. Fan, B. Xu, S. Liu, C. Cui, J. Wang, and F. Yan, “Transfer-Printed PEDOT:PSS Electrodes Using Mild Acids for High Conductivity and Improved Stability with Application to Flexible Organic Solar Cells,” *ACS Appl. Mater. Interfaces*, vol. 8, no. 22, pp. 14029–14036, **2016**.
- [15] A. W. M. Diah, J. P. Quirino, W. Belcher, and C. I. Holdsworth, “Investigation of the doping efficiency of poly(styrene sulfonic acid) in poly(3,4-ethylenedioxythiophene)/poly(styrene sulfonic acid) dispersions by capillary electrophoresis,” *Electrophoresis*, vol. 35, no. 14, pp. 1976–1983, **2014**.
- [16] Q. Jiang *et al.*, “Paper: An effective substrate for the enhancement of thermoelectric properties in PEDOT:PSS,” *J. Polym. Sci. Part B Polym. Phys.*, vol. 52, no. 11, pp. 737–742, **2014**.
- [17] B. J. Worfolk *et al.*, “Ultrahigh electrical conductivity in solution-sheared polymeric transparent films,” *Proc. Natl. Acad. Sci. U. S. A.*, vol. 112, no. 46, pp. 14138–14143, **2015**.
- [18] Y. Xia, K. Sun, and J. Ouyang, “Solution-processed metallic conducting polymer films as transparent electrode of optoelectronic devices,” *Adv. Mater.*, vol. 24, no. 18, pp. 2436–2440, **2012**.
- [19] N. Kim *et al.*, “Highly conductive PEDOT:PSS nanofibrils induced by solution-processed crystallization,” *Adv. Mater.*, vol. 26, no. 14, pp. 2268–2272, **2014**.
- [20] N. Kim, H. Kang, J. H. Lee, S. Kee, S. H. Lee, and K. Lee, “Highly conductive all-plastic electrodes fabricated using a novel chemically controlled transfer-printing method,” *Adv. Mater.*, vol. 27, no. 14, pp. 2317–2323, **2015**.
- [21] R. Bhargav *et al.*, “Copper Bromide as an Efficient Solution-Processable Hole Transport Layer for Organic Solar Cells: Effect of Solvents,” *ACS Omega*, vol. 4, no. 3, pp. 6028–6034, **2019**.
- [22] B. Kadem, W. Cranton, and A. Hassan, “Metal salt modified PEDOT:PSS as anode buffer layer and its effect on power conversion efficiency of organic solar cells,” *Org. Electron.*,

- vol. 24, pp. 73–79, **2015**.
- [23] J. Blochwitz, M. Pfeiffer, T. Fritz, and K. Leo, “Low voltage organic light emitting diodes featuring doped phthalocyanine as hole transport material,” *Appl. Phys. Lett.*, vol. 73, no. 6, pp. 729–731, **1998**.
 - [24] E. L. Hanson, J. Guo, N. Koch, J. Schwartz, and S. L. Bernasek, “Advanced surface modification of indium tin oxide for improved charge injection in organic devices,” *J. Am. Chem. Soc.*, vol. 127, no. 28, pp. 10058–10062, **2005**.
 - [25] J. Blochwitz et al., “Interface electronic structure of organic semiconductors with controlled doping levels,” *Org. Electron. physics, Mater. Appl.*, vol. 2, no. 2, pp. 97–104, **2001**.
 - [26] M. Zhang et al., “Highly efficient ternary polymer solar cells by optimizing photon harvesting and charge carrier transport,” *Nano Energy*, vol. 22, pp. 241–254, **2016**.
 - [27] Q. An et al., “Efficient organic ternary solar cells with the third component as energy acceptor,” *Nano Energy*, vol. 26, pp. 180–191, **2016**.
 - [28] W. Gao and A. Kahn, “Electronic structure and current injection in zinc phthalocyanine doped with tetrafluorotetracyanoquinodimethane: Interface versus bulk effects,” *Org. Electron. physics, Mater. Appl.*, vol. 3, no. 2, pp. 53–63, **2002**.
 - [29] X. Chen, B. Jia, Y. Zhang, and M. Gu, “Exceeding the limit of plasmonic light trapping in textured screen-printed solar cells using Al nanoparticles and wrinkle-like graphene sheets,” *Light Sci. Appl.*, vol. 2, no. AUGUST, pp. 1–6, **2013**.
 - [30] Z. C. Holman, S. De Wolf, and C. Ballif, “Improving metal reflectors by suppressing surface plasmon polaritons: A priori calculation of the internal reflectance of a solar cell,” *Light Sci. Appl.*, vol. 2, no. OCTOBER, p. 0, **2013**.
 - [31] Y. H. Su, Y. F. Ke, S. L. Cai, and Q. Y. Yao, “Surface plasmon resonance of layer-by-layer gold nanoparticles induced photoelectric current in environmentally-friendly plasmon-sensitized solar cell,” *Light Sci. Appl.*, vol. 1, no. JUNE, pp. 2–6, **2012**.
 - [32] L. Duan et al., “Relationship between the diode ideality factor and the carrier recombination resistance in organic solar cells,” *IEEE J. Photovoltaics*, vol. 8, no. 6, pp. 1701–1709, 2018.
 - [33] B. Y. Kadem, “P3HT:PCBM-based organic solar cells: optimisation of active layer nanostructure and interface properties,” *Sheffield Hallam University*, **2017**.
 - [34] B. Kadem, R. K. F. Alfahed, A. S. Al-asadi, and H. A. Badran, “Optik Morphological , structural , optical , and photovoltaic cell of copolymer P3HT : ICBA and P3HT : PCBM,”

- Opt. - Int. J. Light Electron Opt., vol. 204, no. September 2019, p. 164153, **2020**.
- [35] J. Ouyang, ““ Secondary doping ”” methods to significantly enhance the conductivity of PEDOT: PSS for its application as transparent electrode of optoelectronic devices,” Displays, vol. 34, no. 5, pp. 423–436, **2013**.
- [36] C. Badre, L. Marquant, A. M. Alsayed, and L. A. Hough, “Highly Conductive Poly (3 , 4-ethylenedioxythiophene): Poly (styrenesulfonate) Films Using 1-Ethyl-3-methylimidazolium Tetracyanoborate Ionic Liquid,” pp. 2723–2727, **2012**.
- [37] J. Gasiorowski, R. Menon, K. Hingerl, M. Dachev, and N. S. Sariciftci, “Surface morphology, optical properties and conductivity changes of poly(3,4-ethylenedioxythiophene):poly(styrenesulfonate) by using additives,” Thin Solid Films, vol. 536, pp. 211–215, **2013**.
- [38] B. Y. Kadem, “P3HT:PCBM-based organic solar cells: optimisation of active layer nanostructure and interface properties,” Sheffield Hallam University, **2017**.
- [39] V. E. Ferry et al., “Light trapping in ultrathin plasmonic solar cells,” vol. 18, no. May, pp. 237–245, **2010**.
- [40] L. C. Kimerling, “Demonstration of enhanced absorption in thin film Si solar cells with textured photonic crystal back reflector,” vol. 221105, no. December, pp. 1–4, **2008**.
- [41] C. E. Petoukhoff and D. M. O. Carroll, “Absorption-induced scattering and surface plasmon out-coupling from absorber-coated plasmonic metasurfaces,” pp. 1–13, **2015**.
- [42] F. Cheng et al., “Solar Energy Materials & Solar Cells Enhancing the performance of P3HT: ICBA based polymer solar cells using LiF as electron collecting buffer layer and UV – ozone treated MoO₃ as hole collecting buffer layer,” Sol. Energy Mater. Sol. Cells, vol. 110, pp. 63–68, **2013**.
- [43] B. Kadem, W. Cranton, and A. Hassan, “Metal salt modified PEDOT:PSS as anode buffer layer and its effect on power conversion efficiency of organic solar cells,” Org. Electron., vol. 24, pp. 73–79, **2015**.
- [44] M. H. Jao, H. C. Liao, and W. F. Su, “Achieving a high fill factor for organic solar cells,” J. Mater. Chem. A, vol. 4, no. 16, pp. 5784–5801, **2016**.
- [45] Y. S. Kim et al., “Effect of solvents on the performance and morphology of polymer photovoltaic devices,” Curr. Appl. Phys., vol. 10, no. 4, pp. 985–989, **2010**.

- [46] T. M. Alshahrani, “Advanced Materials for Organic Solar Cells : Influence of Generation and pH on PAMAM-Based Devices By,” Bangor University, **2016**.
- [47] D. Rauh, A. Wagenpfahl, C. Deibel, and V. Dyakonov, “Relation of open circuit voltage to charge carrier density in organic bulk heterojunction solar cells,” *Appl. Phys. Lett.*, vol. 98, no. 13, **2011**.
- [48] Y. Lin, Y. Li, and X. Zhan, “Small molecule semiconductors for high-efficiency organic photovoltaics,” *Chem. Soc. Rev.*, vol. 41, no. 11, pp. 4245–4272, **2012**.
- [49] K. Sun, Y. Xia, and J. Ouyang, “Improvement in the photovoltaic efficiency of polymer solar cells by treating the poly(3,4-ethylenedioxythiophene): Poly(styrenesulfonate) buffer layer with co-solvents of hydrophilic organic solvents and hydrophobic 1,2-dichlorobenzene,” *Sol. Energy Mater. Sol. Cells*, vol. 97, pp. 89–96, **2012**.
- [50] B. Fan, X. Mei, and J. Ouyang, “Significant conductivity enhancement of conductive poly(3,4- ethylenedioxythiophene): Poly(styrenesulfonate) films by adding anionic surfactants into polymer solution,” *Macromolecules*, vol. 41, no. 16, pp. 5971–5973, **2008**.
- [51] C. Badre, L. Marquant, A. M. Alsayed, and L. A. Hough, “Highly conductive poly(3,4-ethylenedioxythiophene):Poly (styrenesulfonate) films using 1-ethyl-3-methylimidazolium tetracyanoborate ionic liquid,” *Adv. Funct. Mater.*, vol. 22, no. 13, pp. 2723–2727, **2012**.
- [52] J. Ouyang, ““secondary doping” methods to significantly enhance the conductivity of PEDOT:PSS for its application as transparent electrode of optoelectronic devices,” *Displays*, vol. 34, no. 5, pp. 423–436, **2013**.

Chapter 6

Effect of Graphene as an Electron Transport Layer

6.1 Introduction

In solar cells, the electron transport layer (ETL) plays a fundamental role. Recently, graphene (Gr) based ETLs have been proved to be a promising candidate for scalable fabrication processes and to achieve higher carrier injection compared to most used ETLs [1].

In the last two decades, graphene has attracted remarkable attention due to its beneficial material properties, including high charge mobility, mechanical strength, transparency, flexibility and environmental stability [1,2]. These exceptional properties of the graphene offer many opportunities for the performance improvement of electronic devices. It has already demonstrated its potential in the development of high-performance electronic devices. Hence, in next-generation electronic devices, graphene is estimated to play an important role as a transparent and conductive electrode [3]. Graphene, a two-dimensional atomically thick carbon atom arranged in honeycomb lattice, was recently isolated by frequently peeling highly oriented pyrolytic graphite (HOPG) using sticky tape [4]. Since then, outstanding physical properties predicted and measured for graphene have been explored for practical applications such as field-effect transistors [5], chemical sensors [6] and composite reinforcement [7]. Monolayer graphene has high crystallographic quality and ballistic electron transport on the micrometre scale with only 2.3% of light absorption [8]. Furthermore, the mixture of its high chemical and thermal stability [9], high stretchability [10,11], and low contact resistance with organic materials [12] offer great benefits for using graphene as a promising transparent conductor in organic electronic devices, e.g. solar cells, organic light emitting diodes (OLEDs) [13,14], liquid crystal displays (LCDs) [1], touch screens [15], field effect transistors (FETs) [16] and Spectro-electrochemistry investigation [17]. Organic photovoltaics (OPVs) have gained much attention as possible candidates for the generation of clean electricity due to the organic semiconductors' high absorption coefficients, light weight and flexibility, and low-cost, high throughput fabrication methods [18,19]. The fact that they can be directly deposited onto various substrates also makes flexible photovoltaic configurations feasible [20]. Superior flexibility, as well as abundance of source material (carbon) at lower costs compared

to Indium tin oxide (ITO) put graphene into a suitable position as an alternative transparent conducting electrode material, with a potential in various applications such as solar cells, liquid crystal displays, and touch screens [21-24].

In this chapter, thin film of graphene is used as an electron transport layer (ETL) to enhance the performance of the OPV devices. The P3HT:IC₇₀BA BHJ thin films were prepared by solution processing technique and their optical analysis have been performed in the favour of the formation of polymer blends. The absorption spectra confirm the validity of the individual presence of polymers in the resulting blend. By analysing the *J-V* characteristics of the devices, the improvement in the performance with addition of graphene is clearly identified. This indicates addition of graphene ETL influence the charge extraction and collection mechanism.

6.2 Effect of Graphene as an electron transport layer

To find the optimum thickness for fabricated devices, different speeds of spin-coating have been selected as shown later in this section.

6.2.1 Different thickness conditions

Thickness of (ETL) plays a crucial rule for the transportations of electrons. For this reason, different thicknesses have been fabricated to study the effect of this parameter.

6.2.1.1 Fabrication process

In this chapter, the results are of my own investigations except the last section of chemical treatment of graphene samples which were treated chemically in collaboration with the Biocomposite Research Centre, Bangor University, UK.

Regio regular P3HT, IC₇₀BA, poly(3,4-ethylenedioxythiophene polystyrene sulfonate) (PEDOT:PSS), dichlorobenzene (DCB) of molecular weight 147.00 g/mol with 99% purity, and indium-tin-oxide (ITO) coated glass substrates with resistivity 8–12 Ω /cm square were purchased from Sigma-Aldrich. Graphene was procured from Sigma-Aldrich.

The organic photovoltaic devices depicted schematically in Figure 6.1 were fabricated by spin coating doped PEDOT-PSS onto clean ITO-coated glass substrates. The substrates were thoroughly cleaned using DI water, acetone, and iso-propanol for 10 minutes each in ultrasonic

bath, respectively, and then dried with dry N₂ gas. All cleaned substrates were treated with O₂ plasma treatment for 20 minutes. Doped PEDOT:PSS was spin coated at a spin speed of 4000 rpm for 40 seconds and annealed on a hot plate at 150 °C for 30 minutes in ambient air. P3HT:IC₇₀BA active layer (17 mg.ml⁻¹) was dissolved in dichlorobenzene (DCB) with the ratio 1:1. The active layer was spin coated with spin speed of 600 rpm inside a nitrogen-filled glove box, followed by annealing inside the glove box at 150 °C for 20 minutes. The active layer thickness was estimated to be 100 nm using Dektak Stylus Profilometer.

Related to electron transport layer (ETL), Lithium Fluoride (LiF) was used as described in detail in chapter 4, section 4.6. For graphene preparation, two different concentrations of 10 mg and 20 mg were dissolved in 2 mL of DI water each and stirred for 24 hours at 45 °C to obtain the graphene solution. Graphene layers, which function as the ETL were spun coated at different speed (1000 rpm, 3000 rpm and 7000 rpm) for 60 seconds and annealed at 120 °C for 20 minutes. All depositions were performed at room temperature inside the glove box. Then, a contact of aluminum (Al) was then thermally evaporated with a thickness of 100 nm through a shadow mask with an active area of 0.125 cm². This process was carried out under a vacuum of about 10⁻⁶ mbar (~10⁻⁴ Pa), at the deposition rate of 1 nm/sec. Film thickness and deposition rate were monitored using a quartz crystal thickness monitor. All the devices were subjected to further heat treatment inside the glove box at 150 °C for 20 minutes and left to cool down for 30 minutes before measurements were carried out.

Different devices based on different graphene layer deposition were fabricated by following the above-described process and compared with which has LiF as ETL. The devices designated as:

D1: Standard structure with LiF as ETL (ITO/PEDOT:PSS/P3HT:IC₇₀BA/LiF/Al).

D2: Standard structure with Gr as ETL (ITO/PEDOT:PSS/P3HT: IC₇₀BA /Gr/Al).

Devices have been fabricated with graphene that has concentration of 10 mg/2mL (different thickness) were symbolised by S101, S102 and S103 for spin speed of 1000 rpm, 3000 rpm and 7000 rpm, respectively. Likewise, devices were fabricated with graphene that has concentration of 20 mg/2mL were symbolised by S201, S202 and S203 for speed of 1000 rpm, 3000 rpm and 7000 rpm, respectively.

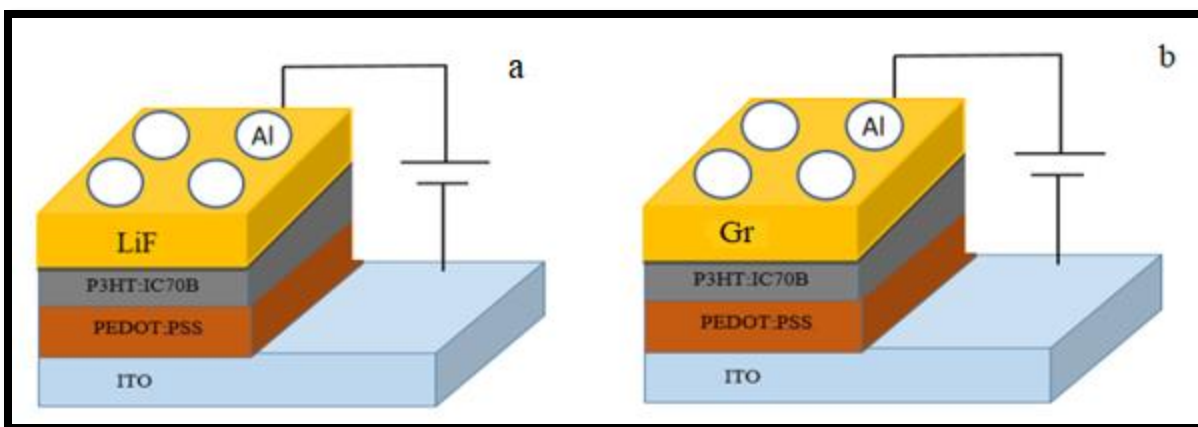


Figure 6.1: Schematic diagram of P3HT:IC₇₀BA devices a) with LiF as ETL. b) with Gr as ETL.

6.2.1.2 Morphological analysis using AFM

Variation in the surface morphology of P3HT:IC₇₀BA BHJ films with LiF as ETL and with Gr as ETL as well, prepared using different thickness of Gr layers to find out the reasons leading to different photovoltaic behaviour. With LiF as ETL-based film has revealed a surface with rms roughness of 1.68 nm correlating with noticeable pinholes as shown in Figure 6.2. On the other hand, as shown in Figure 6.3, S101, S102 and S103 films have demonstrated surface roughness with values of 1.7 nm, 1.3 nm and 0.9 nm, respectively. Mainly, the brighter regions are associated with the active layer P3HT:IC₇₀BA domains while the darker regions are related to the graphene domains [25-29]. The highest surface roughness was for higher concentration group. Devices S201, S202 and S203 have demonstrated surface roughness with values of 2.48 nm, 1.95 nm and 1.15 nm, respectively as shown in Figure 6.4 and the results listed in Table 6.1. The rms roughness of the Gr layer decreases with decreasing Gr layer thickness which could be beneficial to the higher fill factor (*FF*) of the corresponding OSCs. The diffusion of graphene molecules on and within the P3HT:IC₇₀BA main matrix has influenced the phase separation between the active layer and the respective electrode. Further enhancement in the surface morphology has been observed using low concentration of graphene which was attributed to the further improvement in the diffusion and distribution of charge carriers. The improvement in the interpenetrating network could facilitate charge carrier transport, and hence improved solar cell performance. The darker region is higher

in the case of Gr-based films, which suggests that the phase separation has become more resulting in improved dissociation rate of the photo-generated excitons [30].

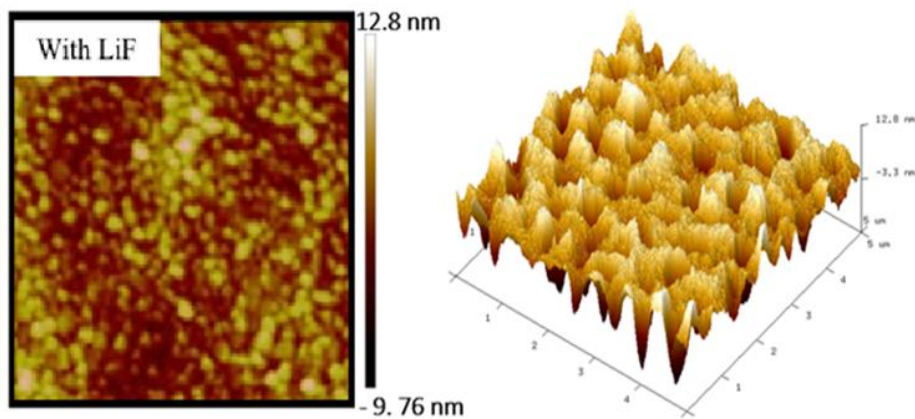


Figure 6.2: 2D and 3D AFM images and phase analysis of reference device with LiF as ETL layer.

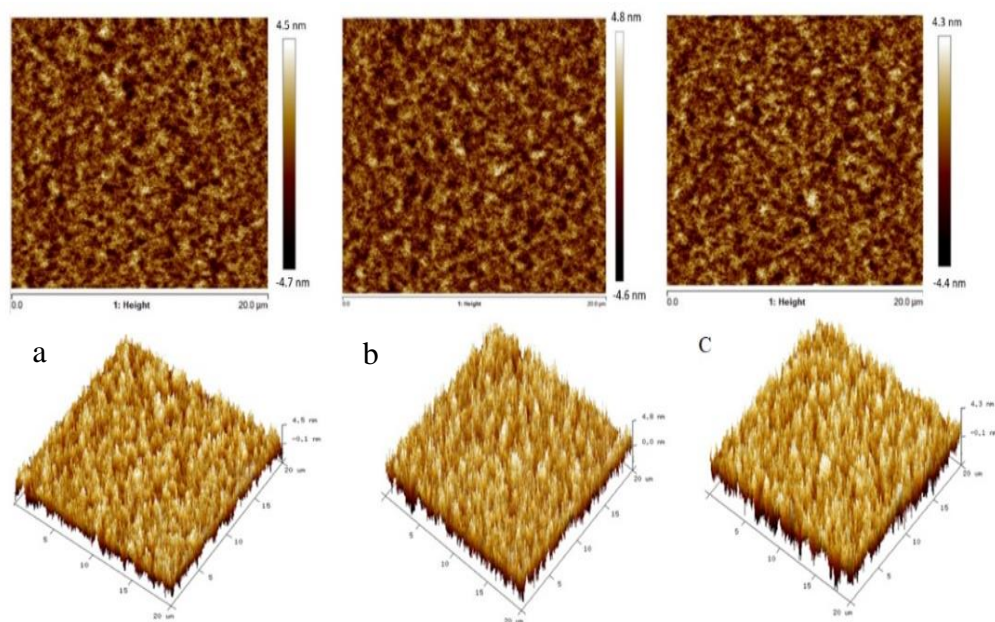


Figure 6.3: 2D and 3D AFM images and phase analysis of Gr (10mg/2mL) as ETL layer on ITO/PEDOT:PSS/P3HT:IC₇₀BA. a) S101, b) S102, c) S103.

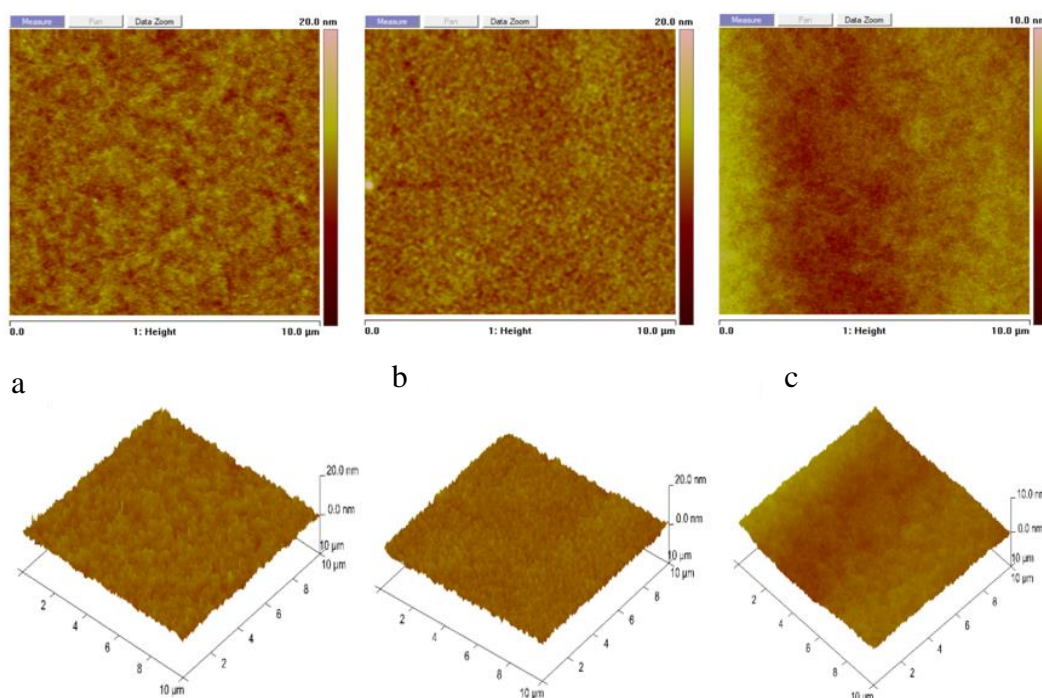


Figure 6.4: 2D and 3D AFM images and phase analysis of Gr (20mg/2mL) as ETL layer on ITO/PEDOT:PSS/P3HT:IC₇₀BA. a) S201, b) S202, c) S203

Device	Spin-coat speed (rpm)	Thickness (nm)	Roughness (nm)
S101	1000	45~55	1.7
S102	4000	25~30	1.3
S103	7000	8~12	0.9
S201	1000	50~65	2.48
S202	4000	35~45	1.95
S203	7000	10~15	1.15
With LiF	Evaporation deposition	0.75	1.68

Table 6.1: Roughness for P3HT:IC₇₀BA based OPVs with LiF and Gr as ETL.

6.2.1.3 Optical Absorption measurements

Figure 6.5 shows the absorption spectrum of the devices with LiF and with Gr. It is clearly noticeable the significant increase in the absorbance using Gr in the wavelength range 460-625 nm, while the absorbance decreases in further increase of wavelength i.e. the region beyond 650 nm. This can be attributed to the increment of inter-reflections which can improve interchain vibrational absorption induced by the strong interchain interaction in the ordered P3HT crystalline regions in the films [31]. The P3HT:IC₇₀BA/LiF absorption edge at 680 nm where the bandgap at this point is 1.82 eV, with peak absorption at 500 nm (2.48 eV). No significant change in the peak position has been observed for all devices. However, the P3HT:IC₇₀BA/Gr (10 mg/2mL) with different thickness have almost the same values of bandgaps. For S101, the absorption edge at 709 nm where the bandgap at this point 1.75 eV, with peak absorption at 496 nm (2.5 eV). Related to S103 device, the absorption edge at 712.6 nm where the bandgap at this point 1.74 eV, with peak absorption at 496 nm (2.5 eV). No significant change in the peak position has been observed for all devices in this group.

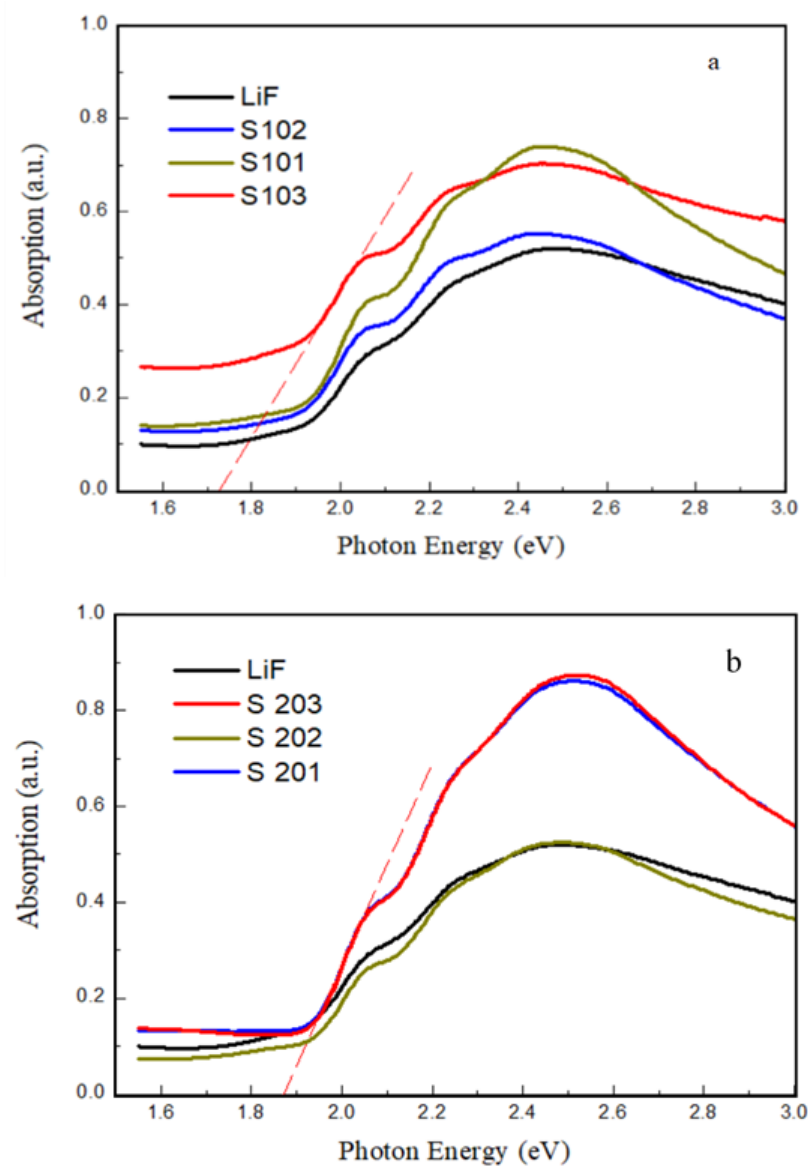


Figure 6.5: The optical absorption of the IC70BA based OBHJ with LiF and with Gr layer for a) concentration of 10 mg/2mL. b) concentration of 20 mg/2mL.

For the second group of graphene-based devices, which has a higher concentration of Gr, there is a significant change in the values of bandgaps compared to the reference sample. For S201, the absorption edge at 652.6 nm where the bandgap at this point 1.9 eV, with peak absorption at 617 nm (2.4 eV). Both S202 and S203 have the same absorption edge at 667 nm where the bandgap at this point is 1.86 eV, with the same peak absorption at 617 nm (2.4 eV).

Table 6.2 shows bandgaps for P3HT:IC₇₀BA based OPVs and P3HT:IC₇₀BA/Gr. As it is clear, the absorption intensity for deposited Gr thin film is much higher than which without Gr layer, this shows that the emission only comes from the Gr [32]. Compared with the active layer with LiF, the absorption peak of annealed films did not shift, only the intensity of absorption peak changed. The peak intensity is determined by the structural order of the Gr and the active layer film. All values of bandgaps for all devices are listed in Table 6:2.

Device	Bandgap (eV)
LiF	1.82
S 101	1.75
S 102	1.75
S 103	1.74
S 201	1.9
S 202	1.86
S 203	1.86

Table 6.2: *The variation of P3HT:IC₇₀BA blend optical bandgaps with LiF and Gr as ETL.*

6.2.1.4 Electrical measurements

In this section, diode measurements and J-V characteristics have been calculated in details as shown later on in this section.

6.2.1.4.1 Diode measurements

The electrical characteristics of the studied devices were measured in the dark using current – voltage (*J-V*) measurements. The latter can provide useful information about the diode parameters.

All devices demonstrated rectifying behaviour, with exponential dependence of the current in the forward voltage region and slow variation of current in reverse bias region as shown in the dark J - V curves in Figure 6.5. The forward and reverse current under dark condition is nearly same for all the devices. The observed photocurrent behaviour in the devices can be described as follows: Upon excitation with white light, firstly the excitons are created in the BHJ layer upon absorption of light. Subsequently, these excitons are separated into free electron and holes. Finally, these free electrons and holes transport towards respective electrodes through ETL and HTL and produce photocurrent. The photo response can be easily obtained in all the devices because the dissociation of excitons and transport of free charge carriers occur under the application of external applied voltage (electric field).

The R_s and R_{sh} of the diodes produced using different concentrations of graphene and different thicknesses have been estimated using dark J - V characteristics. The S10 group-based devices has exhibited lower series resistances (R_s) compared to S20 group-based devices as shown in Figure 6.5(a) and Table 6.3. However, both groups have higher (R_s) in comparison to (LiF) device. The main reason for this high series resistance is attributed to the clear presence of pinholes and the thickness of ETL. However, improved contact properties between the active layer and the back (Al) electrode will result in low series resistance due to the stronger interfacial adhesion [33]. Under dark condition, the devices displayed good rectifying characteristics as current stayed at almost 0 A from -1V and turned on at 0.3 V for S10 group-based device and 0.5 V for S20 group-based device except S202 device which turned on at almost 0.4 V as shown in Figure 6.5 (b), where it started to increase showing clear rectifying behaviour. This indicates that the very low current from -1 V until 0.5 V reflects the lack of carriers in the structure and thus a non-conducting behaviour.

For shunt resistances (R_{sh}), from Table 6:3 and Figure 6.5, it is clear that device which has LiF as ETL, has the highest leakage current with the lowest value of R_{sh} (75 k Ω) followed by S201-based device with (85 k Ω), respectively. This is also reflected in the R_s , where S201-based device has the highest R_s . Such large variation in the leakage current of organic solar cells is not uncommon and is known to be affected by substrate cleaning procedures, film thickness, electrode interlayers, and film deposition techniques [34]. In case of S103-based device, it recorded the highest (R_{sh}) with (1M Ω), and this range in R_{sh} is most likely a consequence of spin coating from a hot solution

which led to variations in film thickness and film density which in turn affects the degree of cathode diffusion into the active layer [35].

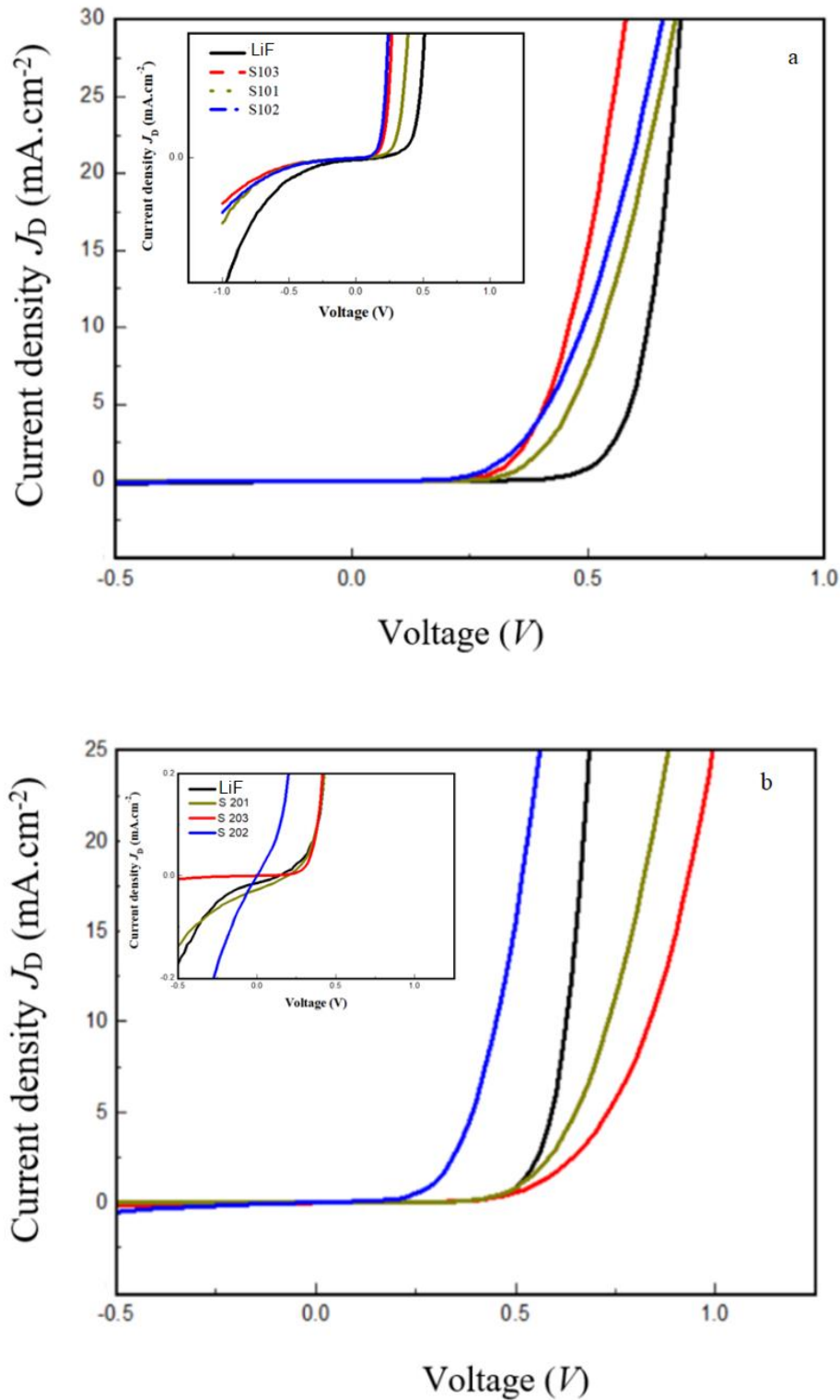


Figure 6.5: Diode behaviours for different devices with LiF and Gr as ETL. a) devices with concentration 10 mg/ml of Gr. b) devices with concentration 20 mg/ml of Gr. The inset figure represents leakage current for devices

Parasitic Resistances		
Devices	Shunt resistance ($k\Omega$)	Series resistance (Ω)
LiF	90	4
S101	200	17
S102	660	14
S103	1000	12
S201	85	33
S202	150	18
S203	500	15

Table 6.3: *Diodes parasitic resistances for P3HT:IC₇₀BA device with using LiF and Gr as ETL.*

Obtained results presented in Figure 6.6 and listed in Table 6:4 show the ideality factor of the diodes, which contain critical data on the recombination and transport processes in organic solar cells, ranging from 1.34 to 1.95. It was found that the diode with S201 has the highest ideality factor. Evidently, the ideality factor of the fabricated diodes is much larger than that of an ideal diode. Such a behaviour suggests that the transport mechanism consists of defect-assisted tunnelling with conventional electron–hole recombination [36].

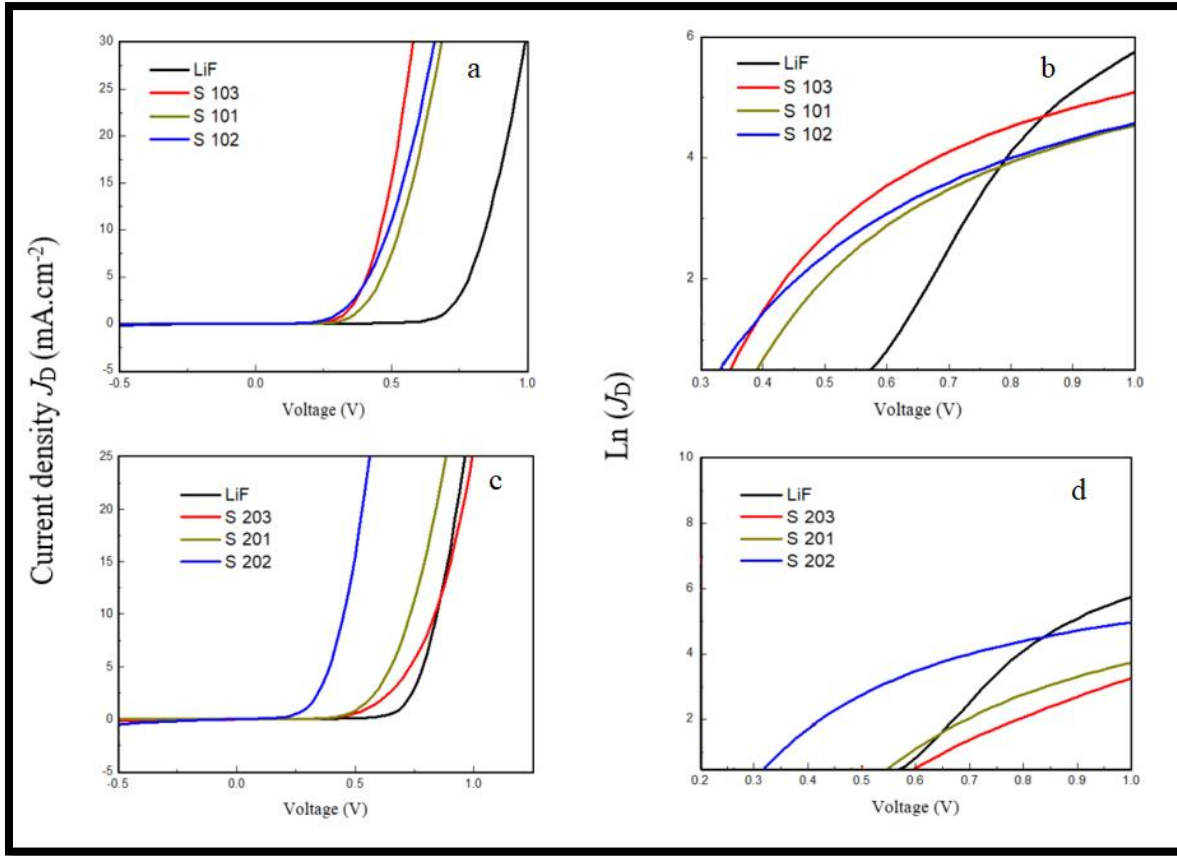


Figure 6.6: *J-V characteristics of the OBHJ solar cells under dark condition for different devices with LiF and Gr as ETL with concentration of a) 10 mg/ml of Gr, c) 20 mg/ml of Gr. Variation of $\ln(J_D)$ versus the bias voltage for different devices with LiF and Gr as ETL with concentration of b) 10 mg/ml of Gr. d) 20 mg/ml of Gr.*

Device	Ideality factor (n)
LiF	1.9
S101	1.87
S102	1,69
S103	1.34
S201	1.95
S202	1.84
S203	1.73

Table 6.4: Ideality factors for diode devices.

6.2.1.4.2 Photovoltaic performance

Figures 6.7 (a) and 6.7 (c) show the J - V curves of two groups of different concentrations of graphene S10 and S20 under the illumination of AM1.5G, 100 mW.cm^{-2} . The efficiency of devices can be obtained from the peak power curve of devices as shown in Figure 6.7 (b) and Figure 6.7 (d). The device with LiF as ETL shows a PCE of 5.5 % with J_{sc} of 12.5 mA.cm^{-2} , V_{oc} of 0.79 V, and fill factor (FF) of 56 %. The J_{sc} of device S101 with highest thickness of Gr (1000 rpm/ 60 seconds) shows a clear improvement. The J_{sc} increases from 12.5 mA.cm^{-2} to 25 mA.cm^{-2} , while V_{oc} decreased to 0.33 V, which results in a low PCE of 4.0%. For S102 device, The J_{sc} has significantly improvement. The J_{sc} increased from 12.5 mA.cm^{-2} to 29.4 mA.cm^{-2} , but V_{oc} also decreased to 0.65 V, however it results in a higher PCE of 8.94% (more the 90% improvement) with a fill factor (FF) of 47%. Related to S103 device (the lowest thickness of graphene in S10 group), J_{sc} significantly improved by more than 300% to a value of 67.4 mA.cm^{-2} which leads to the highest PCE of 10.4% with FF of 42% and V_{oc} of 0.37 V.

Regarding S20 devices group, the J_{sc} of device S201 with highest thickness of Gr (1000 rpm/ 60 seconds) increased from 12.5 mA.cm^{-2} to 29.4 mA.cm^{-2} , V_{oc} decreased to 0.65 V, which results in a high PCE of 8.9% compared to Ref. device with FF of 47%. device. For S202 device, J_{sc} increases to 26.2 mA.cm^{-2} , V_{oc} decreased to 0.53 V, which results in a PCE of 5.5% (FF) of 40%. Related to S203 device (the lowest thickness of graphene in S20 group), J_{sc} has significant improvement as a double in comparison to Ref. device to enhance from 12.5 mA.cm^{-2} to 41.7 mA.cm^{-2} . With 0.55 V V_{oc} which leads to a high PCE of 9% with FF of 40%.

For R_{sh} and R_s , it is clear from Table 6.5 that the values of R_s are proportional in inverse with the thickness of graphene layer. When compared to other conventional cathode materials, the higher sheet resistance of the graphene layer poses a major problem [37]. The highest PCE for both groups S10 and S20, showed the lowest values 2Ω and 2.75Ω , respectively. These results clearly show that graphene can serve as a functional interlayer to enhance the solar cell efficiency.

When light irradiates on the photoactive layer of the PSCs through ITO electrode, the active layer will absorb photons to produce excitons, and the excitons will diffuse towards and dissociate at the P3HT/IC₇₀BA interface into electrons in the LUMO (the lowest unoccupied molecular orbital) of the acceptor IC₇₀BA and holes in the HOMO (the highest occupied molecular orbital) of the donor P3HT. Since the work function is (-4.66 eV) of Gr is very close to LUMO level of IC₇₀BA, the barrier height for electron collection could be reduced. The photo-generated electrons are directed toward the Al electrodes. However, unlike semiconducting carbon nanotube, graphene is a zero-bandgap material and it is simply treated as a metal [work function]. So that it blocks the hole transport from P3HT to Al cathode and move faster to anode and participate with conducting and device performance as well. Therefore, the Gr/Al cathode can be expected to be an electron-selective electrode in nature, which can efficiently collect electrons and blocks the hole transport from P3HT to the Al cathode. At the same time, the holes pass through the HOMO level of P3HT to PEDOT:PSS layer, and finally are collected by ITO anode. Thus, from the viewpoint of energy levels, the device could show high charge collection efficiencies on both electrodes [38]. Thus, improve the device performance by reducing separated charge recombination losses at the interface. On the other hand, the insertion of Gr layer can prevent the reactive hot Al atoms from diffusing into the photoactive layer during the thermal evaporation process. Because of the above factors, a higher V_{oc} can be expected. Besides the significant enhancement in J_{sc} , the V_{oc} is also

increased upon the insertion of Gr interlayer for most of Gr devices. It is known that if ohmic contact can be achieved at each electrode, the V_{oc} is governed by the difference between the lowest unoccupied molecular orbital (LUMO) of IC₇₀BA and the highest occupied molecular orbital (HOMO) levels of P3HT [39]. In addition, the series resistance (R_s) maximized when Gr was inserted, however, the shunt resistance (R_{sh}) was minimized. The low shunt resistance is due to higher roughness.

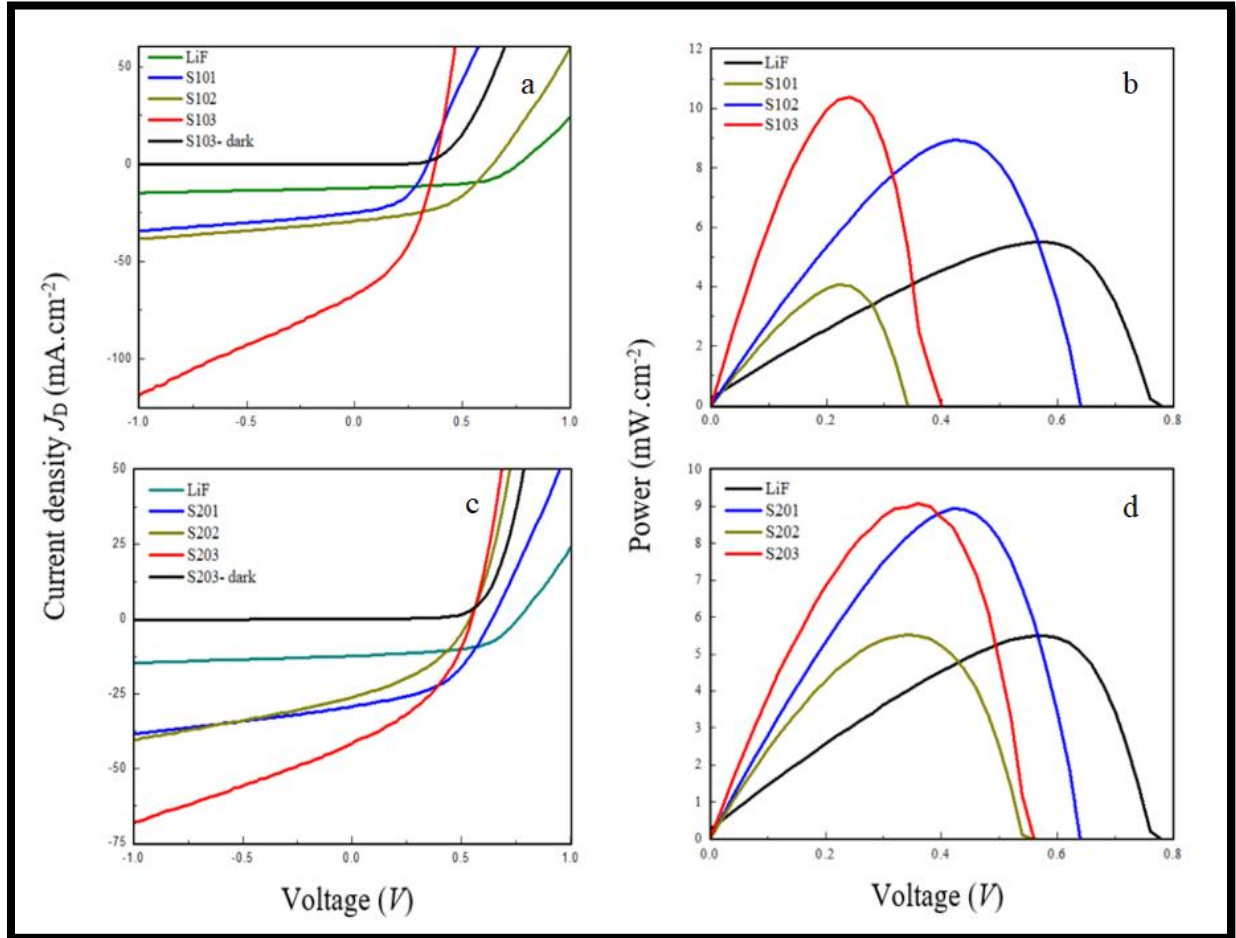


Figure 6.7: *J-V characteristics of the OBHJ solar cells under the illumination for different devices with and without ETL with concentration of a) 10 mg/ml of Gr. c) 20 mg/ml of Gr. Variation of power curves for different devices with LiF and Gr as ETL with concentration of b) 10 mg/ml of Gr. d) 20 mg/ml of Gr.*

Devices	J_{sc} ($mA.cm^{-2}$)	V_{oc} (V)	FF (%)	PCE (%)	R_{sh} (Ω)	R_s (Ω)
LiF.	12.5	0.79	56	5.5	2500	1.5
S101	25	0.33	49	4.0	1800	12
S102	29.4	0.65	47	8.94	1600	8
S103	67.4	0.37	42	10.4	950	2
S201	29.4	0.65	47	8.9	2500	15
S202	26.2	0.53	40	5.5	2000	7
S203	41.7	0.55	40	9	1800	2.75

Table 6.5: *The J-V characteristics for the P3HT: IC70BA based devices under illumination for different graphene concentrations.*

6.3 OSCs using graphene with chemical treatment conditions

As it is clear from the results in last section with regards to different photovoltaic parameters and the values of PCE, the optimum thickness for both groups of graphene-based devices was at spin-coating at 7000 rpm for 60 seconds, then annealed at 120 °C for 20 minutes. This part of work was in collaboration with the Biocomposite centre at Bangor University.

6.3.1 Fabrication process

20 mg of graphene was used as supplied from Thomas Swan mixed with 1 g of the polymer/surfactant and dissolved in 10 ml methanol and placed in ultrasonic bath for 3-4 hours. Two different polymer/surfactants were used during this work:

S143: Poly(styrene-co-acrylic acid) (in house mixture with Intellectual property for Biocomposite Centre).

S144: JONCRYL HPD 496 was used as received from BASF.

6.3.2 Morphological analysis using AFM

To understand the morphological changes that occur in the active layer due to the use of modified graphene layer, AFM images of the graphene surface were studied. The tapping-mode AFM images in Figure 6.8 shows the variation in graphene layer morphology after chemical treatment. As a reference, the roughness of LiF device surface is 1.68 nm. The surface roughness for S143 device is 6.04 nm which is higher compare to the roughness of LiF device. While the rms roughness of the S144 surface is 2.94 nm which is much lower than the roughness of S143. These values of roughness for S143 and S144 should have a clear effect on the value of fill factor FF .

It is clear that the concentration of graphene can affect the roughness of the active layer. The increase in roughness is attributed to P3HT self-organization and phase separation of the blend. P3HT chains self-organizing into an ordered structure can significantly enhance hole mobility. Meanwhile, the aggregation of IC₇₀BA molecules can form separate paths for electron transport. The nanoscale phase separation can finally result in the enhancement of J_{sc} of the PSCs. The values of roughness's for devices are listed in Table 6.6.

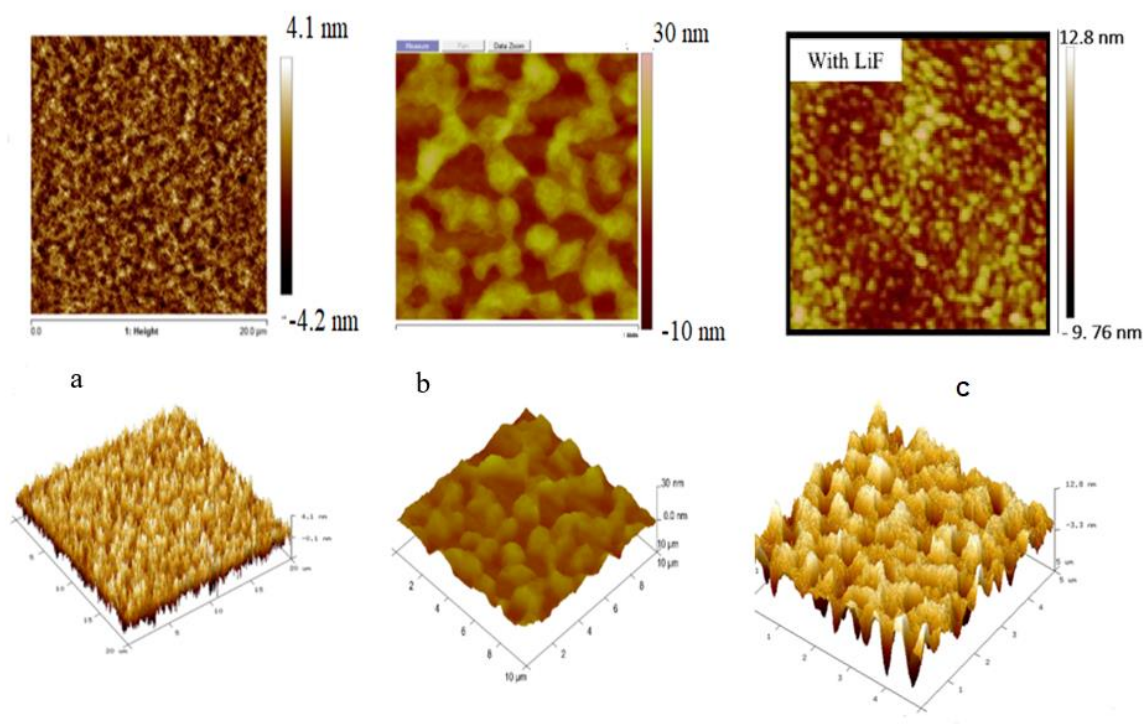


Figure 6.8: 2D and 3D AFM images and phase analysis of Gr as ETL layer on ITO/PEDOT:PSS/P3HT:IC₇₀BA. a) S144, b) S143, c) LiF

Device	Roughness (nm)
LiF	1.68
S143	6.04
S144	2.94

Table 6.6: *Roughness for P3HT:IC₇₀BA based OPVs according to chemical treatment for Graphene as ETL.*

6.3.3 Optical Absorption measurements

UV-Vis spectra of graphene samples (S143 and S144) are shown in Figure 6.9. Device based on sample (S144) has higher absorption intensity with peak at 590.5 nm (2.1 eV) and edge at 785 nm where the bandgap at this point is 1.58 eV, which is the lowest value of all devices that have graphene as ETL.

Meanwhile, device based on sample (S143) has a little lower absorption intensity with edge at 775 nm where the bandgap at this point 1.6 eV, with peak absorption at 590.5 nm (2.1 eV) as shown in Figure 6.9. For P3HT:IC₇₀BA/LiF, absorption edge at 680 nm where the bandgap at this point is 1.82 eV, with peak absorption at 500 nm (2.48 eV).

Table 6.7 shows bandgaps for P3HT:IC₇₀BA based OPVs and P3HT:IC₇₀BA/Gr. As it is clear, the absorption intensity for deposited Gr thin film is much higher than which without Gr layer, this shows that the emission only comes from the Gr [40]. The peak intensity is affected in this case by the structural order of the Gr and (polymer/surfactant).

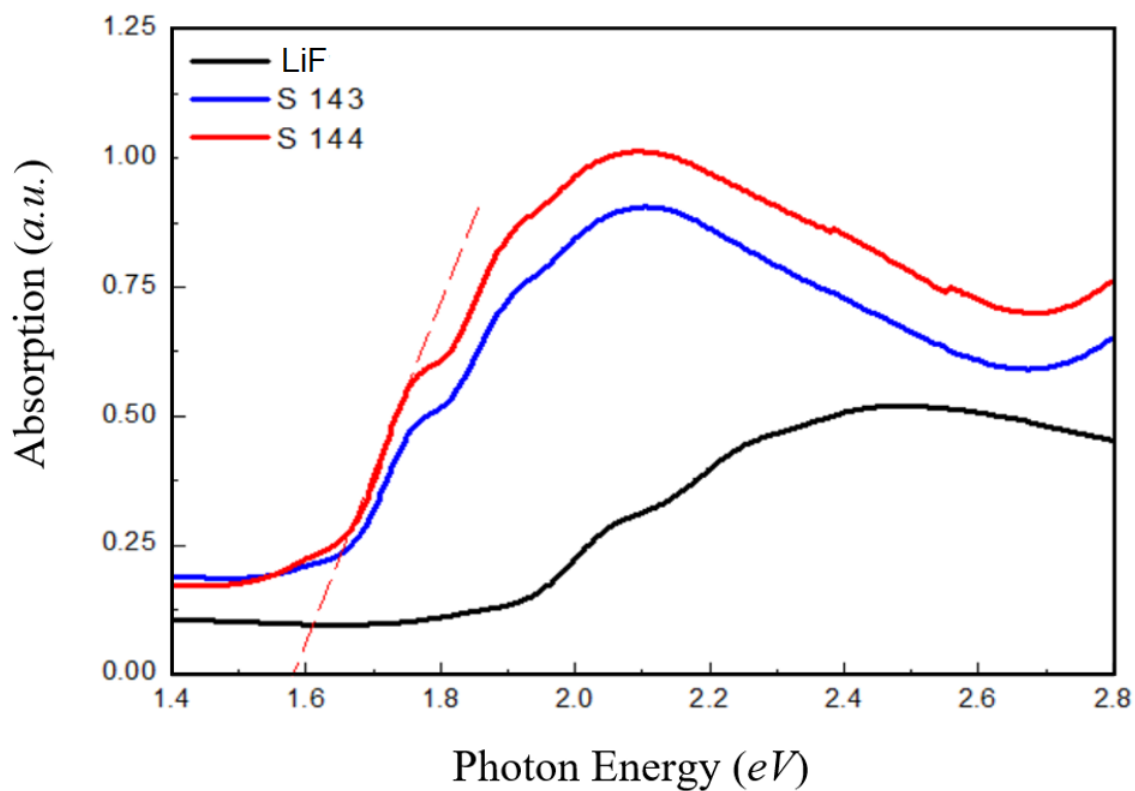


Figure 6.9: *The optical absorption of the IC₇₀BA based OBHJ with and without treated Gr layer.*

Device	Bandgap (eV)
LiF	1.82
S 143	1.60
S 144	1.58

Table 6.7: *The variation of P3HT:IC₇₀BA blend optical bandgaps with and without treated Gr as ETL.*

6.3.4 Electrical measurements

6.3.4.1 Diode measurements

The series (R_s) and shunt (R_{sh}) resistances of the diodes fabricated using chemically treatment graphene have been estimated using the dark J - V characteristics as shown in Figure 6.10. The series resistance can be obtained by calculating the inverse of the slope of the J - V curve at the open-circuit voltage and the shunt resistance could be determined from the inverse of the slope of the J - V curve at the short circuit condition $V=0$. As a reference, LiF-based device has exhibited the lowest values for both resistances R_s (4 Ω) and R_{sh} (90 k Ω) compared to the two treated devices S143 and S144 as shown in Table 6.8. For series resistance R_s , treated devices have high values in comparison to Ref. device, with S143 and S144 obtained 13 Ω and 9 Ω , respectively. The main reason for these high series resistances is attributed to the clear presence of pinholes and due to polymer/surfactant which has been added to the buffer layer. However, improved contact properties between the active layer and the back (Al) electrode will result in low series resistance due to the stronger interfacial adhesion [2]. In general, under dark condition, the devices displayed good rectifying characteristics as current stayed at almost 0 mA from -1V and turned on at almost 0.75 V for the all three devices as shown in Figure 6.10, where it started to increase showing clear rectifying behaviour. This non-linear behaviour indicates that the very low current from -1 V up to 0.5 V reflects the lack of carriers in the structure and thus a non-conducting behaviour.

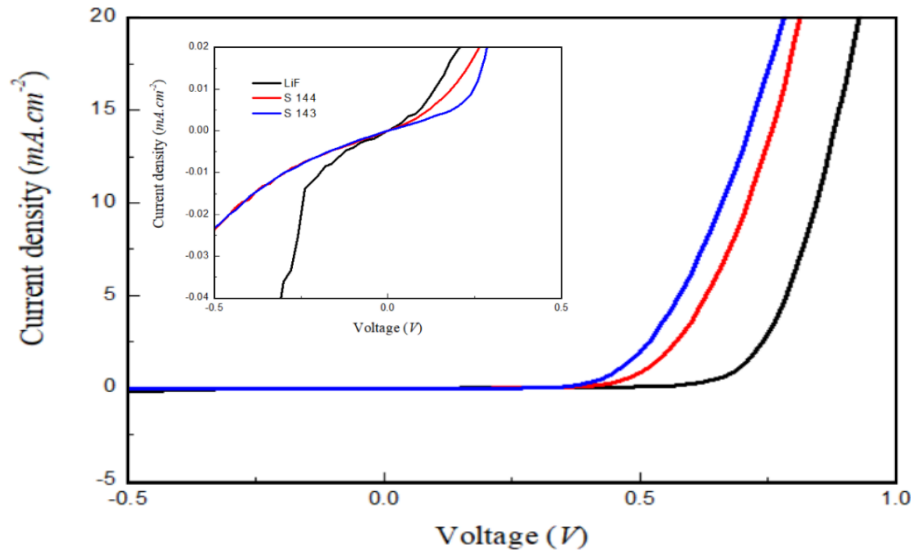


Figure 6.10: J - V characteristics of the OBHJ solar cells under the dark for different devices with and without treated Gr. The inset figure represents leakage current for devices.

As for R_{sh} , treated devices presented significant increase compared to the LiF-based device which has R_{sh} of 90 k Ω . For S143 device, R_{sh} = 550 k Ω while for S144 device, R_{sh} = 870 k Ω . These values indicate that the power loss in the solar cell through an alternate current path is very small.

Parasitic Resistances		
Devices	Shunt resistance (k Ω)	Series resistance (Ω)
LiF	90	4
S143	550	13
S144	870	9

Table 6.8: *Diodes parasitic resistances for P3HT:IC₇₀BA device with LiF and treated Gr.*

To investigate the recombination under dark condition, the diode ideality factor n is extracted from the dark J – V curve in Figure 6.11 using following equation

$$E = \frac{hc}{\lambda} \quad (6.1)$$

Under high voltage (>0.5 V) for all three devices, most of the current density is influenced by the parasitic effects raised by shunt resistance and series resistance. The values of ideality factors are responsible for the reduced slope of dark J – V curves due to the series resistance and shunt resistance. For the LiF device, the value of the minimum diode ideality factor is found as 1.90, while for the S143 treated devices, the value of diode ideality factor is the maximum and be found 1.4. For the S144 treated devices, the value of diode ideality factor is 1.15 as demonstrated in Table 6.9. S144 device has exhibited lower recombination rate as indicated by the device ideality factor.

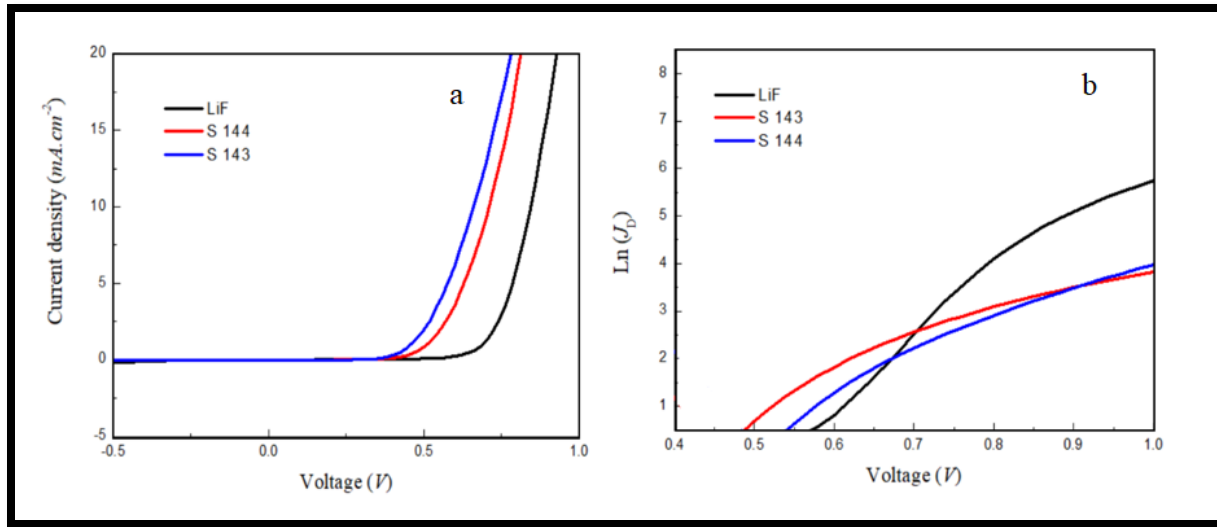


Figure 6.11: a) J - V characteristics of the OBHJ solar cells under the dark for different devices with and without treated Gr. b) Variation of $\ln(J_D)$ versus the bias voltage for different devices with and without treated Gr.

Device	Ideality factor (n)
LiF	1.90
S143	1.4
S144	1.15

Table 6.9: Ideality factors for diode devices.

6.3.4.2 Photovoltaic performance

The influence of chemically treated graphene on device photovoltaic behaviour has been investigated. Figure 6.12 (a) shows the J - V curves of the two different treated device under the illumination of AM1.5G, 100 mW.cm^{-2} . The efficiency of devices can be obtained from the peak power curve of devices as shown in Figure 6.12(b). The device parameters are listed in Table 6.10. The device with LiF shows a PCE of 5.5% with a J_{sc} of 12.5 mA.cm^{-2} , a V_{oc} of 0.79 V, and a fill

factor (FF) of 56%. The J_{sc} of device S143 increased from 12.5 mA.cm^{-2} to 42.3 mA.cm^{-2} , while V_{oc} decreased to 0.49 V, which results in a reasonably high PCE of 9.4% with a fill factor (FF) of 54%. For S144 device, The J_{sc} can be simultaneously and significantly improved. The J_{sc} increased to 50.8 mA.cm^{-2} , with V_{oc} decreased to 0.61 V, which results in a high PCE of 13.7% (more the 300% improvement) with a fill factor (FF) of 55%.

For shunt resistances R_{sh} and series resistances R_s , it is clear from Table 6.10 that the values of shunt resistances R_{sh} are better in comparison to Ref. device. Further analysis of the device characteristics appears to indicate that the OPVs with the graphene as ETLs have a reduced series resistance (R_s) compared to the Ref. device. the graphene positively affects the charge extraction (transportation) in the OPVs studied.

This increase in the device's performances could be assigned to graphene and polymer/surfactant inducing photon harvesting as well as improving charge carriers transport. The obtained higher FF could be ascribed to the lower recombination rate in these devices as demonstrated by the lower ideality factor values as well as low R_s and high R_{sh} . FF represents the efficiency of charge collection before they recombine inside the cell, which basically depends on the charge carriers' mobility and the charge carriers' recombination rate [41] as well as the improvement in the series resistance (R_s). The enhancement in OSC device performance after chemical treatment could be ascribed to the enhancement in the electrical conductivity of the new blends as well as the increase in charge carriers' mobility, which in turn improves the short circuit current density. The effect of the distribution of treated graphene within the P3HT:IC₇₀BA blend could increase the interface area within the blend, and thus result in improved charge carrier's generation (larger J_{sc}) and charge transport (larger FF) [46]. However, the higher concentration S143 film has shown slightly smaller PCE and FF . The smaller values of J_{sc} could be attributed to the higher concentration of treated graphene, which is thought to provide lower photons absorption intensity compared to lower one; the V_{oc} has demonstrated significant change. These results provide further confirmation of the reproducibility of these devices [41].

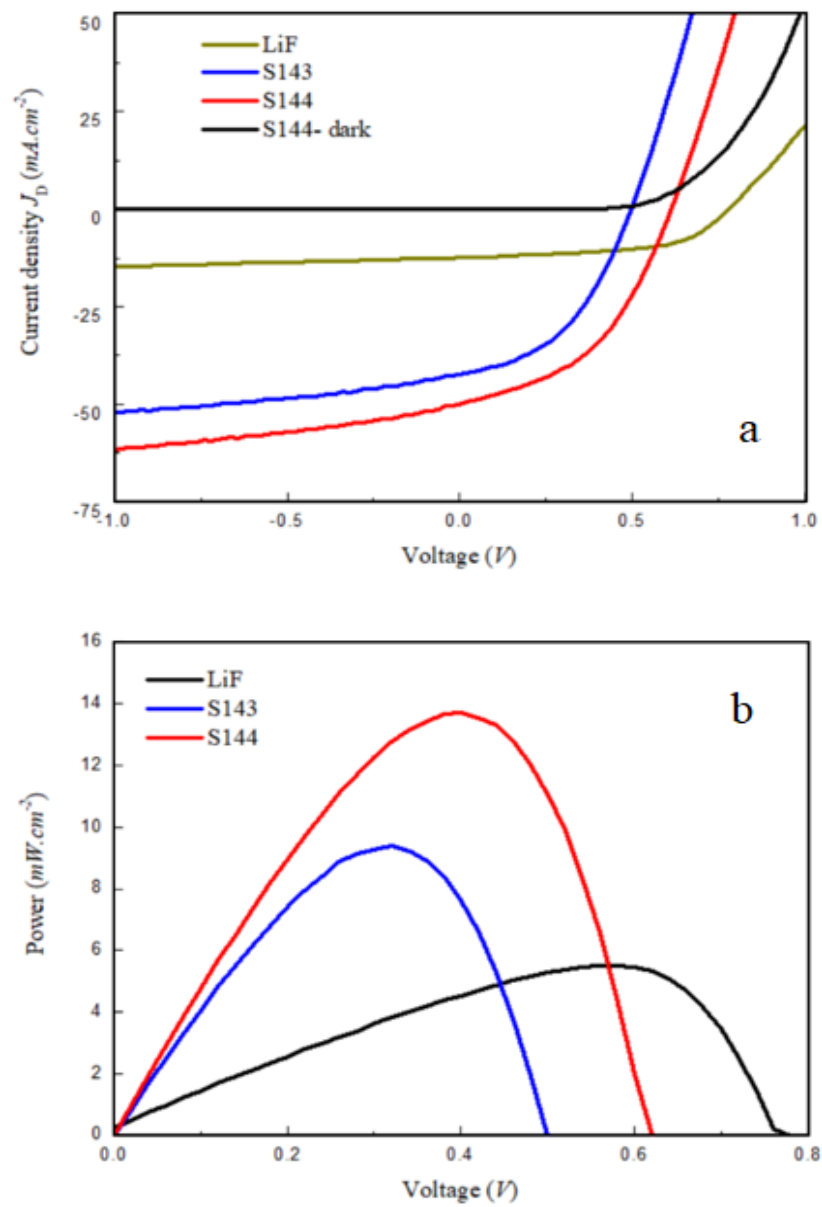


Figure 6.12: a) J - V characteristics of the OBHJ solar cells under the illumination for different devices with and without treated Gr as ETL. b) Variation of power curves for different devices with and without treated Gr as ETL.

Device	Jsc (mA.cm ⁻²)	Voc (V)	FF (%)	PCE (%)	R _{sh} (Ω)	R _s (Ω)
LiF	12.5	0.79	56	5.5	2500	1.5
S143	42.3	0.49	54	9.4	3200	2.95
S144	50.08	0.61	55	13.7	4300	2.64

Table 6.10: *The J-V characteristics for the P3HT: IC₇₀BA based devices under illumination for different concentrations of treated graphene.*

6.4 Summary

The aims of this chapter is to improve the efficiency of fabricated devices. This chapter can be divided to two main parts: first: investigation of graphene as electron transport layer on the performance of devices, and second: study the influence of chemically treated graphene on the parameter of solar cell.

For the first part, S103 and S203 showed remarkable improvement in the current density values, which are $J_{sc} = 67.4 \text{ mA.cm}^{-2}$ and 41.7 mA.cm^{-2} for S103 and S203, respectively compared to reference device which is $J_{sc} = 21.3 \text{ mA.cm}^{-2}$. The devices which have Gr as ETL shown slight decrease improvement for shunt R_{sh} , whereas series R_s resistances have shown slight improvements under illumination for just S103 and S203 devices. The current density has raised to 50.08 mA.cm^{-2} for S144 device and 42.3 mA.cm^{-2} for S143 device compared to reference device which is $J_{sc} = 21.5 \text{ mA.cm}^{-2}$. For open circuit voltage V_{oc} , improvements have been noticed for most of devices, especially for S102 and S201 which are 0.65 V for both. For fill factors FF , both groups devices showed decrease values.

For the second part, it was observed that treated graphene influenced significantly the OHJ solar cells efficiency. Reference device used with LiF electron transport layer has shown PCE of 5.5% , this value has increased to 9.4% and 13.7% , which are of the highest reported parameters for OSCs using P3HT:IC₇₀BA blend, for S143 and S144, respectively. The treated Gr devices have shown slight decrease improvement for shunt R_{sh} , whereas series R_s resistances have shown slight improvements under illumination. J_{sc} has raised to 50.08 mA.cm^{-2} for S144 device and 42.3 mA.cm^{-2} for 143 device compared to LiF device which is $J_{sc} = 12.5 \text{ mA.cm}^{-2}$. For V_{oc} , a decrease in both devices which are 0.49 V and 0.61 V for S143 and S144, respectively. Finally, for FF , both devices showed slight improvement.

References

- [1] A. K. Geim and K. S. Novoselov, "The rise of graphene," *Nat. Mater.*, vol. 6, no. 3, pp. 183–191, Mar. **2007**.
- [2] A. K. Geim, "GRAPHENE: STATUS AND PROSPECTS A. K. Geim Manchester Centre for Mesoscience and Nanotechnology, University of Manchester, Oxford Road M13 9PL, Manchester, UK," *Prospects*, no. 6, pp. 1–8, **2009**.
- [3] M. Kadhem and B. A. Hasan, "11 . 4 % efficiency of organic solar cells using Graphene electron collecting buffer layer as a novel work 11 . 4 % efficiency of organic solar cells using Graphene electron collecting buffer layer as a novel work," no. December 2019, 2018.
- [4] S. Ganguly and J. J. Ghosh, "Steroid hormone induced alterations in endometrium: I. Changes in lipid content, swelling pattern & lipid peroxidation of mitochondria," *Indian J. Biochem. Biophys.*, vol. 16, no. 2, pp. 61–65, **1979**.
- [5] V. C. Tung, M. J. Allen, Y. Yang, and R. B. Kaner, "High-throughput solution processing of large-scale graphene," *Nat. Nanotechnol.*, vol. 4, no. 1, pp. 25–29, **2009**.
- [6] P. K. Ang, W. Chen, A. T. S. Wee, and P. L. Kian, "Solution-gated epitaxial graphene as pH sensor," *J. Am. Chem. Soc.*, vol. 130, no. 44, pp. 14392–14393, **2008**.
- [7] Y. Xu, W. Hong, H. Bai, C. Li, and G. Shi, "Strong and ductile poly(vinyl alcohol)/graphene oxide composite films with a layered structure," *Carbon N. Y.*, vol. 47, no. 15, pp. 3538–3543, **2009**.
- [8] R. R. Nair et al., "Fine structure constant defines visual transparency of graphene," *Science (80-.)*, vol. 320, no. 5881, p. 1308, **2008**.
- [9] P. Blake et al., "Graphene-based liquid crystal device," *Nano Lett.*, vol. 8, no. 6, pp. 1704–1708, **2008**.
- [10] L. Gomez De Arco, Y. Zhang, C. W. Schlenker, K. Ryu, M. E. Thompson, and C. Zhou, "Continuous, highly flexible, and transparent graphene films by chemical vapor deposition for organic photovoltaics," *ACS Nano*, vol. 4, no. 5, pp. 2865–2873, **2010**.
- [11] D. I. Son et al., "Flexible organic bistable devices based on graphene embedded in an insulating poly(methyl methacrylate) polymer layer," *Nano Lett.*, vol. 10, no. 7, pp. 2441–2447, **2010**.

- [12] C. A. Di, D. Wei, G. Yu, Y. Liu, Y. Guo, and D. Zhu, "Patterned graphene as source/drain electrodes for bottom-contact organic field-effect transistors," *Adv. Mater.*, vol. 20, no. 17, pp. 3289–3293, **2008**.
- [13] P. Matyba, H. Yamaguchi, G. Eda, M. Chhowalla, L. Edman, and N. D. Robinson, "Graphene and mobile ions: The key to all-plastic, solution-processed light-emitting devices," *ACS Nano*, vol. 4, no. 2, pp. 637–642, **2010**.
- [14] G. Jo et al., "Large-scale patterned multi-layer graphene films as transparent conducting electrodes for GaN light-emitting diodes," *Nanotechnology*, vol. 21, no. 17, **2010**.
- [15] S. Bae et al., "Roll-to-roll production of 30-inch graphene films for transparent electrodes," *Nat. Nanotechnol.*, vol. 5, no. 8, pp. 574–578, **2010**.
- [16] W. Liu et al., "Large scale pattern graphene electrode for high performance in transparent organic single crystal field-effect transistors," *ACS Nano*, vol. 4, no. 7, pp. 3927–3932, **2010**.
- [17] T. CamposHernández et al., "Electrochemical and Spectroelectrochemical Characterization of Graphene Electrodes Derived from Solution-Based Exfoliation," *Electroanalysis*, vol. 27, no. 4, pp. 1026–1034, **2015**.
- [18] J. Nelson, "Organic photovoltaic films," *Mater. Today*, vol. 5, no. 5, pp. 20–27, **2002**.
- [19] H. Hoppe and N. S. Sariciftci, "Organic solar cells: An overview," *J. Mater. Res.*, vol. 19, no. 7, pp. 1924–1945, **2004**.
- [20] A. Gombert and A. Luque, "Photonics in photovoltaic systems," *Phys. Status Solidi Appl. Mater. Sci.*, vol. 205, no. 12, pp. 2757–2765, **2008**.
- [21] Y. Lin et al., "100-GHz Transistors from," *Nano*, vol. 327, no. 5966, p. 100, **2010**.
- [22] ")). These characteristics were measured using two-source measuring units (Keithley **2612**), with a Ag/AgCl gate electrode.," *Science* (80-.), no. Keithley 2612, pp. 1–5.
- [23] S. Sun, L. Gao, and Y. Liu, "Enhanced dye-sensitized solar cell using graphene- TiO₂ photoanode prepared by heterogeneous coagulation," *Appl. Phys. Lett.*, vol. 96, no. 8, pp. 1–4, **2010**.
- [24] F. Traversi, V. Russo, and R. Sordan, "Integrated complementary graphene inverter," *Appl. Phys. Lett.*, vol. 94, no. 22, pp. 1–4, **2009**.
- [25] V. Saini et al., "Electrical , Optical , and Morphological Properties of P3HT-MWNT Nanocomposites Prepared by in Situ Polymerization," pp. 8023–8029, **2009**.

- [26] Mervat Kadhem Erhaima, "Synthesis of P3HT:ICBA for High Efficiency Organic Solar Cell University of Baghdad in Partial Fulfillment of the Requirements for the Degree of Doctor of Philosophy in Physics," University of Baghdad , **2017**.
- [27] A. You, M. A. Y. Be, and I. In, "Enhancement in performance of polycarbazole-graphene nanocomposite Schottky diode," vol. 122120, no. October **2013, 2017**.
- [28] M. Gresil, Z. Wang, Q. Poutrel, and C. Soutis, "Thermal Diffusivity Mapping of Graphene Based Polymer Nanocomposites," Sci. Rep., no. January, pp. 1–10, **2017**.
- [29] E. A. Parlak, "The blend ratio effect on the photovoltaic performance and stability of poly(3-hexylthiophene):[6,6]-phenyl-C 61 butyric acid methyl ester (PCBM) and poly(3-octylthiophene):PCBM solar cells," Sol. Energy Mater. Sol. Cells, vol. 100, pp. 174–184, **2012**.
- [30] R. Bkakri, O. E. Kusmartseva, F. V. Kusmartsev, M. Song, and A. Bouazizi, "Degree of phase separation effects on the charge transfer properties of P3HT:Graphene nanocomposites," J. Lumin., vol. 161, pp. 264–270, **2015**.
- [31] P. Kovacik, "Vacuum Deposition of Organic Molecules for Photovoltaic Applications," p. 151, **2012**.
- [32] X. Jing, D. Zhenbo, L. Chunjun, X. Denghui, X. Ying, and G. Dong, "Effect of LiF buffer layer on the performance of organic electroluminescent devices," Phys. E Low-Dimensional Syst. Nanostructures, vol. 28, no. 3, pp. 323–327, **2005**.
- [33] Y. Shen, K. Li, N. Majumdar, J. C. Campbell, and M. C. Gupta, "Bulk and contact resistance in P3HT:PCBM heterojunction solar cells," Sol. Energy Mater. Sol. Cells, vol. 95, no. 8, pp. 2314–2317, **2011**.
- [34] Y. Zhou, T. M. Khan, J. W. Shim, A. Dindar, C. Fuentes-Hernandez, and B. Kippelen, "All-plastic solar cells with a high photovoltaic dynamic range," J. Mater. Chem. A, vol. 2, no. 10, pp. 3492–3497, **2014**.
- [35] C. M. Proctor and T. Q. Nguyen, "Effect of leakage current and shunt resistance on the light intensity dependence of organic solar cells," Appl. Phys. Lett., vol. 106, no. 8, **2015**.
- [36] A. Mekki et al., "Graphene controlled organic photodetectors," Synth. Met., vol. 217, pp. 43–56, **2016**.
- [37] S. Das, D. Pandey, J. Thomas, and T. Roy, "The Role of Graphene and Other 2D Materials in Solar Photovoltaics," vol. 1802722, pp. 1–35, **2019**.

- [38] H. Hoppe et al., “Nanoscale morphology of conjugated polymer/fullerene-based bulk-heterojunction solar cells,” *Adv. Funct. Mater.*, vol. 14, no. 10, pp. 1005–1011, **2004**.
- [39] B. Y. Kadem, “P3HT:PCBM-based organic solar cells: optimisation of active layer nanostructure and interface properties,” Sheffield Hallam University, **2017**.
- [40] P. S. Chandrasekhar and V. K. Komarala, “Graphene/ZnO nanocomposite as an electron transport layer for perovskite solar cells; The effect of graphene concentration on photovoltaic performance,” *RSC Adv.*, vol. 7, no. 46, pp. 28610–28615, **2017**.
- [41] K. D. G. I. Jayawardena et al., “Solution processed reduced graphene oxide/metal oxide hybrid electron transport layers for highly efficient polymer solar cells,” *J. Mater. Chem. A*, vol. 1, no. 34, pp. 9922–9927, **2013**.

Chapter 7

Conclusions and Further Work

7.1 Conclusions

In this thesis, a scientific approach has been used to optimize organic photovoltaic (OPV) devices by modifying the hole transport layer (HTL) and the use of graphene (Gr) as electron transport layer (ETL). All devices were prepared using Poly(3-hexylthiophene-2,5-diyl) (P3HT) as the donor and indene-C70 bisadduct (IC₇₀BA) as the acceptor in the fabrication of the active layer. Poly(3,4-ethylenedioxythiophene):poly(styrenesulfonate) (PEDOT:PSS) was used as the bases of the hole transport layer, and all these layers were deposited using spin coating method. Indium tin oxide (ITO) used as anode and aluminium (Al) was evaporated as a cathode. Optical, electrical, and the morphological properties were investigated in all stages of these fabricated organic solar cells using different techniques such as UV visible spectrophotometer, atomic force microscopy (AFM) and *J-V* calculations. In this work, it is demonstrated that graphene (Gr) and metal salts such as Copper Chloride (CuCl₂) and Lithium Chloride (LiCl) are potential candidates to be used as ETL and to modify HTL, respectively to obtain highly efficient organic solar cells.

Generally, the practical work in this research could be divided into three chapters. First one is the optimisation of P3HT:IC₇₀BA-based organic solar cells. The second part is improvement of OPV performance using modified hole transport layers using different metal salts. The last chapter is investigated the use of graphene (Gr) as ETL. The power conversion efficiency (*PCE*) has been raised from 2.8%, for devices without electron transport layer (ETL), to 13.7% by using chemically treated thin film Gr as ETL. (*J*_{sc}) has a remarkable improvement from 17.04 mA.cm⁻² to 67.4 mA.cm⁻² by using Gr as ETL. In addition to these positive results, (*V*_{oc}) has been raised from 0.33 V, for no ETL devices, to 0.81 V by using copper chloride CuCl₂ (0.1) for the modification of the HTL.

In the first chapter of practical part, blends of IC₇₀BA and P3HT as the active layer were used to fabricate OBHJ solar cells. The *J-V* characteristics for all fabricated devices have been measured in the dark as diodes and under illumination with a halogen lamp (100 mW.cm⁻²). The

optimizations in this part of the research were carried out in a systematic approach through the following modifications:

1. Different solvents for the active layer.
2. Different concentrations of active layer.
3. Different annealing temperature.
4. Different annealing time.
5. Using a buffer layer.

In the case of different solvents optimization, three different solvents were used to dissolve the active layer. These materials are chlorobenzene (CB), dichlorobenzene (DCB) and their co-solvent Mix (DCB:CB). In order to achieve an optimum PV behaviour, the morphology roughness, optical properties and electrical properties of the OPV devices have been investigated. Devices based on DCB solvent has shown the best results for all parameters. (*PCE*) of 2.8%, (J_{sc}) of 17.04 mA.cm⁻², (V_{oc}) of 0.33V, (*FF*) of 55% and the lowest (*n*) of 1.5. This was ascribed to the improvement in the interpenetrating network, which facilitates charge carriers transport properties, and hence improved solar cell performance.

For different concentrations of the active layer (P3HT:IC₇₀BA), five different concentrations have been investigated as follow: (10 mg:10 mg), (17 mg:17 mg), (25 mg:25 mg), (15 mg:20 mg) and (20 mg:15 mg) in 1 mL of (DCB). The concentration of 17 mg:17 mg has given the highest results. With respect to (*PCE*), the performance of the device has raised from 2.8% to 3.5%, and (J_{sc}) of 15 mA.cm⁻². For V_{oc} , it improved from 0.33V to 0.46V and with *FF* of 49%. Moreover, the ideality factor (*n*) decreased from 1.5 to 1.35. This is attributed to electrons have more mobility than holes in semiconductor materials and therefore increasing the ratio between donor material (P3HT) and acceptor material (IC₇₀BA) to (17 mg:17 mg) leads to increase in molar mass of compound which creates more excitons.

Furthermore, three different annealing temperatures have been investigated which are 150 °C, 175 °C and 200 °C. The best results were for 150 °C which show the same behaviour of the previous (17mg:17mg) concentrations. It is noticed that, as the heat-treatment temperature was increased the *FF* and the surface roughness decrease. However, the ideality factor increases with the increasing of annealing temperature.

Different annealing times have been also investigated through different times as follow; 10 minutes, 20 minutes, 30 minutes, 40 minutes and 50 minutes. From all of these annealing times, the best results were for devices annealed for 20 minutes, which yielded significant improvement in *PCE* from 3.5% to 4.7% and J_{sc} of 15 mA.cm⁻² to 21.2 mA.cm⁻². However, a slight decrease in V_{oc} from 0.46 V to 0.43 V was observed, while the ideality factor is almost ideal with 1.05. Generally, increasing the time of annealing may cause damage for the active layer.

The last investigation in this part of the research was for using lithium fluoride (LiF) as a buffer layer, which made a significant enhancement to most of the parameters. An improvement in *PCE* from 4.7% to 5.5%, V_{oc} = 0.79 V, *FF* of 56% and J_{sc} = 12.5 mA.cm⁻². The main reason for such improvement can be attributed to the fact that the LiF layer protects the active layer underneath when the (Al) is evaporated, resulting in less Al diffuses into the film which may be responsible for forming high conducting channels leading to recombination.

In the second part of the research, improved OSC performance by modified (HTL) by using different metal salts, which are copper chloride (CuCl₂) and lithium chloride (LiCl) have been used to modify Poly(3,4 ethylenedioxythiophene):poly(styrenesulfonate) (PEDOT:PSS). Three different concentrations of each metal salt have been used in this investigation. This study aimed to investigate the effect of metal salts with (0.1, 0.2, and 0.4) % concentrations on the performance of organic heterojunction solar cells. The device based on the typical hole transport layer (PEDOT:PSS) has shown a *PCE* of 5.5%. In the case of CuCl₂, it was observed that increasing the concentration of the metal salt influence negatively the solar cells efficiency performance. The highest results were recorded for CuCl₂ (0.1) with high *PCE* of 17.11% and J_{sc} , was of 35.12 mA.cm⁻². The open circuit voltage has slight increase from 0.79V to 0.81V, *FF* has also improved from 56% to 60%.

On the other hand, the typical hole transport layer (PEDOT:PSS) which has *PCE* of 5.5% showed a remarkable improvement to 18.4% as a result of doping the PEDOT:PSS layer with LiCl(0.2). For (J_{sc}), it enhanced almost 400% from 12.5 mA.cm⁻² to 43.12 mA.cm⁻² and slight decrease for V_{oc} from 0.79 V to 0.77 V. For (*FF*), it is almost the same at 55%.

In the last practical chapter, the effect of graphene (Gr) as an electron transport layer (ETL) has been investigated. This part contains two sections of work. The first one, for untreated graphene preparation, two different concentrations of 10 mg and 20 mg of graphene (Gr) were dissolved in

2 mL of deionised water (DI) water each were used as ETL. The second part, same Gr but treaded chemically as follow:

20 mg of graphene was mixed with 1 g of the polymer/surfactant and dissolved in 10 ml methanol and placed in ultrasonic bath for 3-4 hours. For the sample S143, the surfactant of Poly(styrene-co-acrylic acid) was used and for S144, the surfactant of JONCRYL HPD 496 was used.

Initially, the device based on LiF as electron transport layer has shown a *PCE* of 5.5%. Devices based on Gr with concentration of 10 mg/2 mL with the lowest thickness (~ 8-12 nm) showed significant improvement in J_{sc} by more than 300% from 12.5 mA.cm⁻² to a value of 67.4 mA.cm⁻², which leads to a high *PCE* of 10.4% with *FF* of 42% and V_{oc} of 0.37 V.

For treated graphene device S144, the J_{sc} increased to 50.8 mA.cm⁻², with V_{oc} decreased to 0.61 V, which results in a high *PCE* of 13.7% (more the 300% improvement) with a *FF* of 45%. Table 7.1 summarizes the key findings in this research. The improvement of *PCE* by using Gr, ascribed to the high conductivity of Gr.

Device	J_{sc} (mA.cm ⁻²)	V_{oc} (V)	<i>PCE</i> (%)	Chapter
Without ETL	17.04	0.33	2.8	4
With (LiF) as ETL	12.5	0.79	5.5	4
HTL modified with LiCl (0.2)	43.12	0.77	18.4	5
HTL modified with CuCl ₂ (0.1)	35.12	0.81	17.11	5
Untreated Gr (S103) used as ETL	67.4	0.37	10.4	6
Treated Gr (S144) used as ETL	50.08	0.61	13.7	6

Table 7.1: Summary of key findings in this research.

7.2 Further work

For pursuit as a result of this work in order to improve the efficiency of organic solar cells based on these new materials, there are many methods available:

1. Determine the HOMO and LUMO energy levels of modified transport layers as the molecular energy level control are of great importance in improving photovoltaic properties of conjugated polymers.
2. Study of thermal annealing effect on these material at low temperatures between 0⁰C and 50⁰C to determine the optimal temperature to enhance the branches and improve their efficiency.
3. Study the photovoltaic parameters for what have been done in one time instead of investigating the effect each modification separately.
4. Fabrication and characterisation of organic solar cells with salt-based modified HTL and Gr as the LTL.